Jónas Thór Snæbjörnsson

Full- and model scale study of wind effects on a medium-rise building in a built up area

NTNU Trondheim
Norges teknisk-naturvitenskapelige universitet

Doktor ingeniøravhandling 2002:95
Institutt for konstruksjonsteknikk

FULL- AND MODEL SCALE STUDY OF WIND EFFECTS ON A MEDIUM-RISE BUILDING IN A BUILT UP AREA

by

Jónas Thór Snæbjörnsson

Doctoral Thesis

Department of Structural Engineering
Norwegian University of Science and Technology
Trondheim, Norway

September 2002

Abstract

The present study deals with full- and model scale study of wind effects on a medium-rise building in a built up area.

Most low-rise building experiments have been based on an isolated building placed in a relatively uniform terrain. Similarly, the very tall buildings often extend out from their environment in a similar fashion. However, buildings are constructed in various shapes and placed in different types of terrain and topography. Therefore, despite a number of studies made in the past, there are still problems that remain unsolved.

As the majority of office- and residential buildings in populated areas fall in the intermediate height category, it should be of interest to examine the wind effects acting upon such a building, as well as its dynamic response. For this purpose, an experimental program was initiated utilising a combination of full-scale measurements and wind tunnel studies, where the fluctuating wind actions are evaluated from recorded simultaneous point pressure fluctuations. Recent improvements in experimental techniques and data handling enable a more detailed information gathering that should eventually lead to an improved understanding of the pressure field around buildings.

The investigation studies, experimentally, the wind induced dynamic loading and response of a multi-story building of intermediate height. The presented work evolves on one hand around experimental data acquisition in both full- and model scale, whereas on the other it evolves around basic data reduction, understanding and interpretation of the acquired data.

The objective of the study is, in a way, to attempt to provide a sound wind loading chain a la Davenport [29], in the form of data that would facilitate the study of the links connecting the main parameters i.e. Wind – Load – Response. This entails the definition of the relevant wind parameters, the description of the aerodynamic loading process, such as the time-dependent variations of pressure fluctuations on the building surface, and an investigation of the wind induced response of a medium-rise building.

Information on the study-building and the experimental setup and procedures is given, for both full-scale and model scale. The full-scale and model scale data are systematically compared through the evaluation of descriptive parameters of both wind turbulence and surface pressures.

In general, the evaluated full-scale parameters are found to be in qualitatively good agreement with the model scale parameters. However, the investigation revealed some characteristic differences between full-scale and model scale behaviour. These differences are largely related to the fact that significant variability is found to be inherent in the full-scale data, whereas considerably less variability seems to be associated with the wind tunnel data.

Acknowledgments

As can be expected, this work is a product of the combined effort of many and I would like to extend my appreciation to all who contributed to its making.

I especially thank my advisors Professor Erik Hjorth-Hansen of the Norwegian University of Science and Technology (NTNU) in Trondheim and Professor Ragnar Sigbjörnsson of the University of Iceland in Reykjavik for their support and valuable suggestions during the course of this research. They gave me freedom to pursue the research in the manner I saw fit, while providing guidance when requested.

Tanks are due to Professor Tom A. Wyatt of the Imperial Collage of Science, Technology and Medicine in London UK, Svend Ole Hansen of Svend Ole Hansen ApS in Copenhagen Denmark and Professor Einar Strømmen of the Norwegian University of Science and Technology in Trondheim for participating as members on the thesis committee.

The author is in debt to Per-Åge Krogstad and his people in the Experimental Fluid Dynamics Research Group at NTNU for their assistance during the wind tunnel experiment, as well as the people at the Department of Structural Engineering at NTNU for their assistance during my stay in Trondheim.

I am grateful to Dr. Roger P. Hoxey at the AFRC Silsoe Research Institute for his advice during the preparation of the full-scale experiments and for the loan of one of his static pressure sensors.

Thanks are also due to my colleagues at the Applied Mechanics Laboratory of the Engineering Research Institute of the University of Iceland for their miscellaneous assistance in the acquisition and handling of the full-scale data, as well as their patience toward this venture.

Landsvirkjun, the National Power Company, graciously allowed the use of their office building for the full-scale experiment. The support of Jóhann Már Maríusson, Deputy Director, is especially acknowledged.

The data provided by the Icelandic Meteorological Office is gratefully acknowledged as well as the assistance of Trausti Jónsson and Hreinn Hjartarsson in acquiring the meteorological data.

Financial support was provided by the following organisations: Engineering Research Institute at the University of Iceland, the Norwegian Univ. of Science and Technology, the Icelandic Research Council, the University of Iceland Research Fund, the Icelandic Research Fund for Graduate Students, NorFA (mobility scholarship), the Research Council of Norway (Norwegian government scholarship) and NATO (science fellowship). This financial support is gratefully acknowledged.

Finally, I would like to convey my gratitude to my wife Ingunn and my children, Thorunn and Bergthor, for their endurance and quiet support throughout this endeavour.

Contents

List of symbols

Scalars, functions, matrices and vectors

A_b	parameter describing the bandwidth of a spectral density peak
A, B, C, D	state-space system matrices
A_x, A_y	constants for a particular building shape,
a	slope parameter of a best line fit to wind velocity versus temperature data for a specific wind directional sector.
a_{x1}	acceleration recorded at location no. 1 in the x-direction
a_{y1}	acceleration recorded at location no. 1 in the y-direction
a_{x2}	acceleration recorded at location no. 2 in the x-direction
a_x	acceleration, uncoupled translational component in the X direction
a_y	acceleration, uncoupled translational component in the Y direction
a_θ	acceleration, uncoupled rotational component
a_{1i}, a_{2i},…a_{ni}	AR-parameters of a system
a_j	AR-parameters of a system
a_{max}	maximum of recorded acceleration time series
a_{min}	minimum of recorded acceleration time series
B	building width
b	zero-offset parameter of a best line fit to wind velocity versus temperature data for a specific wind directional sector.
b_i	body forces (gravity etc.)
b_j	MA-parameters of a system
C_{xy}	coherence function of time series X and Y
C_p	pressure coefficient
$\overline{C}_P$, C_{Pm}	mean pressure coefficient
c_f	correction coefficient for the wind velocity recorded above the roof of the study-building
D_{ij}	rate-of-deformation tensor
e	zero-mean disturbance of stochastic process, i.e. white-noise exogenous input
F_u, F_v, F_w	parameter in the ESDU turbulence spectra, see Table 4.2
f_c	Coriolis parameter ($f= 2\,\Omega \sin\Phi$)
f	frequency in Hz
f_1	natural frequency for the first mode of vibration
f_j	natural frequency for the j-th mode of vibration
f_a, f_b	frequency band limits
G_u	gust factor
g	acceleration of gravity (9.81 m/s^2)
g_a	peak factor for acceleration

g_p	peak function
$H(z)$	complex transfer function
$H_j(z)$	complex transfer function for the j-th mode of a system
h	height
h_a	anemometer height
h_b	building height
I_i	turbulence intensity of the i-th fluctuating wind velocity component, $i \in \{u,v,w\}$
I_u	turbulence intensity of the fluctuating along-wind velocity component
I_w	turbulence intensity of the fluctuating vertical wind velocity component
i	index
j	index
K_m	kinematic eddy viscosity
k	index
k_a	von Karmans coefficient (generally taken to be 0.4)
k_x	exponent (Eq. 6.2)
k_y	exponent (Eq. 6.3)
L	Monin-Obukov length
${}^xL_i, {}^yL_i, {}^zL_i$	length scales of turbulence relating to the i–th component of turbulence in the x (along) , y (across) and z (vertical) direction respectively
${}^xL_u, {}^xL_v, {}^xL_w$	length scales of turbulence in the x-direction (along wind direction) relating to u, v and w turbulence components respectively
m	modal mass
N	number of samples
n_c	number of cycles in an autocorrelation function
n	total number of estimated parameters
$\tilde{n}$	normalised frequency
n_a	order of an AR-model, number of autoregressive parameters and number of poles in the transfer function $H(z)$
n_b	number of moving average parameters
O_f	static pressure offset
P	pressure
P_r	reference pressure
P_s	surface pressure
p_i	the i-th pole of $H(z)$
q_s	spectral density ratio i.e. $\lvert S(f)\rvert_{\max}/S(f_1)$
q_i	the i-th residue of $H(z)$
Q_R	mean dynamic velocity pressure
Q_{rc}	required, or corrected, mean dynamic velocity pressure
$R_i(X, Y, Z+z, t)$	cross-covariance function of the i-th velocity component along the Z axis in space, $i \in \{u,v,w\}$
$R_i(\tau)$	auto-covariance function of the i-th turbulence component at a single point for time-lag τ, $i \in \{u,v,w\}$

R_u	auto-covariance function of the along-wind turbulence component at a single point
$R_{x\theta}$	cross-correlation function of a_x and a_θ
$R_y(k)$	auto-correlation function of $y(t)$ for lag k
r_j	modulus of the j-th pole
r_{x1}	distance between accelerometer location no. 1 and the centre of rotation along the x-axis in a rectangular co-ordinate system
r_{x2}	distance between accelerometer location no. 2 and the centre of rotation along the x-axis in a rectangular co-ordinate system
r_{y1}	distance between accelerometer location no. 1 and the centre of rotation along the y-axis in a rectangular co-ordinate system
r_{uw}	correlation coefficient of the u and w wind components
S_a	auto spectral density of acceleration
S_i	one-sided auto-spectral density of the i-th turbulence component
S_{pp}	one-sided power spectral density of pressure
S_u	one-sided power spectral density of turbulence
S_{uu}	auto spectral density of along wind turbulence
S_{xx}, S_{yy}	auto spectral densities of the respective time series X and Y
S_{xy}	cross spectral density of time series X and Y
$S_{x\theta}$	cross spectral density of a_x and a_θ
$S_{\theta\theta}$	auto spectral density of a_θ
T	mean ambient temperature in degrees Celsius
T_i	integral time scale of the i-th turbulence component
T_u	integral time scale of along-wind turbulence
T_w	integral time scale of vertical turbulence
t	time
U_i	three dimensional velocity vector
$\overline{U}_i$	mean wind velocity vector
$\overline{U}$	mean along wind velocity.
$\lvert U_u \rvert_{\max}$	largest maximum (observed) along wind velocity during a given period
$\overline{U}_h$	mean wind velocity at roof level of the building
$\overline{U}_c$	corrected reference mean along wind velocity
$\overline{U}_R$	mean wind velocity at some reference height
u_*	shear frictional velocity
u_i	three dimensional gust vector
u	along-wind turbulence component
V	loss function (quadratic fit) for a model fitting
v	across-wind turbulence component
v	state vector
w	zero-mean disturbance of stochastic process
w	vertical turbulence component
$X(z)$	z-transform of an input sequence

x	input sequence
x_i	three dimensional space variable
x_t	input sequence
x_D, x_H, x_K	normalised frequency, see Table 4.2
$Y(z)$	z-transform of an output sequence
y	displacement response
y	output sequence
y_t	output sequence
$z = \exp(j\omega\Delta t)$	complex variable
z	height above ground
z_0	surface roughness length
z_R	reference height
Δt	sampling interval (period)
Δf	sampling rate in Hz
$\Delta\theta$	change in temperature or temperature difference (degrees Kelvin)
α	power law exponent (Table 4.3) and parameter in the ESDU turbulence spectra, see (Eq. 4.42)
α_1, α_2	autoregressive parameters
β_1, β_2	moving average parameters
β_a, β_b	parameters in the ESDU turbulence spectra, see Table 4.2
β_u, β_v, β_w	ratio of the variance of wind velocity component and the shear velocity squared
χ_P	The velocity-pressure admittance function
δ_{ij}	Kronecker's delta.
Φ	angle of latitude at site
ϕ	wind direction, i.e. angle of attack
ϕ_j	argument of the j-th pole (or its complex conjugate)
κ	surface roughness coefficient
λ, μ	coefficients of molecular viscosity
μ_0, μ_1, μ_2	spectral moments, i.e. the 0^{th}, 1^{st} and 2^{nd}, respectively
π	ratio of the circumference of a circle to its diameter i.e. 3.14159265...
θ	temperature in degrees Kelvin
ρ_a	density of air
ρ_b	average building density
$\sigma_{\ddot{x}}$	standard deviation of acceleration in the along-wind direction
$\sigma_{\ddot{y}}$	standard deviation of acceleration in the across-wind direction
σ_a	standard deviation of acceleration
σ_d	standard deviation of displacement
σ_e	standard deviation of a noise process feeding an AR model
σ_i	standard deviation of the i-th fluctuating wind velocity component, $i \in \{u,v,w\}$
σ_{ij}	stress tensor
σ_u	standard deviation of along-wind velocity

σ_v	standard deviation of velocity
σ_w	standard deviation of vertical wind velocity
σ_ϕ	standard deviation of wind direction
σ_θ	standard deviation of temperature (degrees Kelvin)
τ	time lag
τ_{ij}	Reynolds stress tensor
τ_{xz}	Reynolds shear stress in the *xz* plane
Ω	angular rotation of the earth (= 72.9×10^{-6} rad/s)
ω	circular frequency in radians per second
ω_a, ω_b	circular frequency band limits
ω_j	natural circular frequency for the *j*-th mode
ψ_m	a similarity function for the mean wind velocity profile
ζ	critical damping ratio
ζ_1	critical damping ratio for the first mode of vibration
ζ_j	critical damping ratio for the *j*-th mode of vibration
(X, Y, Z)	global system co-ordinates
(x_1,y_1) ; (x_2,y_2)	co-ordinates of accelerometers
(x_R,y_R)	co-ordinate of the centre of rotation (or overall motion)

Operators

$\mathrm{E}[\cdot]$	expectation operator
$\ln(\cdot)$	natural logarithm
∇	gradient operator
∂	partial derivative
$\forall_f$	for all frequencies
$\langle X \rangle$	time average value of X
$\hat{X}$	peak value of X
$\overline{X}$	mean value of X
σ_X	standard deviation of X
X_{median}	median value of X
$\lvert X \rvert$	absolute value of X
$Z(x_k)$	*z*-transform of process $x(k)$
$\mathrm{d}/\mathrm{dt} = \partial_t + \mathrm{v}\nabla$	Lagrangian (or *total*) time-derivative
$\left[X\right]_{FS}^{tap_i}$	X is recorded at pressure tap no. i, in a full-scale experiment
$i \in \{u, v, w\}$	i can be either u, v or w component
$\exp(\cdot)$	exponential operator
$\times$	multiplication (“times”)
$\mathrm{f}[\cdot]$	function of the variable within the bracket
$\max(R_y)_k$	maximum amplitude of the autocorrelation function of response y at cycle k

Abbreviations

AR	autoregressive
AR(n)	AR of order n
ARMAX	autoregressive moving average with exogenous variables
ARX	autoregressive with exogenous variables
CFD	computational fluid dynamics
equiv.	equivalent
ERI	Engineering Research Institute, University of Iceland
FIR	finite impulse response
FPE	final prediction error
FS	full-scale signature
IMO	Icelandic Meteorological Office
MA	moving average
max	maximum
min	minimum
MS	model-scale signature
NTNU	Norwegian University of Science and Technology
tap_i	pressure tap number i

Chapter 1 Introduction

1.1 Background and related studies

The present work deals with full- and model scale study of wind effects on a medium-rise building in a built up area.

Proper consideration of wind effects is an important aspect of successful building design. The effects are multifaceted and depend on various physical conditions. The wind flow around buildings creates loading and associated response of both structural and cladding elements. Wind effects are inherently of dynamic nature, whereas the structural loading and response can be considered either as quasi-static, dynamic or aero-elastic depending on the response characteristics of the structure.

The slenderness ratio of buildings gives an indication of the wind flow around buildings and the respective response characteristics. When the building is tall, $2H/B > 1$, the larger part of the approaching wind flows around the sides of the building, rather than over the top. However, when the building is low or squat, $2H/B < 1$, the wind flows mainly above the building, rather than around its sides [22]. Because of this characteristic difference it is appropriate to discuss these two building categories separately.

1.1.1 High-rise buildings

High-rise buildings are generally wind sensitive structures. Their dynamic response dominates the total response, which affects the structural design with regard to both structural safety and serviceability. In addition to this, because of their height, cladding loads are substantial. The wind flow around the high-rise buildings also affects the comfort of pedestrians in the surrounding area, the ventilation of the building etc.

Numerous full-scales studies of high-rise buildings have been undertaken, especially in the late 1960s and early 1970s when several interesting studies were ongoing in different countries. BRE conducted a programme of full-scale wind pressure measurements on tall buildings in the UK, such as the Vickers Building [141] and Royex House ([140],[139]) in London. Dalgliesh et. al ([23],[24],[33]) carried out a similar, although perhaps more extensive, experiment at the Commerce Court Tower in Toronto, Canada, recording wind induced pressures, acceleration response and window deflections and supplementing the investigation with wind tunnel studies. Holmes reported on an experiment using the Menzies building in Australia [63]. In Japan full-scale activities include experiments at the Waseda University [129]. Later studies include: The BRE investigation of the Hume Point building in UK [122]; several projects in Japan ([88], [143]) including the Chiba Port Tower [144]; and the Main Building of Eindhoven Univ. of Technology [45].

Full-scale studies of high-rise buildings have often concentrated on dynamic response and system identification rather than wind induced pressure distributions or structural loading ([123], [119], [76]). This is partly due to the various practical difficulties in recording valid surface pressures on a large full-scale building. Recording the structural response with accelerometers is on the other hand relatively simple operation and even to include some type of reference wind velocity recording is not an excessive task. Already in 1983, Jeary and Ellis found data from 163 studies in which building motion was measured [80].

Pressure measurements and evaluation of wind loading has on the other hand been dealt with in wind tunnels, using various approaches ([162], [105], [16], [161], [90], [130], [27], [32]). Dynamic response has also been studied in wind tunnels using either aero-elastic models [77] or force-balance techniques [228]. In fact, the wind tunnel has traditionally been the key research and design tool in the mitigation of wind effects on and around tall buildings. This fact inspired the CAARC study [130] in the early seventies, where the CAARC standard tall building model was tested at six establishments in order to compare the model dynamic response and pressure measurements from different simulations of the natural wind characteristics. Its aim was to consolidate the different wind-tunnel techniques and increase confidence in wind tunnel testing of tall buildings.

High-rise buildings have in many ways been more challenging to engineers and researchers, partly because of a more complex dynamic behaviour. Also, such projects are large enough to warrant the funding of wind-tunnel investigations and sophisticated research and design work.

1.1.2 Low-rise buildings

The majority of structures built all over the world can be categorized as low-rise or medium-rise buildings used for residential, commercial and other purposes. Therefore, a large part of wind damage to houses has been restricted to the envelope of low-rise buildings, in particular to the roof sheathing. These evidences indicate that an improvement in wind resistance of the building's envelope will result in a significant reduction in overall

economic losses. This has created a worldwide interest in studying the various aspects of wind effects on low-rise building, and in particular, on roof sheathing.

Jensen in Denmark was probably the first to do a "full-scale" and wind tunnel comparison. In a classic series of experiments [83], he established the need for equality of the ratio of characteristic body dimension and surface roughness length (h/z_0) i.e. the *Jensen number*. Following Jensen's experiments, a number of full-scale and wind tunnel studies have been made with reference to wind effects on low-rise buildings. Uematsu and Isyumov [233], for example, collected and arranged more than 200 research papers on the subject and constructed a database. Stathopoulos [209] and Krishna [103], among others, have presented "state of the art" reviews and Kasperski [96] has published a review of wind load specifications for low-rise industrial buildings in various wind load codes.

Compared to high-rise buildings, relatively many full-scale pressure measurements have been carried out on low-rise buildings. This is probably related to the fact that full-scale pressure measurements can be made more easily for low-rise buildings than for high-rise buildings. This is also be linked to fact, that the determination of wind loads for low-rise buildings from wind tunnel experiments is not entirely straightforward.

One of the problems encountered in wind tunnel testing of low-rise buildings is the determination of geometric scale. The length scale of wind tunnel flows generated by using naturally grown boundary layers ranges from 1/200 to 1/500 in most cases. If building models were scaled according to this length scale, they would be as small as a matchbox, which would result in instrumentation problems and make it impossible to model architectural details such as eaves and parapets, which may play an important role in the wind loading function. Low Reynolds numbers, resulting from small model size, may also cause a distortion of the flow and resulting variations in pressure distributions. Several methodologies have been suggested to solve the question of scale ([83], [62], [209], [32]).

Another problem encountered in the wind tunnel testing is the appropriate modelling of the atmospheric surface layer, in particular close to the ground, at height level of low-rise buildings.

Extensive research has therefore been done using full-scale experimental buildings, in an attempt to reveal the characteristics of both the atmospheric surface layer and the wind pressure on low-rise buildings in natural winds. Another important aspect of the full-scale results is verification and discussion of appropriate wind tunnel methodologies, but comparative wind tunnel studies has been an integral part of most full-scale studies. Reliable full-scale results are also essential for verification and development of CFD modelling of atmospheric flow around buildings.

In this context it is of interest to discuss some of the most noteworthy full-scale low-rise studies:

- The Aylesbury experiment by BRE led the way in the early 1970s [37]. An experimental building with a gable roof was constructed in Aylesbury, England. The plan form, represented by the width (B) x length (L), was 7 m by 13.3 m, and the eaves height (h) was 5 m. A unique feature of this building was that the roof pitch could be varied to any angle ranging from 5° to 45°. One of the more interesting aspects of the Aylesbury project was the Aylesbury comparative experiment that followed [192].

Comparative wind tunnel experiments were conducted at 17 laboratories worldwide using the identical 1:100 model of the Aylesbury building. A comparison between full-scale and wind tunnel measurements indicated that the traditionally used similarity parameter, h/z_0 (Jensen number), is not sufficient to ensure similarity when significant isolated local roughness, such as trees and hedges, are present. Furthermore, it was found that the lab-to-lab variation in pressure coefficients was attributed to differences in the method of data acquisition and in the measuring point of the reference static and dynamic pressures.

- Tests on the Silsoe Structures Building started in the late 1980s ([173],[168],[166]) and were running well into the nineties [170]. This experimental building, constructed at the Silsoe Research Institute in England, was 12.93 m wide, 24.13 m long, 4.14 m high and had a roof slope of 10° (gable roof). The structure consists of seven cold-formed steel portal frames at 4 m centres. Two different eaves cladding details, i.e. a curved eaves detail and a conventional sharp eaves detail, were tested. Extensive measurements have been made of the wind pressures at many locations on the envelope as well as of the strains in some structural members. The full-scale measurements provided a set of benchmark data for verifying wind tunnel experiments and numerical simulations [20-30]. Among the topics investigated is the application of a quasi-steady approach to the evaluation of the design wind loads [31-37]. The Environment Group at the Silsoe Research Institute in UK is still very active in full-scale studies [166], although having recently built a new Atmospheric Flow Laboratory [71].

- The Wind Engineering Research and Flow Laboratory (WERFL) at Texas Tech. Univ. in the USA was initiated in the late 1980s when an experimental building, 9.1 m wide, 13.7 m long and 4.0 m high with an almost flat roof, was constructed at Texas Tech University ([113],[114]). The building can be rotated, permitting control over wind angle of attack. Instruments mounted on a 46 m tower located at the site monitor meteorological conditions. A significant amount of data on the winds and building surface pressures has been collected in various acquisition modes. The recorded data, which are open to all interested researchers, have been used for various analyses [41-47]. Wind tunnel simulations have been carried out at many laboratories all over the world [48-55]; comparisons of the data with the full-scale measurements contributed to a significant improvement in the wind tunnel simulation technique. Experiments and data acquisition at the site are still ongoing [240].

Another full-scale study that deserves to be mentioned is the Smuts experiment in South Africa ([132],[133]), where a hanger at the Jan Smuts Airport in South Africa was instrumented with pressure transducers.

Recently, the following institutes have initiated research programs to study the wind-induced pressures on low-rise structures: The Belgian Building Research Institute (BBRI) is utilising a low-rise experimental building (5 m wide, 10 m long and 5.2 m high, with 30° gable roof) built especially for this purpose [150]; The Johns Hopkins University is

currently taking full-scale measurements on the Kern P. Pitts Center in the town of Southern Shores, North Carolina, USA [160].

1.1.3 Medium-rise buildings

As the above discussion indicates, the great majority of full-scale/wind tunnel investigations have evolved around either comparatively tall or relatively low-rise buildings. Few investigations involve medium or intermediate-rise buildings. Sanni et al [184] defined intermediate height buildings as buildings whose heights are between 20 and 120 m and whose ratio of height to minimum width are not more than four. Only two of the studies mentioned in section 1.1.1 above fall in this category, i.e. Holmes' study of the Menzies building [63] and Geurts' study of the Main Building of Eindhoven Univ. of Technology [45]. The Menzies building is 13 m deep, 140 m wide and 43 m in height whereas the Eindhoven building is 20 m deep, 167 m wide and 44.6 m in height. Both studies were limited to pressure measurements on the two wider sides of the building.

Wyatt [242] presented results of investigations following observations of wind-induced motion of a building of relatively modest size, the main block being a simple rectangular prism 27 m by 12 m in plan and 26 m high above a podium of pre-cast concrete construction. The motion was strongly perceived by the building users but the high response levels were judged to be primarily a result of the exposure of the site. It was also found that torsional motion makes a very important contribution to the response.

Stathopoulus et al. [210] have put forward recommendations for wind loading on buildings of intermediate height. They tested five square building models in the wind tunnel simulating an open country exposure. Statistics of wind-induced pressures were measure and compared with code specifications for low and tall buildings. Low building provisions were found to be satisfactory for design of walls, but not sufficient for the design of roofs.

Sanni et al. [184] studied wind loading on intermediate height buildings. Their wind tunnel study was carried out to assess the applicability of the detailed approach of the NBCC to the class of common intermediate height buildings, such as apartment buildings. General agreement between the test and the code-estimated responses was obtained in the comparisons. The small resonant responses observed provided a basis for deriving a simplified method for estimating the gust factor in the detailed method without the requirement of knowing the structure's dynamic properties. Since intermediate height buildings are often arranged in groups, an experimental study of the interference effects between adjacent buildings was also undertaken. Significant interference effects were found, particularly for the across-wind and torsional moments on buildings in an open exposure. Although the interference effects were not likely to result in amplification of member stresses or forces a set of additional factors of safety were proposed to cover load amplification by interference effects for those members that are very sensitive to overall wind-induced torsional moments.

The cube can often, at least in a non-dimensional sense, be considered an intermediate height building ($2H/B=2$). The geometry of the cube or a square prism is very

popular in various parametric studies of the flow around bluff bodies. The wind tunnel and CFD literature demonstrates this clearly ([14], [72], [186], [194], [227]) and even in full-scale studies, this simple geometry is being studied [166]. These studies will not be described herein, but it is apparent that they are in many respects relevant to the subject of this study.

1.1.4 The present study

Most of the low-rise building experiments mentioned above, have been based on an isolated building placed in a relatively uniform terrain. Similarly, the very tall buildings often extend out from their environment in a similar fashion. However, buildings are constructed in various shapes and placed in different types of terrain and topography. Therefore, despite a number of studies made in the past, there are still problems that remain unsolved. Simplified models based on neutral homogenous flow conditions often give an insufficient description of wind induced effects and response of buildings located in non-homogenous surroundings ([60], [124]). A better understanding and description of the aerodynamic loading process is therefore required. In addition, recent improvements in experimental techniques and data handling enable a more detailed information gathering that should eventually lead to an improved understanding of the pressure field around buildings. As the majority of office- and residential buildings in populated areas fall in the intermediate height category, it should be of interest to examine the wind effects acting upon such a building, as well as its dynamic response.

For this purpose an experimental program was initiated utilising a combination of full-scale measurements and wind tunnel studies, where the fluctuating wind actions are evaluated from recorded simultaneous point pressure fluctuations. The building studied herein is an intermediate height building, 22 m wide, 19 m deep and about 30 m in height (excluding a small one story roof blockhouse). Although its response to wind action is expected to be largely of quasi-static nature, human perception of wind-induced vibration has been reported [197]. Surface point pressure is recorded both on a full-scale building located in a built-up area as well as on a scale model in the wind tunnel.

The investigation, although limited in scope, examines experimentally the wind induced dynamic loading and response of a multistory building of intermediate height. The aim is to provide valid information on the time-dependent variations of pressure fluctuations on the building surface and to investigate the wind induced response of a medium-rise building.

1.2 Outline of the thesis

This study is organized in chapters 2 through 7 as follows:

In Chapter 2 the study-building is introduced, its surroundings described and the full-scale experiment presented. The full-scale experimental setup is described and discussed. Overview is given on the weather conditions during the recording period and some examples of the recorded data displayed.

Chapter 3 presents the wind tunnel experiment. Its set-up is described, the modelling and similarity requirements discussed and an example of recorded data introduced.

Chapter 4 presents an overview on the engineering description of turbulence. Background information on wind characteristics in full- and model scale is introduced, with reference to the wind climate in Reykjavik.

In Chapter 5, the recorded surface pressures from both full-scale and wind tunnel testing are analysed. Pressure coefficients are evaluated and compared. For the full-scale recordings, this required some wind directional and temperature dependent calibration of the reference wind recordings. Spectral characteristics of recorded pressure fluctuations are studied and discussed. Comparison is made between full- and model scale results.

In Chapter 6, a statistical analysis of the acceleration data is performed, the wind induced acceleration response studied and system identification parameters evaluated.

Chapter 7 presents a summary of the results and conclusions of the investigation, along with comments on the work done and suggestions for further research.

In addition to the above seven chapters, there are three Appendices. Appendix A contains photographs of the local surroundings of the study-building. Appendix B has additional information on the coherence of recorded pressure. Finally, Appendix C describes three traditional methods of system identification.

Chapter 2 The full-scale experiment

2.1 The building

The study is focusing on an office building made of reinforced concrete, poured in situ. The building, see Figure 2.1, is a six story tower (cube) approximately 19 x 22 m in area and 22 m high, built upon a two story shopping centre, making it totally eight stories with a height of 30 m. The first floor of the tower above the base structure is slightly inset (~ 1 m).

The structural system of the tower consists of a central shear-core, frames on the outer sides and self-supporting slabs (see Figure 2.2). The structural system of the shopping centre consists mainly of columns and beam-floors, with exterior shear-walls on the lowest level. Stairs and two lifts are located in the shear-core that extends about 3 m above the roof level of the tower, creating a service room where ventilation equipment and lift motors are located.

The building is well suited for a study of this kind. It has a rather simple shape and relatively high wind exposure, as it is located on high ground and extends well above the surrounding buildings. From the service-room on the rooftop, there is an easy access to the flat roof. This makes it possible to investigate the pressure distribution and related parameters around the top part of the tower, without interrupting normal activities in the building.

Wind velocity and wind induced acceleration have been recorded in the building on several occasions. That data has, to some extent, been studied and reported already [197].

Although the building cannot be considered as a particularly wind sensitive structure, according to traditional criteria [196], wind induced vibrations are easily perceived on the upper floors during moderately strong windstorms.

(a) (b)

Figure 2.1 The study-building. (a) View from southeast. (b) View from northwest.

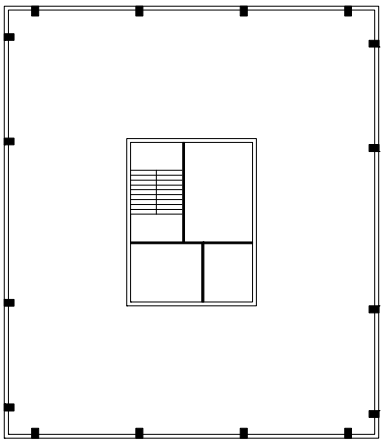

Figure 2.2 A plan of the study-building, showing its structural system, i.e. a central shear core and a column-beam system around the exterior perimeter.

2.2 The site

The building is located in a built up residential area in the city of Reykjavík. Figure 2.3 shows an aerial photo of the western part of Reykjavik. As can be seen, Reykjavik is located on a peninsula surrounded by sea on one hand and mountains on the other. This influences the wind environment considerably and the conditions when the wind blows from the sea can be expected to differ from the conditions when the approaching wind blows from the inland mountains.

Figure 2.3 An aerial view of Reykjavik [163]. The study-building is marked by a star.

Reykjavík is, for the most part, not a densely built city, as is demonstrated in Figure 2.4 which gives an aerial view of the building surroundings. It should be noted that the site of the Icelandic meteorological office (IMO), where reference meteorological data is obtained, is marked on the figure. A closer view of the building neighbourhood is given by Figure 2.5. The houses around the study-building are predominantly residential. To the west of the building, there are rows of single-family houses, mostly 2-stories high. Behind them at the edge of the figure there is a shopping mall and commerce centre with larger and taller buildings, for example one 45 m tall at 500 m distance. To the east of the building, there are several apartment blocks. They are all 4-stories and less than 15 m high. Behind them are smaller two story houses. To the north, there is a similar mixture of apartment blocks and lower houses. The area south of the study-building is more open and there are fewer but larger buildings. For example a 4-story apartment block about 100 m south of the building. The apartment blocks are therefore the nearest and most dominant obstacles. It is likely that they may generate wakes that could influence the approaching wind and thereby the flow pattern around the building.

Figure 2.4 An aerial view of the surroundings of the study-building, which is marked by a white circle. The site of the Icelandic meteorological office (IMO), where reference wind data is obtained, is marked by a white triangle. [163]

Figure 2.5 An aerial view of the neighbourhood of the study-building [138].

2.3 The instrumentation and experimental setup

In preparing and planning the experiment, a notice was taken of the instrumentation used in other similar full-scale studies, as discussed in Chapter 1. The experience from other studies was especially useful with regard to the surface pressure measurements. Dr. Roger P. Hoxey at the Silsoe Research Institute in UK [173] was consulted and the Wind Engineering Research Field Laboratory (WERFL) [113] at Texas Tech University had been visited on earlier occasion. It is only fair to say that use was made of the pressure measurement methodology established in these studies. The main differences lie in the prerequisite that the measurements were not allowed to disrupt the daily operation in the building, which was and is a fully functioning office building. In effect, this meant that the access to the building was limited to the roof and the rooftop service room. Therefore, the pressure taps had to be placed externally on the walls. The reference pressure system was also somewhat different from what has commonly been used in comparable studies.

Figure 2.6 The data acquisition unit and computer in the control room.

The measurement system included 23 data channels connected to sensors that are sampled simultaneously, supplying acceleration (3 channels), surface pressures (12 channels), reference pressures (2 channels), horizontal and vertical wind velocity along with wind direction (3 channels), atmospheric temperature (1 channel), barometric pressure (1 channel) and input voltage to pressure transducers (1 channel).

The data was sampled by a computer, which controls a HP data acquisition unit. The sampling period was 13 minutes, including a 1 minute zero calibration. The sampling rate was 30 Hz. Data recording was triggered by the mean horizontal along wind velocity. If the 13 minute mean horizontal along wind velocity was above 12 m/s, the sampled data was stored in a file on the computer. The computer and data acquisition unit is shown in Figure 2.6. The figure also shows the main power supply, wires, and tubes entering the control room, which was located in the rooftop service room in the centre core of the building.

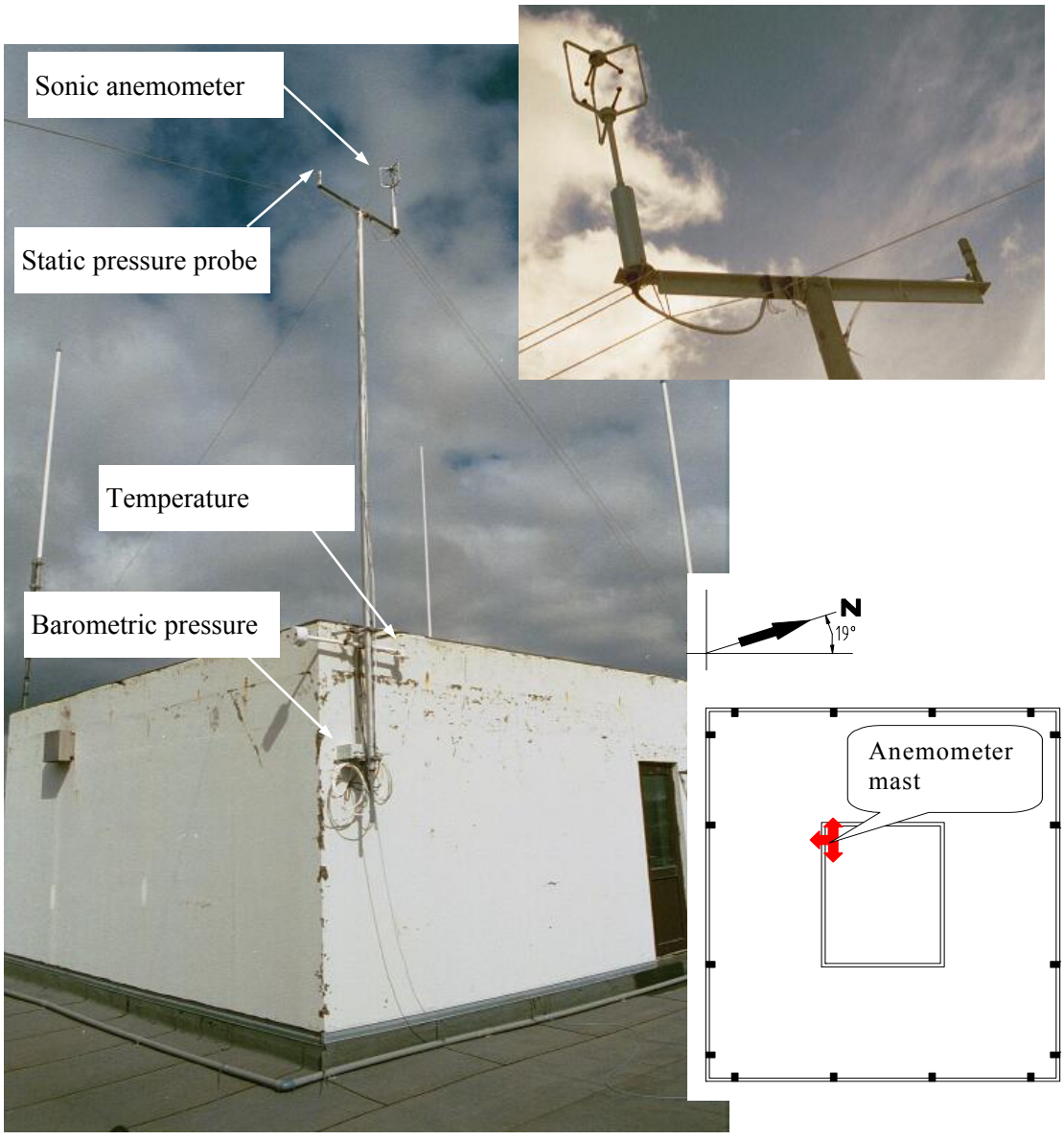

Figure 2.7 The meteorological mast containing the Gill sonic anemometer, reference static pressure sensor [135], temperature sensor and barometric pressure sensor.

2.3.1 Micro-meteorological data

The reference micro-meteorological data measured consists of atmospheric temperature,

barometric pressure, horizontal and vertical wind velocity and wind direction. Temperature was measured at 2 m height above roof level using transducer of the type R.M. Young, model 43347LC. Barometric pressure was also obtained at 2 m height above roof level applying sensors of the type Setra, model 276. Horizontal and vertical wind velocity and wind direction was measured by a Solent meteorological sonic anemometer from Gill Instruments placed on top of a mast extending 8 m above the roof. The mast was fixed to the southwest corner of the service room on the roof.

The choice of the anemometer location is obviously not ideal, but then few places are in a built up environment. During earlier short-term recordings at the same building, an anemometer had been located at the southeast corner of the building. Although that may be a better location considering the along wind velocity from common wind directions, a strong influence from building induced vertical flow was noticed in the vertical velocity. It was therefore decided to try the present location in order to reduce the vertical velocity effect. Wind tunnel measurements also indicated that the speed-up effect of the along wind velocity above the roof was less than 10%.

Meteorological data is also available from a 30 m mast located at the Icelandic Meteorological Office site, about 720 m west of the building.

Figure 2.8 Location of tapping points, view on the southwest and northeast corners of the building.

2.3.2 External pressure

Surface pressures were measured on the face of the building at 12 tap points, utilising differential pressure transducers of the type Honeywell 163PC01D36. The tapping points were located 1.35 m below the edge of the roof and 0.35 m above the windows on the top floor. The tapping points were placed in the centre of 12 plates (60 cm squares) [69], which were distributed around the building perimeter in a single horizontal row. Figure 2.8, gives an idea about the placement of the tapping point plates, whereas Figure 2.10, shows another perspective and how the plates were fixed to the railing on the building roof.

Each tapping point was connected to a transducer by a 2 m long plastic tube with a 5 mm internal diameter. The length and diameter of the tubes controls the frequency response of the pressure system. The tube diameter should not be less than 4 mm to avoid condensation problems [115]. The length of the tube should be as short as possible to maximise the frequency resolution of the system [47]. In this case, 2 m were judged to be a reasonable compromise between the wish to place the tapping points at a comparable height level as the taps on the wind tunnel model, while obtaining a satisfactory frequency resolution.

Each transducer, was placed in a watertight box along with an electrically controlled solenoid valve, see Figure 2.9. The valves were connected to an electric timer. At 12 minute intervals, the valves connected the background pressure to both sides of the transducer for a period of one minute, in order to check zero drift and provide zero calibration. Figure 2.11 shows how the transducer boxes were fixed to the railing on the roof of the building, directly above each tapping point.

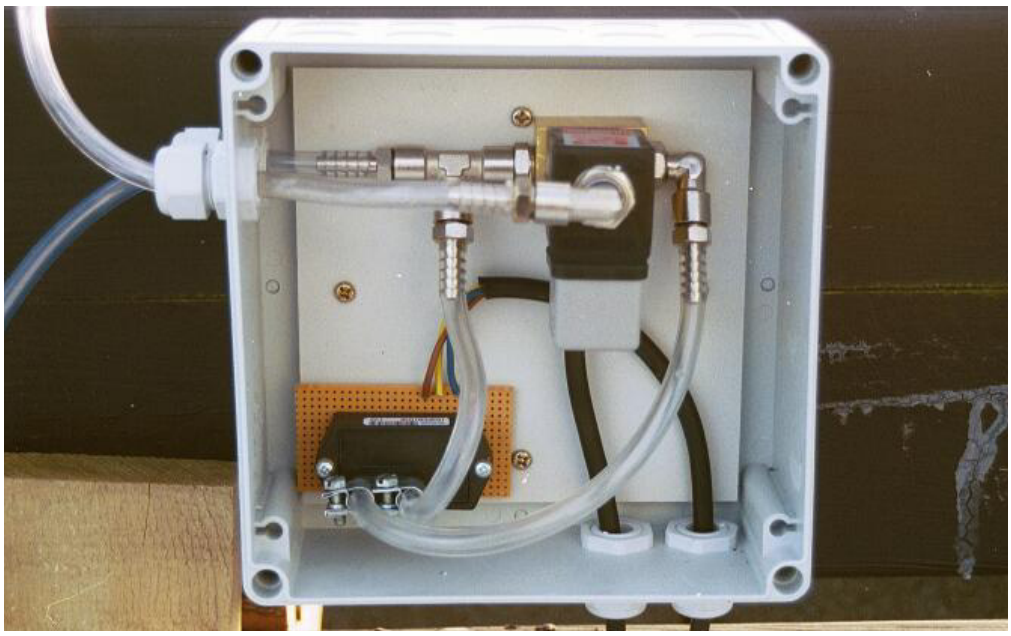

Figure 2.9 A transducer box, containing a pressure transducer, Honeywell 163PC01D36, and a solenoid valve.

Figure 2.10 Location and fixture of tapping point plates on the southward side of the building.

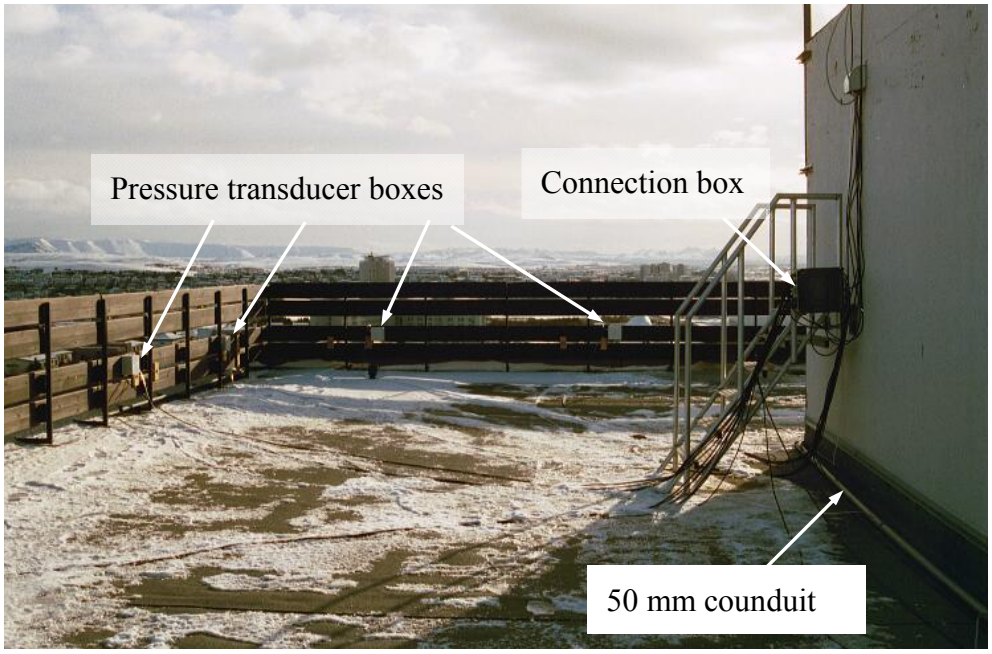

Figure 2.11 Location of pressure transducer boxes on the railing on the roof. Also seen is the connection box, which is fixed to the side of the stair, as well as the tubing system between the transducer boxes and the common pressure reference, i.e. the 50 mm conduit that circles the central service core on the roof.

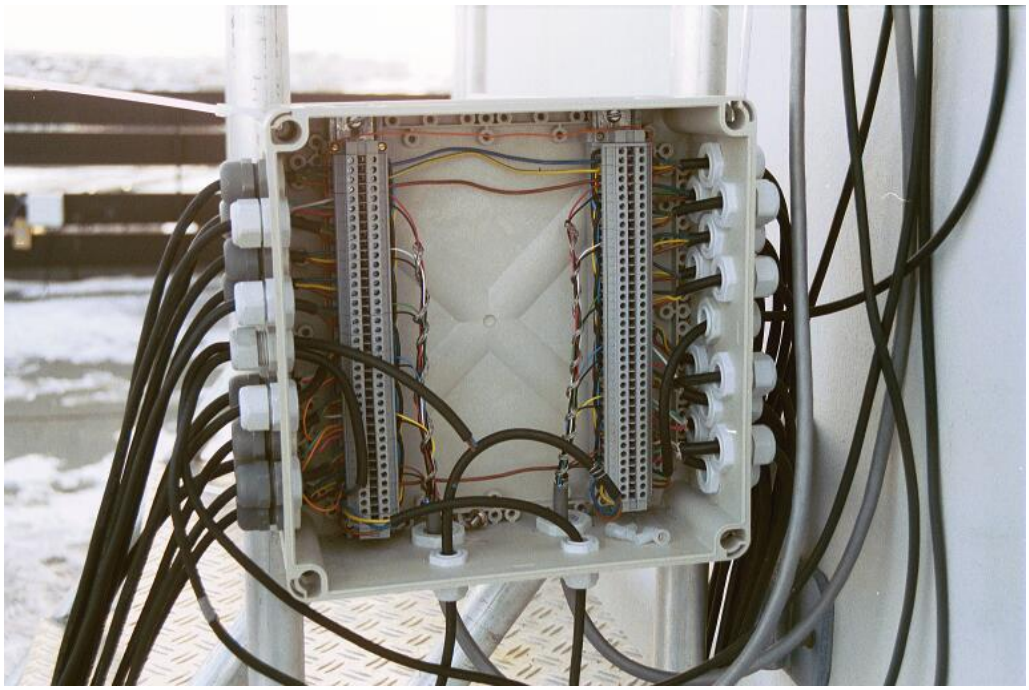

Figure 2.12 The connection box**.**

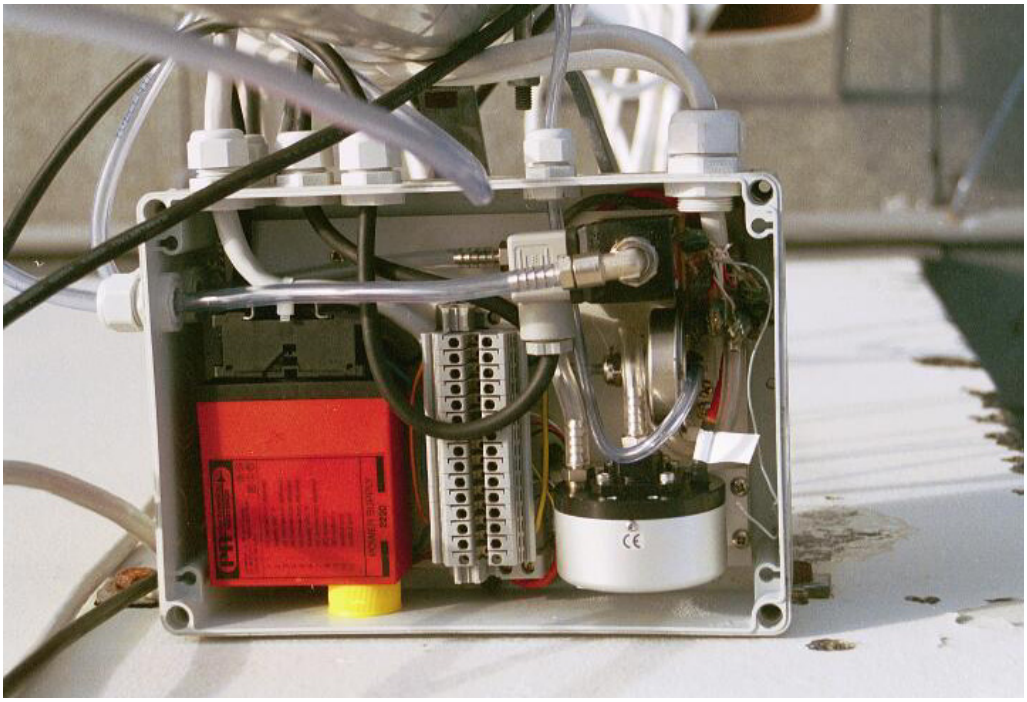

Figure 2.13 A transducer box containing a barometric pressure sensor, Setra 276, reference pressure sensor, Setra 239, solenoid valve and power supply for both pressure sensors as well as the temperature sensor.

Each transducer box was connected via signal-cable to a connection box, which was fixed to the side of a staircase on the roof at the eastward wall of the service core. The connection box is necessary to minimise the number of cables going through the wall into the control room. The connection box allowed for a common power supply for the

transducers on one hand and the solenoid valves on the other. It made it also possible to combine the different signal wires into two signal cables, which then went through a hole in the wall to the data acquisition unit (see Figure 2.6).

2.3.3 Reference pressure

A reference (static) pressure probe [135] was located on top of the mast on the roof, and connected to a differential transducer of the type Setra Model 239 (see Figure 2.13) via a 6 m long plastic tube with a 5 mm internal diameter. Additional differential pressure transducer, Honeywell 163PC01D36, was placed inside the building to record the internal pressure. It was located in a closed service area where occupant disturbance is at a minimum. A solenoid valve was connected to these transducers in the same way as to the surface transducers, and they underwent the same type of zero checking.

All transducers were connected to a single background pressure source located outside the building in a form of a 50 mm conduit that circles the central service core on the roof (see Figure 2.11). Each surface pressure transducer was connected to the conduit by a 9 m long plastic tube with a 5 mm internal diameter. The reference pressure transducers were also connected to the conduit with a plastic tube of 5 mm internal diameter, but the tube lengths were 2 m for the one in the mast and 7 m for the one inside the building.

As the reference tubes are identical for all sensors and the whole system is placed in the same environment, disturbances such as temperature effects should cancel out.

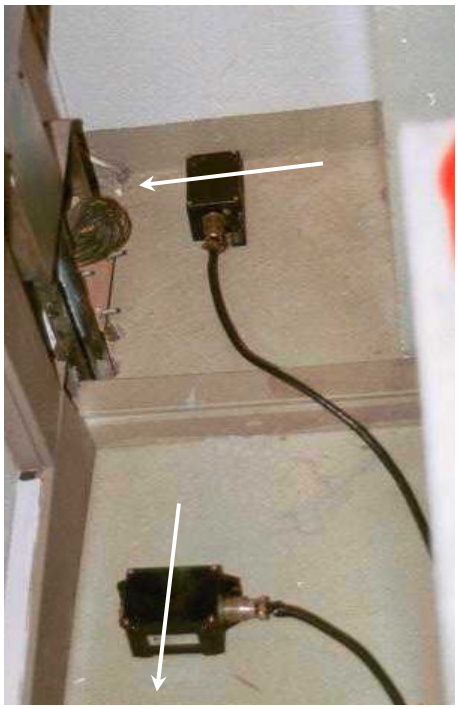

(a)

(b)

Figure 2.14 Accelerometers recording horizontal acceleration. (a) Two are located at the east wall and (b) one at the west wall of the rooftop service room. The arrows indicate the directionality of each acceleration component.

2.3.4 Acceleration

Horizontal acceleration was measured on one level in the building. Three uni-axial accelerometers, Kinemetrics FBA-11, are located on the top floor of the shear core, i.e. at roof level. One sensor recorded acceleration in the east to west direction and two sensors located on opposite sides recorded acceleration in the north to south direction, making it possible to evaluate the rotational component of motion. Figure 2.14, shows the three accelerometers. As can be seen, two perpendicular components of horizontal acceleration are recorded on the floor at the east wall of the rooftop service room whereas one component is recorded at the west wall of the room. Figure 6.1 gives a further overview on relative location and directionality of the accelerometers.

2.4 Overview on the recording period

2.4.1 Introduction

The sampling of full-scale data started on February 15th, 1997 and the instrumentation was dismantled on May 26th, 1997. During this period, a significant amount of data ware collected or approximately 2 Gb, which equals about 475 hours of continuous recording. Figure 2.15, shows the time and date of each sampled data file. Each dot represents a recorded data file, which contains 22 time series of 13-minute duration.

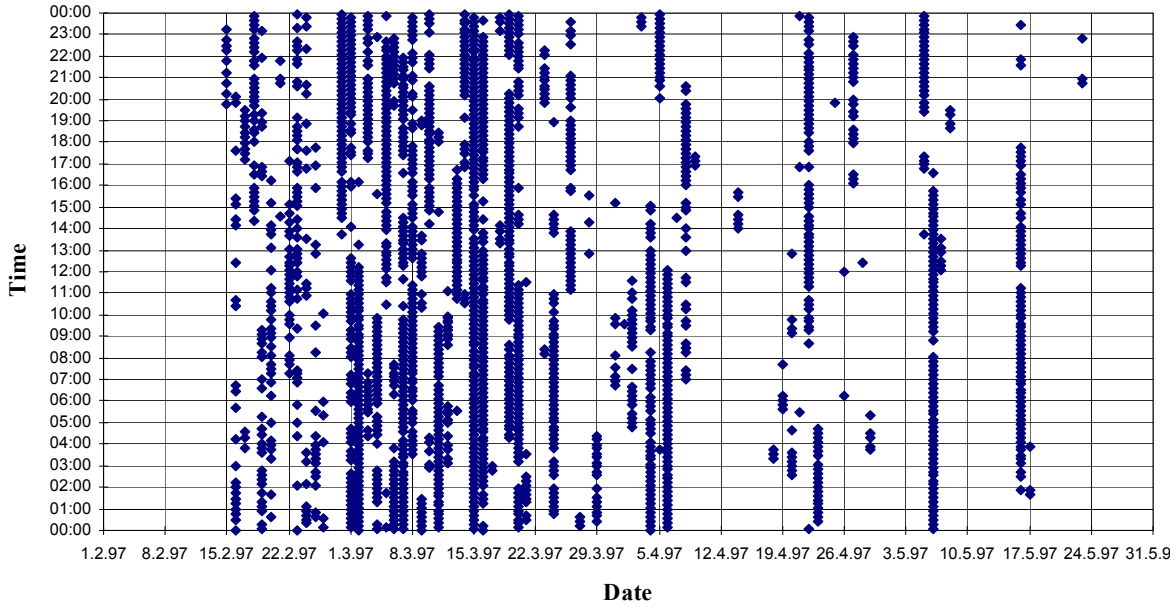

Figure 2.15 Time and date of sampled data. Each dot represents a recorded data file, which contains 22 time series of 13 minute duration.

2.4.2 The weather conditions during the recording period

An overview on the weather conditions during the recording period of full-scale data is given in Figure 2.16, Figure 2.17, and Figure 2.18. The graphs for each parameter are based on a single value for each 24 hours. The date is recorded at the Icelandic Meteorological Office (IMO) at their site about 720 m west of the building. These data are assumed representative for the study area as a whole.

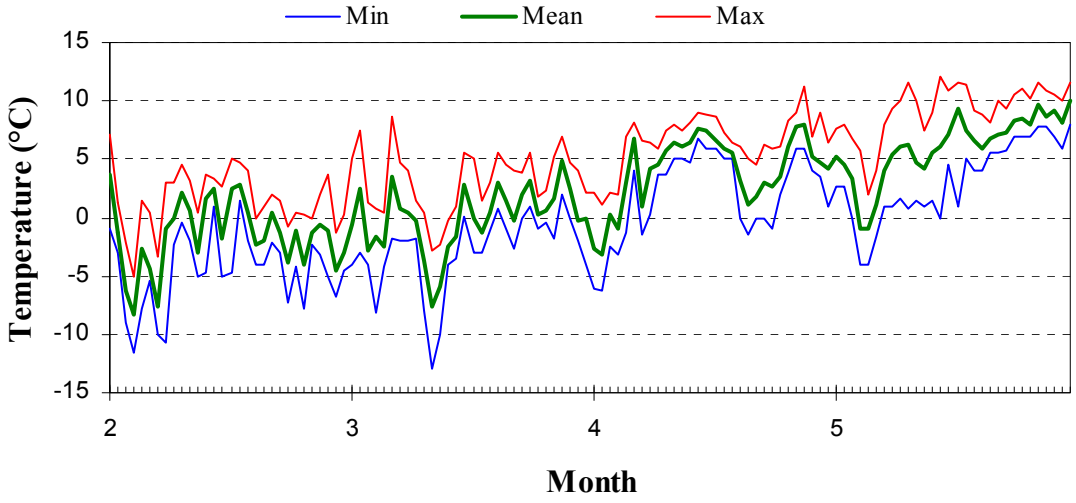

Figure 2.16 Ambient temperature at the IMO site in Reykjavík during the period of February through May 1997. The middle line represents a 24-hour mean value whereas the bottom line and the top line represent the minimum and maximum temperature observed during a 24-hour period, respectively [226].

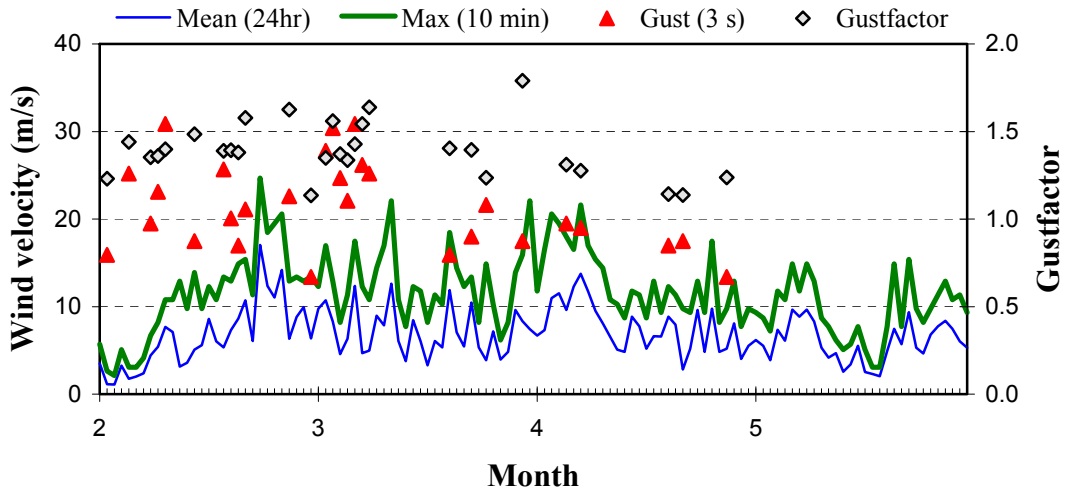

Figure 2.17 Wind velocity at the IMO site in Reykjavík during the period of February through May 1997. The bottom line represents 24-hour mean value, whereas the upper line represents maximum observed 10-minute mean value during 24-hour period. The triangles represent the maximum gust velocities recorded, and the diamonds represent the corresponding gust factors [226].

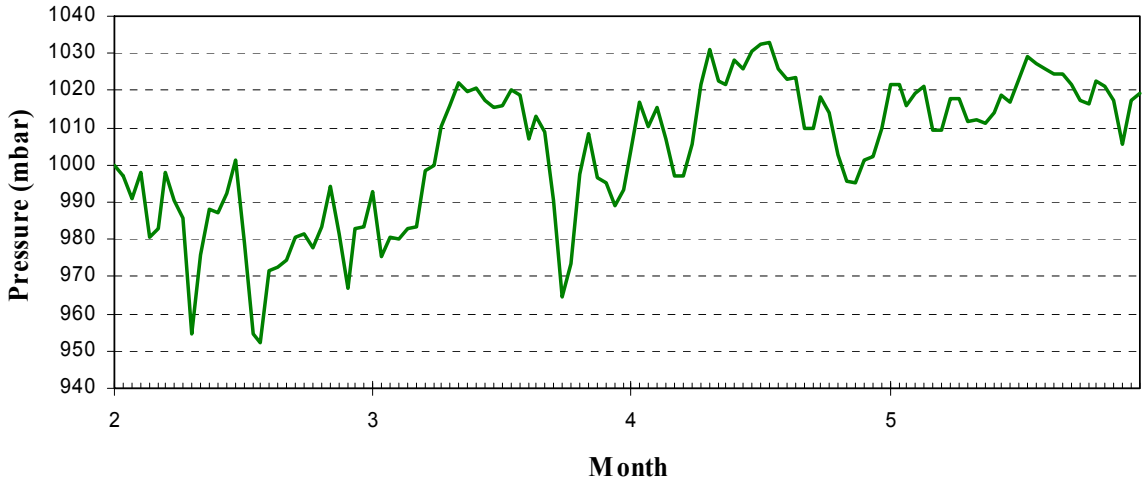

Figure 2.18 Mean barometric pressure at the IMO site in Reykjavík during the period of February through May 1997 [226]. The line represents a 24-hour mean value.

Figure 2.16 shows the variations in temperature during the period of recording. During the study period, the mean temperature was varying between -5 and +5 degrees of Celsius. The general trend of an increasing temperature throughout the recording period is also evident.

Figure 2.17 shows the velocity at 10 m standard reference height. As can be seen there are many days where mean 10-minute wind velocity exceeds 10 m/s. This corresponds well with the amount of recorded full-scale data at the building, presented by Figure 2.15. The gust factor at the Meteorological Office site seems to be around 1.4 on the average, assuming that the mean wind velocity data and the gust data are concurring.

Figure 2.18 shows the variation in mean barometric pressure during the period of recording. The barometric pressure is at its lowest in February, or about 950 mbar. In March, April and May it is generally above 1000 mbar, although occasionally lower values are observed. A general trend of increasing mean barometric pressure throughout the recording period is also evident.

2.4.3 Examples of the recorded data

A brief example of recorded wind velocity and corresponding pressure coefficients is given in the following.

Data recorded during a fairly typical storm on the 5th of April is shown in Figure 2.20 through Figure 2.24. The development of mean wind velocity and mean wind direction during the storm is displayed in Figure 2.20, as recorded in the mast above the roof. As can be seen the wind direction varies from 58° to 77° and the mean wind velocity is above 12 m/s for a period of 16 hours. The maximum mean wind velocity recorded was nearly 23 m/s.

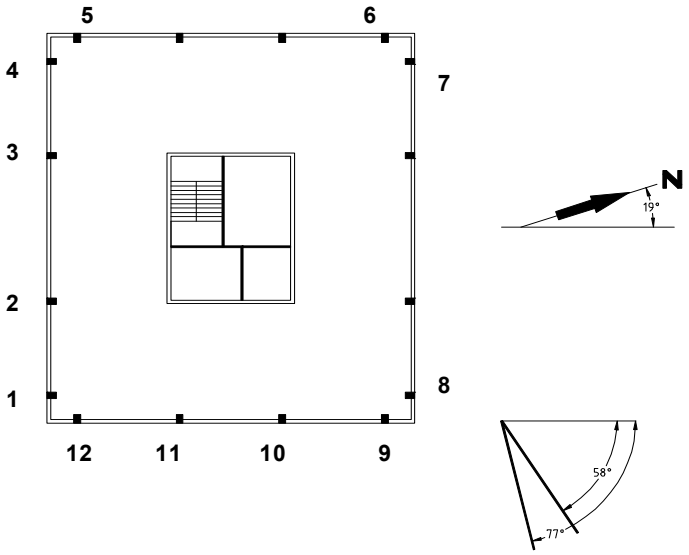

Figure 2.19 A plan of the building, indicating the location of pressure taps and variation in wind direction during a storm a storm on 5 - 6 April 1997.

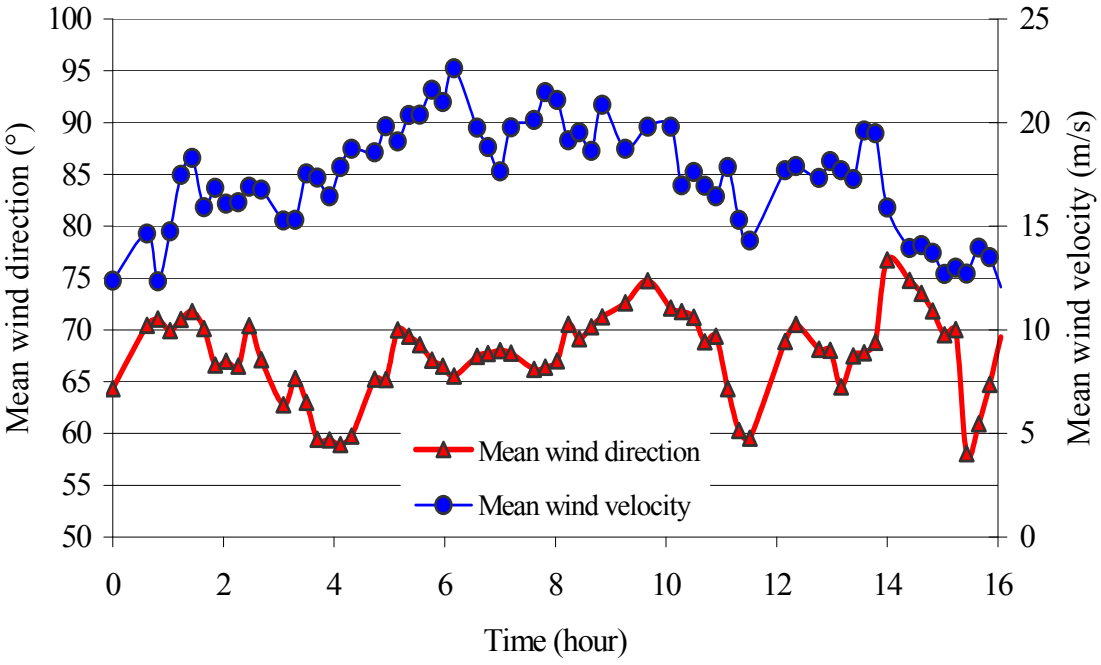

Figure 2.20 Mean wind direction and mean along wind velocity during a storm on April 5-6 1997.

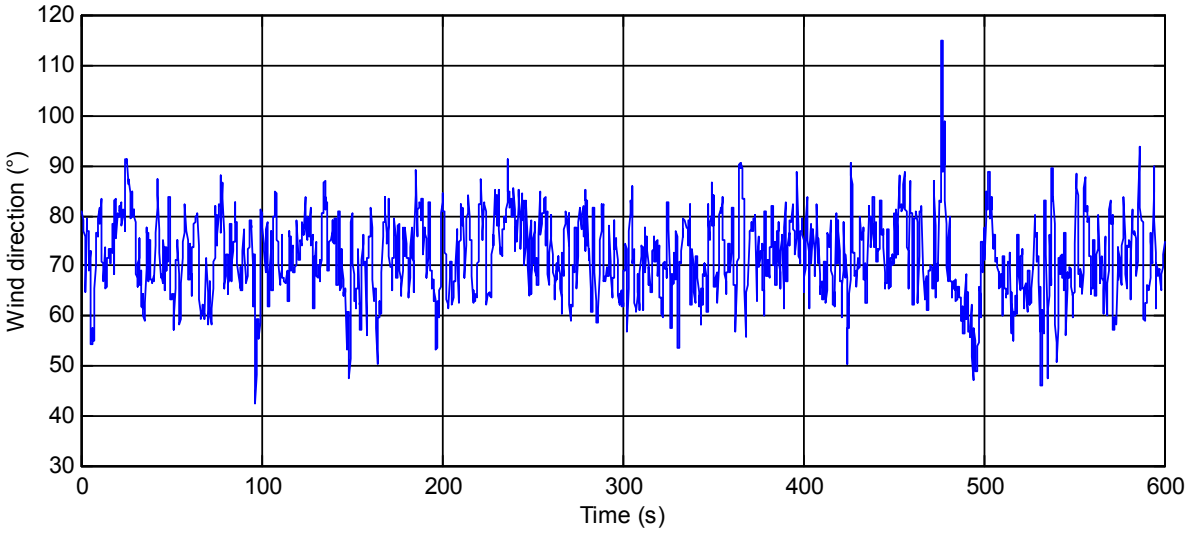

Figure 2.21 Example of a time series of wind direction, recorded during a storm on 5 - 6 April 1997.

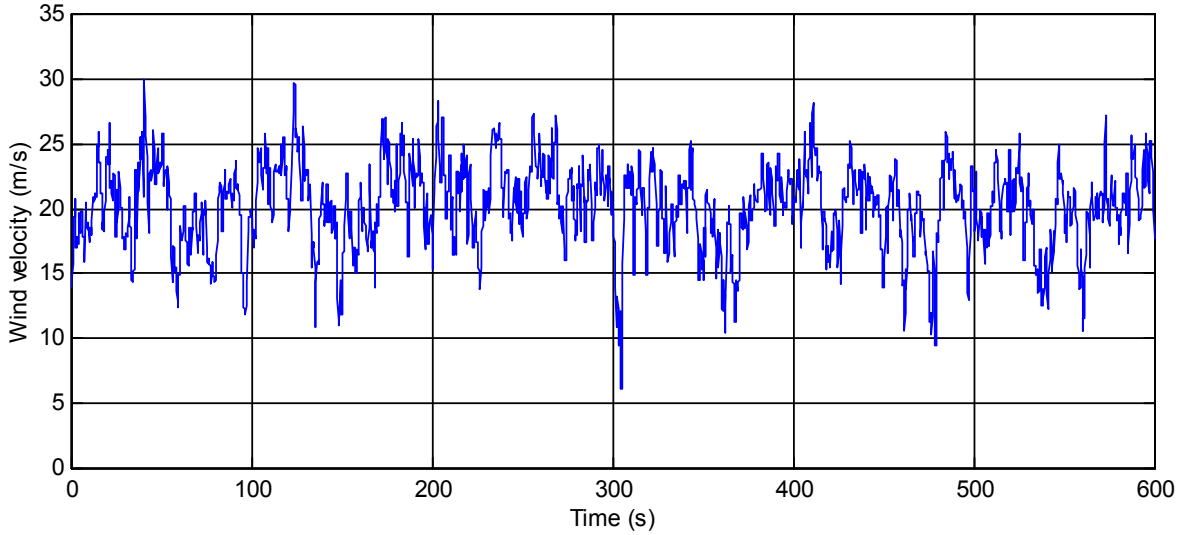

Figure 2.22 Example of a time series of along wind velocity, recorded during a storm on 5-6 April 1997.

Time series of simultaneous recordings of wind direction, wind velocity and pressure are shown in Figure 2.21 through Figure 2.24. Tap location and the wind direction are indicated on Figure 2.19. As can be seen in Figure 2.23, the pressure at tap no. 9 is positive most of the time and follows quite closely the variation in wind velocity, shown in Figure 2.22, this is as expected for an upwind tap. On the other hand, at tap no. 4 (see Figure 2.24), which is located on the leeward side of the building, the pressure is negative, i.e. suction. Some correspondence to the wind velocity is seen at tap no. 4, but not as clearly as for the pressure at tap no. 9, which is normal as the pressure at tap no. 4 is influenced by the turbulence created by interaction between building and flow.

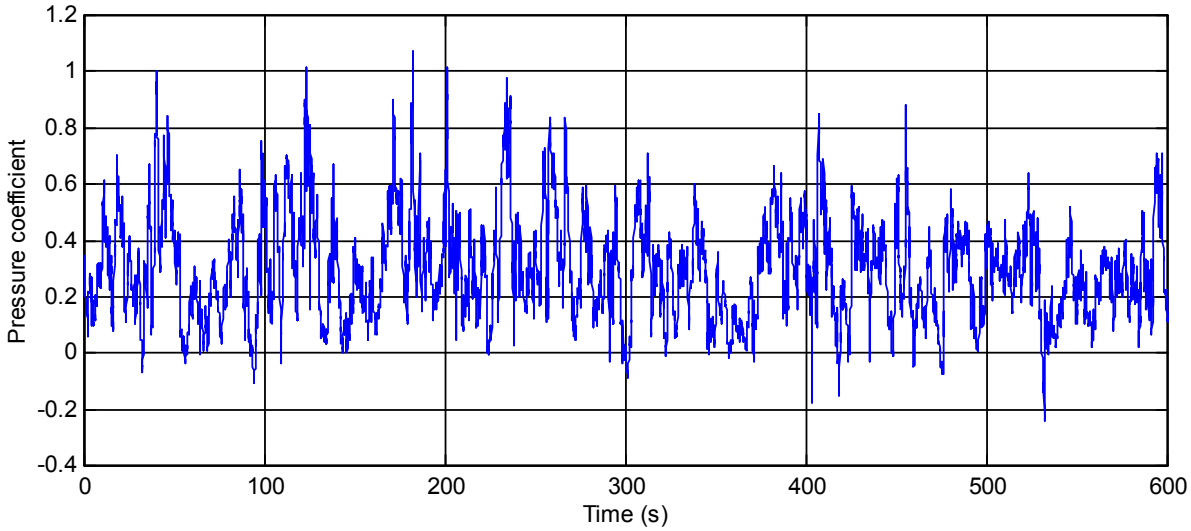

Figure 2.23 Example of recorded time series of pressure measured at tap no. 9 during a storm on 5 - 6 April 1997

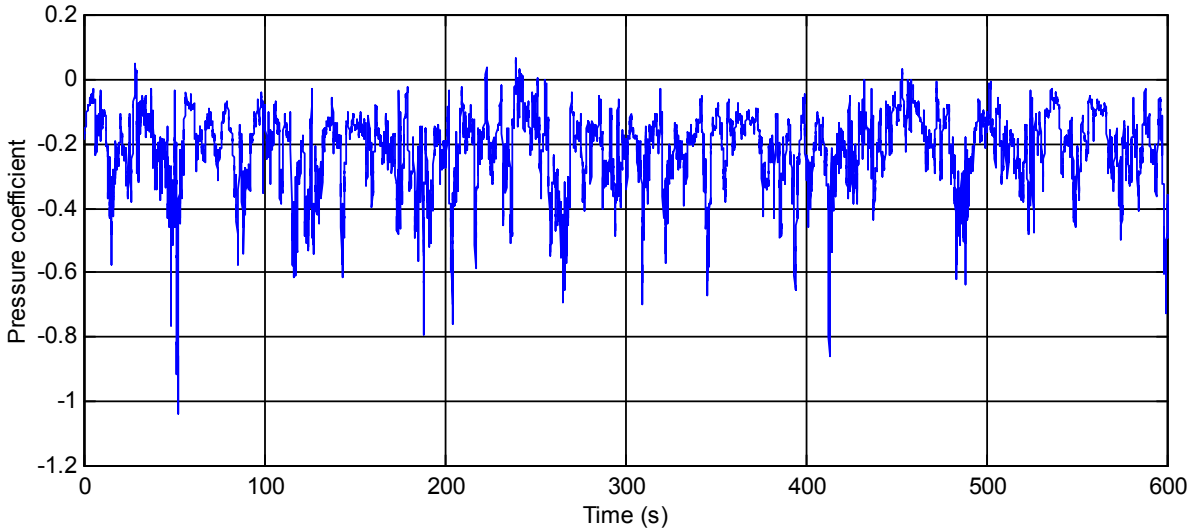

Figure 2.24 Example of recorded time series of pressure measured at tap no. 4 during a storm on 5 - 6 April 1997.

Another example of recorded data is shown in Figure 2.25, which presents recorded wind velocity and corresponding pressure coefficients at tap no. 4 and tap no. 5 on different occasion. This time, the mean wind direction is from WSW and the mean airflow meets the W-face of the building at about 16-degree angle towards south. As before, tap no. 5 is located on the W-face of the building about 90 cm from the SW-corner, while tap no. 4 is located on the S-face of the building about 90 cm from the SW corner. It can be seen that the pressure at tap 5 is positive (pressure) and follows the changes in the wind velocity closely, whereas the pressure at tap 4 can be either positive or negative (suction). It is also seen that the variation (i.e. standard deviation) of pressure is considerably greater at tap 4 than at tap 5. It should be noted that the variation in wind direction is +/- 10 degrees from the mean direction for this particular sample.

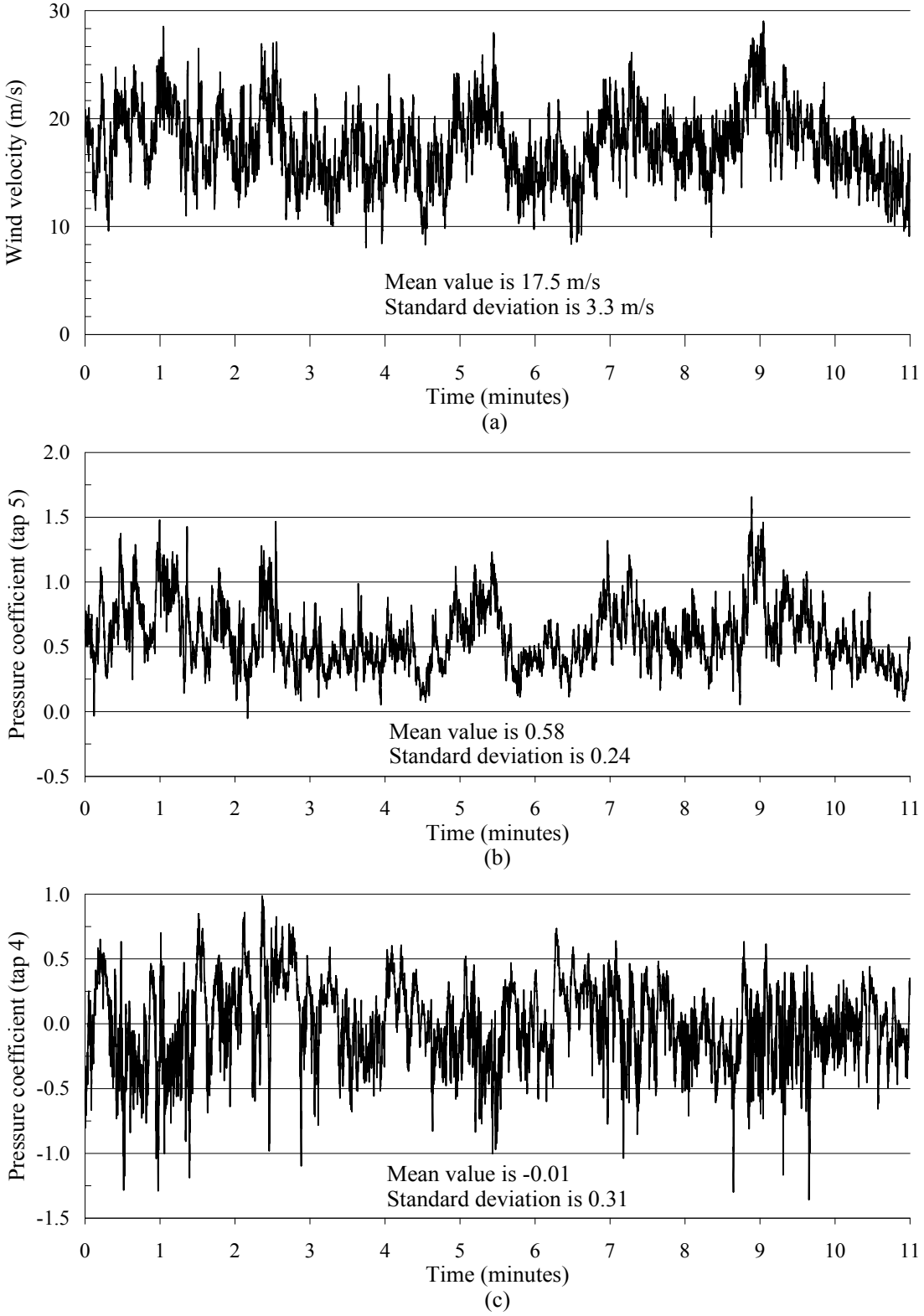

Figure 2.25 An example of recorded time series at the building. (a) Horizontal wind velocity and (b) corresponding pressure coefficients at tap no. 5 and (c) tap no. 4.

Chapter 3 The wind tunnel experiment

3.1 Introduction

A wind tunnel investigation was conducted in a wind tunnel owned and operated by the Department of Mechanics, Thermo- and Fluid Dynamics at the Norwegian University of Science and Technology [225]. The wind tunnel is a closed loop, low velocity wind tunnel. It has a centrifugal fan with a 220 kW capacity. The resulting nominal velocity range is 0.5 to 30 m/s in an empty tunnel. The test section of the wind tunnel is 12.5 m long, 2.7 m wide and 1.8 meters high. The model, see Figure 3.5, was located on a rotating platform, turntable, approximately 11 m downstream in the test section.

When preparing and planning the wind tunnel experiment, notice was taken of tests carried out in the tunnel on earlier occasions ([6] [94] [104] [213]). Lessons were also drawn from other sources, such as [162] and [22].

3.2 Basic similarity requirements

Simulation occurs at reduced geometric scale, under controlled flow conditions, which are generally somewhat different from the natural wind. The question of physical similitude is therefore of importance. The following scaling issues generally need to be considered [162]:

- The geometric scaling of the atmospheric boundary layer simulation, i.e. same statistics in non-dimensional time and space of flow velocity.
- The need to fit surrounding large structures or topography, which may constrain the scaling ratio.

- The geometric similarity of structural shape and modelling of surface features on the building with sufficient accuracy.
- The statistical similarity of strain and displacement response.
- Possible blockage effects (corrections are generally not needed if area ratios less than 5% are maintained and reference static and dynamic pressures are measured in the same cross section as the building model).
- The match between the frequency response of the available pressure measurement system and the desired full-scale frequency response.

When analysing a physical problem that is to be studied experimentally, it is usual to identify a set of governing dimensionless parameters. This is especially true in fluid dynamics. The key non-dimensional parameters considered for similarity requirements for both static and dynamic structures are the following [22]:

- Reynolds number ($R_e=\rho_a UB/\mu_a=UB/\nu_a$) describes the relative importance of fluid inertia and viscosity. The full scale Reynolds numbers cannot be approached in conventional wind tunnels (normally ${}^{m}R_e << {}^{p}R_e$). However, Reynolds number similarity is considered a secondary effect for sharp edged buildings where points of flow separation are more or less fixed.
- Strouhal number ($S_t=fB/U$) defines a reduced frequency. Its reciprocal is known as reduced velocity. Similarity of Strouhal number is needed to match the duration of gust loads between model and prototype and is required in all models in which time or frequency dependence is represented.
- Jensen number ($J_e = h/z_0$ in full-depth simulation, or z_g/h in part-depth simulation) relates the length scale factors of the structure (i.e. its height) and the atmospheric boundary-layer simulation. A mismatch of J_e by a factor of two to three is acceptable.

For the study-building, there are four key similarity requirements that should be followed. Firstly, to use the same geometric form, although some deviations in smaller details are allowed. Secondly, to have the same statistics (in dimensionless time and space) of mean- and fluctuating wind. Especially the mean wind profile and the along wind turbulence intensity should full fill similarity. Some distortion in length scales is usually unavoidable. This is a very important scaling requirement as pressures on the windward face have been found to be strongly dependent on the incident velocity profile, whereas pressures on the other faces depend on the intensity and integral length parameters of the incident turbulence ([22], [72]). Thirdly, the reduced velocity (U/f_oB) should be the same in full-scale and model-scale. This usually follows from other requirements and gives the velocity/frequency scaling as the frequency ratio (ratio of model to full scale frequency, λ_f) is related to the geometric scaling ratio (λ_B) and the velocity ratio (λ_U), i.e. $\lambda_U = \lambda_B \lambda_f$ or $\lambda_f = \lambda_U/\lambda_B$. Fourthly, similar Jensen number (h/z_0) should be maintained.

Mismatching the linear scales of the building and the atmospheric boundary layer simulation by a factor of two has been found to change the loading on the windward face by between 5% and 10%. In the high local suction regions, the error can be between 20%

and 30%. The load is underestimated when the building model is too large and overestimated when the building model is too small ([22], [72]).

3.3 Boundary layer simulation

A boundary layer simulation was undertaken. A hot-wire probe (single wire) was used to measure the flow velocity in the tunnel. Several different arrangements of roughness elements were tested. For each arrangement, a velocity profile was recorded downstream in the tunnel at the centre of the rotating table and/or just in front of the turntable. The velocity was sampled at 666.5 Hz for a period of 30 sec. The probe was attached to a special fixture, which could be moved up and down mechanically. At each measurement height the mean and standard deviation of the tunnel velocity was recorded, giving the mean velocity and turbulence intensity profile. Time series were also recorded at two specific heights, i.e. corresponding to 10 m and 30 m (roof height) in full scale.

Based on the profile and turbulence information, boundary layer no. 9 was selected as the most appropriate one (see Figure 3.1 and Figure 3.2). Figure 3.3, shows the mean velocity profile for boundary layer no. 9 and a comparable power-law and logarithmic profile. It should be noted that the profile is based on several profile measurements, i.e.:

- At the centre of the rotating table, without the terrain-model, at a motor rate of 1300 (3006_13 and 0207_13)
- At the centre of the rotating table, without the terrain-model, at a motor rate of 1500 (C2707_15)
- At the centre of the rotating table, with the terrain-model but excluding the buildings, at a motor rate of 1300, for two wind directions (T2707B, T2707B)

The results indicate that the terrain-model-plate and a motor rate above 1300 do not affect the profile significantly. Figure 3.4, shows the turbulence intensity for the mean wind profile of Figure 3.3. As can be seen the turbulence intensity decreases slowly with increasing height and is about 17 % at roof height of the building which corresponds roughly with wind data from Reykjavik (see [196] and Chapter 1).

3.4 The building model

A model scale of 1:160 was chosen. This was considered a reasonable scaling for the present investigation. It is in line with commonly used ratios for low- to medium-rise buildings [162]. The same scaling had been used on other occasions in the wind tunnel [213], which allowed utilisation of available information, for example with regard to turbulence modelling. A larger scaling ratio would have limited the possibilities of including the nearest obstacles, such as the apartment blocks, in the model. In addition, the desired incident wind conditions are more difficult to achieve as the linear scale factor increases ([22], [72]). A smaller scaling ratio would have made it more difficult to model the details of the building.

A terrain model was built of the closest surroundings of the building, i.e. an area of a

circle with a diameter of about 350 m full scale (see Figure 3.5). The topographic height difference modelled was from 50 m to 56 m m.s.l. Surrounding buildings were included as simple blocks. A group of four story apartment buildings could be removed from the model. This was done in order to evaluate the influence of these buildings on the study-building.

Figure 3.1 The roughness elements and the model of the building and its surroundings, a view from behind the spires downstream in the tunnel looking towards the turntable.

Figure 3.2 The spires and the roughness elements as seen from the turntable.

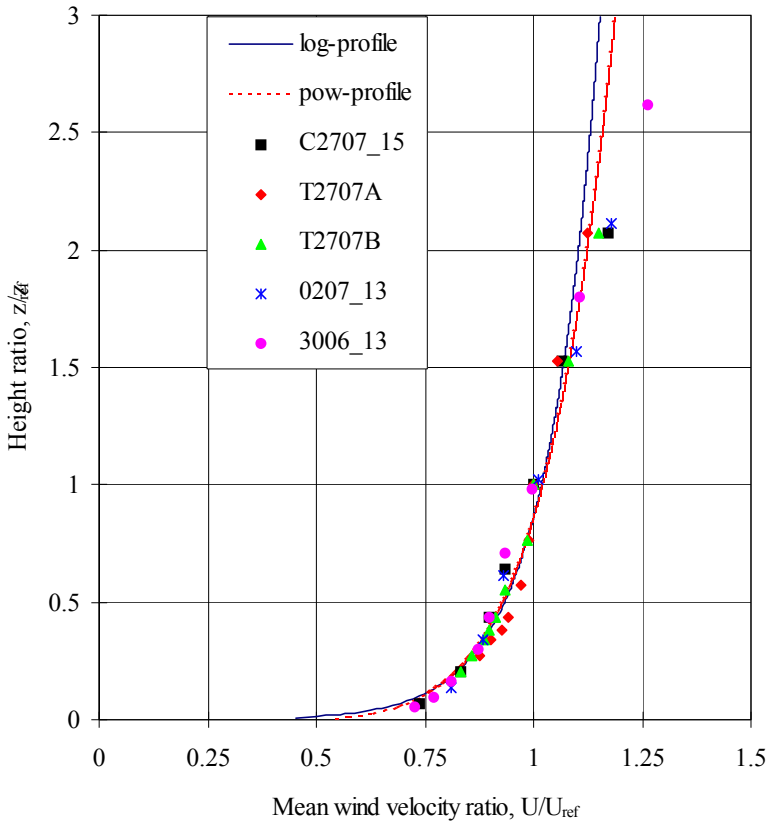

Figure 3.3 Wind tunnel boundary layer velocity profiles. The reference velocity is the velocity at the reference height, i.e. the roof height of the building or 184 mm above the tunnel floor.

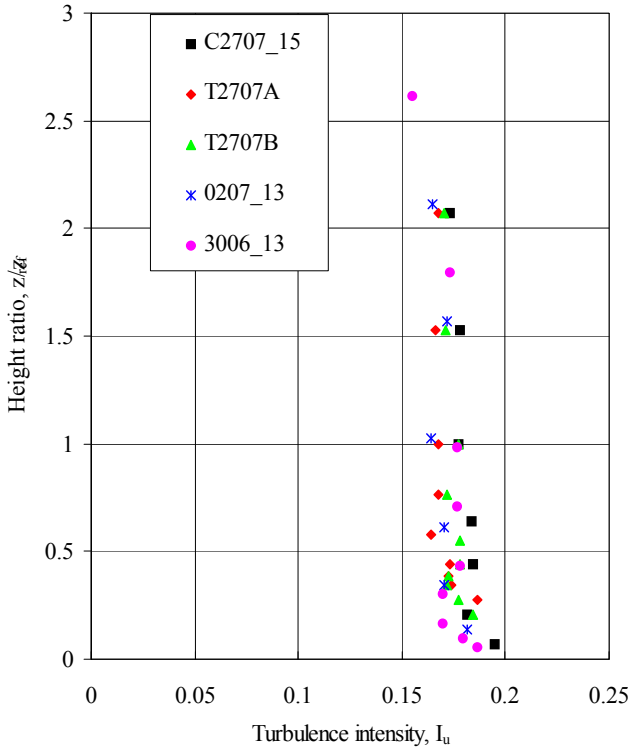

Figure 3.4 Wind tunnel boundary layer turbulence intensity profile. The reference height is the roof height of the building, i.e. 184 mm above the tunnel floor.

The first two floors of the building (the shopping centre) were modelled without taps. A Plexiglas model was built of the tower itself (see Figure 3.5). The model of the tower was equipped with 82 taps in total.

Reinhold [161] conducted series of tests to select the optimum number and location of transducers to obtain reliable measurement of force and moment fluctuations through analogue integration. He found that at least four transducers on each side of a typical building should be used to sufficiently represent the instantaneous characteristics of a fluctuating pressure field.

Figure 3.5 The model of the building with neighbouring buildings and terrain in place in the wind tunnel. Note also the reference pitot tube up wind from the model.

In view of this result, it was decided to place 12 main taps, in three rows, on each side of the building and 8 main taps on the roof. The SE and SW upper corners had 9 extra taps each, and 4 extra taps were located on the roof at the SE and NE corners. The main taps were supposed to supply information about overall pressure distribution and loading, whereas the extra corner taps were intended to give more detailed pressure distributions at the upper corners. Figure 3.5 shows the model in place in the wind tunnel.

Reference pressure is supplied by a pitot tube located up wind in roof-height of the model (see Figure 3.5).

3.5 The measurement system

The measurement system consisted of 16 differential pressure transducers, combined with filters and amplifiers (see Figure 3.7 and Figure 3.8). As the number of taps was considerably greater than the number of pressure transducers, the pressure measurements were performed in several phases, each concentrating on a specific face or section of the model.

The transducers were connected to a data acquisition system (see Figure 3.6), consisting of an A/D converter, a multiplexer, computer and data acquisition software. The pressure data was sampled at 500 Hz and filtered at 400 Hz with an analogue filter.

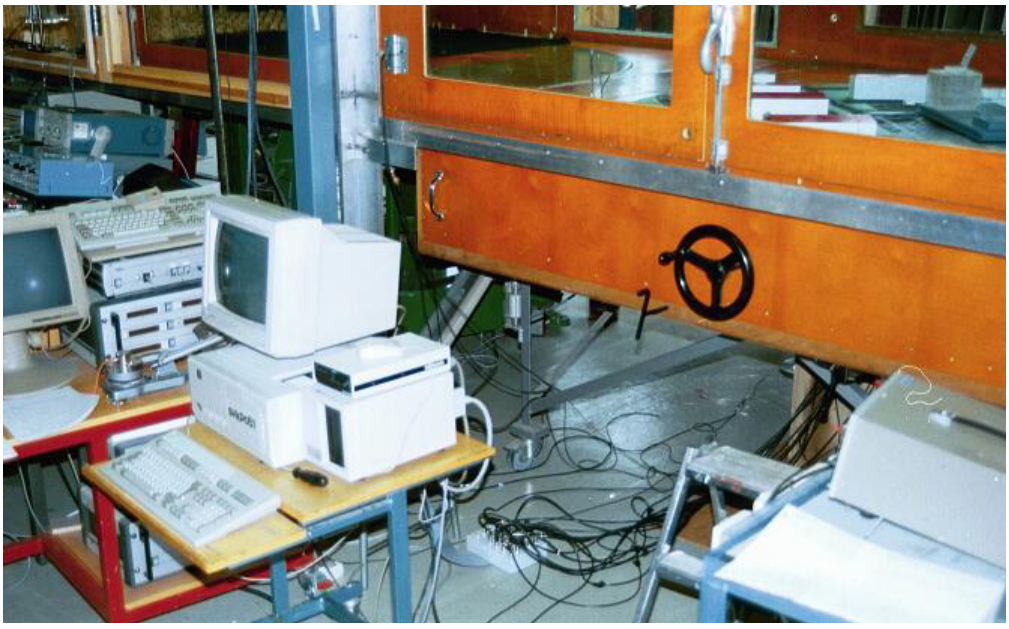

Figure 3.6 The data acquisition computer.

3.6 Examples of recorded pressure

For a brief introduction of the recorded data, one example will be presented. The flow meets the south face of the building at about 19-degree angle towards east. Figure 3.9

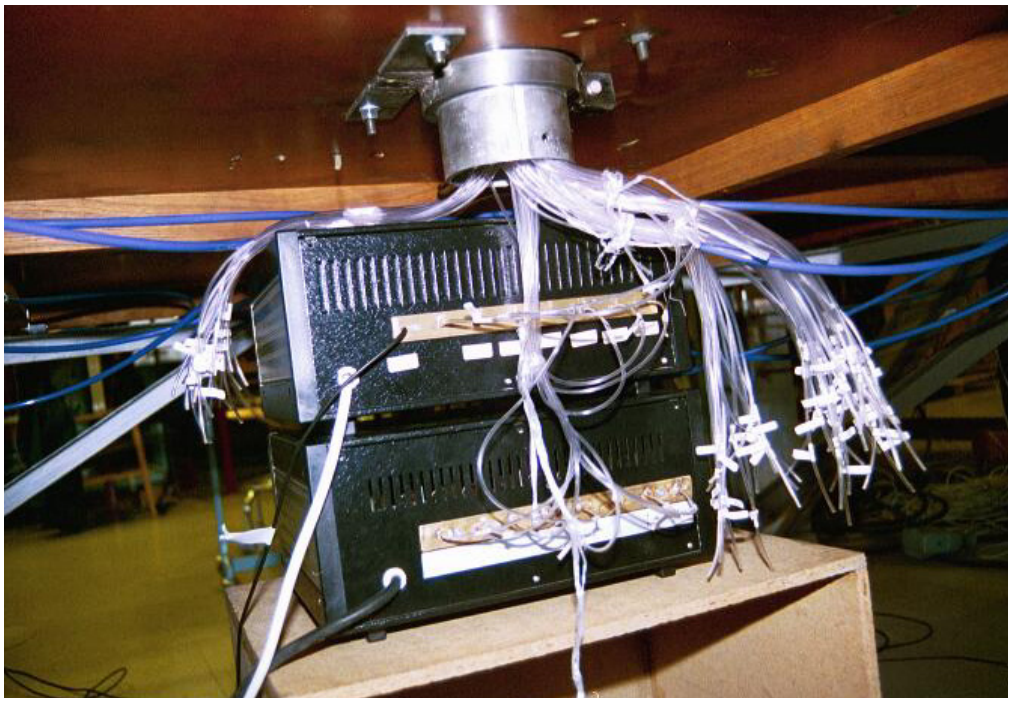

Figure 3.7 Tubes going from the taps on the model through the wind tunnel floor to the pressure transducers boxes.

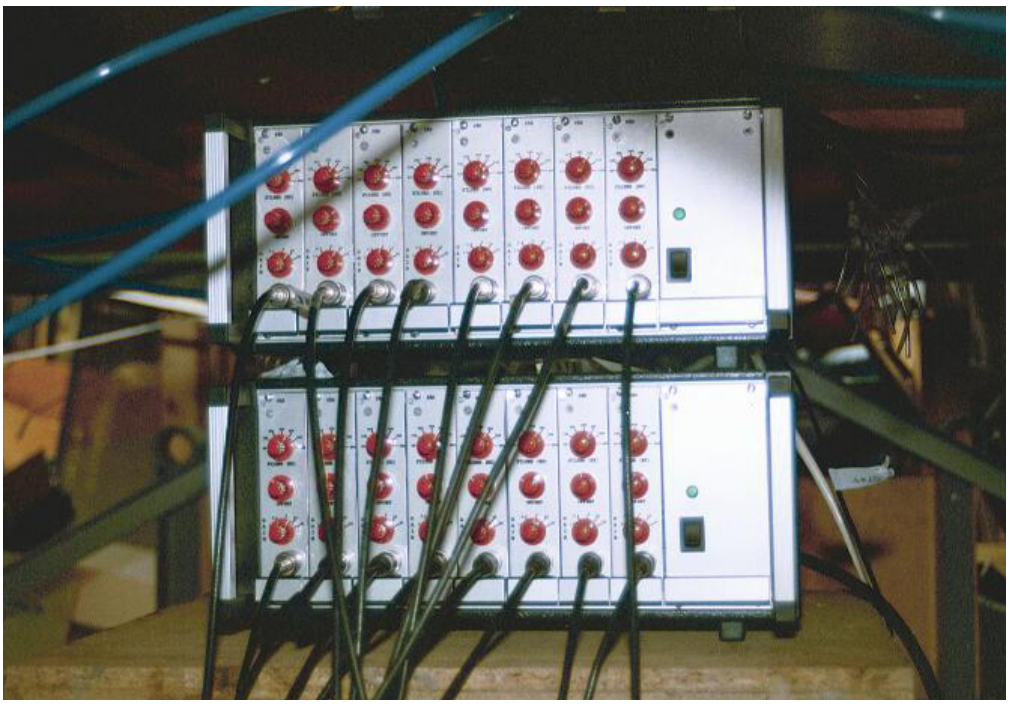

Figure 3.8 The front side of the transducer boxes, showing gain and magnification controls. Signal cables from the transducer boxes go to an A/D converter before sampling.

shows an example of recorded pressure coefficients at tap no. E12 and tap no. S22 on the building model (see Figure 5.1). The surface pressure is normalised with respect to dynamic pressure based on the mean wind velocity in the wind tunnel at model height. Tap no. S22 is located on the south face of the building about 170 cm (full-scale) from the SE-

corner, but tap no. E12 is located on the east face of the building about 240 cm (full-scale) from the SE-corner. The situation corresponds therefore roughly to the one shown for the full-scale data in Figure 2.25, although it is for a different corner of the building, i.e. the southeast corner instead of the southwest corner.

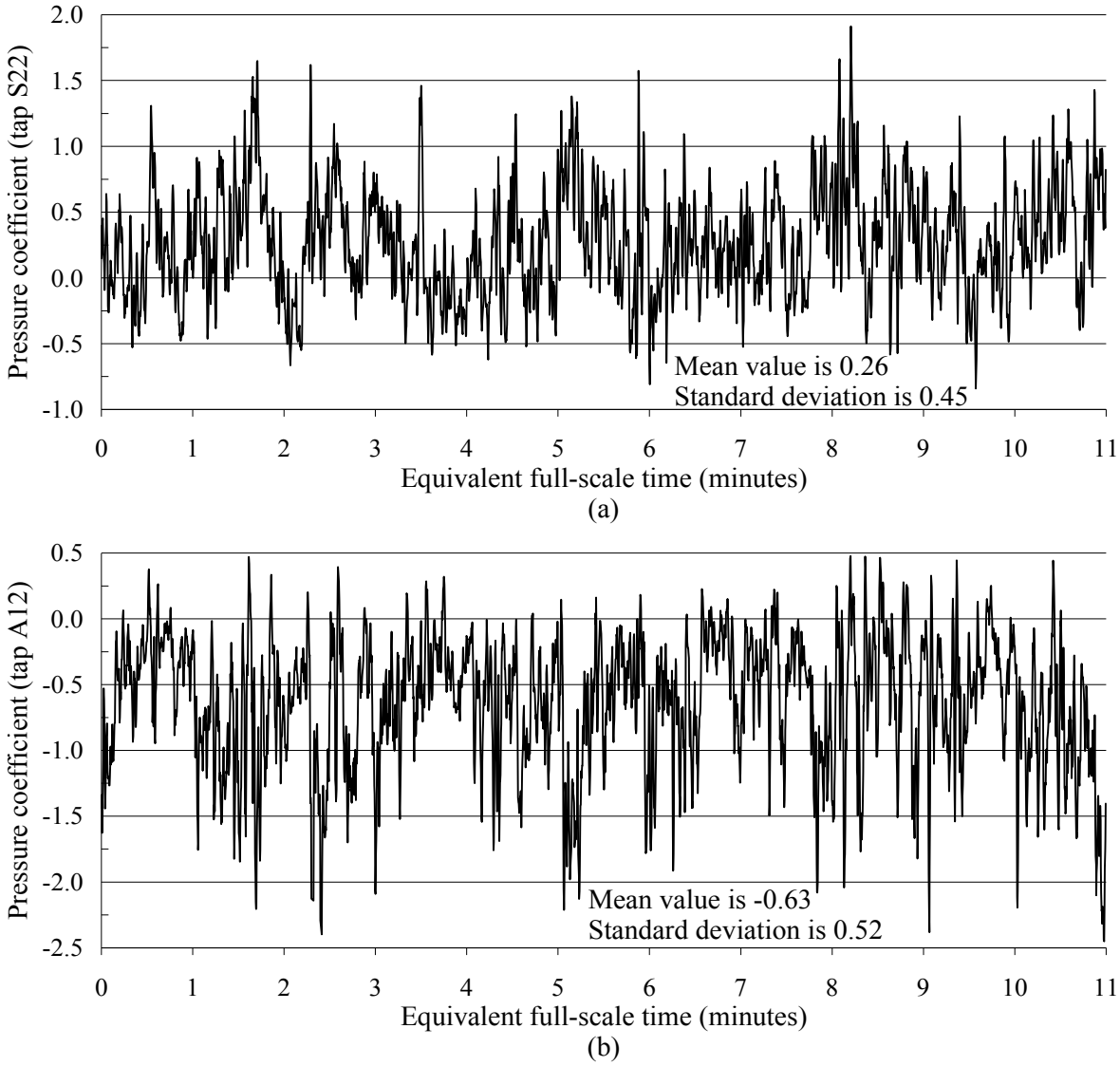

Figure 3.9 Time series of model-scale pressure coefficients: (a) at tap no. S22 and (b) at tap no. E12.

A largely similar pattern emerges as seen before in Figure 2.25 for the full-scale data. It can be seen that the pressure at tap no. S22, on the windward side, is for the most part positive (pressure), whereas the pressure at tap no. E12, around the corner, is predominantly negative (suction). It is also seen that the variation (i.e. standard deviation) of pressure is greater at tap no. E12 than at tap no. S22.

The time series are displayed as function of equivalent full-scale time in minutes. The corresponding real recording time in the wind tunnel is about 6 seconds for the 11 minutes displayed.

Considerable correlation in pressure at the two taps can be noticed as high positive

pressure at tap S22 is generally seen to correspond to high suction (negative pressure) at tap E12. This trend is also noticeable in the full-scale data in Figure 2.25, but less strongly which is probably caused by greater variation in full-scale wind direction.

Chapter 4 The wind environment

4.1 Introduction

This chapter gives an engineering description of turbulence and demonstrates the analysis of wind and meteorological data.

The local surround environment is described through descriptions of roughness, topography nearest obstacles (wakes). Upwind conditions are investigated, both mean flow characteristics and the three-dimensional turbulence field. Climatic conditions are discussed in terms of prevailing winds, atmospheric stability and the probability of occurrence of strong winds.

4.2 Description of turbulence

Conditions of the atmosphere at a particular location over a long period of time; it is the long-term summation of the atmospheric elements (and their variations) that, over short time periods, constitute weather. These elements are solar radiation, temperature, humidity, precipitation (type, frequency, and amount), atmospheric pressure, and wind (speed and direction).

Atmospheric pressure and wind are both significant controlling factors in the Earth's weather and climate. Although these two physical variables may at first glance appear to be quite different, they are in fact closely related. Wind exists because of horizontal and vertical differences (gradients) in pressure, yielding a correspondence that often makes it possible to use the pressure distribution as an alternative representation of atmospheric motion.

The changing wind patterns can be described within the framework of Newtonian mechanics. Newton's laws of motion are valid in any set of coordinate system moving with constant velocity and without rotation relative to the inertial frame. A coordinate system attached to the Earth is not an inertial reference although the solutions to many engineering problems can be obtained to a satisfactory degree of accuracy by assuming that an Earth-based reference frame is an inertial one. However, in some applications the rotation of the Earth cannot be neglected.

To describe the position of a particle that moves relative to the Earth, it is usually convenient to use a reference frame attached to the Earth. Reference frames that rotate are usually non-inertial, and, in order to apply Newton's laws, additional fictitious forces must be introduced; among these are centrifugal forces and Coriolis forces.

Assuming the Earth is sufficiently inertial for the problem at hand, the kinetic equation of motion can be written as:

$$\rho\left(\frac{\partial U_i}{\partial t}+U_k\frac{\partial U_i}{\partial x_k}\right)=\frac{\partial \sigma_{ij}}{\partial x_j}+\rho b_i \tag{4.1}$$

Here σ_{ij} is a stress-tensor, ρ the air density, b_i represents body forces (gravity etc.), U_i is the wind velocity but x_i and t are space and time variables. The indexes i and j refer to the coordinate axis x, y and z, further more they follow the Einsteinian summation convention. Equation (4.1) was put forward by *Augustin-Louis Cauchy* (1789-1857) in 1827 and is often referred to as *Cauchy's 1. law*. The kinematics of the motion is contained in the so-called rate-of-deformation tensor, which can be related to the flow velocity as follows:

$$D_{ij}=\frac{1}{2}\left(\frac{\partial U_i}{\partial x_j}+\frac{\partial U_j}{\partial x_i}\right) \tag{4.2}$$

The stress-strain relations are contained in the constitutive law, described by the *Cauchy-Poissons* law. It can be written as:

$$\sigma_{ij}=-P\delta_{ij}+\lambda D_{kk}\delta_{ij}+2\mu D_{ij} \tag{4.3}$$

Here P is pressure, λ and μ are coefficients of molecular viscosity and δ_{ij} is the Kronecker delta. Substitution of Eq. (4.2) and (4.3) into (4.1) leads to the one of the fundamental equations of fluid mechanics, i.e. the *Navier-Stokes* equations:

$$\rho\left(\frac{\partial U_i}{\partial t}+U_k\frac{\partial U_i}{\partial x_k}\right)=-\frac{\partial P}{\partial x_i}+(\lambda+\mu)\frac{\partial^2 U_j}{\partial x_i\partial x_j}+\mu\frac{\partial^2 U_i}{\partial x_k\partial x_k}+\rho b_i \tag{4.4}$$

Assuming that air is an incompressible gas, at least for common wind velocities, then $D_{kk} = 0$, which can be written as:

$$\frac{\partial U_i}{\partial x_i}=0 \tag{4.5}$$

This is the equation of continuity, originally put forward by Euler. This assumption simplifies Eq. (4.4), which can now be written as:

$$\rho\left(\frac{\partial U_i}{\partial t}+U_k\frac{\partial U_i}{\partial x_k}\right)=-\frac{\partial P}{\partial x_i}+\mu\frac{\partial^2 U_i}{\partial x_k\partial x_k}+\rho b_i \tag{4.6}$$

By comparing this equation with Eq. (4.1), it is seen that for the given conditions it is possible to write:

$$\frac{\partial \sigma_{ik}}{\partial x_k}=\mu\frac{\partial^2 U_i}{\partial x_k\partial x_k}-\frac{\partial P}{\partial x_i} \tag{4.7}$$

Integrating gives the following relation for shear stress:

$$\tau_{ij}=\sigma_{ij}=\mu\frac{\partial U_i}{\partial x_j},\qquad i\neq j \tag{4.8}$$

This equation is generally known as *Newton's equation*. Experience has shown that this equation is valid with an adequate engineering accuracy for many common fluids, which in turn are often called Newtonian fluids.

Although the natural wind is a 3-dimensional phenomenon, random in space and time, the wind velocity may be idealised as high frequency gusts superimposed upon a slowly varying mean wind carrying the bulk of the energy. In a *xyz*-Cartesian co-ordinate system with the *x*-axis in the direction of the mean air flow and *z*-axis vertical, this may be expressed as

$$U_i(x,y,z,t)=\overline{U}_i(z)+u_i(x,y,z,t) \tag{4.9}$$

Here U_i is the three dimensional velocity vector as a function of time and space, u_i is the gust vector containing the turbulence components, $\overline{U}_i$ is the mean wind velocity vector and i is an index referring to the axis *x, y* and *z*. The mean wind velocity vector is traditionally assumed to be only a function of height above ground, if the wind is stationary and the surface conditions uniform.

The wind speed may be described reasonably well as a stochastic Gaussian process. Further, it is acceptable to assume that the expected value of wind velocity is equal to its time average, i.e. the turbulence components can be treated as an ergodic process:

$$E\left[U_i(x,y,z,t)\right]=\overline{U}_i \quad\Rightarrow\quad E\left[u_i(x,y,z,t)\right]=0 \tag{4.10}$$

$$E\left[u_iu_j\right]=\left\langle u_iu_j\right\rangle_t$$

Therefore, the description of gusty wind is reduced to a description of random variables by means of the theory of stochastic processes.

If Reynolds decomposition in the form of Eq. (4.9) and similar relation for pressure, is applied to the Navier-Stokes equation and the expected value found in accordance to Eq. (4.10), the so-called *Reynolds momentum equation* emerges:

$$\overline{U}_k\frac{\partial\overline{U}_i}{\partial x_k}=-\frac{1}{\rho}\frac{\partial\overline{P}}{\partial x_i}-\frac{\partial E\left[u_iu_k\right]}{\partial x_k} \tag{4.11}$$

Here the effects of molecular viscosity has for the sake of simplicity, been assumed negligible.

The contribution of the turbulent motion to the mean stress tensor is now seen to be:

$$\tau_{ij} = -\rho E\left[u_i u_j\right] \tag{4.12}$$

τ_{ij} is called the Reynolds stress tensor [223]. It is symmetric and contains normal stresses (pressures) on the diagonal whereas the off-diagonal elements are shear stresses, which play a dominant role in the theory of mean momentum transfer by turbulent motion. In traditional boundary layer shear flow over a uniform surface, a consistent correlation is primarily found between the turbulence components in the vertical and along wind direction, i.e.:

$$\begin{aligned} \tau_{xy} &= -\rho E[uv] \approx 0 \\ \tau_{yz} &= -\rho E[vw] \approx 0 \\ \tau_{xz} &= -\rho E[uw] \neq 0 \end{aligned} \tag{4.13}$$

For high wind velocities, when thermal effects on the flow are relatively negligible, it is generally found that:

$$E[uw] \leq 0 \tag{4.14}$$

This indicates that when u is positive (i.e. in the direction of the mean wind) then w is negative (i.e. downward), similarly when u is negative, w is positive. In other words an eddy is formed. The larger eddies loose energy to smaller eddies, momentum is transferred downward and consequently the wind velocity near the ground is reduced. Therefore, the interaction of the Reynolds stresses with the mean velocity gradient plays an important role in the dissipation of kinetic energy in the atmosphere.

The correlation between the u and w turbulence components also gives an indication of the roughness of the underlying surface. A so-called surface drag coefficient, κ, is often used as a measure of surface roughness. It can be defined as a non-dimensional Reynolds shear stress.

$$\kappa = \frac{\tau_{xz}}{\rho \overline{U}^2} \tag{4.15}$$

The shear stress and thereby κ, increases as the surface roughness increases.

The shear velocity, u_*, is often used as a characteristic variable for turbulent flow. It is based on the Reynolds shear stress and defined as:

$$u_* = \sqrt{\frac{\tau_{xz}}{\rho}} \tag{4.16}$$

The shear frictional velocity can be related to the local mean wind speed through the dimensionless surface drag coefficient, κ, by using the equations (4.11), (4.13) and (4.15):

$$u_* = \sqrt{-E[uw]} = \sqrt{\kappa}\overline{U} \tag{4.17}$$

assuming that Eq. (4.14) is fulfilled.

4.2.1 Mean wind velocity profile

The wind speed near the ground approaches that of an aerodynamic boundary layer over a rough surface. For most structural design problems, it is assumed that the boundary layer flow is horizontally homogeneous, which implies that the terrain is considered horizontal and the roughness of the terrain is assumed uniform over a sufficiently large fetch.

As already mentioned the mean wind velocity, $\overline{U}$, decreases with a decreasing height, or distance from the surface, because of the frictional effects of the surface. A simple model describing these turbulence effects is the eddy-viscosity model (*K*-theory) [151], which is a first-order closure. The shear stress, or the momentum flux, is then written as:

$$\tau_{xz} = \rho K_m \frac{\partial \overline{U}}{\partial z} \tag{4.18}$$

There is an obvious resemblance between Eq. (4.18) and Eq. (4.8). The difference is that instead of the molecular viscosity in (4.8) an exchange coefficient, called the kinematic eddy viscosity, K_m, is introduced in (4.18). The eddy viscosity value depends on the characteristics of the flow, such as the size and velocity of eddies as described by the Reynolds stresses. By taking K_m as proportional to a product of eddy size and velocity and further assuming, that the eddy size is proportional to height z, and that eddy velocity is proportional to u_* the value of K_m is obtained as:

$$K_m = k_a z u_* = k_a z \sqrt{\kappa} \overline{U} \tag{4.19}$$

Here k_a is the so-called *von Karman coefficient*, which is generally taken to be about 0.4. Combining Eq. (4.16), (4.18) and (4.19) gives the following differential equation which describes changes in mean wind velocity with height.

$$d\overline{U} = \frac{\sqrt{\kappa}}{k_a} \overline{U}_R \frac{dz}{z} \tag{4.20}$$

Here $\overline{U}_R$ is the mean wind velocity at the reference height. Integration of (4.19) gives the so-called *logarithmic mean wind profile* for neutral atmospheric conditions as:

$$\frac{\overline{U}(z)}{\overline{U}_R} = \frac{\sqrt{\kappa}}{k_a} \ln\left(z/z_o\right) \qquad z \geq z_o \tag{4.21}$$

Here z_0 is an integration coefficient called *roughness length*. It can be thought of as the height at which *U(z)* vanishes, and is therefore another measure of the surface roughness and can be related to the surface drag coefficient at the reference height z_R as:

$$z_o = z_R \exp\left(-k_a / \sqrt{\kappa}\right) \tag{4.22}$$

It should be stressed, that the logarithmic profile is only “correct” over a uniform terrain, because the local u_* is not even approximately independent of height, as can been seen from Eq. (4.8), (4.16) and (4.17). Further, the profile in Eq. (4.21) does not take into account possible heat convection effects, i.e. the atmospheric stability.

4.2.2 Stability

Stability is a term applied qualitatively to the property of the atmosphere, which governs the acceleration of the vertical motion of an air parcel. The acceleration is positive in unstable atmosphere (turbulence increases), zero when the atmosphere is neutral and negative (deceleration) when the atmosphere is stable (turbulence suppressed).

In section 2.1, the basic assumption regarding the planetary boundary layer (PBL) has been that of neutral stability. That is neutral stratification (temperature decreasing upward at the adiabatic rate) throughout the depth of the PBL. This occurs for example with strong winds on cloudy nights or days, when mechanical turbulence is created and heat is lost to the ground by turbulent mixing throughout the PBL. The PBL is then fully turbulent, and its depth determined by wind velocity and surface roughness. However, truly neutral PBL conditions are quite rare. Most of the time, the temperature interaction between surface and atmosphere plays an important role in the mixing within the PBL.

Unstable conditions occur for example on sunny and clear days. Then a positive heat flux is created at the ground, which causes heat convection in addition to the mechanical turbulence created by the wind. The generation of boundary layer turbulence decreases rapidly with height, as it is proportional to the vertical wind shear. On the other hand, the generation of heat convection varies slowly with height and determines the depth of the mixing layer. Conditions are stable on clear nights with weak winds, when only the lower portion of the inversion layer is continuously turbulent.

Several parameters are used in micrometeorology to determine the degree of stability or instability. Two such stability parameters are the Monin-Obukhov length (L) and the Richardson number [147], but many others, such as the standard deviation of wind direction fluctuations, are also used [134].

The logarithmic wind profile of Eq. (4.21) can be modified to account for atmospheric stability by adding a heat convection term:

$$\frac{\overline{U}(z)}{\overline{U}_R} = \frac{\sqrt{\kappa}}{k_a}\left[\ln\left(z/z_o\right) - \psi_m\left(z/L\right)\right] \qquad z \geq z_o \tag{4.23}$$

Here L is the Monin-Obukov length and ψ_m (z/L) is a similarity function for mean wind, which takes on different forms for stable (z/L positive, ψ_m negative) and unstable (z/L negative, ψ_m positive) air.

A simple stability classification is the *standard deviation of the wind direction method*, which is recommend by the US Nuclear Regulatory Commission (USNRC) [134]. Table 4.1 presents the statement of USNRC correlation between σ_ϕ and Pasquill stability following Sedefian and Bennet [188].

Table 4.1 Stability classification following Sedefian and Bennet [188]

Pasquill stability classes		**Standard deviation of wind direction**
Description	Group	(°)
Highly unstable or convective	A	$22.5 < \sigma_\theta$
Moderately unstable	B	$17.5 < \sigma_\theta < 22.5$
Slightly unstable	C	$12.5 < \sigma_\theta < 17.5$
Neutral	D	$7.5 < \sigma_\theta < 12.5$
Moderately stable	E	$3.75 < \sigma_\theta < 7.5$
Extremely stable	F	$2.0 < \sigma_\theta < 3.75$
Low wind night time stable conditions	G	$\sigma_\theta < 2.0$

4.2.3 Gustiness

Within an appropriate time period, usually between 10 and 60 minutes, the wind velocity has been idealised as high frequency gusts superimposed upon a slowly varying mean wind carrying the bulk of the energy. The turbulence intensity is a simple measure of the variability of the wind within the period used to define the mean wind velocity. It is defined as:

$$I_i = \frac{\sigma_i}{\overline{U}} \qquad i \in \{u,v,w\} \tag{4.24}$$

Here, σ_i is the standard deviation of a fluctuating wind velocity component, *u, v* or *w* and $\overline{U}$ is the mean along wind velocity.

It is possible to relate turbulence intensity and surface roughness by writing:

$$\kappa = -r_{uw} I_u I_w \tag{4.25}$$

where $r_{uw} = E[uw]/\sigma_u \sigma_w$ is the correlation coefficient of *u* and *w*. Commonly it is found that $-1 < r_{uw} < 0$, for high wind velocities, when thermal effects on the flow are relatively negligible and the surface reasonably uniform. The surface drag coefficient can be determined through single point wind measurements by approximating the expected value of *uw* by a time average, see Eq. (4.10). It should be noted that the value of κ depends on measurement height and the averaging period.

Another commonly used measure of the variability of the wind within a reference period is the gust factor, G_u, which is defined as:

$$G_u = \frac{|U_u|_{\max}}{\overline{U}} \tag{4.26}$$

where $|U_u|_{\max}$ is the largest maximum (observed) along wind velocity during a given period and $\overline{U}$ is the mean along wind velocity during the same period. The gust factor is traditionally only defined for the along wind, but as for the turbulence intensity similar expressions could be introduced for the across- and vertical wind components.

The gust factor is clearly related to the turbulence intensity. A common simplified approach for the along-wind component is to write:

$$G_u = 1 + g_p \cdot I_u \tag{4.27}$$

where g_p is a parameter, termed the peak function, which can be evaluated theoretically [13].

4.2.4 Turbulence

One of the key turbulence parameters is the turbulence intensity defined in Eq. (4.24). A more detailed description can be given by the auto-correlation (covariance) function of turbulence:

$$R_u(\tau) = E\left[u(t+\tau)u(t)\right] \tag{4.28}$$

Here the gust component has been assumed to be a locally stationary process within the period used to define the mean wind velocity. Equivalent definitions are valid for the across and vertical turbulence components, *v* and *w*. The one-sided power spectral density can be defined based on the correlation function as:

$$S_u(f) = 4\int_0^\infty R_u(\tau)\cos(2\pi f\tau)\,d\tau \tag{4.29}$$

where *f* is frequency in Hz. Based on this relation the auto-correlation function can also be determined as:

$$R_u(\tau) = \int_0^\infty S_u(f)\cos(2\pi f\tau)\,df \tag{4.30}$$

Therefore, the variance will be:

$$\sigma_u^2 = R_u(0) = \int_0^\infty S_u(f)\,df \tag{4.31}$$

A convenient parameter to assess the correlation of the fluctuating wind components is the integral time scale of turbulence, defined for the along wind as:

$$T_u = \frac{1}{R_u(0)}\int_0^\infty R_u(t)dt \tag{4.32}$$

From Eq. (4.29) and (4.32) it is seen that:

$$T_u = \frac{S_u(0)}{4\sigma_u^2} \tag{4.33}$$

The spectrum of the turbulent velocity fluctuations can be interpreted as a representation of the distribution of turbulent kinetic energy as a function of frequency. In the literature, various researchers have suggested numerous empirical formulae for the gust. The spectrum is commonly presented as a normalised spectral density function and written as a function of non-dimensional frequency, height and roughness, on the form

$$\frac{S_u(f)}{\sigma_u^2} = \mathrm{f}\left[\tilde{n}(z, z_0)\right] \tag{4.34}$$

where $\tilde{n}$ is a normalised frequency, defined as

$$\tilde{n}(z, z_0) = \frac{f\ {}^{x}L_u(z, z_0)}{\overline{U}(z)} \tag{4.35}$$

Here f is frequency in Hz, $\overline{U}$ is the mean wind velocity, z is height above ground, z_0 the surface roughness length and ${}^{x}L_u$ is the integral length scale for the along wind component of fluctuating velocity in the x direction. Although different forms of the function $\mathrm{f}[\tilde{n}(z,z_0)]$ have been suggested, there is a general consensus that the turbulence spectrum, of the along wind component, has some natural boundary conditions. At zero frequency the spectral value should be:

$$S(z, f = 0) = \frac{4\sigma_u^2\ {}^{x}L_u}{\overline{U}} \tag{4.36}$$

The slope at zero frequency should be horizontal, i.e.:

$$\lim_{f \to 0+} \frac{\partial S(z, f)}{\partial f} = 0 \tag{4.37}$$

At higher frequencies ($f >> 1$ Hz), the eddy motion may be assumed independent of viscosity and thus determined solely by the rate of energy transfer by inertia forces. In this range, the inertial sub-range, the spectra should follow the $f^{-5/3}$- equilibrium spectra put forward by Kolmogorov. The turbulence spectrum should also be larger than zero, i.e. $\forall_f\ S_u(f) \geq 0$. Table 4.2 gives the definitions of some spectral shapes commonly used to represent turbulence. It is noted that these formulas fulfil the requirements mentioned above with the exception of Eq. (4.38), which does not have a horizontal tangent at zero frequency. Similar spectral functions have been presented for the lateral and vertical components, for example ESDU [40].

Table 4.2 Some spectral shapes used to represent turbulence

Source	Spectral shape
Davenport: [26]	$\frac{fS(f)}{u_*^2} = \frac{4x_D^2}{\left(1+x_D^2\right)^{4/3}} \quad ; \; x_D = \frac{1200f}{\overline{U}_{10}}$ (4.38)
Harris: [53]	$\frac{fS(f)}{u_*^2} = \frac{4x_H}{\left(2+x_H^2\right)^{5/6}} \quad ; \; x_H = \frac{1800f}{\overline{U}_{10}}$ (4.39)
Kaimal: [87]	$\frac{fS(z,f)}{u_*^2} = \frac{200x_K}{\left(1+50x_K\right)^{5/3}} \quad ; \; x_K = \frac{zf}{\overline{U}(z)}$ (4.40)
von Karman: [239]	$\frac{fS_u(z,f)}{u_*^2} = \frac{4\beta_u \frac{f^x L_u}{\overline{U}}}{\left(1+70.8\left(\frac{f^x L_u}{\overline{U}}\right)^2\right)^{5/6}} \quad ; \; \beta_u = \frac{\sigma_u^2}{u_*^2}$ (4.41)
ESDU: [40]	$\frac{fS_u(z,f)}{u_*^2} = \beta_u\left(\beta_a \frac{2.987\frac{\tilde{n}_u}{\alpha}}{\left(1+\left(2\pi\frac{\tilde{n}_u}{\alpha}\right)^2\right)^{5/6}} + \beta_b \frac{1.294\frac{\tilde{n}_u}{\alpha}}{\left(1+\left(\pi\frac{\tilde{n}_u}{\alpha}\right)^2\right)^{5/6}} F_u\right)$ $\frac{fS_v(z,f)}{u_*^2} = \beta_v\left(\beta_a \frac{2.987\left(1+\frac{8}{3}\left(4\pi\frac{\tilde{n}_v}{\alpha}\right)^2\right)\frac{\tilde{n}_v}{\alpha}}{\left(1+\left(4\pi\frac{\tilde{n}_v}{\alpha}\right)^2\right)^{11/6}} + \beta_b \frac{1.294\frac{\tilde{n}_v}{\alpha}}{\left(1+\left(2\pi\frac{\tilde{n}_v}{\alpha}\right)^2\right)^{5/6}} F_v\right)$ $\frac{fS_w(z,f)}{u_*^2} = \beta_w\left(\beta_a \frac{2.987\left(1+\frac{8}{3}\left(4\pi\frac{\tilde{n}_w}{\alpha}\right)^2\right)\frac{\tilde{n}_w}{\alpha}}{\left(1+\left(4\pi\frac{\tilde{n}_w}{\alpha}\right)^2\right)^{11/6}} + \beta_b \frac{1.294\frac{\tilde{n}_w}{\alpha}}{\left(1+\left(2\pi\frac{\tilde{n}_w}{\alpha}\right)^2\right)^{5/6}} F_w\right)$ $\beta_i = \frac{\sigma_i^2}{u_*^2} \quad ; \quad i \in (u,v,w)$ $\tilde{n}_i = \frac{f^x L_i}{\overline{U}(z)} \quad ; \quad i \in (u,v,w)$ $\alpha = 0,535 + 2.76\left(0.138 - 0.115\left(1+0.315\left(1-6z\,f_c/u_*\right)^6\right)^{2/3}\right)^{0.68}$ $f_c = 2\Omega\sin\Phi$ $F_u = 1+0.455\exp\left(-0.76\left(\tilde{n}_u/\alpha\right)^{-0,8}\right)$ $F_i = 1+2.88\exp\left(-0.218\left(\tilde{n}_i/\alpha\right)^{-0,9}\right) \quad ; \quad i \in (v,w)$ $\beta_a = 2.357\alpha - 0.761$ $\beta_b = 1-\beta_a$ (4.42)

4.2.5 Spatial correlation of velocity components

In addition to the information on the frequency content of the velocity fluctuations at any given point, information is also needed on the spatial correlation of the fluctuations in order to fully characterise the turbulence. This information is usually expressed in terms of the cross-correlation (covariance) or coherence of the wind velocities $u_1(t)$ and $u_2(t)$ at two points in space. Limited data exist on the spatial structure of gusts. However, empirical expressions can be found, for example in ESDU [40].

Convenient indicators of spatial correlation are the integral length scales of turbulence. They, give a measure of the average size of the turbulent eddies in the flow and are key parameters in spectral functions such as those shown in Table 4.2 and others. The integral length scales of turbulence can be defined as follows:

$$^{x}L_i = \frac{1}{\sigma_i^2}\int_0^{\infty} R_i(X+x,Y,Z,t)dx \quad ;\ i \in \{u \quad u \quad w\} \tag{4.43}$$

$$^{y}L_i = \frac{1}{\sigma_i^2}\int_0^{\infty} R_i(X,Y+y,Z,t)dy \quad ;\ i \in \{u \quad u \quad w\} \tag{4.44}$$

$$^{z}L_i = \frac{1}{\sigma_i^2}\int_0^{\infty} R_i(X,Y,Z+z,t)dz \quad ;\ i \in \{u \quad u \quad w\} \tag{4.45}$$

Here R_i represents the cross-covariance functions of corresponding velocity components along specific axis in space (X, Y, Z). As can be seen there are nine different length scales. Empirical relations have been suggested for the integral length scales, see for instance [40].

Based on the Taylor's hypothesis, which postulates that the turbulence pattern is frozen into the wind, and space and time can be related by the mean wind speed, the length scales in the along-wind direction can be related to the time-scales as:

$$^{x}L_i = T_i\overline{U} \tag{4.46}$$

Here the time-scales are defined as:

$$T_i = \frac{1}{R_i(0)}\int_0^{t} |R_i(\tau)|d\tau \quad ;\ i \in \{u \quad u \quad w\} \tag{4.47}$$

where $R_i(\tau)$ is the auto-covariance of different turbulence components at a single point, and the upper limit t is the duration of continuous data sampling i.e. the averaging period of the mean wind velocity.

The relation given by Eq. (4.46) can only be considered an approximation and should be used with care. However, it simplifies the evaluation of the integral length scales, as it is now possible to evaluate the three time- or length scales associated with the along wind direction from a single point data.

4.3 Wind velocity data and related parameters

As discussed in section 4.2, the description of gusty wind can be reduced to a description of statistical variables and functions by means of the theory of stochastic processes. The key parameters and quantities in such statistical description are:

- The mean wind velocity and mean wind direction
- The mean wind velocity profile
- The rms fluctuations of the 3-dimensional wind, often described in terms of a non-dimensional turbulence intensity
- Peak gusts often described in terms of a non-dimensional gust factors
- The Reynolds stresses and surface roughness
- The integral scales of turbulence
- The power spectral densities of turbulence
- The spatial correlation of wind fluctuations generally expressed in terms of the coherence of turbulence at two points in space.

All these parameters can be evaluated, in principle, from a single point data, except of course the spatial correlation, as long the three components of turbulence at the point are recorded. Since the Gill sonic anemometer fulfils that requirement, most of the key wind parameters can be evaluated, at least in principle, from the data at hand. Reference wind data is also available from the Icelandic Meteorological Office, IMO, recorded at their site in Reykjavik.

An example of the parameters representing the first order statistics of turbulence is given in Table 4.3. The presented parameters are evaluated based on data from the sonic anemometer on the building roof, comparative data from the IMO site as well as the wind simulation in the wind tunnel. It is rather encouraging that the similarity between full-scale and wind tunnel seems acceptable with regard to profile and turbulence parameters.

It should be noted that the wind recorded above the building is not measured under free flow conditions. This is especially noticeable in the relatively high mean velocity in the vertical direction, which represents the flow moving upwards along the building side. This does not necessarily make the turbulence statistics invalid. However, it is reasonable to expect somewhat higher wind velocities and higher turbulence due to disturbed flow conditions, than in free flow conditions. The result may be an overestimation of the roughness and turbulence levels. However, Table 4.3 gives the turbulence intensity ratios: $I_u : I_v : I_w \approx 1.0 : 0.75 : 0.53$. This is not much higher than the turbulence intensity ratios recorded in an open exposure environment with relatively flat terrain close to the coast on Reykjanes [199], which were $I_u : I_v : I_w \approx 1.0 : 0.7 : 0.4$.

The available wind data from the IMO site during the test period is 10-minute mean wind velocity and direction at 10 m height. Additional recorded wind statistics are peak wind velocity and standard deviation of wind direction. No wind velocity profile data was recorded at the IMO site during the test period. However, profile data with wind velocity

recorded at four height levels (2, 10, 20 and 30 m) during several storms in the period between 1990 and 1995 was available. In addition to this, traditional 3-hour interval meteorological data is available for the past 50 years.

Table 4.3. An example of characteristic parameters for recorded wind. The table gives the range between minimum and maximum values along with a mean value in ( ), and where appropriate a median value in [ ].

Parameter		Full scale Above the building	Wind tunnel At roof height in front of building	IMO In a mast*)
Anemometer height (m)	h_a	33.10 (+52.4 msl)	26.6 m (full-scale equiv.)	10 (+ 51 msl)
10 minute mean wind direction (°)	$\overline{\phi}$	84.5 – 93.6 (88.0)		77.6 – 92.2 (85.5)
Standard deviation of wind direction (°)	σ_ϕ	7.8 – 10.0° (9.1°)		10.1 – 13.6° (11.9°)
10 minute mean wind speed (m/s)	$\overline{U}$	17.0 - 22.6 (19.9)	10.8 - 11.4 ($\lambda_u \approx 1/2$)	8.6 - 11.9 (10.5)
Gust factor	G_u	1.43 - 1.69 (1.57)	1.72	1.37 - 1.86 (1.53)
Turbulence intensity	I_u I_v I_w	0.16 - 0.23 (0.20) 0.12 – 0.20 (0.15) 0.06 - 0.12 (0.08)	0.16 - 0.19 (0.17)	(0.18) (using Eq. (4.27) with $g_p = 2.93$)
Peak factor	g_p	2.54 - 3.44 (2.93)	4.02	
Reynolds stress (N)	τ_{uw}	0.63 - 1.85 (1.16)	0.28 [1)]	0.60 - 5.91 (2.37) [2.20] [2)]
Shear (friction) velocity (m/s)	u_*	0.70-1.22 (0.94)	0.471 [1)]	0.64 - 1.80 (1.18) [2)]
Surface roughness coefficient	κ	0.0014-0.0044 (0.0023)	0.0019 [1)]	0.0013 - 0.0140 (0.0067) [0.0059] [2)]
Surface roughness length (m)	z_0	0.0008-0.0780 (0.0204) [0.0067]	0.0114 [1)]	0.0003 - 0.3328 (0.0935) [0.0581] [2)]
Power profile	α	0.07 – 0.19 (0.13)	0.14 [1)]	0.09-0.26 (0.16) [2)]

[1)] Estimated using velocity profile data.
[2)] Estimated using velocity profile data, recorded outside of test period.

4.4 Description of the local wind environment

4.4.1 Topography and nearest obstacles

As stated in Chapter 2, the study-building is located in a built up residential area in the city of Reykjavik, enclosed by sea on one hand and mountains on the other. Figure 2.3 through Figure 2.5 give some visual information on the topography and the local surface roughness conditions. The figures in Appendix A show more closely the local surroundings of the building. The building is located on a hill and has a relatively high wind exposure, as the overall height of the office-tower is roughly twice the height of the closest obstacles.

4.4.2 Roughness and turbulence

The surface roughness has been evaluated based on data from the sonic anemometer on the building roof and comparative data from the IMO site. Representative values are given in Table 4.3.

The velocity profile parameters based on the data from the sonic anemometer, were evaluated according to the methodology presented in Eq. (4.18) through Eq. (4.22) and are primarily based on the shear stress, τ_{uw}.

The profile parameters for the IMO-site, on the other hand, have been determined using the logarithmic velocity profile:

$$\ln(z) = \frac{k_a}{\sqrt{\kappa}} \frac{\overline{U}(z)}{\overline{U}(z_R)} + \ln(z_0) \tag{4.48}$$

Here κ is the surface roughness coefficient, k_a is the von Karmans coefficient, z_0 is the roughness length, $\overline{U}$ is the mean wind velocity, z is height and z_R is the reference height (10 m).

The analysis is based on wind velocity data at three height levels in a mast, i.e. 10 m, 20 m and 30 m, recorded during strong winds ($\overline{U}$ > 10 m/s) for various wind directions. Figure 4.1 shows the histograms of the evaluated parameters. A considerable variation is seen in the evaluated parameters, especially the z_0 values. This can partly be traced to the fact that all seasons are included in the dataset. The median values are: κ = 0.006 and z_0 = 0.06 m, which would indicate a terrain category II, as defined in the ENV1991-1-4 [41]. The natural assumption beforehand would have been category III (z_0 = 0.3 m). However, it is in line with the authors former experience that estimated surface roughness values in Iceland tend to be lower than the values predicted by illustrative definitions of terrain categories [199]. This may be related to lack of homogeneity in the terrain or lack of fetch, with the wind profile in a transition state between the smooth terrain (sea or bare land) from where the flow is coming and the rougher urban terrain.

What is also noticeable from Table 4.1 is, that the variance in the profile parameters is considerably greater and the mean and median values higher using the measurements at

the IMO mast than the same parameters evaluated based on the Reynolds stresses above the building. This difference is probably partly caused by the fact that the IMO recordings include data from various storms during all seasons for a period of five years, whereas the recordings above the building only represent two continuous seasons and therefore relatively uniform surface conditions. Another influence could be that the profile parameters at the IMO-site are referred to 10 m height, whereas the building mast is at 33.1 m height. Then again, it is likely that the difference in the methodology has some bearing on the result.

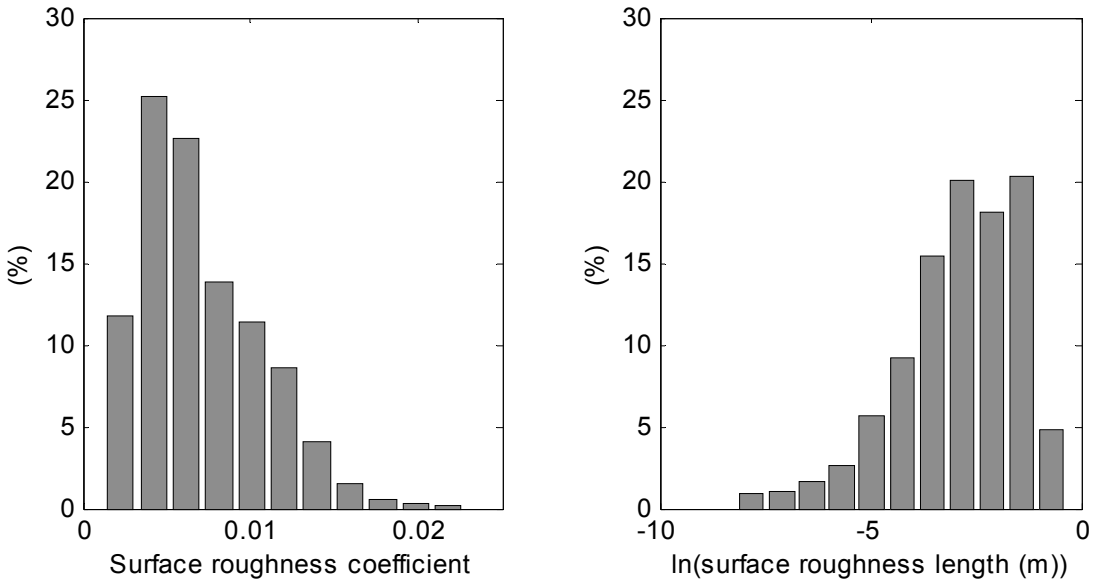

Figure 4.1 A histogram of the evaluated surface roughness parameters κ and $\ln(z_0)$ the median values are 0.006 and 0.06, respectively.

Commonly used measures of the variability of the wind within a reference period are the turbulence intensity, I_u, and the gust factor, G_u, which were defined in Eq. (4.24) and Eq. (4.26), respectively. Both parameters can be evaluated directly from the sonic anemometer wind data above the building as well as from the hot-wire data for the wind tunnel simulation. The data from the IMO-site, on the other hand, only offers direct evaluation of the gust factor.

Figure 4.2 shows the gust factor recorded at the IMO-site as a function of mean wind velocity at 10 m height. The figure also shows the gust factor recorded above the building roof as a function of mean wind velocity. As listed in Table 4.3, the gust factor is seen to be about 1.5 for wind velocities above 10 m/s. Based on Table 4.3 and Figure 4.2 the gust factor and thereby the turbulence level, seems to be similar for both sites. The turbulence parameters are also found to be consistent with the evaluated surface roughness parameters.

Figure 4.3 shows the gust factor at the IMO-site as a function of mean wind direction for mean wind velocities above 10 m/s. It is seen that the gust factor at the IMO-site seems to be lowest for southerly winds. This is different for the building site, where the gust

factor is lowest for northerly winds. However, the variation in gustiness for the same wind direction is considerable and perhaps reduces the significance of the directional variations.

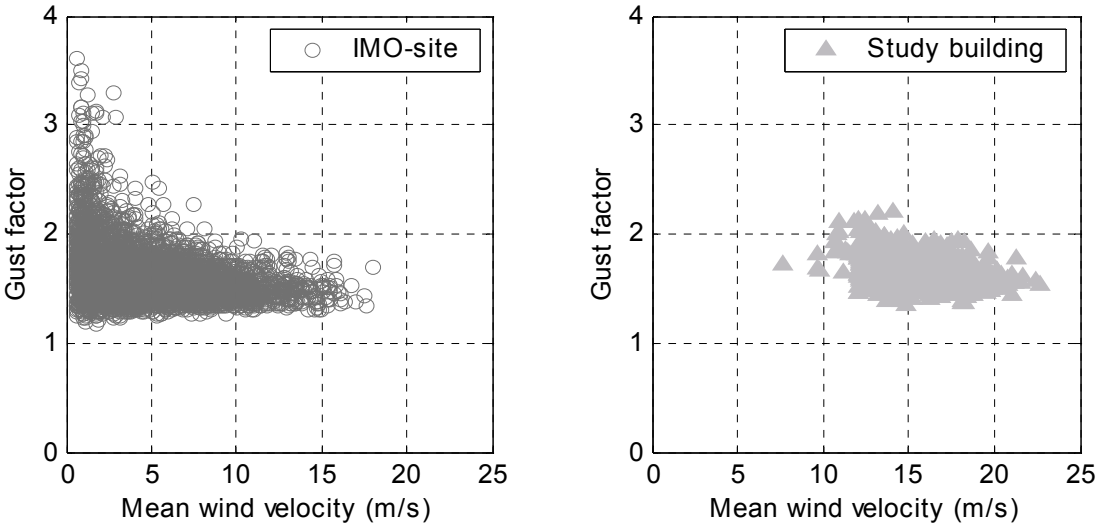

Figure 4.2 Gust factor as a function of mean wind velocity at both the IMO-site and the study-building during the testing period.

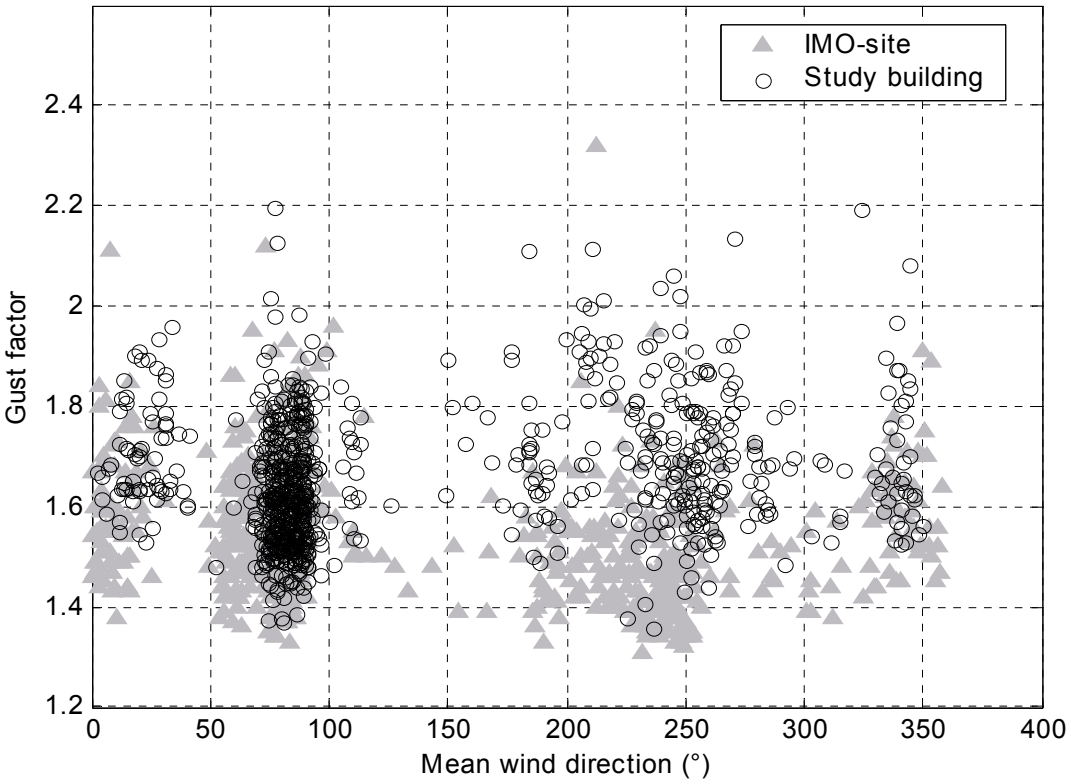

Figure 4.3 Gust factor as a function of mean wind direction for mean wind velocity above 10 m/s at both the IMO-site and the study-building.

4.4.3 Climatic conditions

The climatic conditions at the site will not be accounted for her in any detail, as they are only indirectly relevant with regard to this research. However, few introductory comments on the climatic conditions are appropriate. Especially with regard to prevailing winds, stability and the probability of occurrence of strong winds.

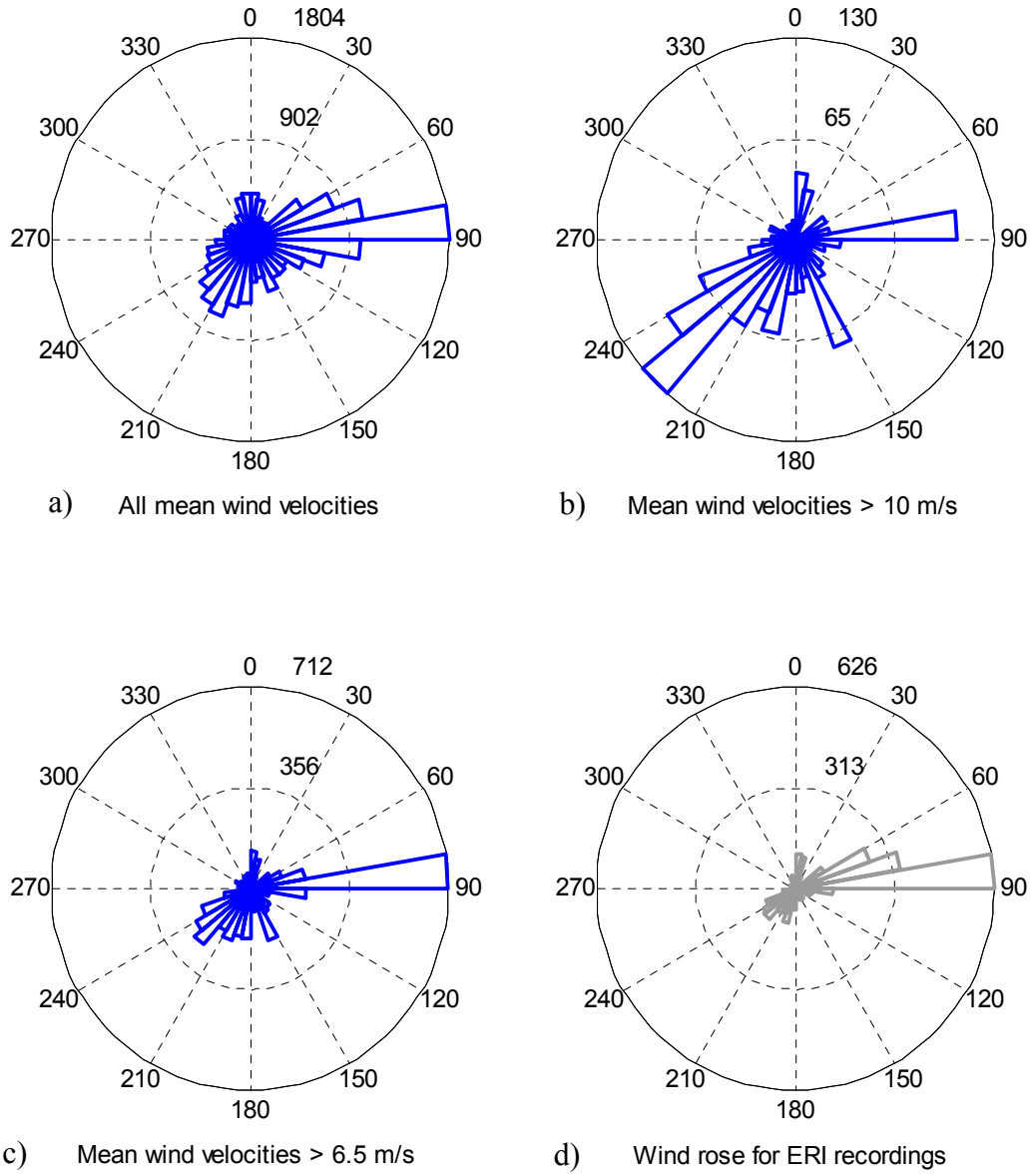

Figure 4.4 Wind roses for the IMO-site during the test period. a) Wind rose for all wind velocities; b) wind rose for mean wind velocities > 10 m/s; c) wind rose for mean wind velocities > 6.5 m/s; d) wind rose for mean winds recorded at the IMO-site during the date and time of recordings at the study-building.

Traditionally, easterly winds have been the prevailing winds at the IMO-site, whereas winds from northwest are uncommon. However, the strongest winds generally come from southerly directions, especially southeast and southwest. During the period of recordings at the study-building, a similar pattern was seen, the prevailing wind directions being easterly. This is displayed in Figure 4.4, which also shows that south-westerly wind directions were common at the IMO-site for storms with mean wind velocity above 10 m/s. It should be noted, that measurements at the study-building were only recorded when the wind velocity above the building roof was above 12 m/s. Therefore it is curious that the wind rose at the IMO-site for the date and time of recordings at the study-building bears closer resemblance to a wind rose for mean wind velocities above 6.5 m/s than the one for wind speeds above 10 m/s. This will be discussed further in Chapter 5.

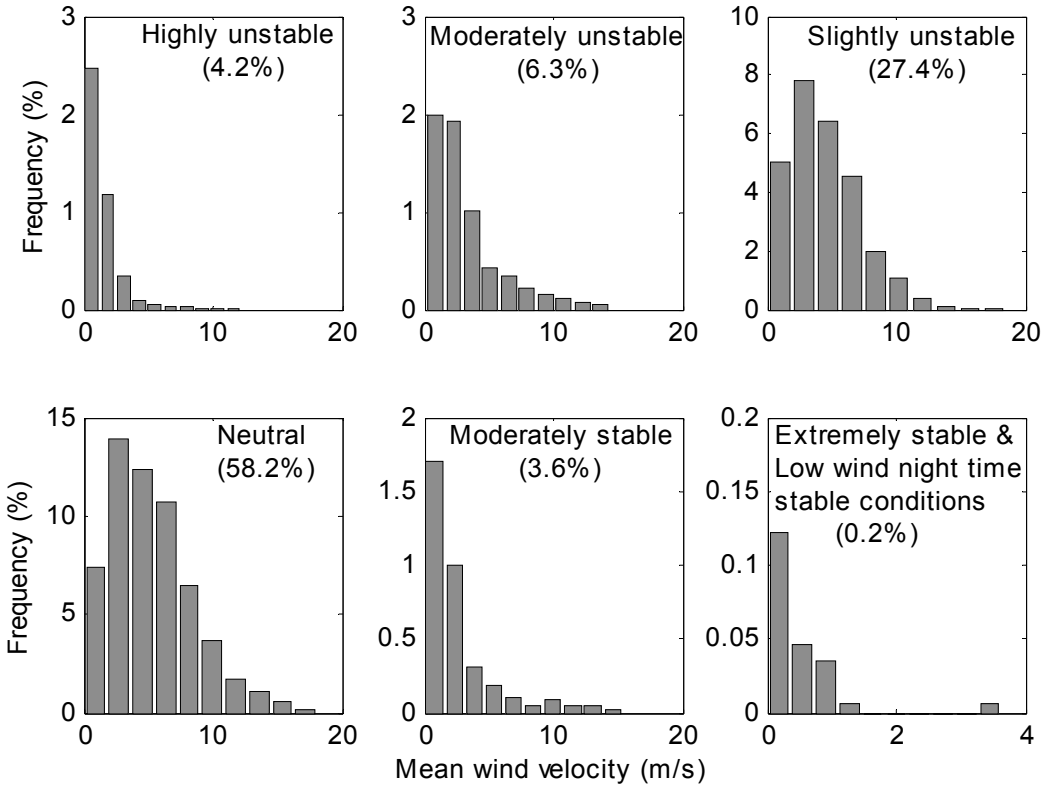

Figure 4.5 Stability conditions at the IMO site during the full-scale test period. The figure shows frequency histograms of recorded mean wind velocities during various stability conditions. The frequency for each stability class is referred to the total number of records.

The stability conditions in Reykjavik are depicted in Figure 4.5, which shows histograms of the recorded mean wind velocities at the IMO-site during the full-scale testing period. The total wind record is split up into stability classes according to the criteria in Table 4.1. Each histogram in Figure 4.5 represents a separate stability class and the frequency percentages in the brackets indicate how common the stability conditions are, i.e. the area in each histogram. It is seen that the stability conditions are neutral 58% of the time. However, it is noteworthy that the atmospheric conditions are unstable to some degree about 38% of the time and that mean wind velocities over 10 m/s are recorded

during such conditions. Moderately stable and extremely stable conditions seem to be rather rare in Reykjavik or less than 4% of the time.

The probability of occurrence of strong winds in Reykjavik has been estimated by the author [196]. Using the maximum yearly mean wind speeds measured at the IMO-site from 1949 to 1987, an extreme distribution was developed by fitting the Gumbel distributions to the data using a transformation of the distribution to a straight line. The mode and the shape parameter were evaluated through the method of moments. Table 4.4 gives the expected maximum wind speeds for 5-, 10-, and 50-year return periods. Unfortunately, such storms did not occur during the test period.

Table 4.4 Expected maximum mean wind velocity in Reykjavik

Return Period:	5 years	10 years	50 years
Mean wind velocity:	31 m/s	33 m/s	38 m/s

4.5 Estimation of integral time scales and spectral densities

Based on the definition given in Eq. (4.47), the integral time-scales scales can be estimated from the auto-covariance function. Using the hypothesized relation given by Eq. (4.46) the time scales can be converted into estimates of integral length scales. The auto-covariance functions for the *u*-, *v*-, and *w*-component, were therefore evaluated. The data series were split up into segments. Auto-covariance functions were evaluated for each turbulence component and each interval and averaged to give mean auto-covariance functions for the recordings. Then the positive part of the auto-correlation was integrated to give time-scale estimates, which are shown in Table 4.5. The time- and length-scales evaluated from full-scale data are lower than expected [199]. However, the wind velocities are not very high and the local surroundings may influence the scaling parameter. The time- and length-scales evaluated from the wind tunnel data were also slightly lower than expected [213]. However, it is promising in terms of similarity that the model- and full-scale scaling values are comparatively similar.

Table 4.5 The time- and corresponding length-scales in the along-wind direction for the *u*- and *w*-component. Estimates are based on integrating the auto-covariance function.

Scaling parameter	Full scale	Model scale
	min – max (mean)	min. – max. (mean) / equiv. full-scale
T_u (s)	1.695 - 2.948 (2.309)	0.013 - 0.040 (0.025 s) / (0.025*160=4.0)
T_w (s)	0.739 - 1.257 (0.974)	
${}^xL_u=UT_u$ (m)	36.42 - 63.24 (46.28)	0.119 - 0.386 (0.236) / (0.236*160=37.8)
${}^xL_w=UT_w$ (m)	14.41 - 25.29 (19.60)	

It is conventional to use an exponential approximation for the auto-covariance functions, of the form:

$$R_i(\tau) = R_i(0)\exp\left(-\frac{\tau}{T_i}\right) \tag{4.49}$$

Using the evaluated time-scales, the corresponding approximate exponential auto-covariance functions were constructed. An auto-correlation function is shown in Figure 4.6, along with the traditional exponential approximation. The auto-correlation can be modelled by a correlation function compatible with the von Karman spectral expression [55]. These are compared with the data in Figure 4.6. As is seen, the difference between the two models is small and the exponential similarity looks reasonably good.

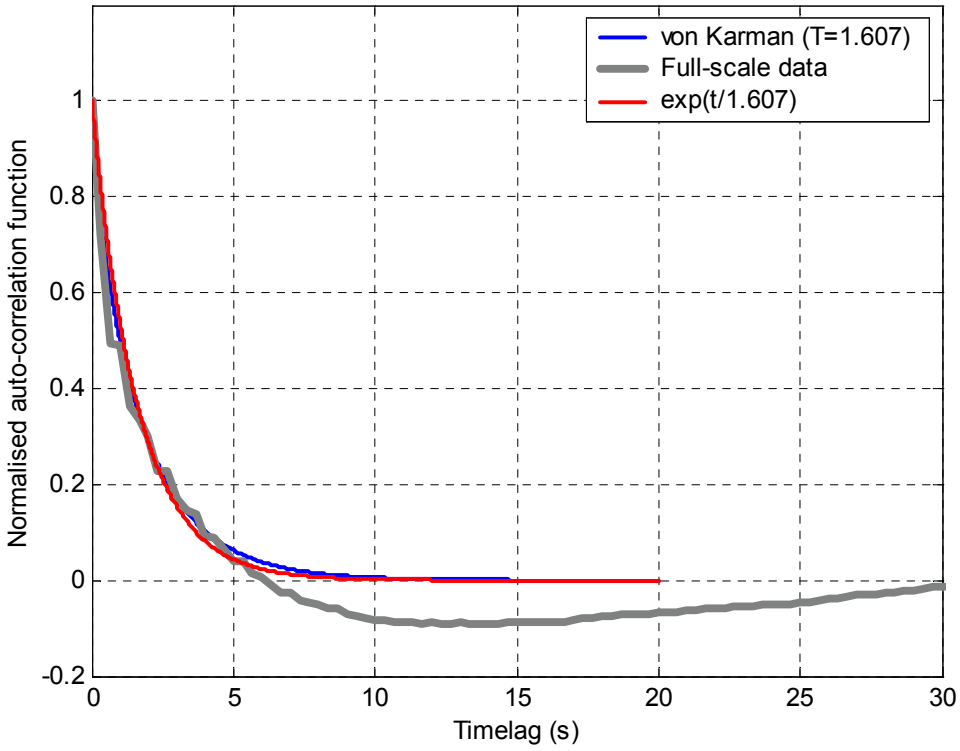

Figure 4.6 Auto-correlation of along wind turbulence as a function of time lag. Full-scale data (▪▪▪), exponential model (– – –) and model based on the von Karman spectrum (—).

The auto-correlation function of the wind data is seen to cross below zero and have a negative part before it stabilises at zero. The above models are incapable of simulating this effect. A refined model, in line with the one proposed by Harris [55], is needed for that.

The integral time scale may also be expressed in terms of the one-sided auto-spectral density, $S_i(\omega)$, given as a function of circular frequency, ω. That is:

$$T_i = \frac{\pi}{2}\frac{S_i(\omega = 0)}{R_i(0)} \tag{4.50}$$

In the present study, the turbulence spectrum was estimated by applying auto-regressive methods. The time series of turbulence are approximated by a parametric auto-

regressive model. The transfer function can then be evaluated directly from the model parameters. When evaluated at $z=e^{-j\omega}$, the transfer function gives the spectral ratio between input and output.

Assuming a band-limited white noise input, with a constant spectral density, the spectral ratio can simply be scaled with the RMS-value of the white noise input to give the auto-spectral density of the output process. The reason for choosing a parametric spectral estimation rather than a FFT-based spectral estimation lies primarily in the fact that the parametric estimate is smooth and less affected by bias and standard estimation errors.

Then, applying Eq. (4.50), the time scale can by computed directly from the AR-parameters as follows:

$$T_i = \frac{1}{\Delta f} \frac{\sigma_e^2}{(1 + a_{1i} + a_{2i} + \cdots + a_{ni})^2} \tag{4.51}$$

Here, Δf is the sampling rate in Hz; σ_e is the standard deviation of the noise process feeding the model; a_{1i}, a_{2i}, to a_{ni} are the AR-parameters; and n refers to the order of the AR-model. The optimum order of the model was selected using Akaike's FPE criterion and appropriate validation tests. It was generally found that the FPE function was very flat. On the other hand, some minor oscillations were observed in the corresponding values of the integral time scale. The presented values of the time scale were therefore obtained by taking the average of ten values around the optimum values. AR-models of the order 5 to 20 were used in the averaging process. This approach is believed to give consistent results. The resulting time scale values are listed in Table 4.6. It is seen that they are greater than the values derived from the auto-covariance functions and shown in Table 4.5.

The length scale estimates were used to evaluate different analytical spectral formulas. Comparing them with spectral quantities estimated from the measured turbulence indicates that the higher length scales give a better comparison. The evaluated time- and length scales are in fact generally lower than was expected. This may be a result of the disturbed flow conditions at the measurement point.

Table 4.6. The time- and corresponding length-scales in the along-wind direction for the *u*- and *w*-component. Estimate based on auto-regressive spectral evaluation.

Scaling parameter	Full scale	Model scale
	min. – max. (mean)	min. – max. (mean) / equiv. full-scale
T_u (s)	1.911 - 4.057 (2.802)	0.014 - 0.039 (0.024) / (0.024*160=3.84)
T_w (s)	0.592 - 1.286 (0.964)	
${}^xL_u=UT_u$ (m)	37.57 - 86.88 (56.27)	0.132 - 0.391 (0.231) / (0.231*160=37.0)
${}^xL_w=UT_w$ (m)	12.24 - 27.59 (19.37)	

The power spectrum of turbulence was evaluated for the *u*- and *w* velocity components. The spectral density was normalised by multiplying it with the frequency and dividing with the shear velocity squared. The spectral density is then plotted versus

normalised frequency by multiplying with the appropriate length scale and dividing by the mean velocity or alternatively, by multiplying with the appropriate time scale. Figure 4.7 shows the recorded spectrum for all three turbulence components, i.e. the along, across and vertical wind-component. The spectra represent 75 full-scale records all within a 5° wind direction sector with a mean at about 87° from north, i.e. at about 68 degree angle to the east wall. In fact, the spectra represent the wind conditions during the pressure recordings represented by Figure 5.27.

The corresponding ESDU spectra (Eq. (4.42)) are shown for the respective turbulence components. It is clear that the frequency content of the turbulence recorded above the roof differs from the homogeneous conditions represented by the ESDU spectrum. It is particularly noticeable that there is a considerable energy at higher frequencies, especially in the across and vertical components. It may even be argued that the energy is shifted from the medium frequency range to the high frequency range. This is reasonable, as the building likely creates smaller scale eddies and turbulence that contribute to the energy at the higher frequency range and in the process may dissipate some of the medium size eddies and related turbulence.

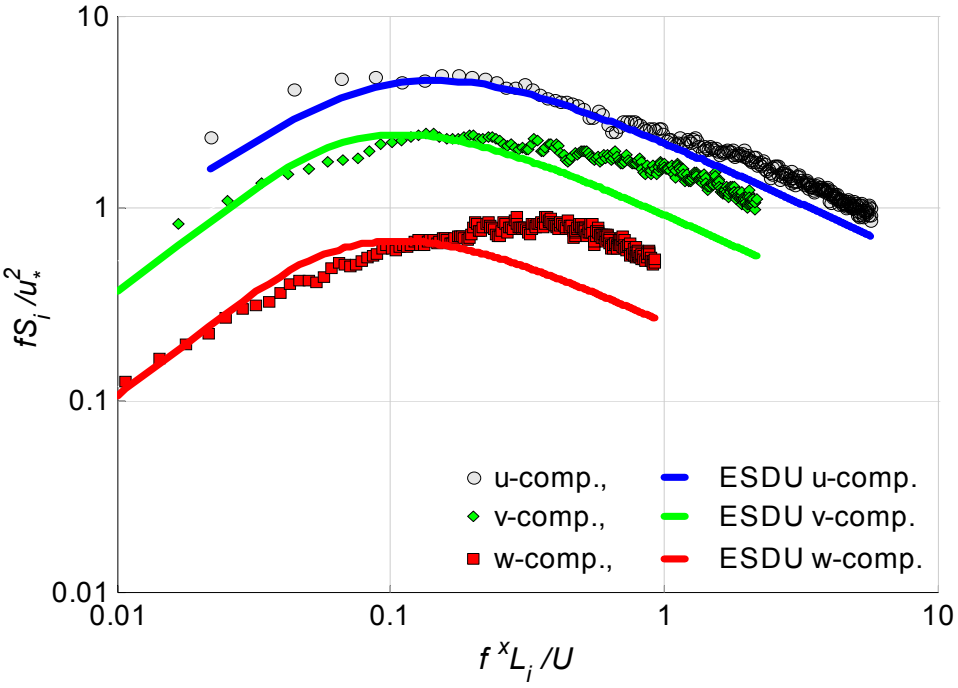

Figure 4.7 Normalised spectral density of the three wind velocity components as a function of frequency based on data from the full-scale site. The ESDU spectra are plotted for comparison.

Figure 4.9 shows the recorded full-scale spectrum for the along wind-component for a different wind direction sector, i.e. perpendicular to the east face of the building. The corresponding ESDU spectrum and the spectrum for the wind tunnel flow is also shown. A

similar shift in energy distribution between medium frequency range and the high frequency range can be seen.

4.6 Turbulence modelling

The turbulence modelling concentrated on simulating a mean wind velocity profile and along wind turbulence corresponding to the available information for the full-scale site. The mean wind velocity profiles from the IMO site, the full-scale building site and the wind tunnel are displayed in Figure 4.8. The full-scale profiles are median mean wind profiles for a large sample of wind data for many wind directions. The simulated wind tunnel profile largely falls within acceptable range, especially considering the variability in the full-scale data.

The simulated turbulence characteristics are compared in Table 4.3 and Figure 4.9, which shows the comparison of the along wind velocity spectra based on full- and model scale recordings with the ESDU spectrum [40]. The simulated turbulence characteristics are judged to satisfy the full-scale condition.

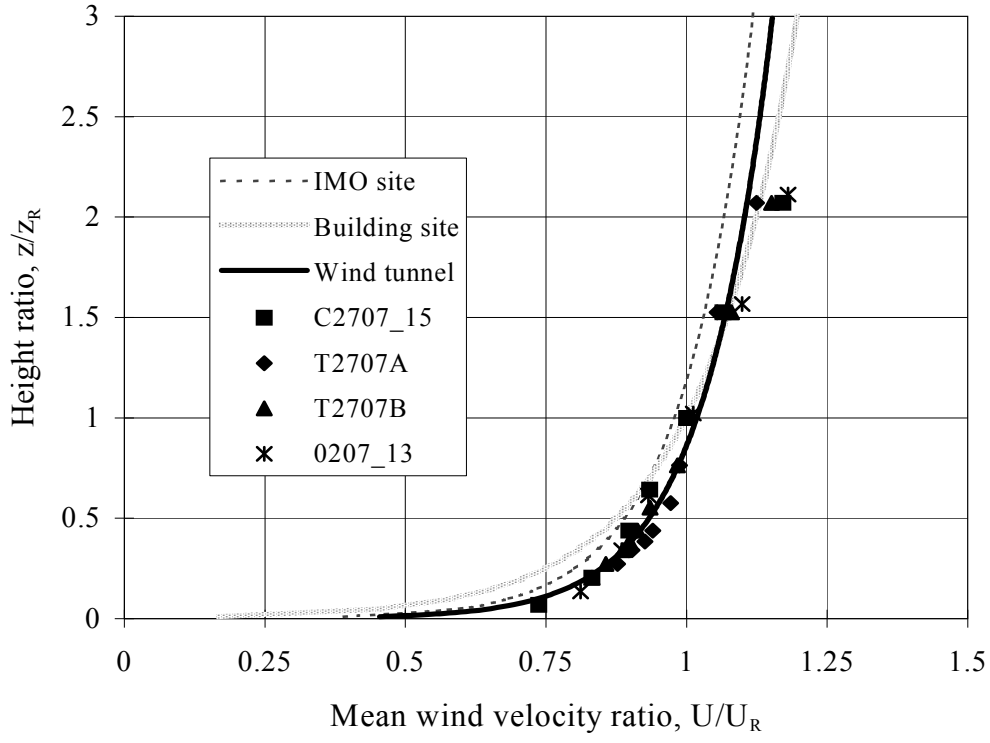

Figure 4.8 Mean wind velocity profiles from full- and model scale data. The grey lines represent the median full-scale profiles and the black line the wind tunnel profile. The data points shown are from hot-wire recordings in the wind tunnel. The full-scale reference height is about 30 m in all cases.

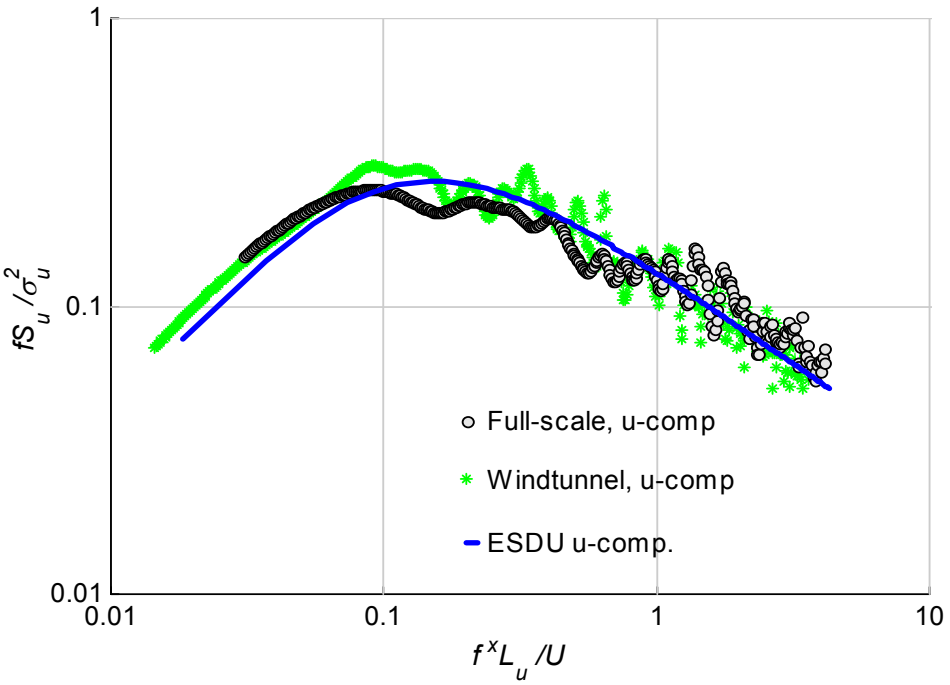

Figure 4.9 Normalised spectral density of along wind velocity as a function of reduced frequency. Data from the full-scale site and the wind tunnel are compared with the ESDU spectrum.

4.7 Summary and discussion

An overview on the engineering description of turbulence has been presented. Background information on wind characteristics in full- and model scale testing was introduced, along with some information about the wind climate in Reykjavik.

In general, the evaluated full-scale wind parameters are in qualitatively good agreement with the model scale parameters, indicating that the wind tunnel simulation was successful.

It is found that the recorded turbulence level at the building site is comparable to the turbulence level at the Icelandic meteorological office. However, the evaluated profile parameters differ in the sense that the variability in the values based on data from the IMO-site is considerably greater than in the values based on data from the study-building. This can be related to more seasonal variability in the IMO data as well as different evaluation methodology and difference in reference height.

The estimated surface roughness parameters were found to be approximately representative of terrain category II as defined in the ENV1991-1-4, which was a smoother terrain category than expected, compared to the illustrative definitions of terrain categories. This may be related to the relatively short distances from the two sites to either, a smooth rural terrain or to the sea. In addition, the fact that Reykjavik is rather sparsely built may result in a terrain that is not very homogeneous, which can increase the required length of fetch for a stable mean wind profile. Therefore, the wind profile may be in a

transition state between the smooth terrain (sea or rural) and the rougher urban terrain. It should be noted that the turbulence parameters I_u and G_u are consistent with the terrain category II definition.

Neutral atmospheric stability conditions were found to exist for about 58% of the full-scale testing period, whereas the conditions were somewhat unstable 38% of the time. Mean wind velocities above 10 m/s were recorded during atmospheric conditions defined as unstable.

The spectral characteristics were similar for full-scale and model scale. That can be explained by the relatively low full-scale time and length scales, which were comparable to the equivalent scales in the wind tunnel. The normalised spectral density was found to follow the ESDU spectral expression reasonably well. However, it was found that for the full-scale turbulence, recorded above the building, the energy was shifted from the medium frequency range towards the high frequency range.

Chapter 5 Pressure data and related parameters

5.1 Introduction

This chapter deals with the analysis of pressure data. The analyses include determination of pressure coefficients for a range of wind directions. Spectral densities and coherence functions are evaluated and presented for various angles of incidence. Spectral density of wind-induced pressures is related to the upstream wind velocity spectral density by a pressure admittance function and a mean pressure coefficient. Due to the large quantities of recorded full-scale data, it is possible to demonstrate some statistical properties for the spectral quantities. Comparison is made between model- and full-scale data.

It is traditional and in many ways convenient, to use a pressure coefficient normalised by the dynamic mean wind pressure. Herein a pressure coefficient time series is evaluated based on the following definition:

$$C_p = \frac{P_s - P_r}{\frac{1}{2}\rho_a \overline{U}_R^2} = \frac{P_s - P_r}{Q_R} \tag{5.1}$$

where P_s is the surface pressure, P_r the reference pressure, ρ_a is the mass density of air and $\overline{U}_R$ is the mean wind velocity at some reference location and Q_R the mean dynamic velocity pressure. The pressure coefficient time series evaluated according to Eq. (5.1) can be represented by different statistical quantities. The key parameters in such a statistical description are:

- The mean, maximum, minimum and standard deviation of pressure fluctuations.
- The power spectral density of pressure fluctuations.
- The spatial correlation of pressure fluctuations.

These parameters will be presented and discussed in the following sections.

5.2 The wind tunnel data - 1st order statistics of pressure coefficients

In the wind tunnel, the static pressure of the approaching flow measured by a pitot tube at roof height is used as reference pressure. Similarly, the reference velocity is taken as the mean wind velocity of the approaching flow, measured by a pitot tube and a hot-wire anemometer at roof height.

Figure 5.1 gives an overview on pressure tap locations on the model. Time series of surface pressure were usually recorded simultaneously at 15 pressure taps. The 16th channel available was generally used to record the static reference pressure. However, for some measurement phases all 16 channels were used to record surface pressures with the static reference recorded separately before and after data sampling.

Figure 5.2 through Figure 5.6 show the evaluated pressure distributions around the building for a mean wind direction perpendicular to the east wall (i.e. 109° from north). The pressure distribution at each tap is given in the form of a histogram of the surface pressure. The mean values of the pressure coefficient at each tap as well as the tap number, is also given. It should be noted that each histogram has a total area of one. The mean C_p values seem to be in general agreement with the results reported in the literature for a box form of this type (see [39]).

Figure 5.7 and Figure 5.8 show the evaluated pressure distributions around the top perimeter of the building for two different wind directions that is 109° and 90° from north, which represent a 90° and 71° angle to the building east wall respectively. These data are recorded in another measurement phase, where the emphasis was put on the top perimeter of the building to prepare for the full-scale study that was to follow. The C_p values of Figure 5.7 compare well with the ones already shown, for wind angle perpendicular to the east wall. The C_p values of Figure 5.8 for wind direction at 71° angle to the east wall are shown for later comparison with full-scale recordings for similar mean wind direction.

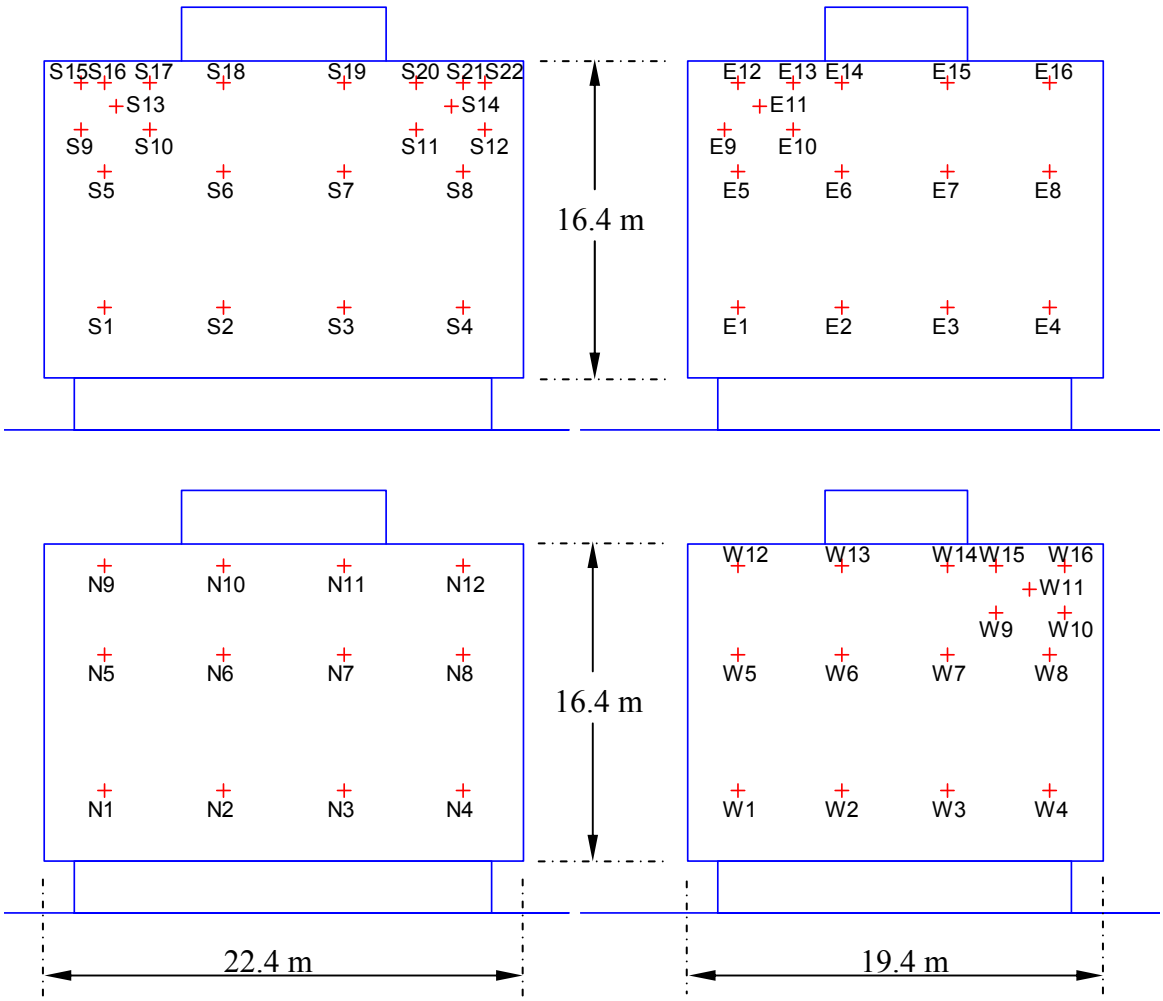

(a) Tap locations on the south, east, north, and west side of the wind tunnel model. The letter before the number denotes the building side.

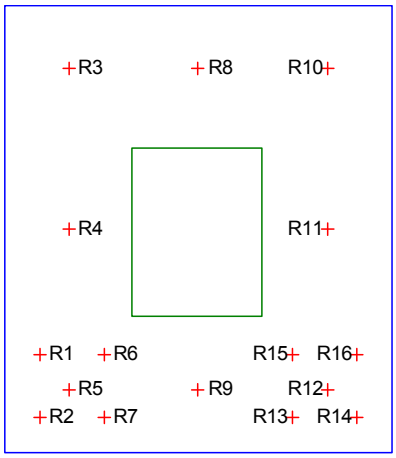

(b) Tap locations on the roof of the model.

Figure 5.1 Overview on the tap locations on the model. The letters refer to the respective sides of the building/model; S numbers refer to the south side, E numbers to the east side, etc.

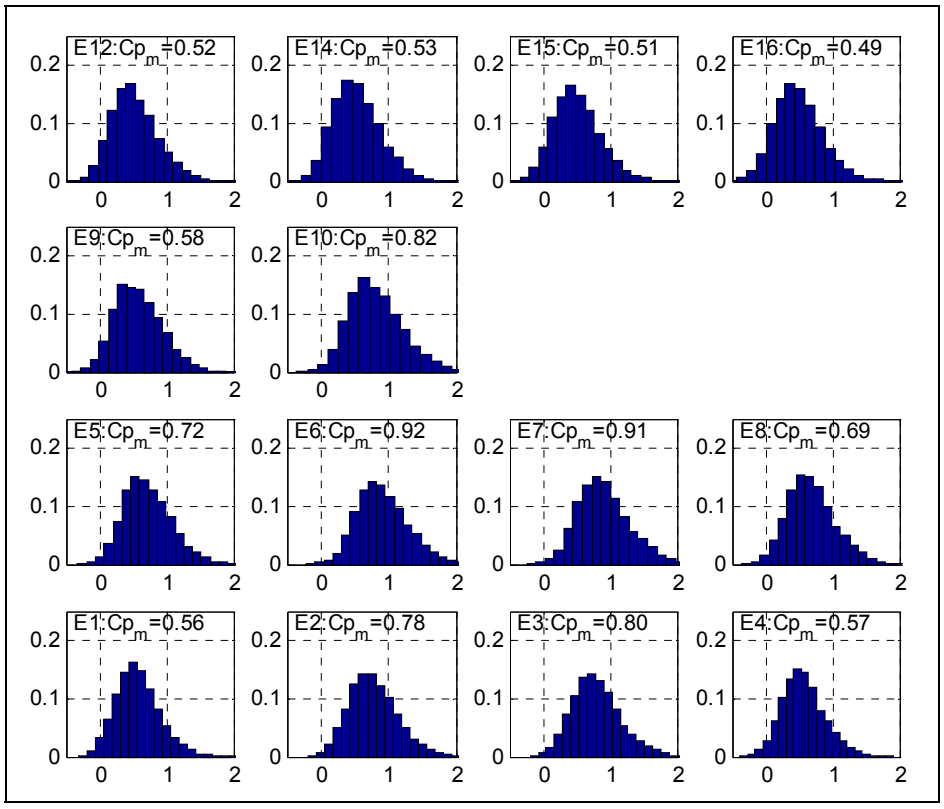

Figure 5.2 Pressure distributions on the east wall for a mean wind direction perpendicular to the east wall. Pressure tap number and mean C_p value is shown above each histogram.

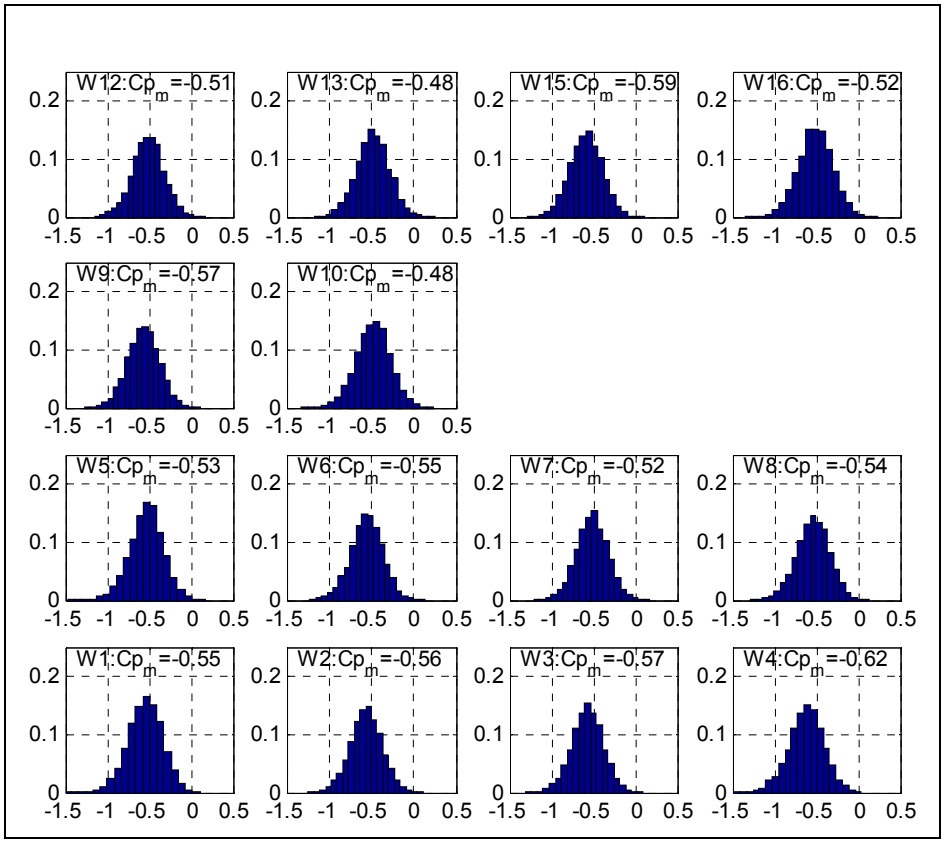

Figure 5.3 Pressure distributions on the west wall for a mean wind direction perpendicular to the east wall. Pressure tap number and mean C_p value is shown above each histogram.

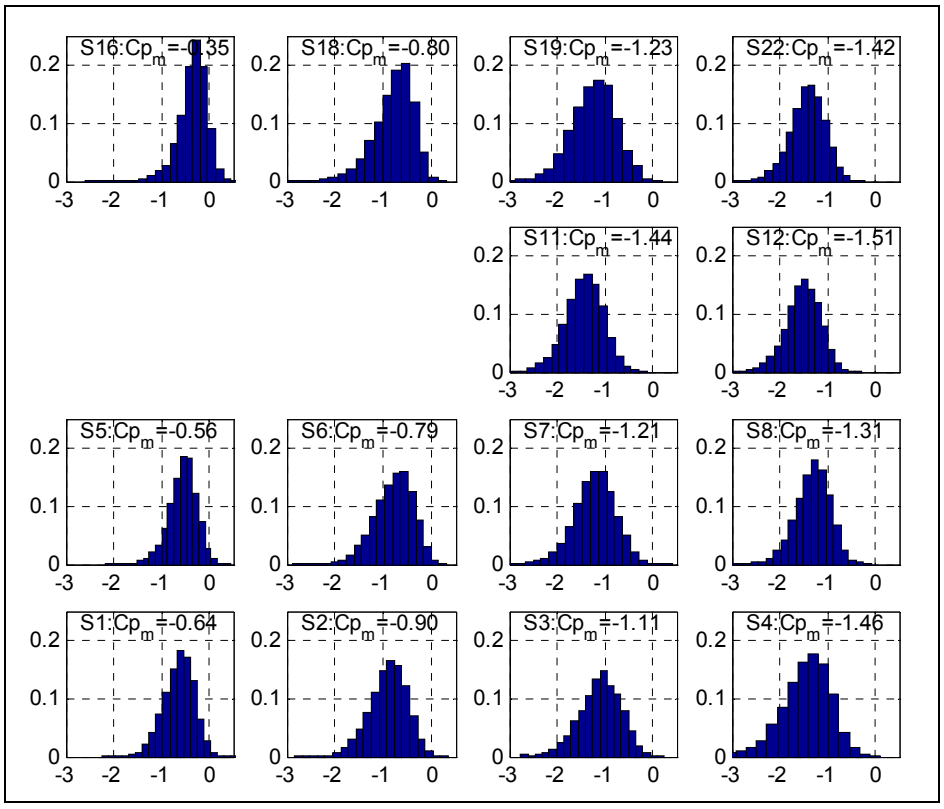

Figure 5.4 Pressure distributions on the south wall for a mean wind direction perpendicular to the east wall. Pressure tap number and mean C_p value is shown above each histogram.

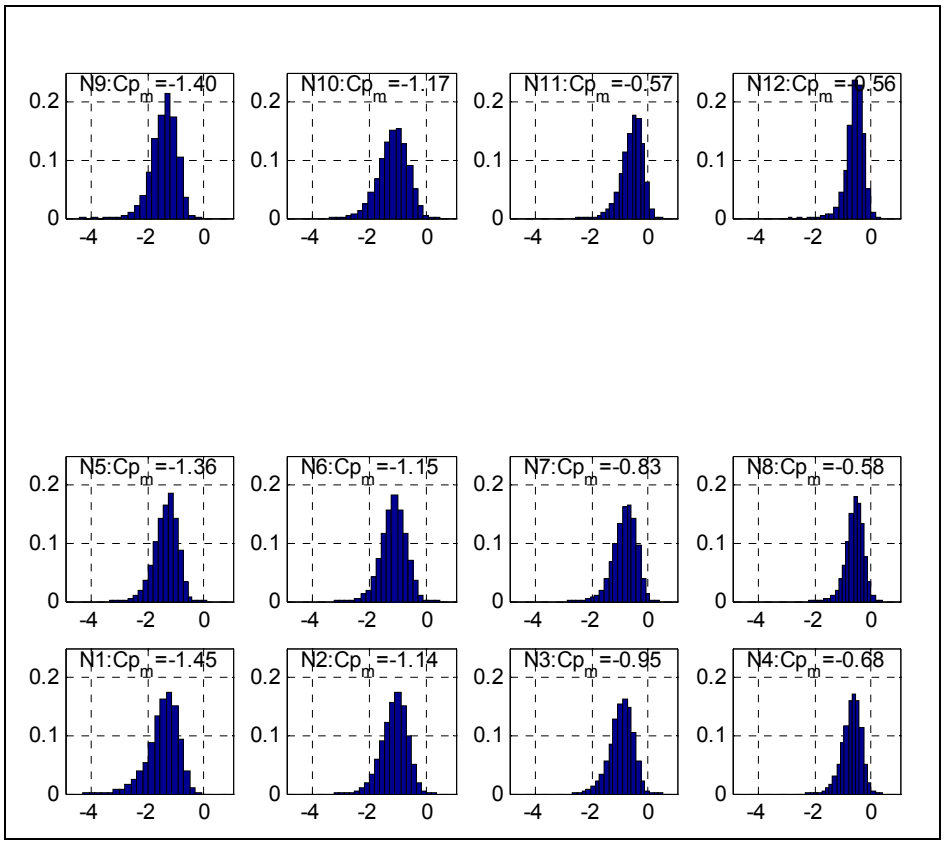

Figure 5.5 Pressure distributions on the north wall for a mean wind direction perpendicular to the east wall. Pressure tap number and mean C_p value is shown above each histogram.

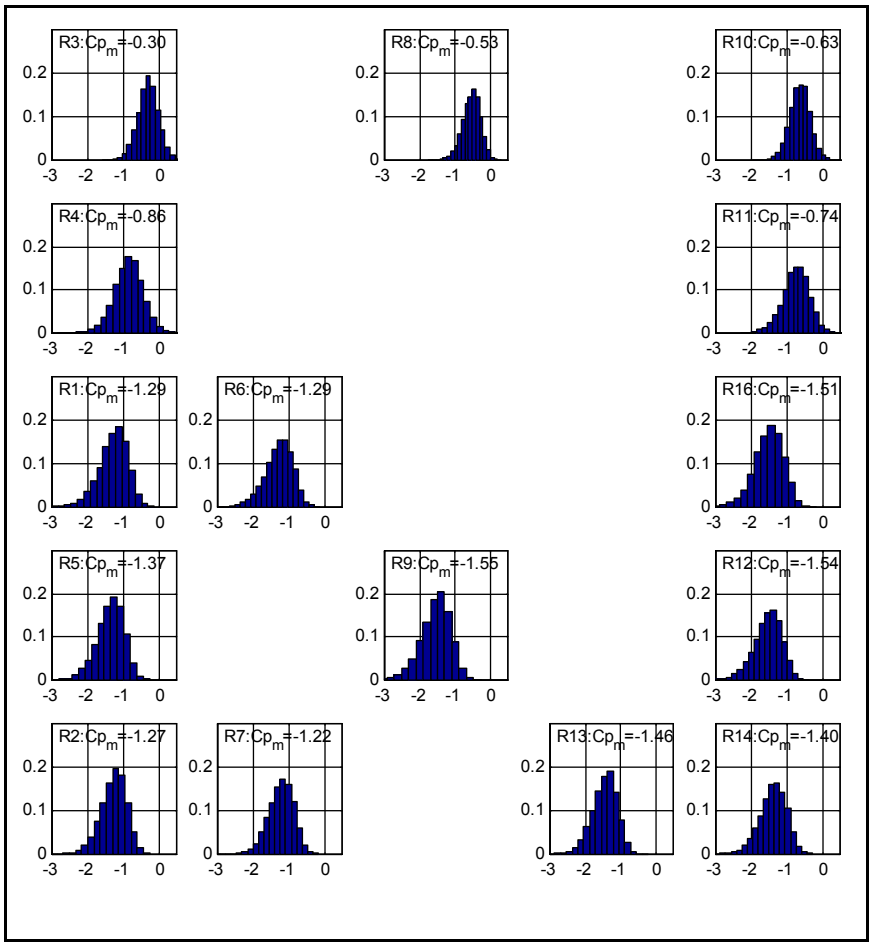

Figure 5.6 Pressure distributions on the roof for a mean wind direction perpendicular to the east wall. Pressure tap number and mean C_p value is shown above each histogram.

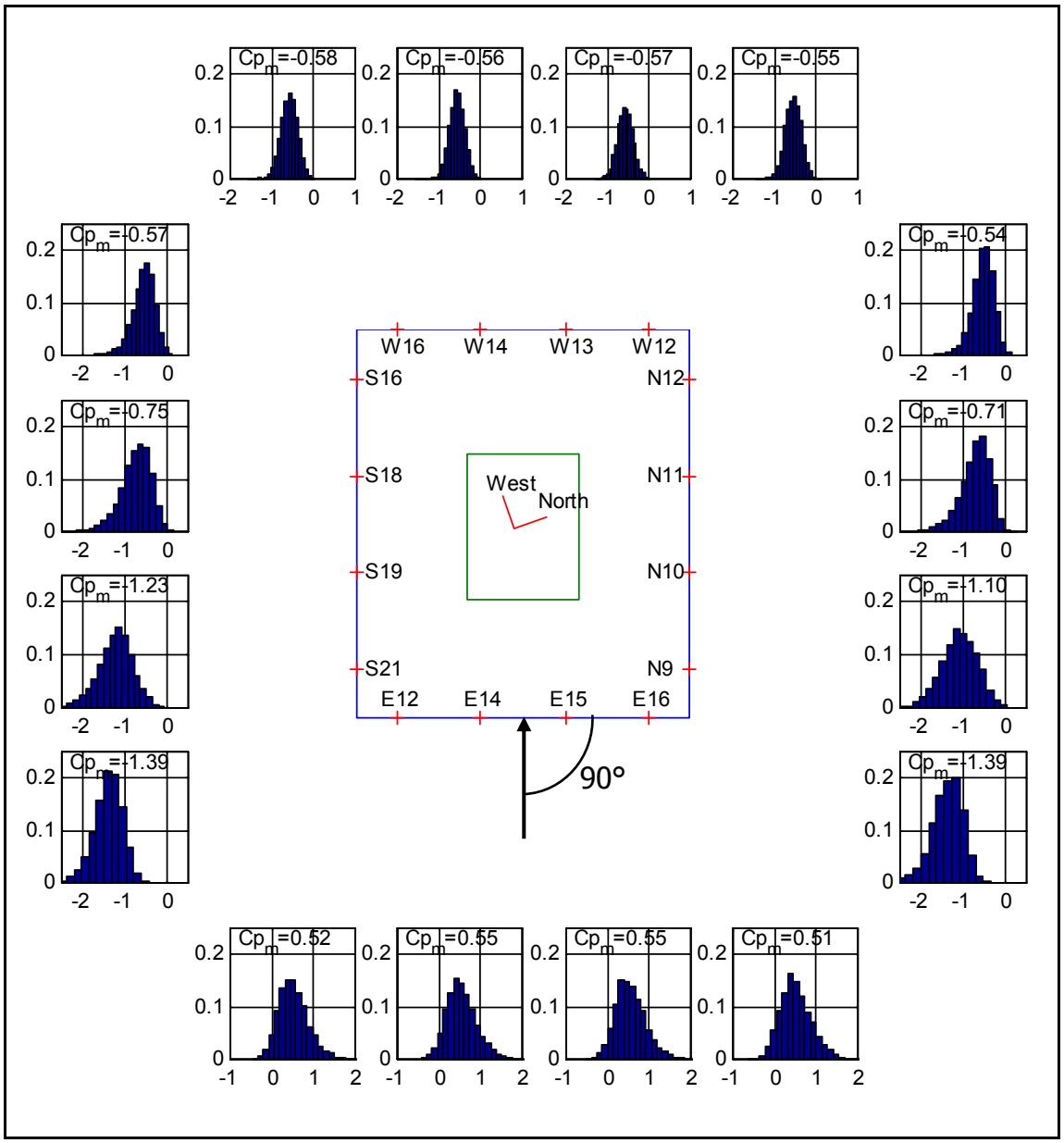

Figure 5.7 Frequency histograms of surface pressure recorded at taps located around the top perimeter of the building model for a mean wind direction perpendicular to the east wall as indicated**.** Pressure tap number and mean C_p value is shown above each histogram.

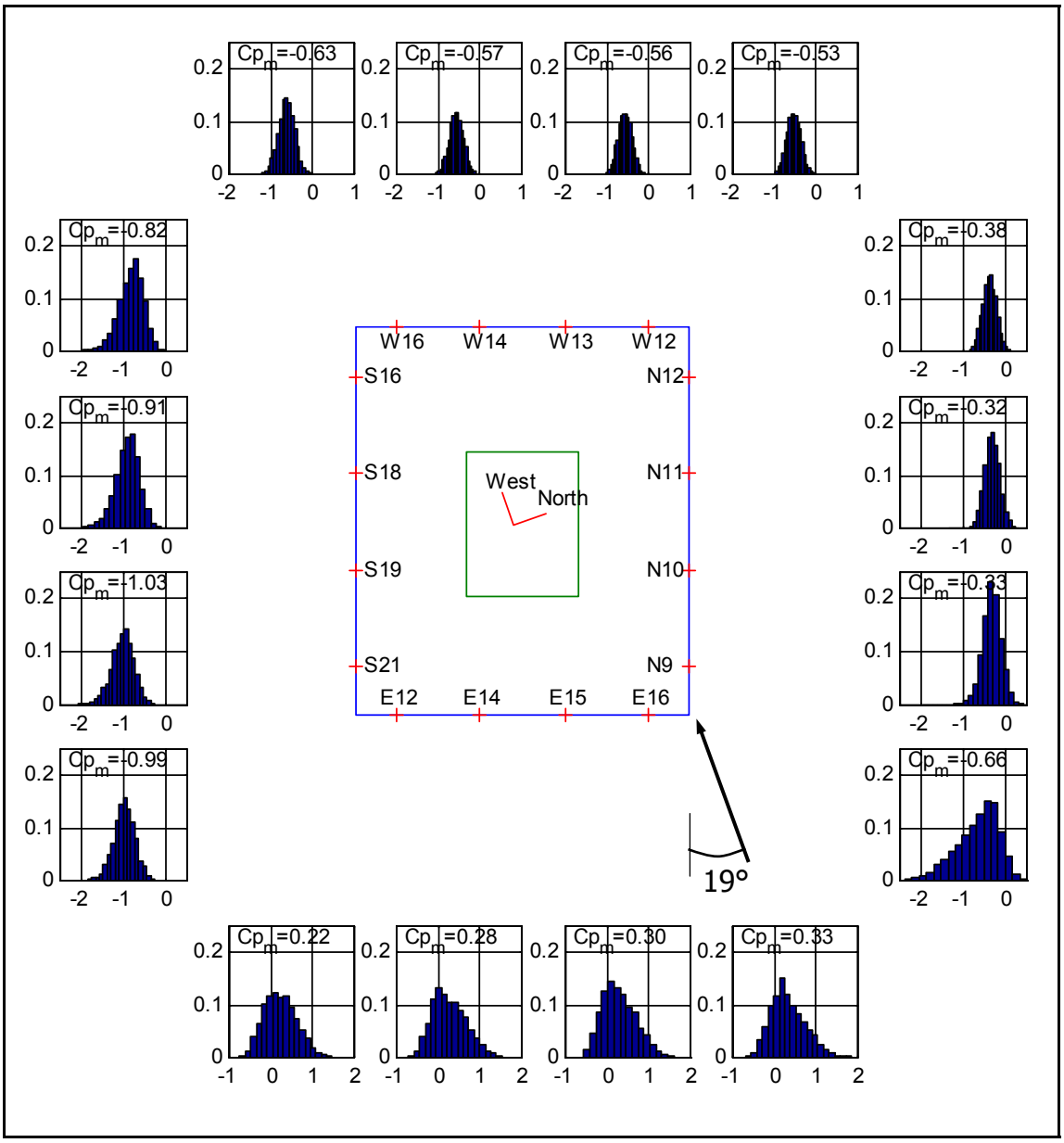

Figure 5.8 Pressure distributions around the top perimeter of the building model for a mean wind direction of 90° from north, i.e. at 19° angle to the east wall, as indicated. Pressure tap number and mean C_p value is shown above each histogram.

5.3 The full scale data - 1st order statistics of pressure coefficients

The traditional definition of a pressure coefficient, given in Eq. (5.1) is used for both model-scale and full-scale data. For the full-scale data, the intention was to base the reference mean wind velocity on the single point wind data recorded about 8 m above roof height. It was soon discovered that this could not be done without some modifications.

The reference static pressure was to be based on the pressure recorded using a static pressure sensor [135] located on the same mast as the sonic wind sensor. The static

pressure sensor had a common background with the surface pressure taps, and simple subtraction was therefore believed to give a usable total pressure. Unfortunately, this was not found to be sufficient.

The recorded mean along wind velocity above the building, was discovered to be considerably higher than the mean wind velocity recorded at the IMO-site, some 720 m west of the building. The difference was of a factor 2 in many instances and could therefore neither be fully explained by difference in height (10 m at IMO, 33 m at building), nor the expected speed up over the building. It was also seen that the difference was dependent on both wind direction and date of recording. In addition, it was seen that a shift in pressure offset was required to get reasonable pressure coefficient values. The spatial pressure distribution looked promising, but the values were shifted and the simple subtraction of the recorded static pressure was not sufficient to eliminate that shift.

It was decided to attempt to backtrack the appropriate values for Q_R and P_r. This could be done by comparing the full-scale C_p values with model-scale C_p values, using the difference between two tap locations on the building and the model. This required choosing different taps for different wind directions, i.e. taps that would give stable C_p difference between the two taps considered. This was formulated as follows:

$$\left[\frac{P_s - P_r - O_f}{Q_{rc}}\right]_{FS}^{tap_i} = \left[C_p\right]_{MS}^{tap_i} \quad \Rightarrow \quad \left[P_s - P_r\right]_{FS}^{tap_i} = Q_{rc}\left[C_p\right]_{MS}^{tap_i} - O_f \tag{5.2}$$

Here O_f is the required static pressure offset and the Q_{rc} is the required velocity pressure to get C_p values comparable to the wind-tunnel results. By using values from two taps (i and j) and assuming that Q_{rc} and O_f are independent of tap location, we get two equations with two unknowns, i.e. O_f and Q_{rc}. The equations can be solved to give Q_{rc} and O_f as:

$$Q_{rc} = \frac{\left[P_s - P_r\right]_{FS}^{tap_i} - \left[P_s - P_r\right]_{FS}^{tap_j}}{\left[C_p\right]_{MS}^{tap_i} - \left[C_p\right]_{MS}^{tap_j}} \tag{5.3}$$

$$O_f = \frac{1}{2}\left(\left[P_s - P_r\right]_{FS}^{tap_i} + \left[P_s - P_r\right]_{FS}^{tap_j}\right) - \frac{1}{2}Q_{rc}\left(\left[C_p\right]_{MS}^{tap_i} + \left[C_p\right]_{MS}^{tap_j}\right) \tag{5.4}$$

By calculating for several sets of tap locations it is possible to increase the reliability of the results. It should be noted that taps of similar location on model and full-scale building are used. Figure 5.9 shows the tap location around the top perimeter of the building for both model and full-scale building.

After the evaluation of Q_{rc} and O_f, further research was needed in order to connect Q_{rc} and O_f in some way to the full scale data. This was important, both because the calibration quantities Q_{rc} and O_f, derived by back tracing, can only be expected to give an average estimate as the variation in wind direction between full-scale recordings can not be reproduced by the limited number of wind directions tested in the wind tunnel. Also, it was important to be able to evaluate independent full-scale C_p values. Furthermore, it was necessary to understand better the reasons behind these discrepancies. What was soon evident was that the difference between the recorded velocity and the "appropriate" velocity as given by Q_{rc}, which in turn is evaluated based on the recorded pressure, is very

dependent on temperature. This is partly shown by Figure 5.10. This indicates that above the building there is a heat driven turbulence that affects both the wind velocity recordings as well as the static pressure recordings. This temperature effect is particularly evident for temperatures below zero. It is also much more effective for northerly wind directions than southerly wind directions. This may be partly related to lower ambient temperatures on average in northerly winds, i.e. greater temperature difference between air stream and other possible sources of heat. Two possible heat sources come to mind. Firstly, the thermal diffusion created when the cold air stream comes in contact with the warmer building, considering especially the window areas. Secondly, the exhaust of the building ventilation system, located on the north side of the small utility building on the roof. The velocity of the ventilation air is low, and when walking around the roof one notices the ventilation primarily through the noise created by the motors driving the exhaust air. All the same, the temperature effects are undeniable although it is difficult to predict how these two heat sources interact with the oncoming air stream.

In this context, it is important to keep in mind that assuming the building was behaving as a radiator placed in an open space and suppose that the radiator heats the air in its vicinity by $\Delta\theta$ degrees Kelvin. This would cause a buoyant acceleration $g\Delta\theta/\theta$, which is of the order 0.3 m/s^2 if $\Delta\theta$ = 10°K. This acceleration probably occurs only near the surface of the radiator. If it has a height h = 20 m or more the kinetic energy of the air above the radiator is $gh\Delta\theta/\theta$, which is of the order 6 m^2/s^2 per unit mass. This corresponds to a velocity of about 3.5 m/s [223]. It is common, when estimating heat loss through a building face, to assume the temperature at the outside surface to be the same as the atmospheric temperature. The same assumption is generally made in flow estimations around buildings. This is of course not true, as anyone who has had to scrape the frost of his car windows in the morning will be able to confirm. Around each building, there is an envelope that is somewhat warmer than the ambient temperature beyond the building envelope. Therefore, it is often only necessary to scrape the frost of car windows facing away from the building. The fact that radiative thermal effects of buildings have considerable effect on the flow around them has for example been demonstrated by Smith et al. [195]:

"*Our simulations demonstrate that radiative heating, including the effects of shading, can significantly influence the overall flow field in the vicinity of a building. The resulting evolution of a tracer released in the vicinity of a building can, therefore, also depend significantly on these influences. Our 2-D simulations show that shading near the windward face of the building can enhance the recirculation of the building. On the other hand, the shading near the leeward face of the building can slightly reduce the strength of the counter circulation in the cavity zone downstream of the building due to the thermal stability induced by the rooftop heating.*

The 3-D simulations of the radiative effects reveal significant convergence of air within the cavity zone and beyond, resulting in substantial lofting of the air mass immediately downstream of the building. This dynamic is the result of the combination of effects that can be attributed to thermal heating of the ground and building roof, and

vortex circulation associated with the horse-shoe eddy along the lateral sides of the building. Namely, warm air near the surface tends to be inducted into the cavity flow. This results in the formation of two counter-rotating vortices at about rooftop level, and a net upward lofting of the air mass downstream of the building."

Correction coefficient for the wind velocity recorded above the roof was evaluated based on a best line fit to data samples like the one presented in Figure 5.10. The correction coefficient was taken as linearly dependent on ambient temperature. Separate correction was evaluated for different directional sectors. The need for that is at least partly caused by the asymmetric location of the anemometer mast on the roof. Table 5.1 gives the correction coefficient for three cases studied. T in Table 5.1 stands for temperature in degrees Celsius.

Table 5.1. Wind velocity correction coefficients for three different directional sectors.

Directional sector (0° being perpendicular to north side of building)	$c_f = aT+b$	
	a	b
225 to 260	-0.0783	1.055
-15 to 25	0.0180	0.660
45 to 80	0.0315	0.558

Figure 5.11 gives a comparison between the mean wind velocities recorded at the IMO-site and above the building during a storm. As can be seen the mean wind velocity recorded above the building is about double the wind velocity recorded at the IMO-site. After the correction coefficient is applied, the values from above the building approach those recorded at the IMO-site fairly well, considering the distance between the two sites and other differences. Figure 5.12 shows that the mean wind direction recorded at the IMO-site and above the building compare fairly well. Figure 5.13 and Figure 5.14 show the same quantities and tendencies as Figure 5.11 and Figure 5.12, but for a different storm. Again, the velocity correction seems to give credible values.

Applying the mean wind velocities recorded at the IMO-site directly as reference mean wind velocities for the evaluation of pressure coefficients was tested, but was found to give inappropriate results. The reason is on one hand, the distance between the two sites and the associated time lag between occurrences at each site and on the other, the time difference, or lack of synchronisation, between the recording intervals at each location.

After the evaluation of appropriate correction for the reference wind velocity, it was necessary to find a suitable offset correction for the pressure data. It was discovered that the required offset was strongly dependent on the corrected velocity pressure. However, an additional quantity was needed to give a suitable offset (see Figure 5.15 and Figure 5.16). The Navier-Stokes equations give a complete description of fluid flow. Considering their time average, or the Reynolds equations, it can be noticed that when the pressure and mean velocity parts have been accounted for it is the Reynolds stresses that show the greatest influence on a shear flow of the type in question (see [40] and [193]). The Reynolds

stresses can be evaluated based on the single point data available from the mast. Further numerical investigations led to the hypothesis that Reynolds stresses of the *u*- and *w*-turbulence components could supply the missing part of the required offset (see Figure 5.15). The evaluated pressure offset can then be written as:

$$O_f = \rho_a \left(\overline{uu} + \overline{uw} + \overline{ww} \right) - \tfrac{1}{2} \rho_a \overline{U}_c^2 \qquad (5.5)$$

Here $\overline{U}_c$ is the corrected mean along wind velocity, u is the along turbulence component, w is the vertical turbulence component and ρ_a is the density of air.

Examples of the full-scale pressure coefficients evaluated by using the corrected reference velocity and the additional pressure offset are given in Figure 5.17 and Figure 5.18, as a function of tap numbers (see Figure 5.9). The figures represent the pressure coefficients for two different wind directions. The values are comparable to the values presented earlier from the wind tunnel study. The pressure coefficients at two taps no. F8 and no. F9 are also shown as function of mean wind direction in Figure 5.19 and Figure 5.20, respectively. The directional dependence of the pressure coefficient at those two taps seems quite reasonable, although some variability is seen which is to be expected for an experiment of this kind.

It should be noted that the reference velocity correction of the pressure data has no influence on second order statistics.

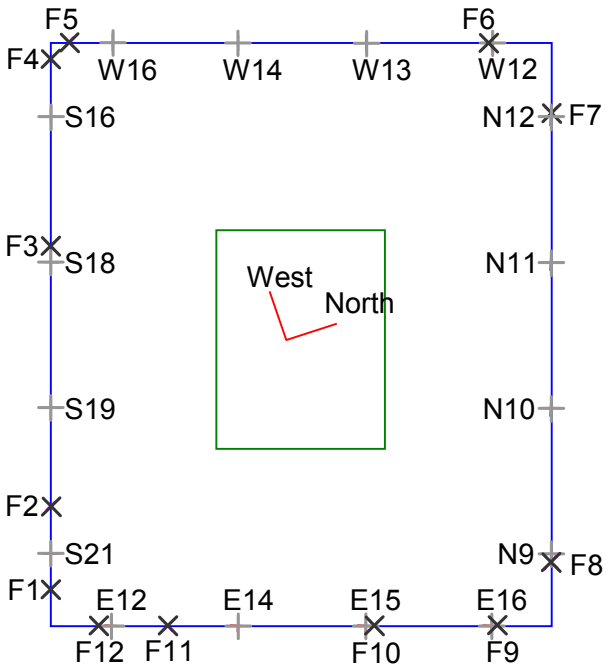

Figure 5.9 Tap identities and location around the perimeter at the top of the building. E, N, S and W numbers refer to the wind tunnel model (+), whereas the F-numbers refer to the full scale set up (×). The taps are located about 1 m below the top edge of the building.

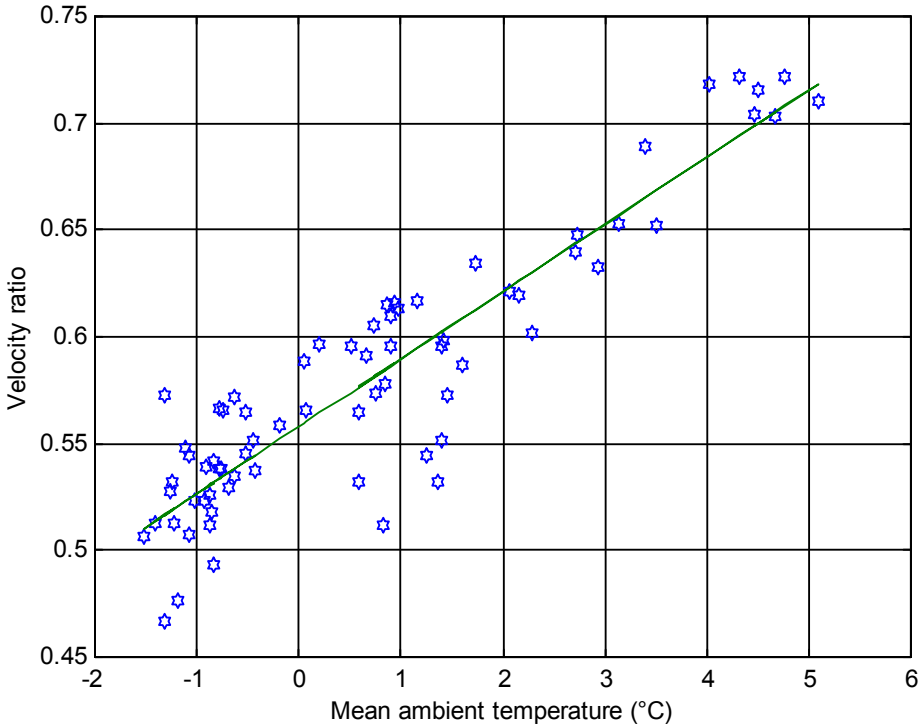

Figure 5.10 The ratio of back-traced velocity values and recorded mean wind velocity above the building as function of temperature. The straight line shown is an estimated best line fit through the data set.

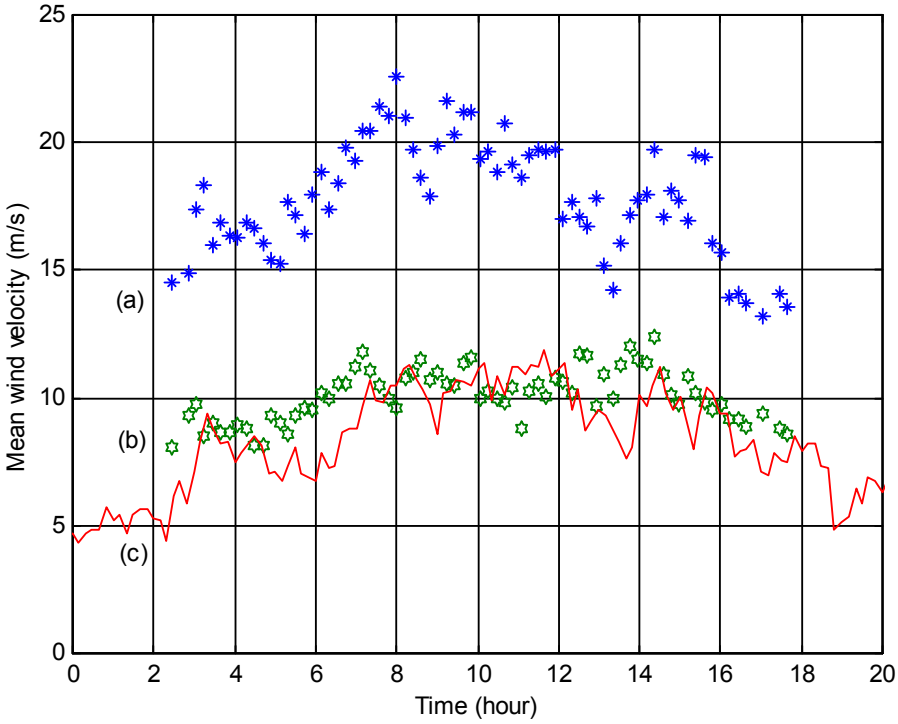

Figure 5.11 The mean along wind velocity as a function of time. (a) Values recorded above the building roof. (b) Corrected values recorded above the building roof. (c) Values recorded at 10 m height at the IMO-site.

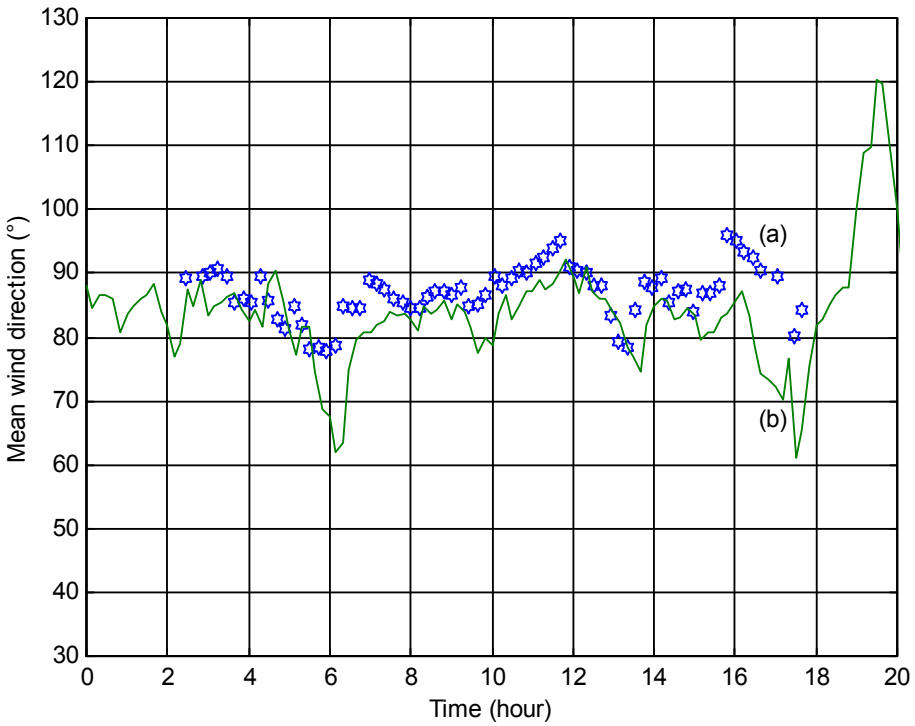

Figure 5.12 The mean wind direction as a function of time (0° refer to north). (a) Values recorded above the building roof. (b) Values recorded at 10 m height at the IMO-site.

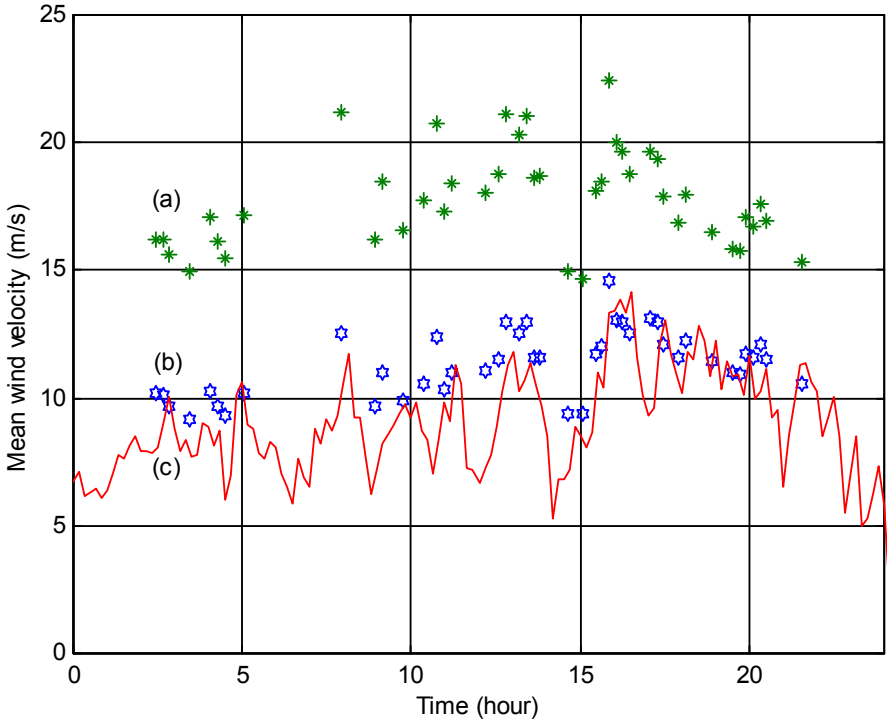

Figure 5.13 The mean along wind velocity as a function of time. (a) Values recorded above the building roof. (b) Corrected values recorded above the building roof. (c) Values recorded at 10 m height at the IMO-site.

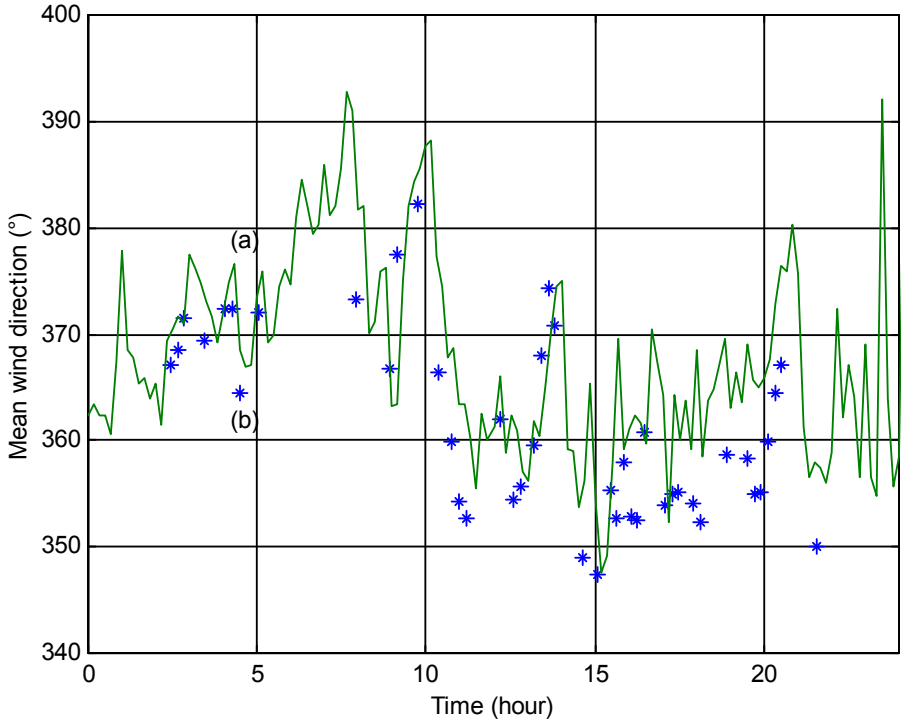

Figure 5.14 The mean wind direction as a function of time (0° refers to north). (a) Values recorded above the building roof. (b) Values recorded at 10 m height at the IMO-site.

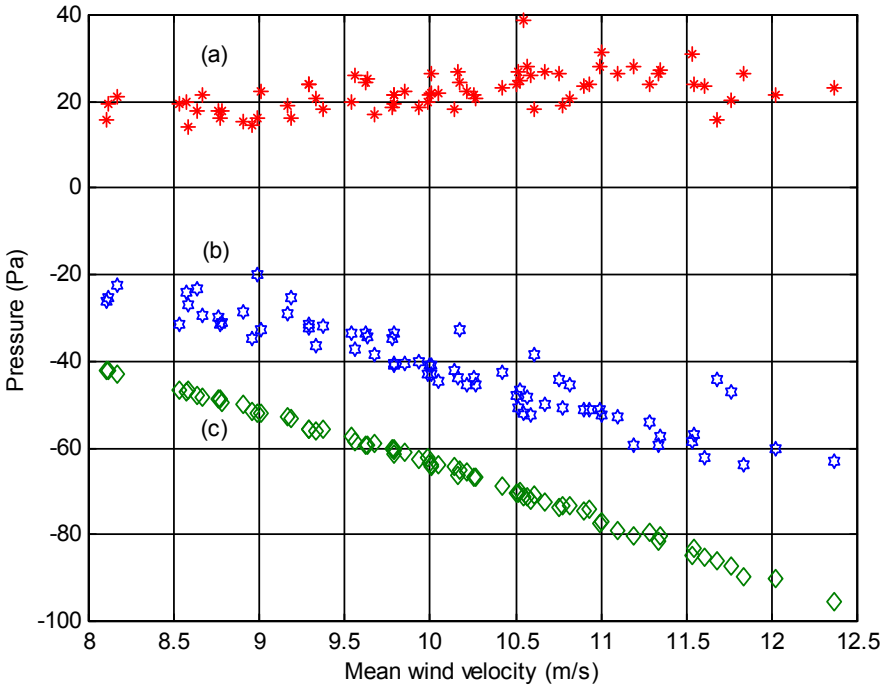

Figure 5.15 Evaluation of pressure offset as a function of corrected reference mean wind velocity for wind direction between 45° and 77°, with zero taken as perpendicular to north-side. The (a) curve represents the Reynolds stresses of the u and w turbulence components. The (b) curve represents the required pressure offset evaluated by comparison with wind tunnel data. The (c) curve represents the corrected velocity pressure with a negative sign.

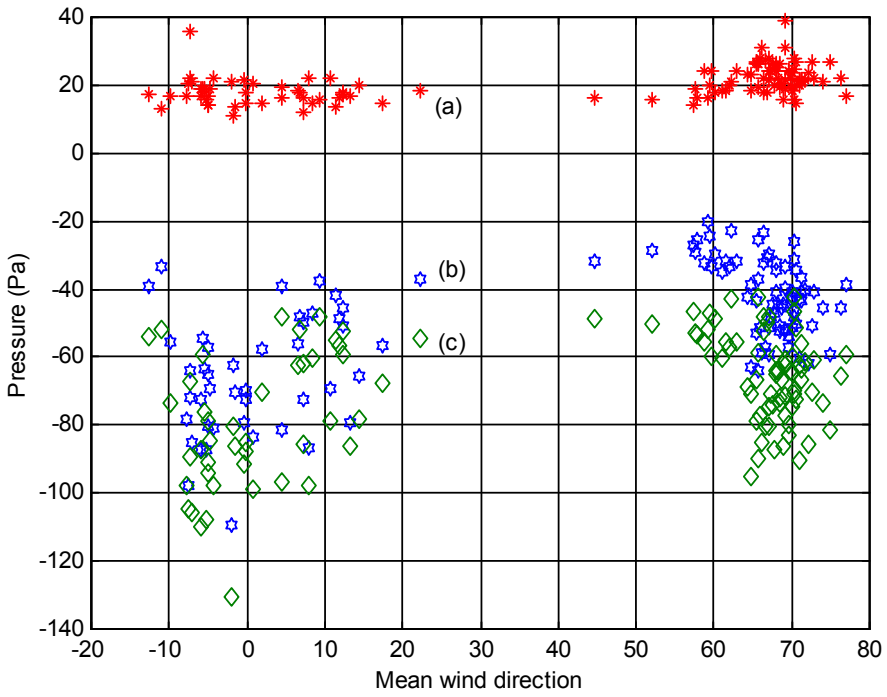

Figure 5.16 Evaluation of pressure offset as a function of mean wind direction, with zero taken as perpendicular to north-side. (a) Data points representing the Reynolds stresses of the u and w turbulence components. (b) Data points representing the required pressure offset evaluated by comparison with wind tunnel data. (c) Data points representing the corrected velocity pressure with a negative sign. Each pair of points represents a 12 minutes record.

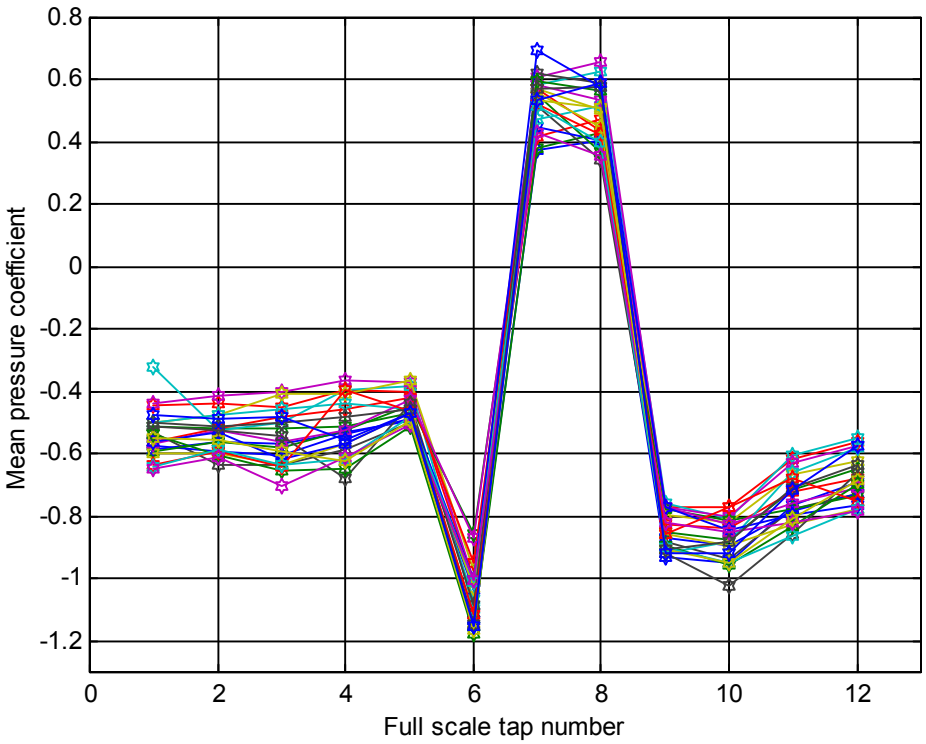

Figure 5.17 Full scale mean pressure coefficients for mean wind directions between 355°-370°, where 0° is perpendicular to the north side of the building. Each line represents a time series.

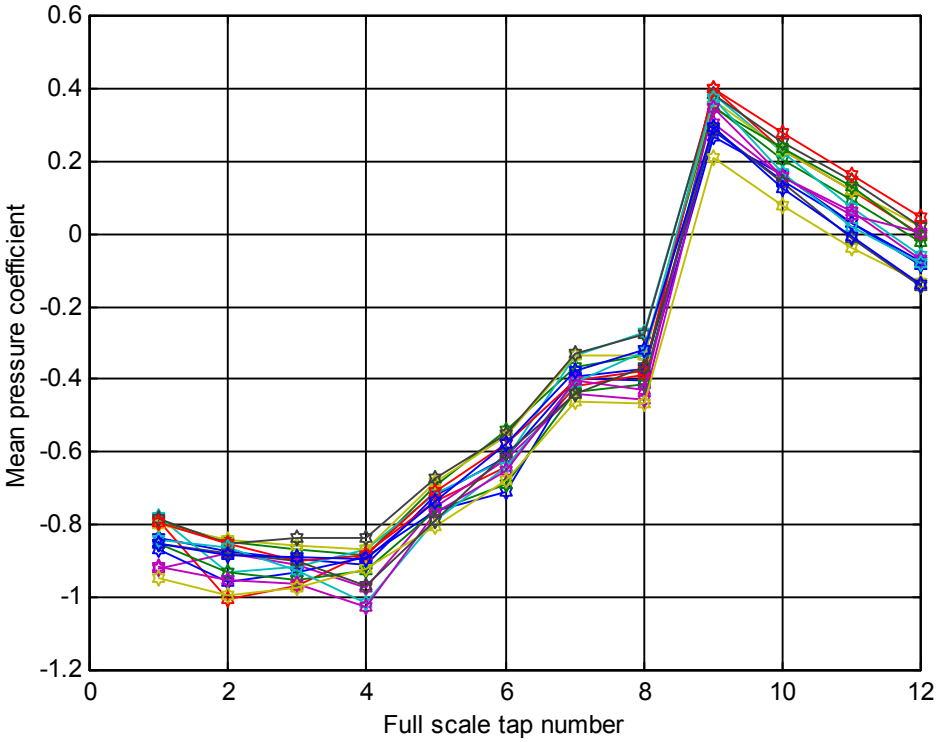

Figure 5.18 Full scale mean pressure coefficients for mean wind directions between 71-72°, where 0° is perpendicular to the north side of the building. Each line represents a time series.

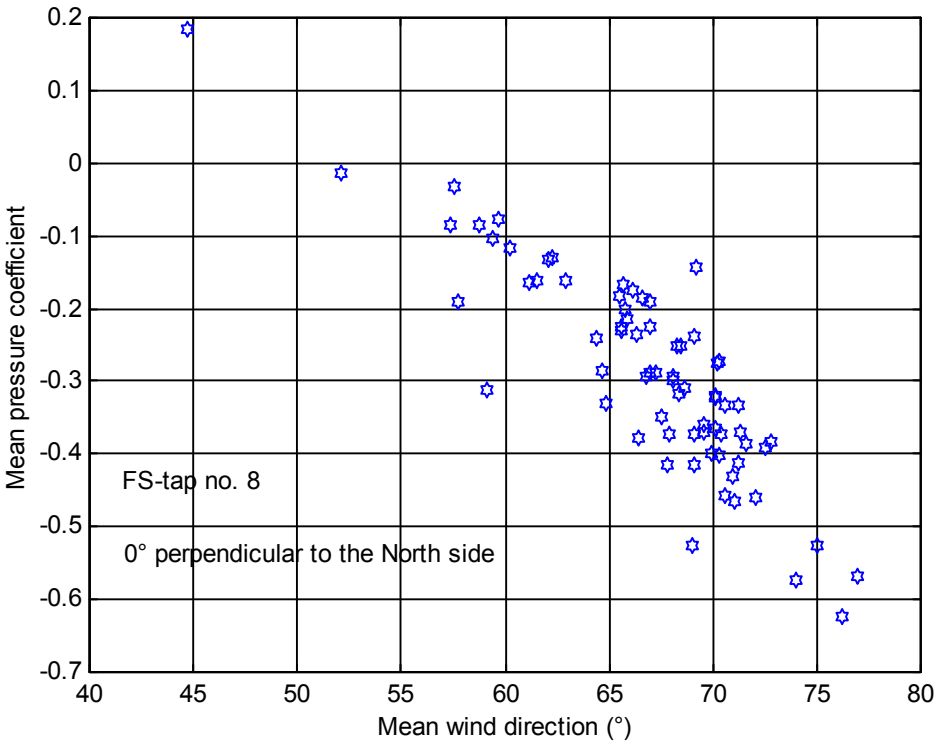

Figure 5.19 Full scale mean pressure coefficients at tap no. F8 for mean wind directions between 45-77°, where 0° is perpendicular to the north side of the building.

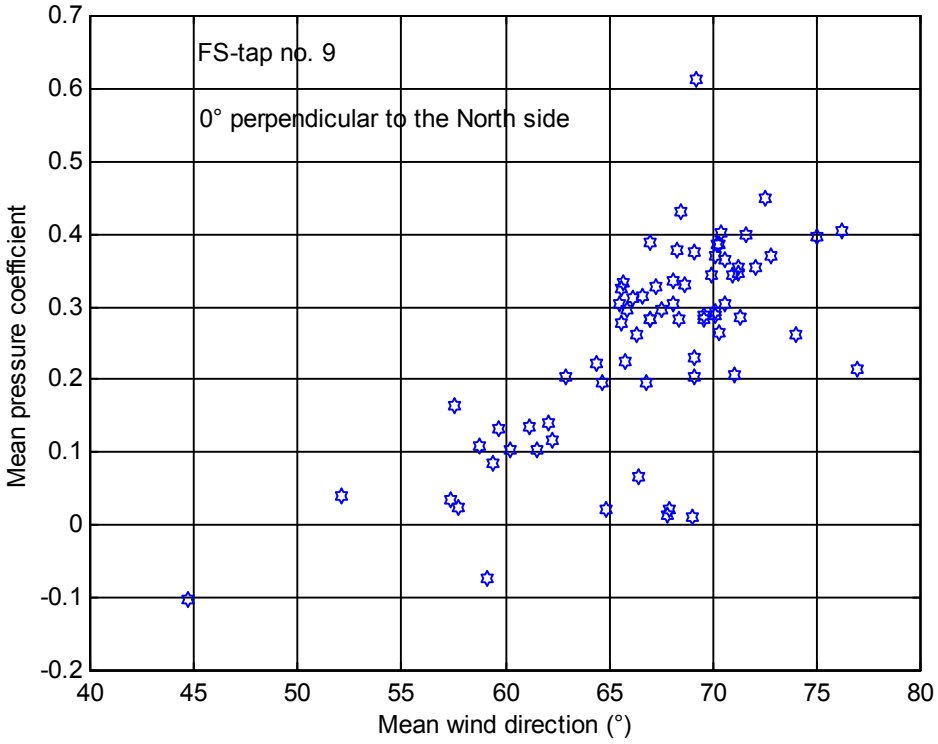

Figure 5.20 Full scale mean pressure coefficients at tap no. F9 for mean wind directions between 45-77°, where 0° is perpendicular to the north side of the building.

5.4 Spectral characteristics of wind induced pressure

The pressure time series recorded in the wind tunnel were corrected by a frequency transfer function correction developed by Kaspersen and Krogstad [7] based on equations derived by Bergh and Tijdeman [9] and Gumley [47]. The frequency response of the tubing/transducer system in the wind tunnel was found to be acceptable up to at least 180 Hz, which roughly corresponds to about 1.1 Hz full-scale. For the full-scale pressure time series, the frequency response is generally acceptable up to at least 7.5 Hz without any type of correction.

Auto spectral densities of the recorded surface pressures were evaluated for the full- and model scale data. The respective spectra are shown in Figure 5.21 and Figure 5.22 for a mean wind direction perpendicular to the east side of the building, i.e. about 109° from the geographical north. The spectral densities are plotted in pairs, one set of spectral curves for each side of the building. The full-scale spectral densities are evaluated based on limited number of runs to keep the natural variability of the mean wind direction at a minimum. This was done in order to get a consistent comparison with the respective model scale runs.

These spectra can also be presented, in a normalised form, as a velocity-pressure admittance function defined as:

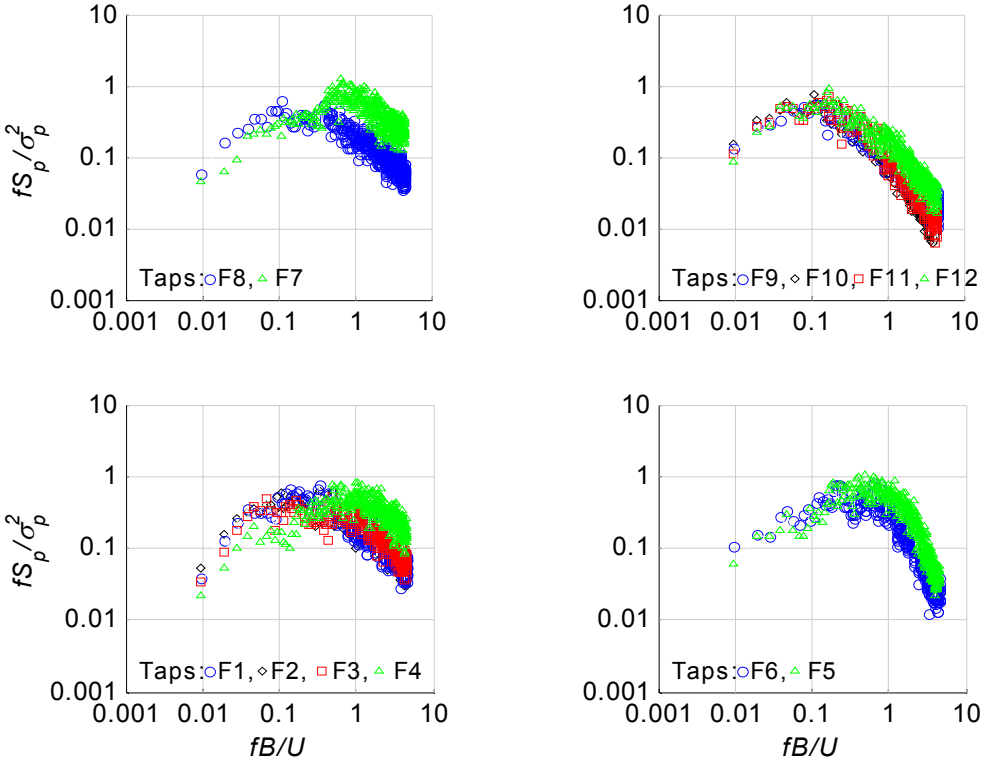

Figure 5.21 Spectral density of surface pressure at taps around the top perimeter of the building based on full-scale data. The mean wind direction is perpendicular to the east side of the building.

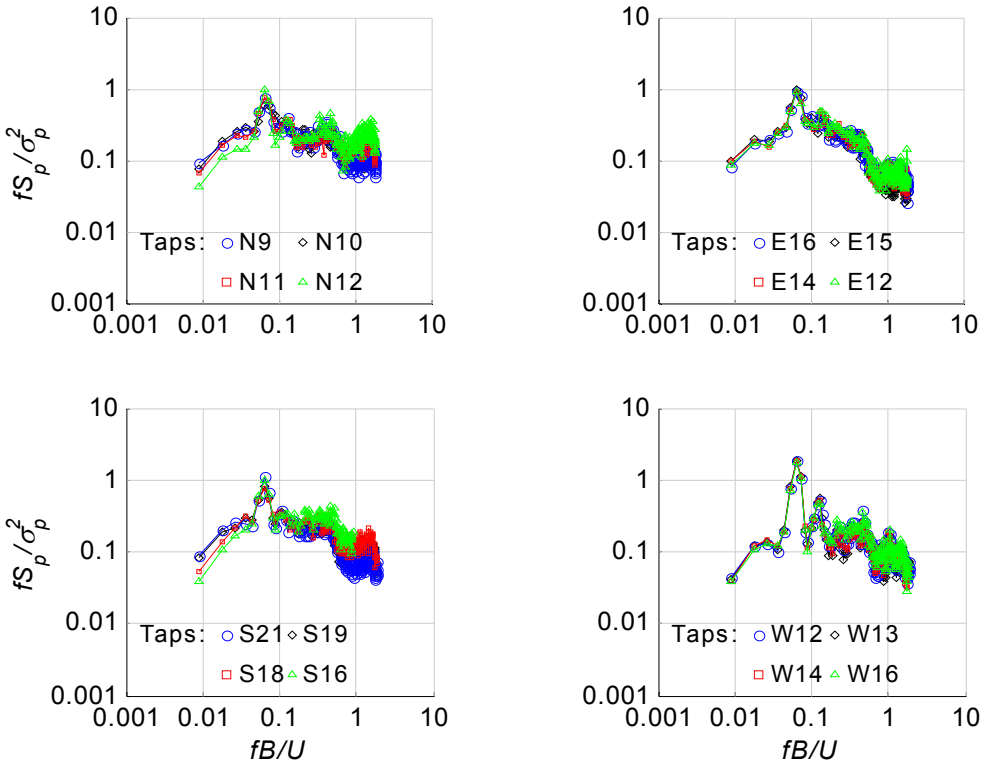

Figure 5.22 Spectral density of surface pressure at taps around the top perimeter of the building based on model scale data. The mean wind direction is perpendicular to the east side of the building.

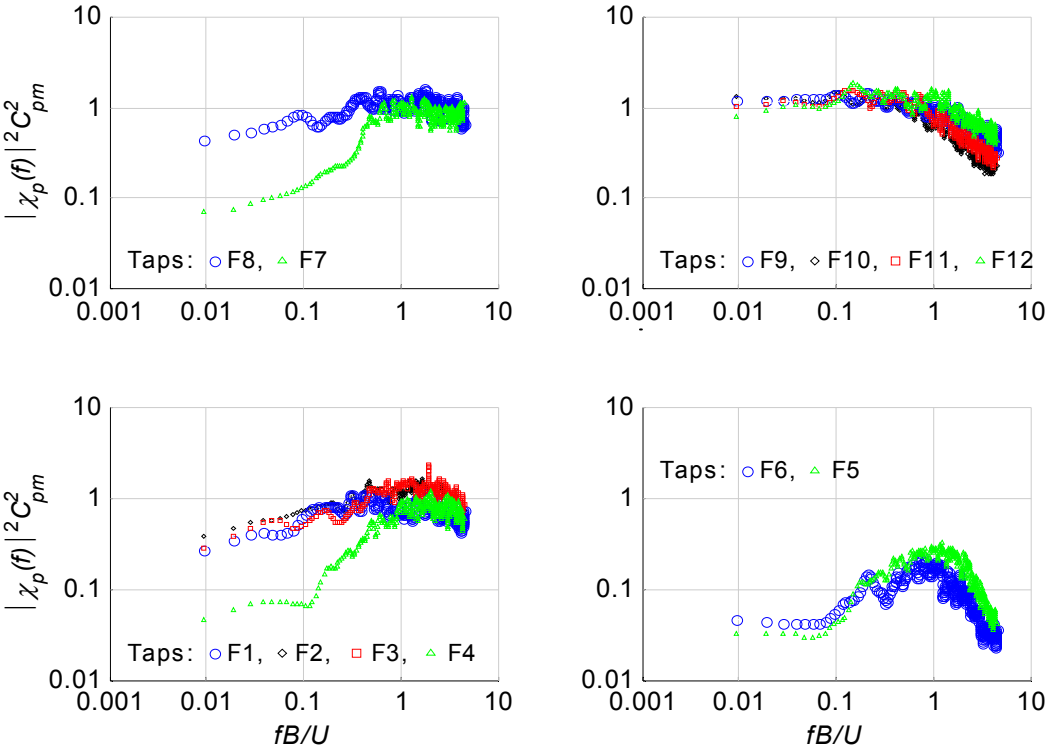

Figure 5.23 Pressure admittance based on full-scale data for a mean wind direction perpendicular to the east side of the building.

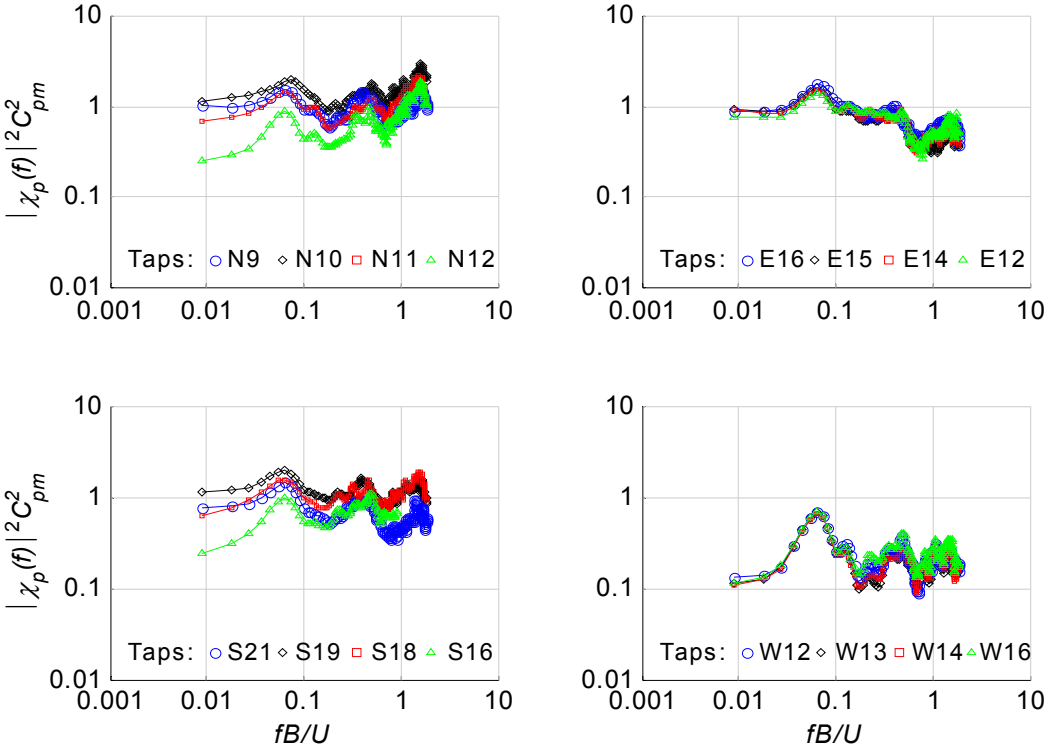

Figure 5.24 Pressure admittance based on model-scale data for a mean wind direction perpendicular to the east side of the building.

$$|\chi_P(f)|^2 = \frac{S_{pp}(f)}{(\overline{C}_P \rho_a \overline{U})^2 S_{uu}(f)} \tag{5.6}$$

Here, S_{pp} is the auto spectral density of pressure, S_{uu} is the auto spectral density of along wind velocity, $\overline{U}$ is the mean wind velocity, $\overline{C}_P$ is the mean pressure coefficient and ρ_a is the density of air. Since the quasi-steady model [66] assumes that that the wind pressures on buildings fluctuate directly with the fluctuations in wind speed immediately upstream, the pressure admittance represents, in principle, the differences between quasi-steady theory and the measured pressure spectra on bluff bodies.

Velocity-pressure admittance based on recorded data is shown in Figure 5.23 and Figure 5.24, for a mean wind direction perpendicular to the east side of the building. It should be noted, that the ESDU spectra is used in normalising the pressure spectra to avoid influence from irregularities in the recorded velocity spectra (see Figure 4.9). Also, in order to eliminate the uncertainty of the mean pressure values, the admittance function multiplied by $\overline{C}_p^{\,2}$ is presented.

The pressure spectra and the respective admittance are plotted in pairs, one set of curves for taps on each side of the building. The pressure tap locations are shown in Figure 5.9. It can be seen that the spectra for the taps on the windward side fall largely together while noticeable difference is observed between spectra on the suction sides. Certain symmetry can be seen in the spectra at sides parallel to the wind direction. Pressure at taps closer to the leeward side of the building shows a lower energy content in the low frequency range but a higher energy content in the high frequency range, relative to the taps closer to the windward side.

The difference between the spectra at taps F5 and F6 on the leeward side can be explained by the fact that tap F5 is placed relatively close to the corner and therefore contains higher turbulence energy. In model scale however, the spectra on the leeward side have similar spectral values, as the taps are not very close to the corners.

The admittance function on the windward side shows a fairly conventional behaviour (see for instance Kawai et. al [99]), i.e. it has an approximately constant value of about 1 at the low frequency range and then more or less linearly reducing admittance with increased frequency. The admittance relation for the suction sides of the building shows a different behaviour, especially data from taps on or close to the leeward side, where the admittance is very low for reduced frequencies below 0.1. For frequencies above 0.1 the admittances increases and peaks at reduced frequencies around 1. This frequency, which can be related to length scales of the same order as the width of the building, shows a very strong admittance for both full-scale and model scale data.

Although the full- and model scale spectral and admittance shapes can in many ways be considered similar in magnitude and frequency dependence, it is clear that the model scale spectral shapes are strongly influenced by energy peaks, most likely induced by vortex shedding in the wake. Such energy peaks are however not as noticeable in the full-scale date. It is useful to look at the cross-spectra, or rather the co- and quad-spectra, in order to study this phenomenon. The co- and quad-spectra for full-scale and model scale data are shown in Figure 5.25 and Figure 5.26 respectively. It is seen, that the co-spectrum

for the leeward side of the wind tunnel model is dominated by an energy peak at a reduced frequency between 0.06-0.07, indicating vortex shedding in the wake.

This type of vortex shedding, around square cylinders, is fairly well documented in wind tunnel studies (Surry and Djakovich [215], Saathoff and Melbourne [179]). If the translated vortices occurred in an alternating fashion, the reduced frequencies of preference would be about 0.06 on the leeward wall and around 0.03 on the sidewalls. The quad-spectra for model scale data show an energy increase at both of these frequency levels. Overall, it seems that the separation/reattachment process is a mixture of alternating and staggered vortex shedding.

Although, the full-scale auto-spectral densities and admittance do not show clearly energy peaks related to vortex shedding, the respective co- and quad- spectra do. As seen in Figure 5.26, the co- and quad-spectra for the full-scale data follow largely the same pattern as the model scale data, and vortex shedding type behaviour can be noticed at reduced frequency bands between 0.05 and 0.06. There are many possible reasons why the vortex shedding phenomenon is less noticeable in full-scale than in model scale. The full-scale turbulence was somewhat larger than in the wind tunnel study, and it is well documented (Surry [215] and Saathoff [179]) that an increase in turbulence reduces vortex shedding for square cross sections. The energy associated with long length scales and low frequency fluctuations may be underestimated in the wind tunnel, which in turn may result in an overestimation of energy at higher frequency bands. However, the main reason is most likely the considerably greater across flow fluctuations (or wind direction fluctuations) in full-scale that limits the possible formation of a stable vortex street. The fact that the Reynolds number scaling is not fulfilled may also play a part.

For both full-scale and model scale data a slight increase in energy in the fluctuating pressure can be noticed in a frequency band centred approximately at twice the Strouhal frequency. This observation is in general agreement with those presented by Isyumov and Poole [78] and confirmed by Surry and Djakovich [215]. The low amplitude peaks seen above that frequency band are most likely associated with various sources of noise in both model and full-scale.

An interesting feature of the Co- and Quad-spectra of Figure 5.25 and Figure 5.26 is the fact that the vortex shedding frequency response is clearly seen in the pressure data recorded at the windward side, especially in the wind tunnel. A closer look reveals that the vortex shedding influence is strongest at the edges, but is also found at centre taps. This was unexpected as the discussion on vortex shedding in the literature is generally focused on the across wind and/or suction side data. However, the phenomena can be found in the literature. In the study by Surry and Djakovich [215], one can see a spectral top at a windward tap close to the corner but not at a tap at the centre of the windward side. However, their model has a very large aspect ratio and different 3-dimensionality than the study-building and there is not a corresponding central tap on the wind tunnel model (four taps over the width, except at the corners). In a paper by Nakagawa [137], one can see strong spectral-peaks in Fig. 9 and 10 for locations p1 and p2 (see Fig 1 in article), which are in the approach flow in front of the sections being tested. Also, in an article by Tamura et. al. [218] figures 1, 2 and 3 demonstrate nicely instantaneous wind pressure distributions

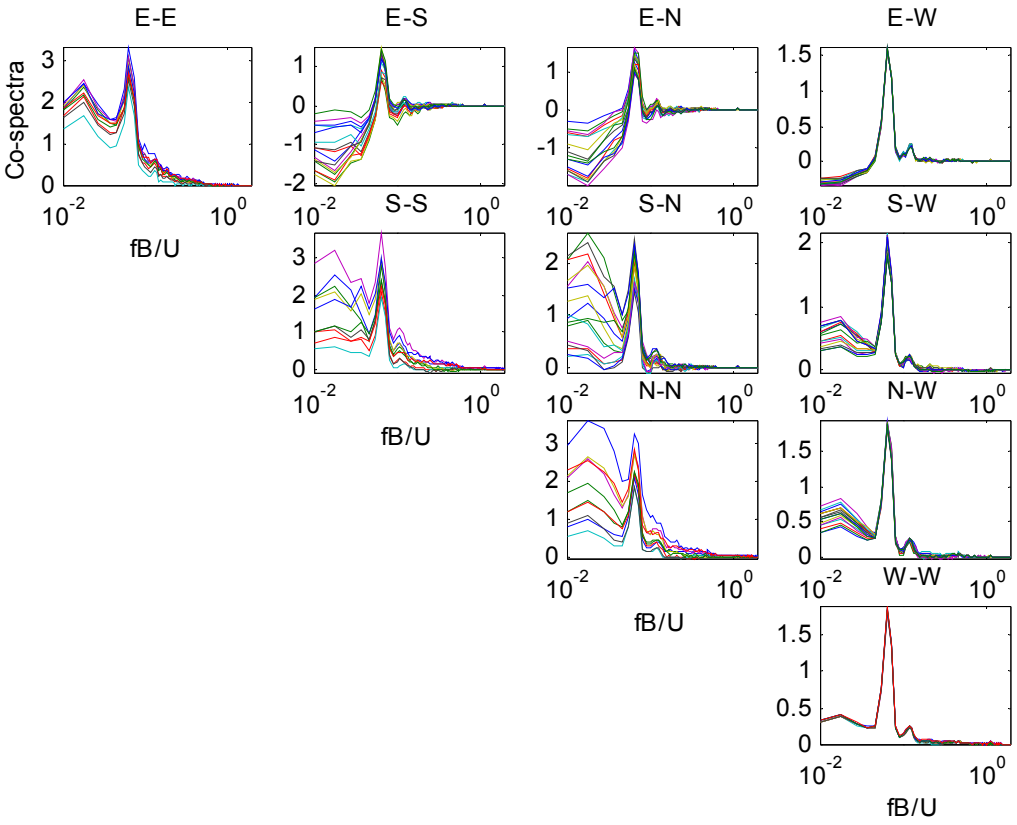

(a)

(a)

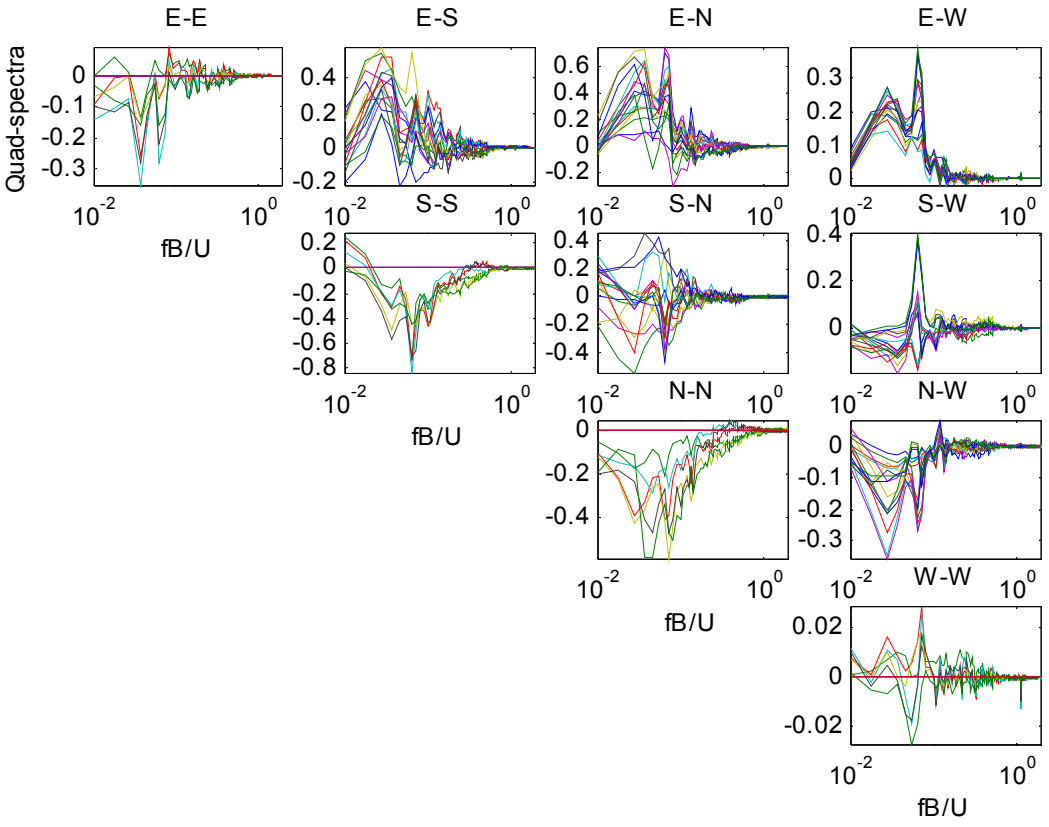

(b)

Figure 5.25 Cross-spectra of model-scale surface pressures series for mean wind direction perpendicular to the east side of the building: a) Co-spectra and b) quad-spectra.

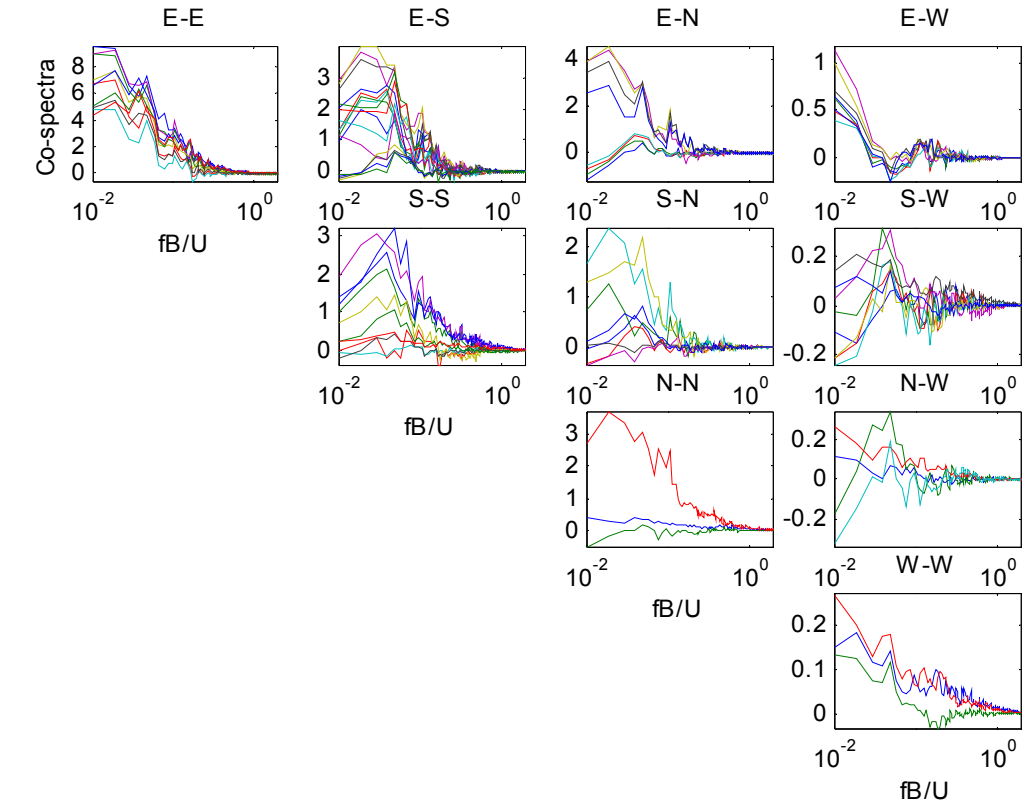

(a)

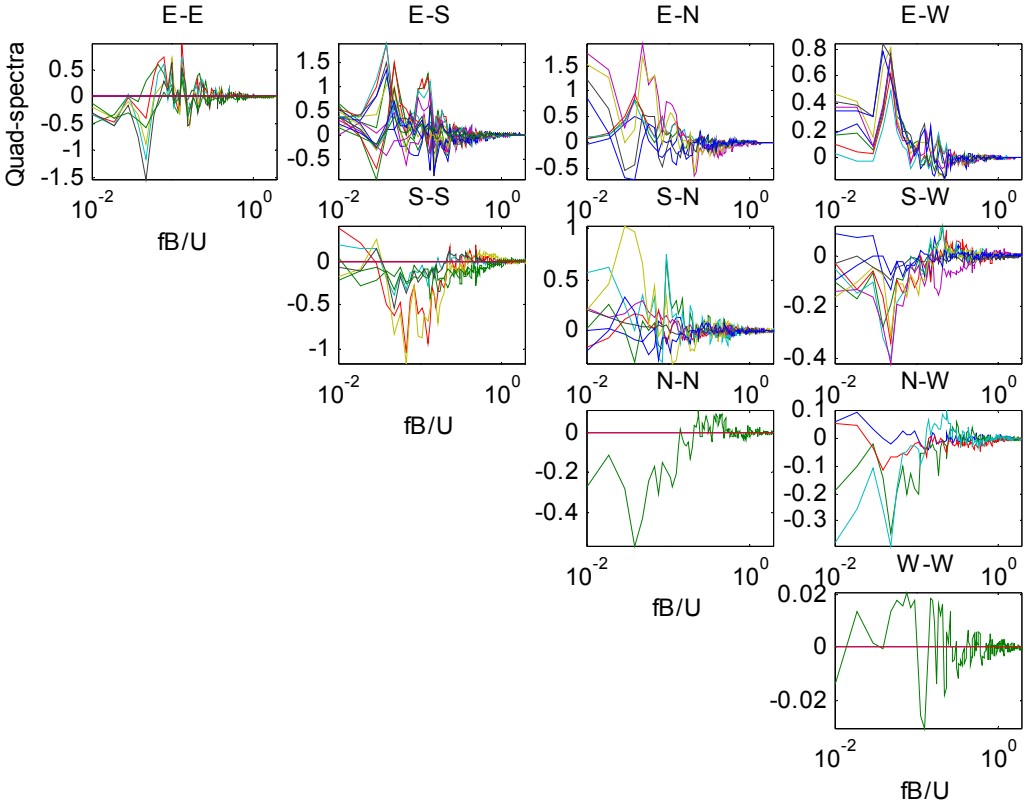

(b)

Figure 5.26 Cross-spectra of full-scale surface pressure series for mean wind direction perpendicular to the east side of the building: a) Co-spectra and b) quad-spectra.

around a low-rise building. From those one can see the close relation in pressure pattern variations between the four sides of the building. It should therefore not be surprising that a key feature in the flow is transparent on all sides.

A comparison between the full- and model scale spectral density has been presented for a mean wind direction perpendicular to the wall facing east. In the following further information will be provided on the full-scale power spectrum of pressure coefficients as well as on velocity-pressure admittance. Figure 5.27 to Figure 5.32 represent similar information as Figure 5.21 to Figure 5.24 but for other wind directions, that is for a mean wind direction of about 90° from north and 19° from north.

The full- and model scale spectral densities are shown in Figure 5.27 and Figure 5.28, respectively, for a mean wind direction of about 90° from north. The full-scale spectral density of Figure 5.27 is evaluated based on 49 runs, all with an individual mean wind direction within ±5° sector. This was done in order to get a consistent comparison with the available model scale runs. As before, the spectral densities are plotted in pairs, one set of spectral curves for each side of the building. The velocity-pressure admittance corresponding to the spectral density of Figure 5.27 and Figure 5.28 is shown in Figure 5.29 and Figure 5.30. As before the ESDU spectrum of wind velocity is used as a reference.

Similar features are seen for model and full-scale, especially considering overall features of spectral magnitude and frequency dependence. As for the case presented in Figure 5.21 through Figure 5.24 the model scale spectral shapes are strongly influenced by energy peaks, most likely induced by vortex shedding in the wake, as already discussed. Such energy peaks are not as noticeable in the full-scale spectral density, although there is a noticeable difference between the frequency content at taps on the leeward sides (F1 through F6) and taps on the windward sides (F7 through F12).

There is also, a clear difference in the frequency content of the spectral densities and respective admittance between the two azimuths (109° and 90°). Although the related energy peaks are seen in the spectra for both incidences, they occur at different frequencies. This is seen both for full- and model scale data. For instance, the pressure admittance peak for the leeward taps is at reduced frequency of one for wind perpendicular to the facade whereas it is at a reduced frequency of about 0.5 for azimuth of 90°. There is also a greater variability in spectral and particularly admittance values depending on tap location for the 90° azimuth than seen for mean wind perpendicular to the east facade.

Full-scale spectral densities for wind direction perpendicular to the north side of the building are shown in Figure 5.31 and the respective pressure-admittances are shown Figure 5.32. The full-scale spectral quantities are based on seven runs, each with an individual mean wind direction within ±5° sector from north. As before, considerable variability is seen in the spectral values for the suction areas, whereas the taps on the windward side, i.e. tap no. 7 and 8, show less variability. Comparing the two cases of wind perpendicular to a building facade, i.e. to the east and the north face shows both similarities and differences. When considering the differences one should recall the asymmetric placement of the office cubical on the shopping mall roof below.

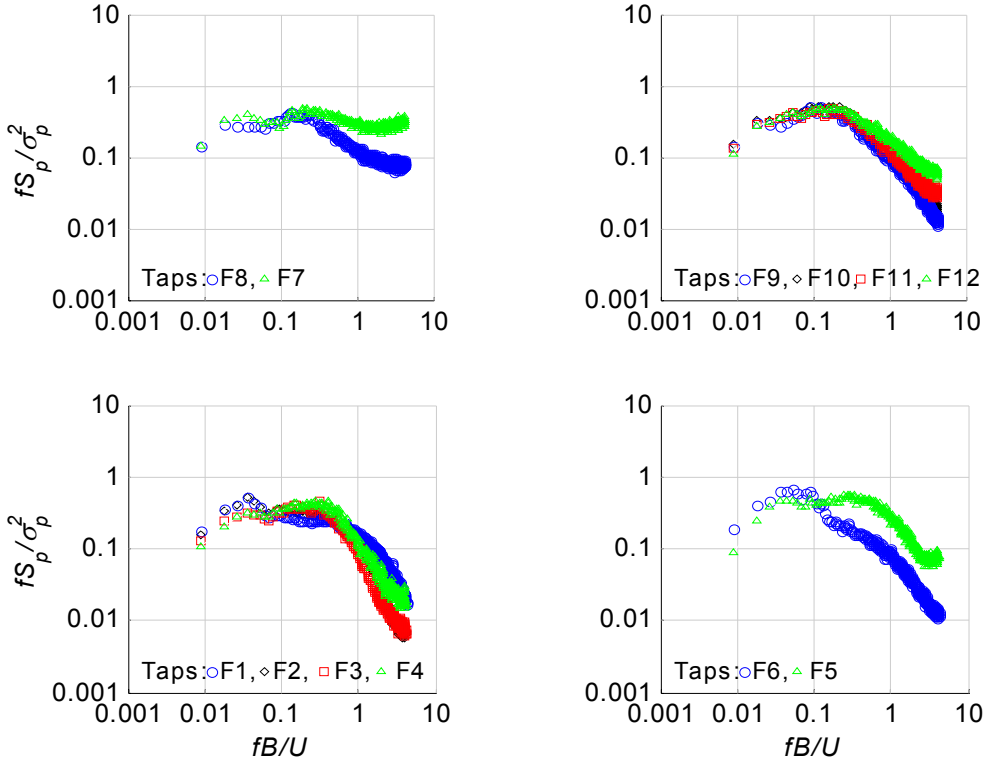

Figure 5.27 Spectral density of surface pressure at taps around the top perimeter of the building, evaluated based on full-scale data. The mean wind direction is about 90° from north, i.e. at about 71° angle to the east wall.

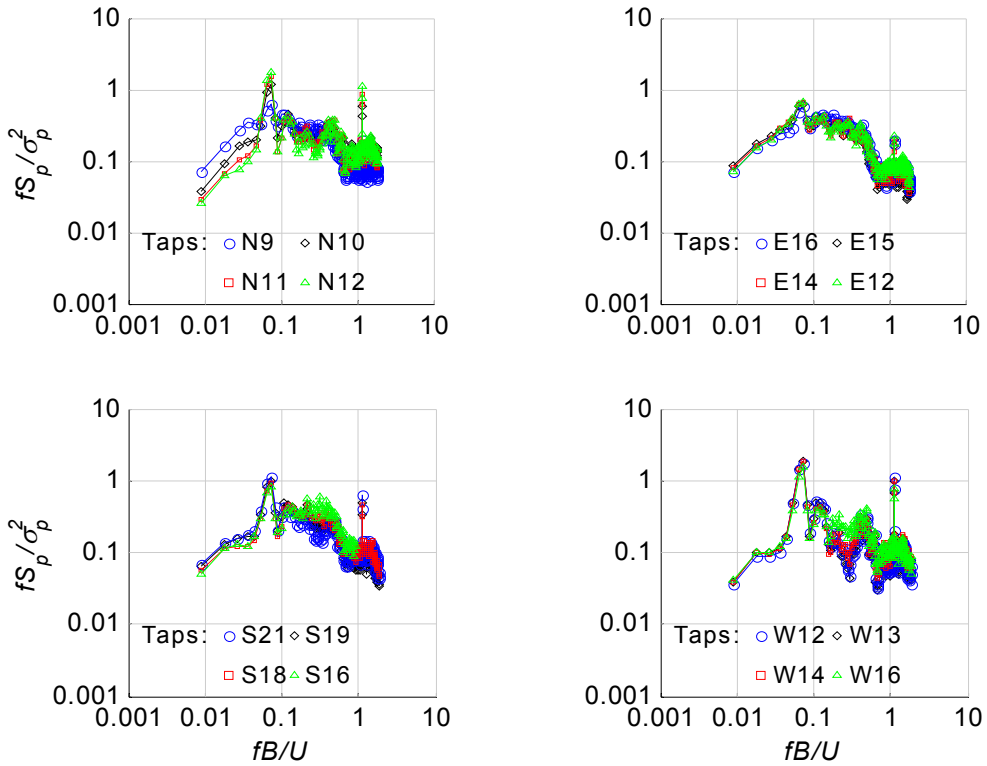

Figure 5.28 Spectral density of surface pressure at taps around the top perimeter of the building, evaluated based on model scale data. The mean wind direction is about 90° from north, i.e. at about 71° angle to the east wall.

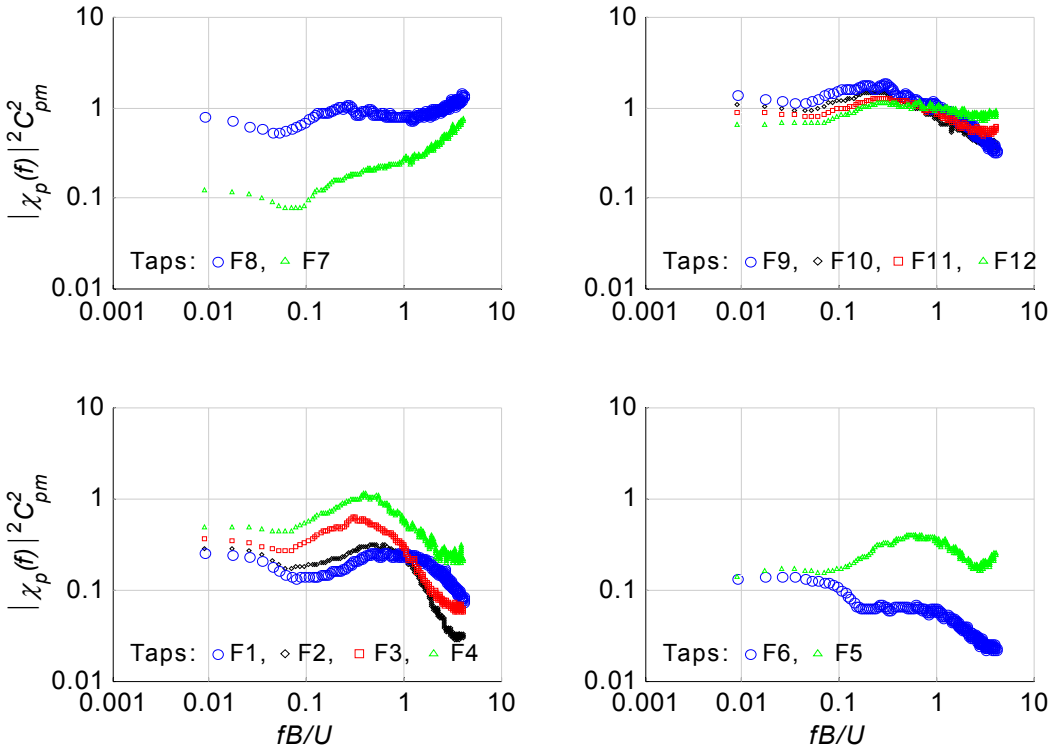

Figure 5.29 Pressure admittance based on full-scale data from taps around the top perimeter of the building. The mean wind direction is about 90° from north, i.e. at about 71° angle to the east wall.

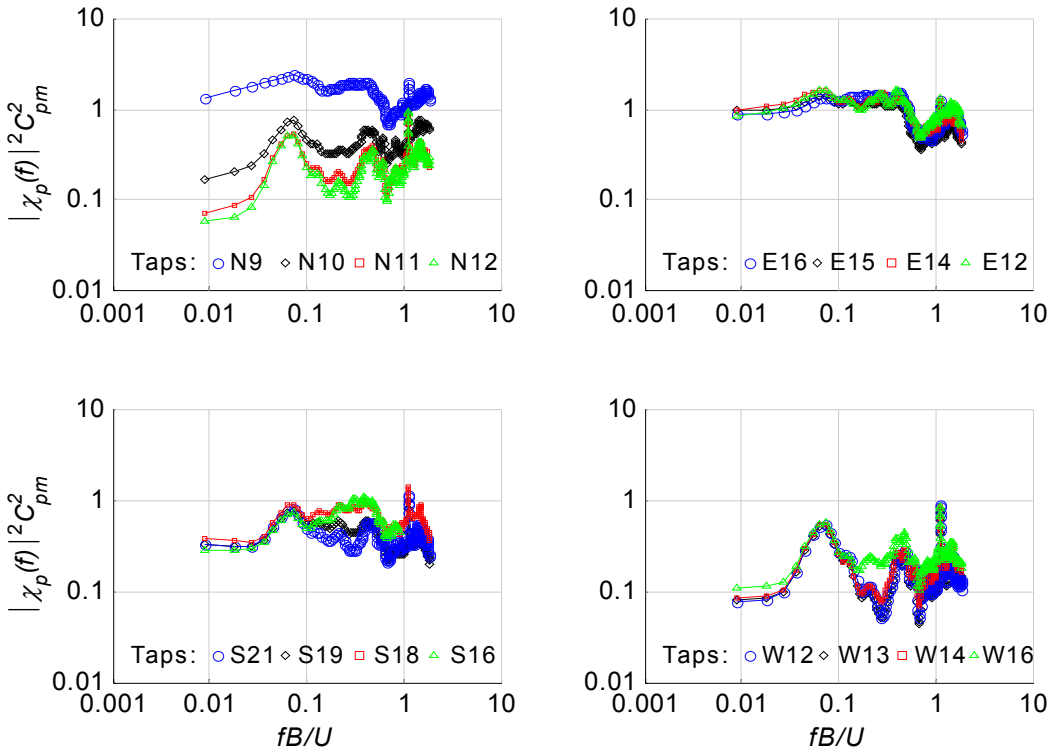

Figure 5.30 Pressure admittance based on model scale data from taps around the top perimeter of the building. The mean wind direction is about 90° from north, i.e. at about 71° angle to the east wall.

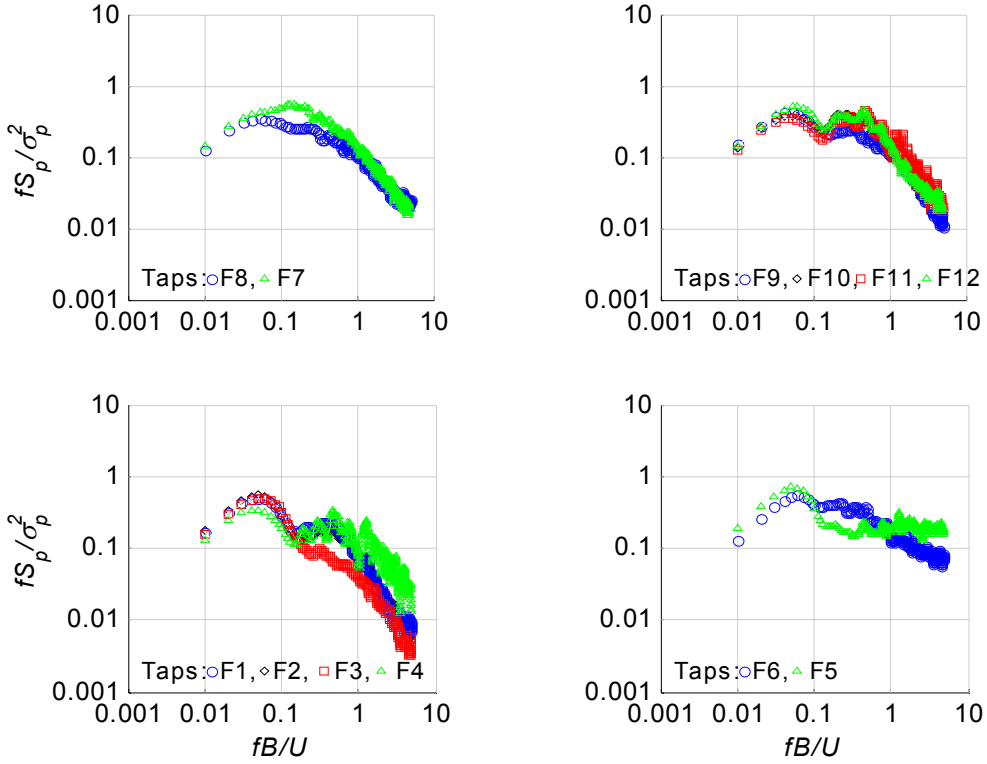

Figure 5.31 Spectral density of surface pressure at taps around the top perimeter of the building, evaluated based on full-scale data. The average mean wind direction is about 19° from north i.e. perpendicular to the wall facing north.

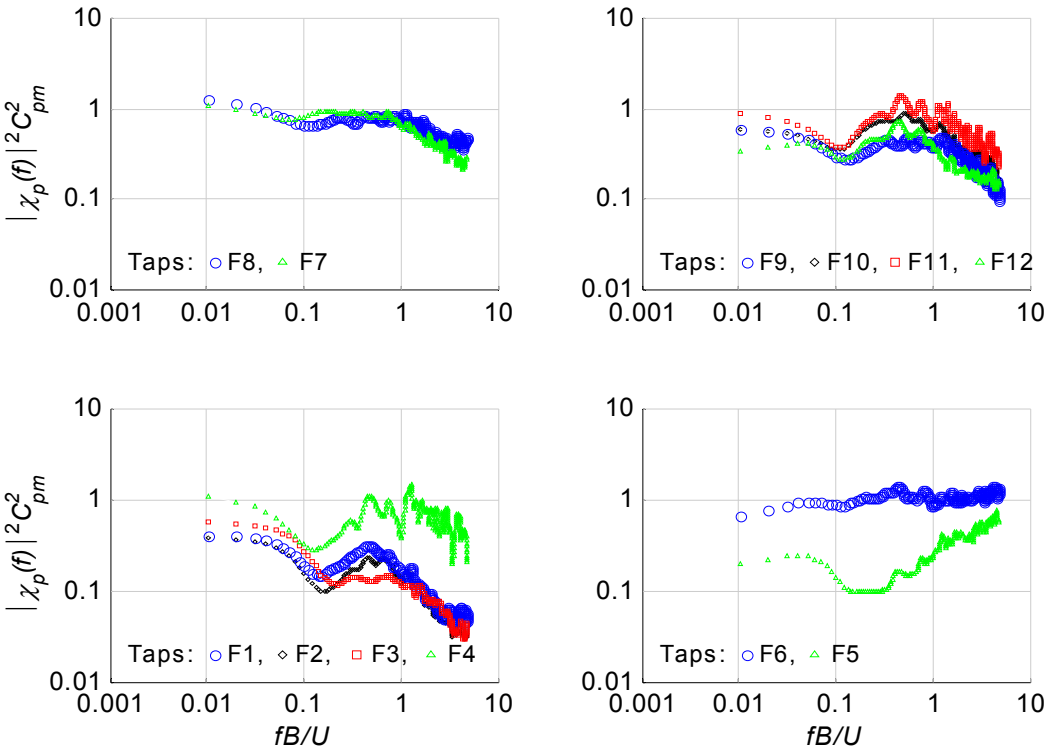

Figure 5.32 Pressure admittance based on full-scale data from taps around the top perimeter of the building. The mean wind direction is about 19° from north i.e. perpendicular to the wall facing north.

No models for velocity-pressure admittance are available from the literature for oblique angles of attack. However, models for pressure admittance at windward walls for flow normal to the facade are available. Two such models will be presented herein and compared to recorded full-scale data, i.e. the models proposed by Kawai [99] and Sharma [190]. Both models are based on wind tunnel experiments and the pressure admittance is defined relative to the wind velocity at pressure tap height, so the strip theory [21] is applied. The model of Kawai is derived for surface mounted prisms with height over width ratio H/B > 1, whereas Sharma derived his model for a scale-model with H < B. However, the height over width ratio for the case at hand is effectively about one.

Kawai proposed the empirical relation:

$$\left|\chi_K(f)\right|^2 = \left(1 + 20\left(\frac{fB}{\overline{U}_h}\right)^2\right)^{-\alpha} \tag{5.7}$$

Here B is the prism width, $\overline{U}$ is the mean wind velocity at tap height and the power α is given as:

$$\alpha = \frac{2}{3}\left(1 - \left(2\frac{y_m}{B}\right)^2\right) \tag{5.8}$$

where y_m is the distance between the vertical symmetry line and the pressure tap.

Sharma proposed a slightly different admittance function, i.e.:

$$\left|\chi_S(f)\right|^2 = \left(1 + 80\left(f_y\right)^2\right)^{-5/6} \tag{5.9}$$

using an alternative reduced frequency, f_y, defined as:

$$f_y = \frac{f\sqrt{BH}}{\overline{U}}\frac{y_e^{3/8}}{5} = \frac{f\sqrt{BH}}{\overline{U}}\frac{\left(1 - 2y_m/B\right)^{3/8}}{5} \tag{5.10}$$

Here y_e is the relative distance between the pressure tap and the vertical edge of the wall.

The two functions are plotted in Figure 5.33 and compared to the pressure admittance for full-scale data recorded at six different taps for wind perpendicular to the building facades. It should be noted that the full-scale admittance is scaled to give an average of one at lower frequencies.

Although both models are, at least up to a point, qualitatively comparable with the velocity-pressure admittance measured at the various taps, the comparison is not strictly adequate. It is noteworthy however, that the models complement each other. The slope of the Kawai model is similar to the slope the recorded admittance, whereas the slope of the Sharma model is generally to steep. On the other hand, the "corner frequency" of the Sharma model is seen to suit the recorded data fairly well, whereas the "corner frequency" of the Kawai model is clearly lower than required by the data. A compromise model could therefore be defined as:

$$\left|\chi_p(f)\right|^2 = \left(1 + 80\left(f_y\right)^2\right)^{-\alpha} \tag{5.11}$$

Using the f_y and α from the Sharma and Kawai model respectively. This modification of the two admittance models is also plotted in Figure 5.33. It is clearly an improvement, although a further refinement is possible, especially the slope at higher frequencies.

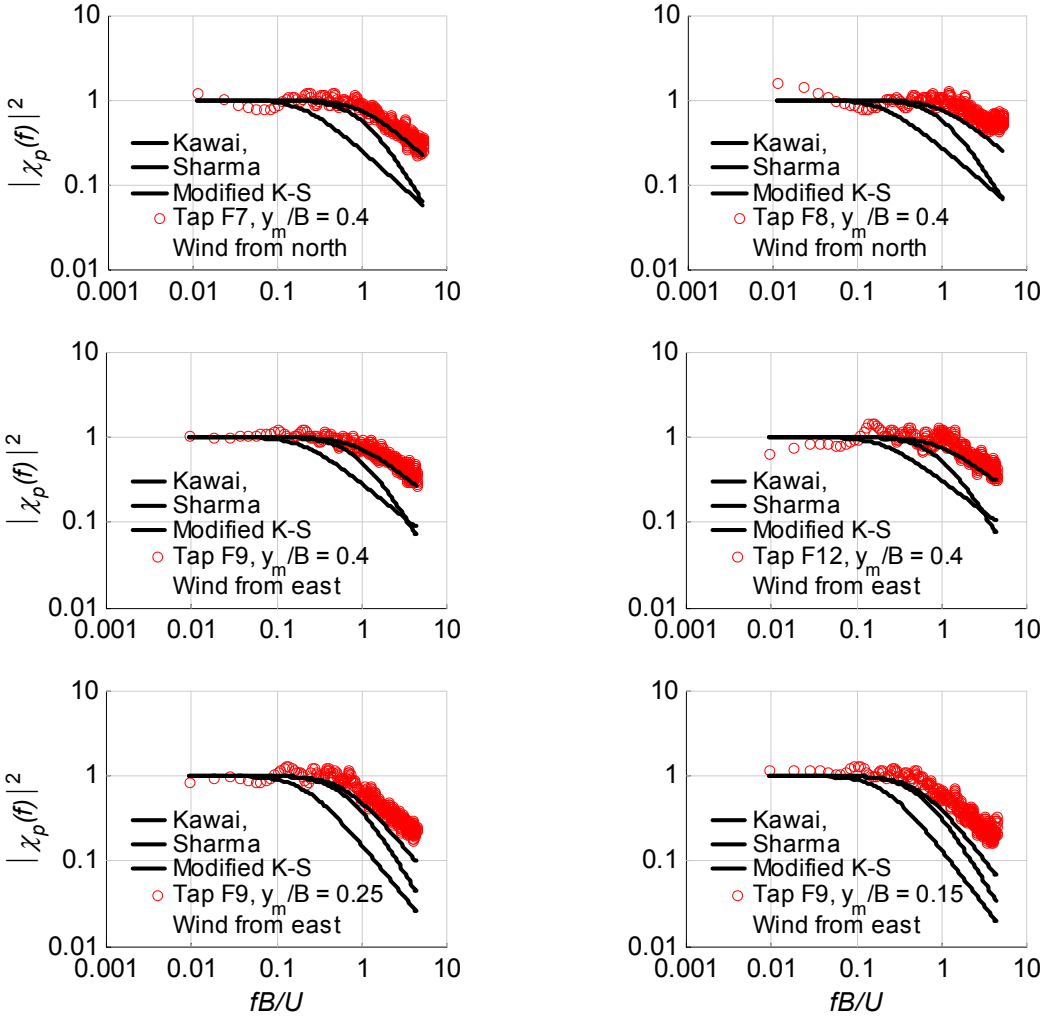

Figure 5.33 Velocity-pressure admittance based on full-scale data from taps on a windward facade for a mean wind direction perpendicular to the same building facade, is compared to models suggested by Kawai and Sharma along with a modification of the two. The Tap numbers and respective y_m/B values are listed on each graph.

5.5 Coherence of pressures

The coherence characteristics of full-scale and model scale pressures have been investigated for various combinations of pressure taps (see also Appendix B). The coherence function of time series X and Y is defined as:

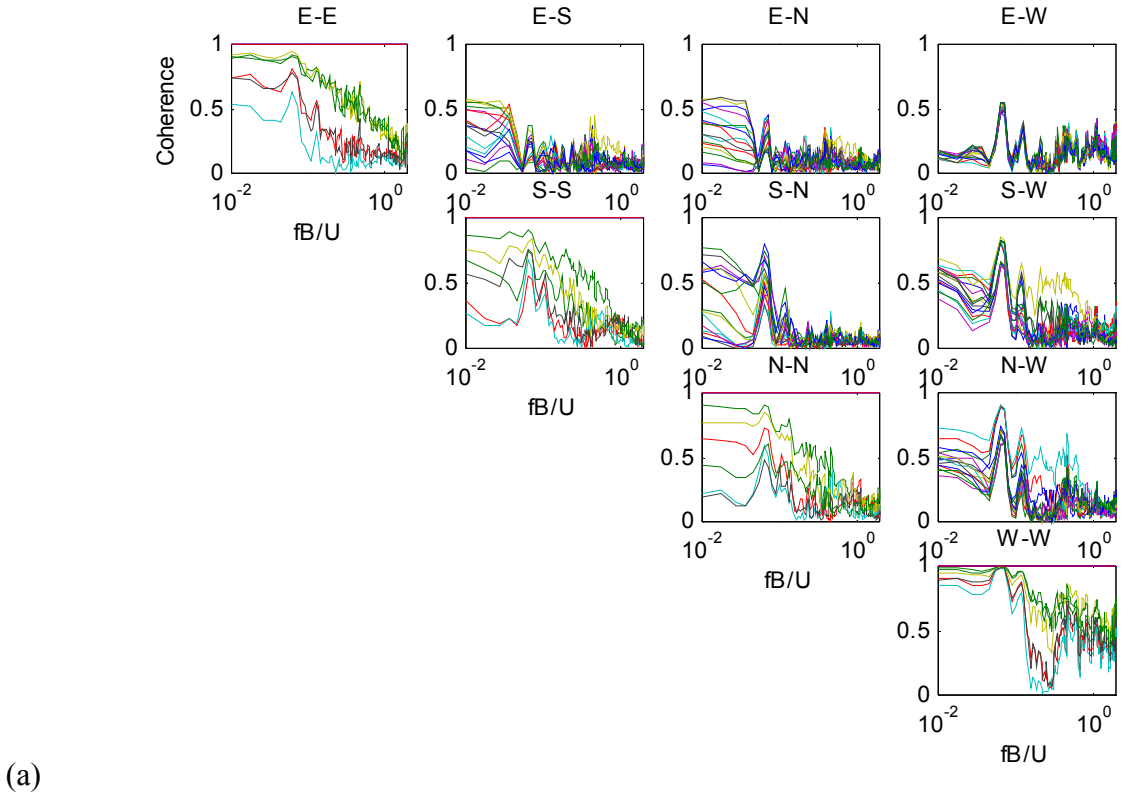

(a)

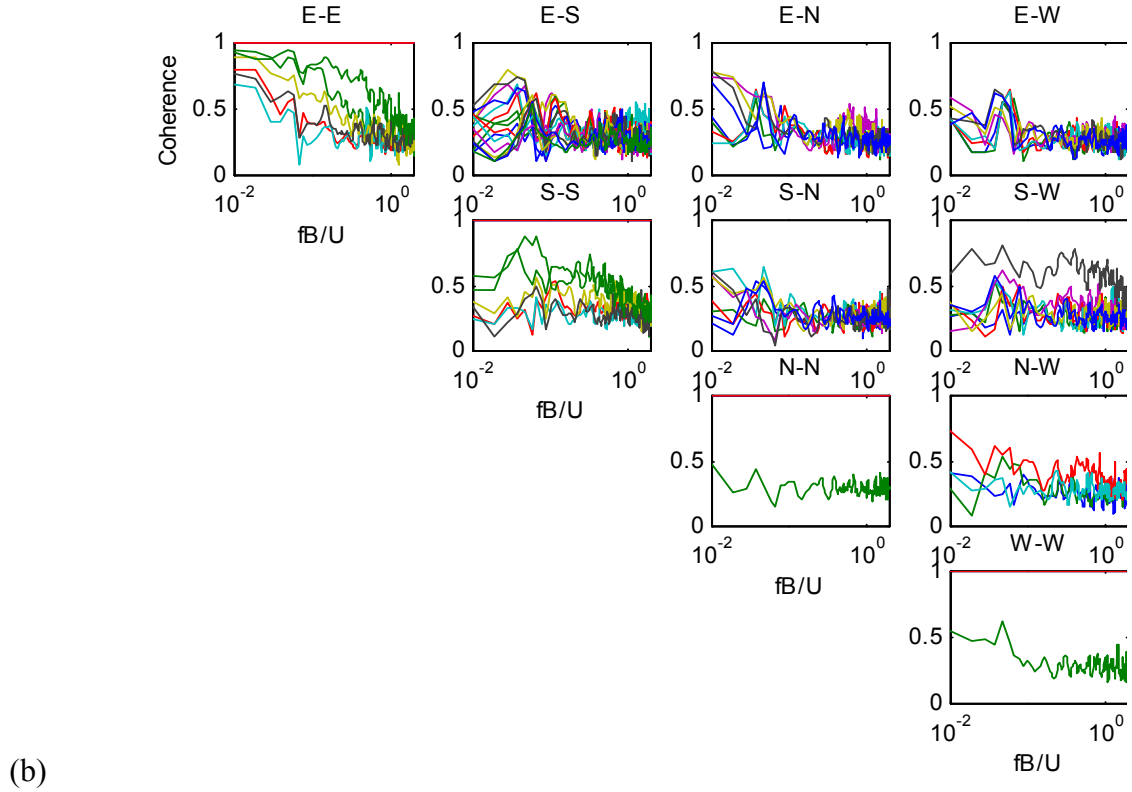

(b)

Figure 5.34 Coherence of surface pressures recorded at different taps around the top perimeter of the building and presented on a wall-to-wall basis as a function of reduced frequency. a) For the wind-tunnel data and b) for the full-scale data. The mean wind direction is perpendicular to the east side of the building.

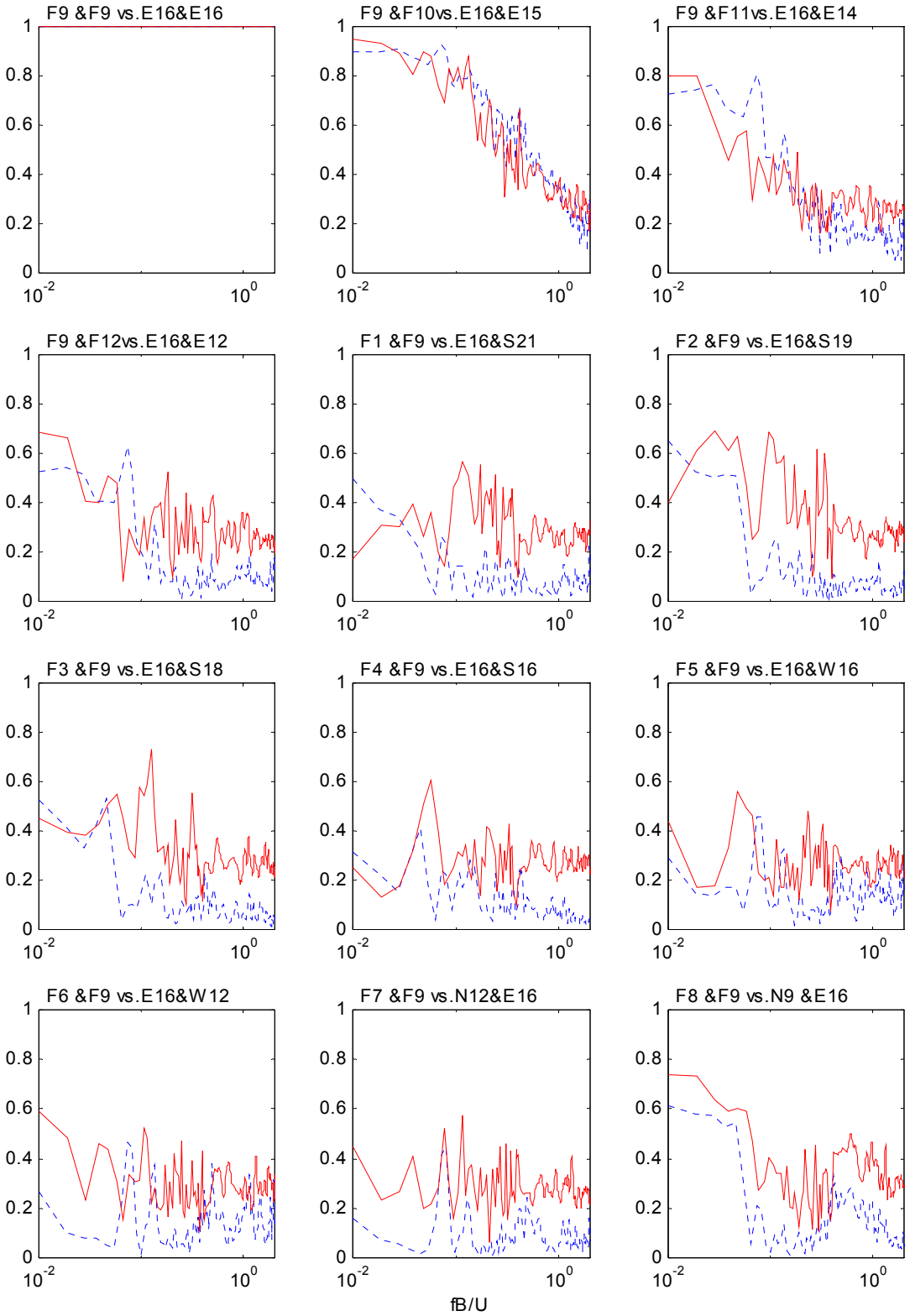

Figure 5.35 Coherence of pressures measured at different taps as a function of reduced frequency for a mean wind direction perpendicular to the east side of the building. The whole lines show coherence evaluated based on full-scale recordings and the dotted line show coherence evaluated based on model scale data. The tap numbers involved are given above each curve and can be referred to **Figure 5.1** and **Figure 5.9**

$$C_{xy}(f) = \frac{\left|S_{xy}(f)\right|^2}{S_{xx}(f)S_{yy}(f)} \tag{5.12}$$

Where S_{xy} is the cross-spectral density of pressure time series X and Y, S_{xx} and S_{yy} are the auto spectral densities of the respective time series of pressure.

Figure 5.34 gives an overview on the coherence between taps on each side of the building as well as for taps on different sides. Each curve represents one coherence relation as a function of frequency. It is seen that the coherence reduces with increased distance as well as frequency. For the windward side the coherence can be represented by an exponential decay function [193]. For instance at the low frequency end, the coherence on the windward side (east side) is about 0.9 for tap spacing of 4.3 m, 0.7 for 8.6 m and 0.5 for 14.4 m. For the suction sides the coherence structure is more complicated as strong coherence is seen at frequency bands related to vortex shedding. However, the coherence at higher frequencies is clearly somewhat exaggerated by "coherent noise" in the data.

Figure 5.35 shows an example of comparison between pressure coherences for both full-scale and model scale. The wind direction is perpendicular to the east side of the building (109° from geographical north). The full-scale coherence shown in Figure 5.35 is referred to Tap F9 on the east side (windward side). The model scale coherence is referred to the corresponding location on the model, i.e. Tap E16 (see Figure 5.9). However, it should be noted that the full- and model scale tap locations compared are not exactly equivalent, which does distort the comparison in some instances. Further examples of comparison between full- and model scale pressure coherences can be found in Appendix B. On average the full- and model scale coherences show a good comparison, especially considering the somewhat different tap locations between model and building. As expected the coherence between pressure at Tap F9 and other taps along the east side of the building reduces with increased tap spacing. On the other hand, it is interesting that pressure at Tap F9 shows clearly a stronger coherence with pressure at Taps F2 and F3 than for Tap F1. This indicates that coherence depends not only on distance, but also strongly on Tap position in relation to the characteristics of the flow regime around the building.

To gain a view on the average coherence involved, the coherence evaluated for each tap combination was averaged over frequency. It can then be plotted as a function of distance between taps along the perimeter of the building. This is shown in Figure 5.36 along with some exponential functions representing the simplified coherence description often used. It is clear that the frequency-averaged coherence could be modelled by a combination of exponential functions. A relatively good comparison is found between the full-scale and model scale frequency averages of coherence, although a slightly more variation is seen in the model scale data. Figure 5.37 shows the standard deviation of coherence as a function of perimeter distance between taps and provides further indication of the variability involved.

Surface pressure coherence evaluated for different wind directions generally showed similar tendencies (see Appendix B), which indicates that the main features of the coherence characteristics are not strongly dependent on wind direction.

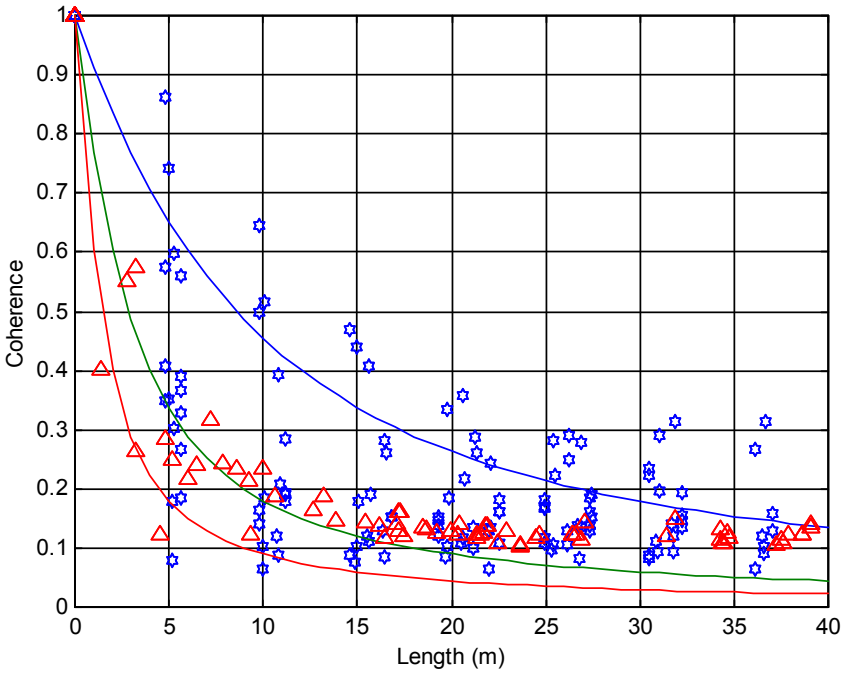

Figure 5.36 Frequency average of coherence of taps distributed around the top perimeter of the building, as a function of perimeter distance between taps. The hexagons represent wind tunnel data while the triangles represent full-scale data. The solid lines represent the frequency average from a traditional exponential coherence model, with decay exponent values of 2, 4 and 12. The data is based on the average of events with a mean wind direction about 90° from north.

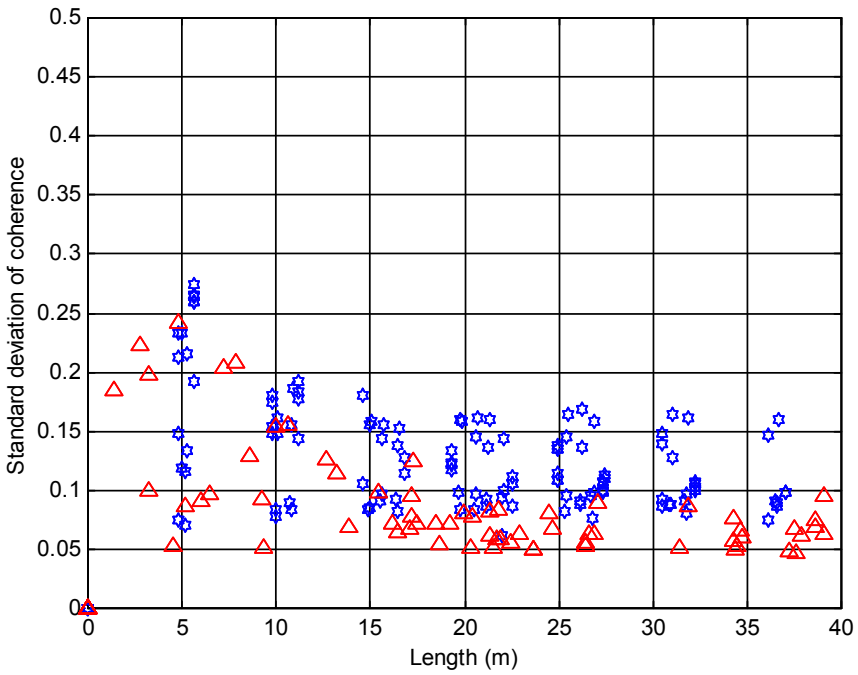

Figure 5.37 Frequency standard deviation of coherence of taps distributed around the top perimeter of the building, as a function of perimeter distance between taps. The hexagons represent wind tunnel data while the triangles represent full-scale data. The data is based on the average of events with a mean wind direction about 90° from north.

5.6 Summary and discussion

The full-scale and model scale pressure data have been systematically compared through the evaluation of descriptive parameters of surface pressure. The comparison is found, generally speaking, to be satisfactory.

The reference data from the full-scale measurements, such as wind velocity and static pressure, are found to be distorted by the flow conditions created by the building. Particularly thermal effects are found to have strong influence on the reference data, and they are most effective during periods of low atmospheric temperatures. It is suspected that these thermal flow effects originate from the heat radiated from the building and/or from the outlet of the ventilation system.

A correction methodology for mean pressure coefficient values from full-scale data has been developed. The methodology is based on a temperature dependent correction factor for mean wind velocity and an offset correction using the difference between the corrected mean velocity pressure and the Reynolds stresses.

Spectral- and coherence analysis of surface pressures were performed and the results from full- and model scale data were compared. The main observations are:

- The comparison is, on the whole, found to be satisfactory, although some characteristic differences are noticeable.
- Spectral analyses of surface pressures indicate that the pressure fluctuations are partly produced by a mixture of alternating and staggered vortex shedding.
- The influence of vortex shedding is much stronger in the wind tunnel date than in full scale.
- The vortex shedding response in full-scale and model scale does not correspond to exactly the same equivalent full-scale frequency bands.
- The normalised spectral values are similar for all taps on sides with positive pressure, whereas the spectral values of taps on suction sides show some variability, depending on tap location. As pressure at taps close to the leeward side of the building show a lower energy content in the low frequency range but a higher energy content in the high frequency range relative to the taps closer to the windward side.
- The velocity-pressure admittance functions for windward sides show a conventional behaviour. A combination of the models by Kawai and Sharma is seen to give an approximate fit to the full-scale data. The admittance relation for the suction sides of the building show a different behaviour, especially data from taps on or close to the leeward side, where admittance is low for normalised frequencies below 0.1 but increases for frequency above 0.1 and peaks at normalised frequencies around 1.
- The full- and model scale coherence of surface pressure shows a fairly good overall comparison.
- Coherence is reduced with an increased tap distance along each wall of the building. However, it is clear that the coherence relation depends not only on distance, but also very strongly on tap position with regard to the characteristics of the flow surrounding the building.

- Coherence of surface pressure on the windward side follows roughly an exponential decay. Coherence on the suction sides is seen to depend on the frequency content of the flow regimes around the building and strong coherence is seen at frequency bands related to vortex shedding.
- In general, similar average coherence behaviour is seen for two different wind directions, indicating that the main features of the coherence characteristics are not strongly dependent on wind direction.
- The variability in wind direction in full-scale results in a greater variance in full-scale pressures. Especially on the windward sides, which are more susceptible to changes in azimuth than the leeward sides. This in turn results in considerable difference in spectral magnitudes on pressure sides between model and full-scale.

Chapter 6 Wind induced acceleration response

6.1 Introduction

As described in Chapter 2.2 three accelerometers were positioned at roof level in the utility room on the top floor of the building shear core. The locations of the sensors are indicated on Figure 6.1, where the local co-ordinate system applied in the following analysis is also defined. Wind induced acceleration response has been recorded in the building before, during separate storms in 1985 and in 1991. In the following sections, some reference will be made to the acceleration data recorded during a storm in 1991. Figure 6.1, shows both the location of the accelerometer during the present experiment as well as the accelerometer location during earlier observations. It should be noted that the floor level where accelerometers A1 and A2 are located is about 60 cm above the floor level of accelerometer A3, which is the roof level. The location of the accelerometers during earlier experiments was on the seventh floor, i.e. one story below roof level. The accelerometers measure the two horizontal components of the response. Acceleration is recorded in the same principle direction on opposite sides of the shear core, in order to be able to distinguish between lateral and torsional effects.

The rotational effects inherent in the dynamics of the building are demonstrated in Figure 6.2, which shows the first three modes of vibration as evaluated by a finite element model, built during earlier studies involving the building [196]. The figure is included here in order to give an idea of how coupled the translational and rotational motion are in the first two modes of vibration.

Since the gustiness of the wind can usually be approximated as a Gaussian process and the system transfer function can be assumed linear, the data is expected to be of

Gaussian character. Assuming, that this stochastic process is at least locally weakly stationary and ergodic, means that each record can fully describe the process.

The stationarity was tested using the *run test*, which is a distribution-free or nonparametric procedure [7]. The hypothesis that the acceleration data are stationary was generally accepted at the 5% level of significance.

The normality of the time series was tested using the single sample *Lilliefors hypothesis test* [20], which is a modification of the Kolmogorov-Smirnov test to determine if the null hypothesis of composite normality is a reasonable assumption regarding the population distribution of a random sample X for a desired significance level. It was found that the acceleration time series generally do not meet the normality criteria. The reason lies in the kurtosis value, which is a measure of how outlier-prone a distribution is. The acceleration series have a varied kurtosis that can lie on either side of 3, the kurtosis value for a normal distribution. However, generally the kurtosis values are above 3, often around 4, which is in agreement with findings in [119].

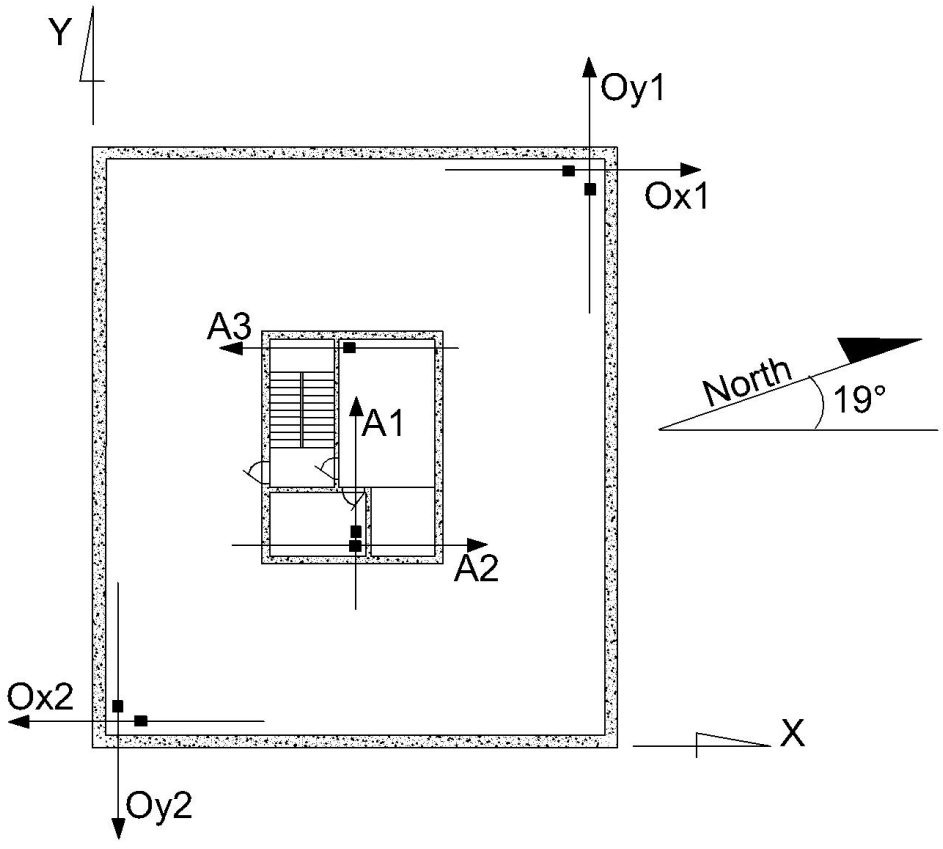

Figure 6.1 A plan view of the tower and its shear core. The location and directionality of accelerometers during the present experiment is given by A1, A2 and A3. The location and directionality of accelerometers during earlier experiments are given by Ox1, Oy1, Ox2 and Oy2. The coordination system is defined by X and Y.

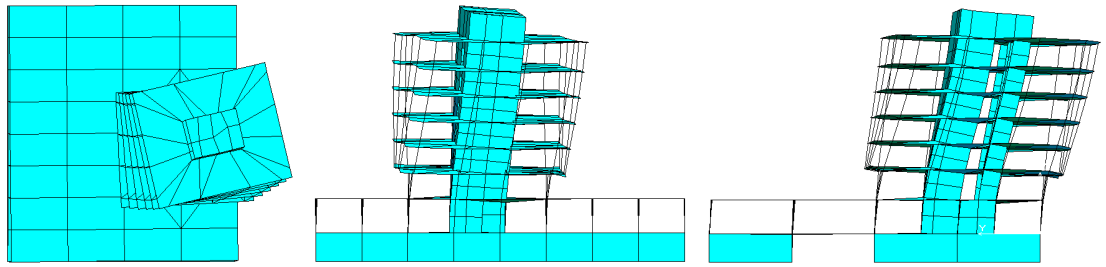

a) The 1. mode of vibration

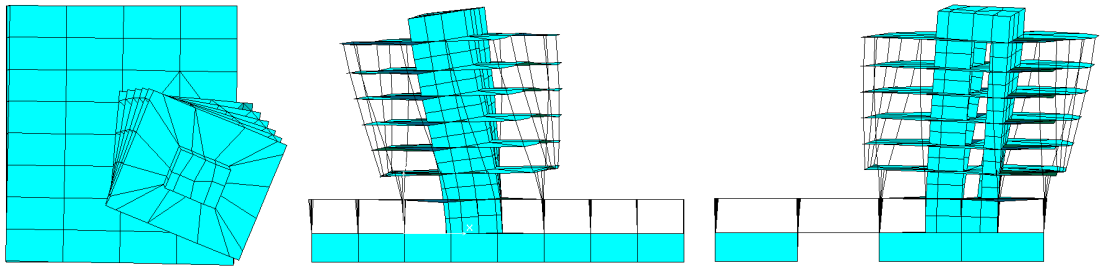

b) The 2. mode of vibration

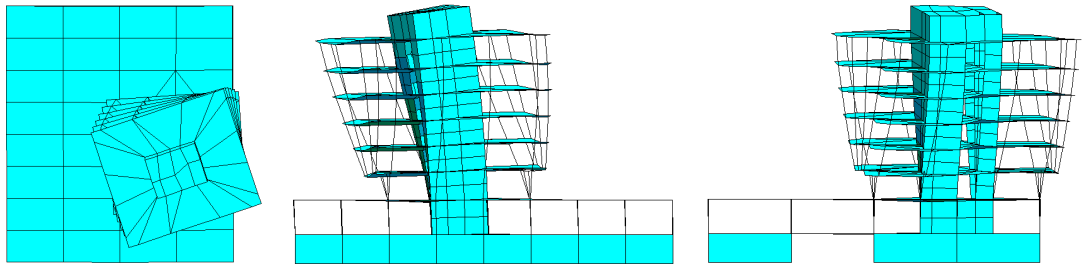

c) The 3. mode of vibration

Figure 6.2 The first three modes of vibration for the building, evaluated by finite-element modelling.

The key elements in any statistical analysis are the mean and the standard deviation of the process involved. Since the building is fixed at its base, the mean acceleration has to be zero. The sensors are not capable of confirming that, since they only detect relative motion. Any apparent mean value in the data is therefore removed in the analysis. In addition to the mean and variance, the extreme values, i.e. the maximum and minimum, are generally of interest. It is common to relate these extreme values to the standard deviation for a zero mean process. One way of doing this is to define a peak factor g_a as:

$$g_a = \frac{\frac{1}{2}(a_{\max} - a_{\min})}{\sigma_a} \tag{6.1}$$

Where $a_{\max}$, $a_{\min}$ and σ_a are respectively the maximum, minimum and the standard deviation of recorded acceleration. In the following sections, the basic acceleration statistics will primarily be described through the standard deviation and the peak factor.

The data is analysed using a traditional spectral analysis. The spectral estimates are derived by applying the fast Fourier technique with data windowing using the Hamming window function. To achieve greater statistical accuracy in the spectral evaluation, a segmental averaging was used with overlapping of the ensemble segments to increase the possible number of segments ([7] [142] [102]). The spectral information is estimated applying 796 selected time series consisting of 10799 data points each with a sampling frequency equal to 15 Hz, which is a decimation from the original sampling frequency of 30 Hz. The spectral information is presented in terms of normalised auto- and cross-spectral densities phase angle and coherence between parallel and perpendicular acceleration channels.

The acceleration data is further used for system identification, where parametric methods based on an ARMA representation of the system is applied.

6.2 The acceleration data, response versus environmental noise

To record and interpret structural acceleration recordings is typically a fairly straightforward affair. In this building, acceleration recordings have generally not been particularly transparent. In the earlier recordings, spectral density information revealed energy content or peaks at various frequencies, which interfered to some extent with the identification of the true structural resonance and related frequency and damping parameters. For example, the data contained considerable amount of energy at frequencies well below 1 Hz in addition to strong resonance type peaks around and above 1 Hz. In addition to this, occasional extreme “spikes” could be seen in the time series ([196] [197] [198]). These phenomena have not been properly identified or explained in the past, but are now judged to be linked to the building environment but not to structural characteristics.

During the latest experiment the accelerometer location was changed, and moved up one floor and into utility rooms in the centre shear core. Accelerometers A1 and A2 were located in the elevator control room close to the motors and the pull wires. Below was the elevator shaft housing two elevators. Accelerometer A3 was located in a room containing ventilation equipment with the ventilation intake and outlet placed on the north wall of that room. As this description reveals, the accelerometers were located in a noisy environment. Unfortunately, the implications of this were not fully realised beforehand. As can be expected the new data turned out to have all the formerly seen disturbances but in a magnified version.

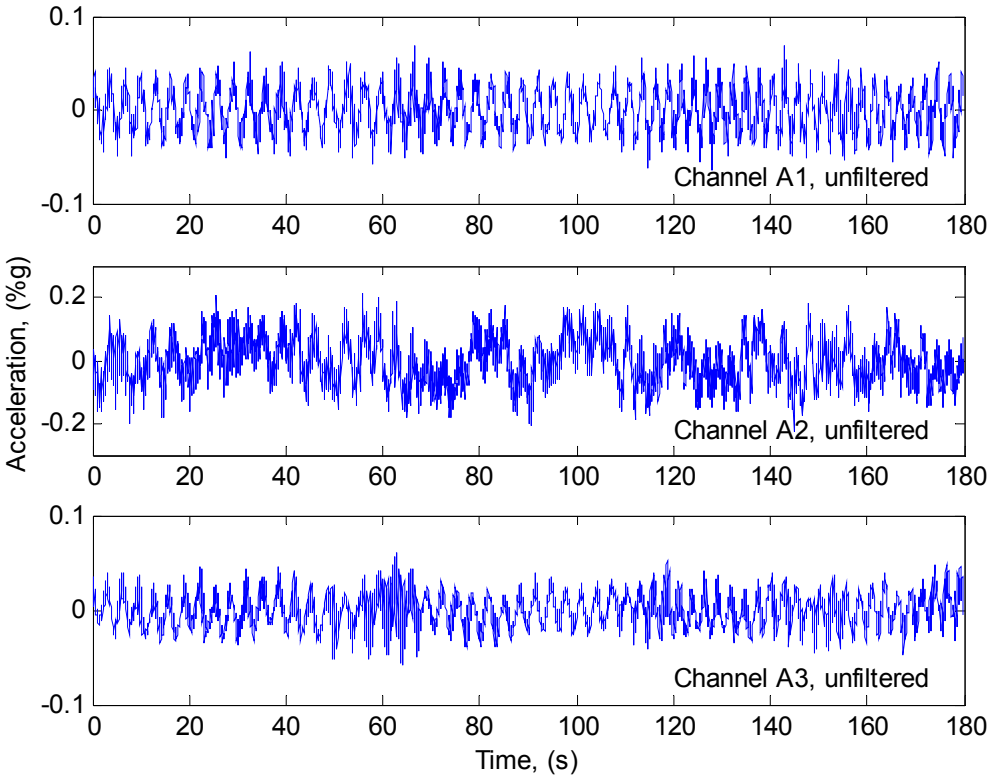

Figure 6.3 An example of recorded acceleration.

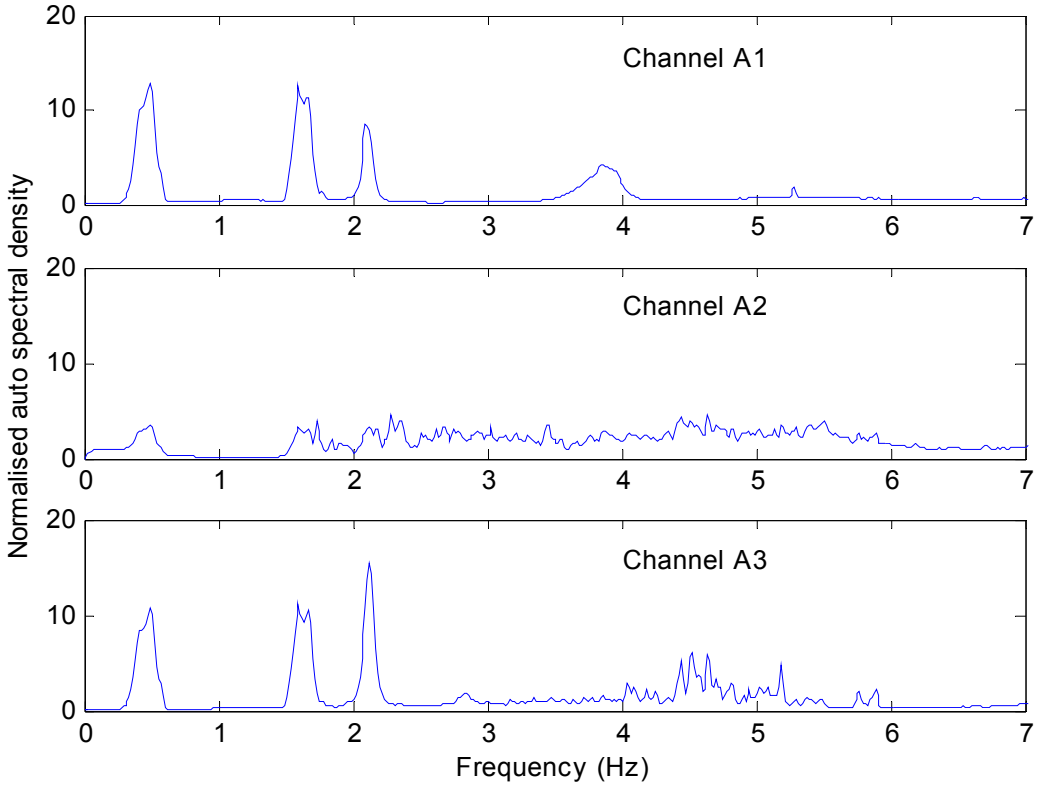

Figure 6.4 Average normalised auto spectral density ($fS_a(f)/\sigma_a^2$) from 796 acceleration records.

An example of the recorded acceleration series is shown in Figure 6.3. The corresponding spectral information is presented in Figure 6.4, which shows the average normalised auto-spectral densities based on 796 acceleration records. The normalised cross-spectral densities are also presented in Figure 6.5 in the form of Co- and Quad spectra. As can be seen from these figures, the data contains considerable amount of energy at frequencies below 1 Hz. Secondly there is a strong resonance peak between 1 and 2 Hz. Thirdly there is a strong resonance peak just above 2 Hz and then another smaller below 3 Hz. Based on earlier experiments these represent the natural frequencies of the building. Then a strong resonance peak is seen just below 4 Hz in the records from channel A1. Channel A3 also shows some unidentifiable energy at frequencies above 4 Hz. In addition, it is evident that channel A2 is badly affected by the environmental noise.

Figure 6.6 shows the average phase information for the acceleration and the average coherence between parallel and perpendicular acceleration is presented in Figure 6.7. Looking at the phase angle of the cross-spectra and the coherence functions, several things are noticeable. The perpendicular signals are out of phase at frequencies around 2.1 Hz but in phase at frequencies 2.8 Hz. Similarly they are coherent at 2.8 Hz but at 2.1 Hz the coherence peak is split. The parallel signals however are in phase at 2.1 Hz, but out of phase around 2.8 Hz. They also show good coherence at 2.1 Hz but not as good at 2.8 Hz, which may be due to the weak presence of that frequency component especially in channel A2. In summary, this suggests that there are two translational modes at frequencies around 2.1 Hz, and a torsional mode at frequency around 2.8 Hz. The split Co-spectrum peak for perpendicular channels in Figure 6.5 further supports the fact, that there are two modes at around 2.1 Hz.

It should be noted that the relatively low phase and coherence values are an effect of the averaging of many different records.

Figure 6.4 through Figure 6.7 give average spectral information and do not fully represent the substantial individual variability of the records, which is linked to recording periods, time of day, the direction and magnitude of the wind and other factors. This variability is partly demonstrated in Figure 6.8, which shows the maximum spectral density values for six different frequency ranges as a function of the record number. Also, the coherence in Figure 6.7 is evaluated for two different time periods. That is for the night (00:00 to 07:00) and for the day (07:00 to 24:00). This reveals some differences in the frequency composition of environmental noise, especially for the frequencies around 1 Hz, that is the frequency range excited by the elevators which are mainly operating during the day. The response at 1 Hz is related to the travelling speed of the lifts (or the motor speed). The reason why the elevator frequency range is not apparent in the average spectral density plot, apart from the daily operational pattern, is most likely the variability in the elevator excitation caused by variable travel speed and distance in addition to the fact that there are two lift-cars in the shaft. In addition to this, the extreme “spikes” that are occasionally seen in the time series are most likely caused by the “jerk” created when the lifts start and stop. As is demonstrated by the coherence, the phenomena associated with the lifts can be mapped by plotting the data versus time of day. The data recorded during night when the lifts are not in use, have no “spikes” and no resonance around 1 Hz. This is validated by

Figure 6.9, which clearly indicates that the resonance at 0.8 Hz to 1.2 Hz is created during the day. A similar histogram in Figure 6.10 shows the number of acceleration values that are larger than six standard deviations ($6\sigma_a$) as function of the hour. The figure demonstrates that the large majority of spikes occur during the day. It should be noted that a single spike may contain more than one value larger than $6\sigma_a$, therefore the number of spikes may be overestimated in Figure 6.10.

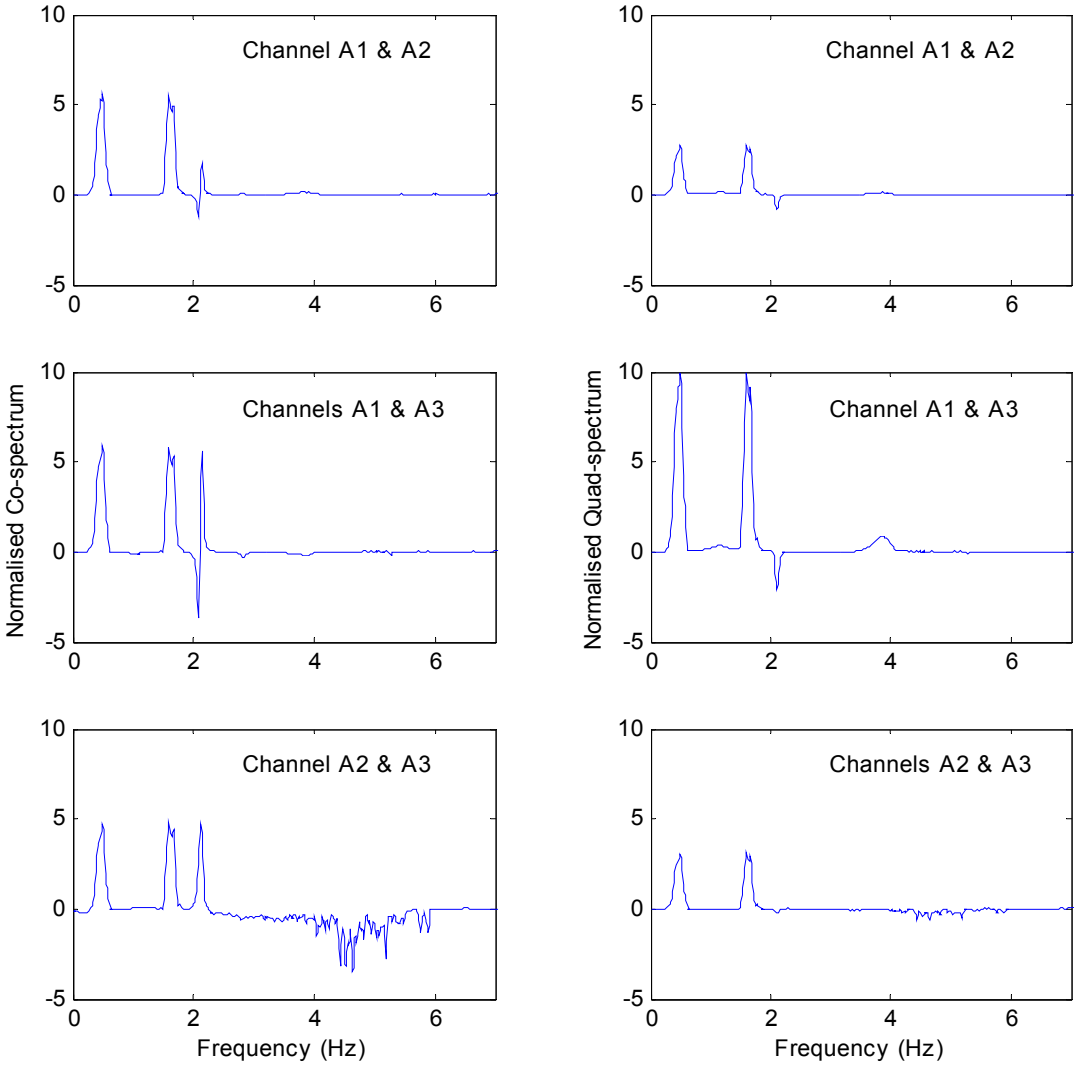

Figure 6.5 Average Co- and Quad spectrum from 796 unfiltered acceleration records.

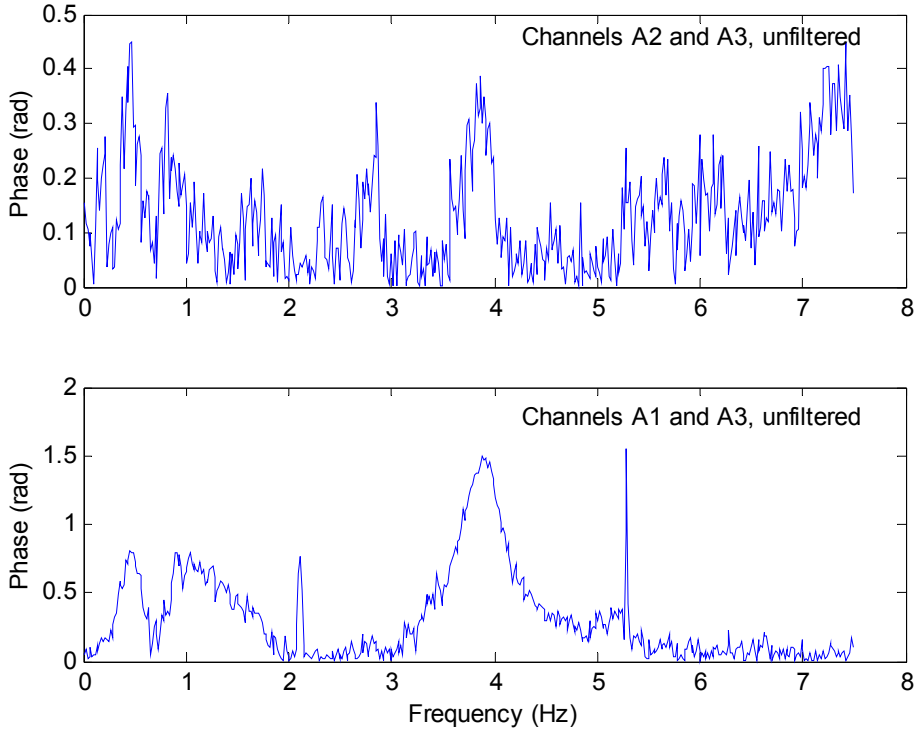

Figure 6.6 Average phase angle of 796 unfiltered acceleration records. Top: Phase difference between parallel sensors (A2 and A3). Bottom: Phase difference between perpendicular sensors (A1 and A3).

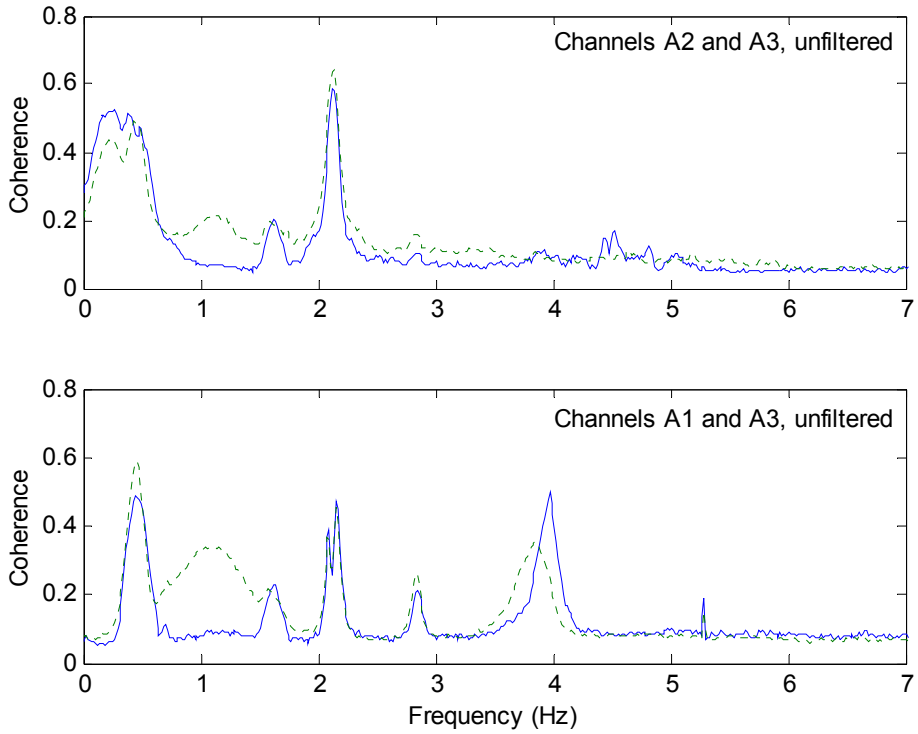

Figure 6.7 Average coherence based on 796 unfiltered acceleration records. Top: Coherence between parallel sensors (A2 and A3). Bottom: Coherence between perpendicular sensors (A1 and A3). The broken line represents measurements between 7:00 and 24:00, whereas the whole line represents measurements between 00:00 and 7:00.

It is more difficult to identify with certainty the other sources of noise and as the building and its equipment was modified right after the recording period, direct measurements are impossible. Some are very consistent, such as the low frequency noise around 0.5 Hz and below, which is most likely related to the ventilation system in the control room. The changes in the acceleration level at various frequency ranges for records no. 200-300 as seen in Figure 6.8 labels the noisy frequency bands and indicates that some equipment has been turned of or had a temporary malfunction of some sort, which in turn has changed the noise pattern. Also, if the low frequency noise is due to ventilation, the change suggests that the noise level at several frequency bands may be influenced by the ventilation system.

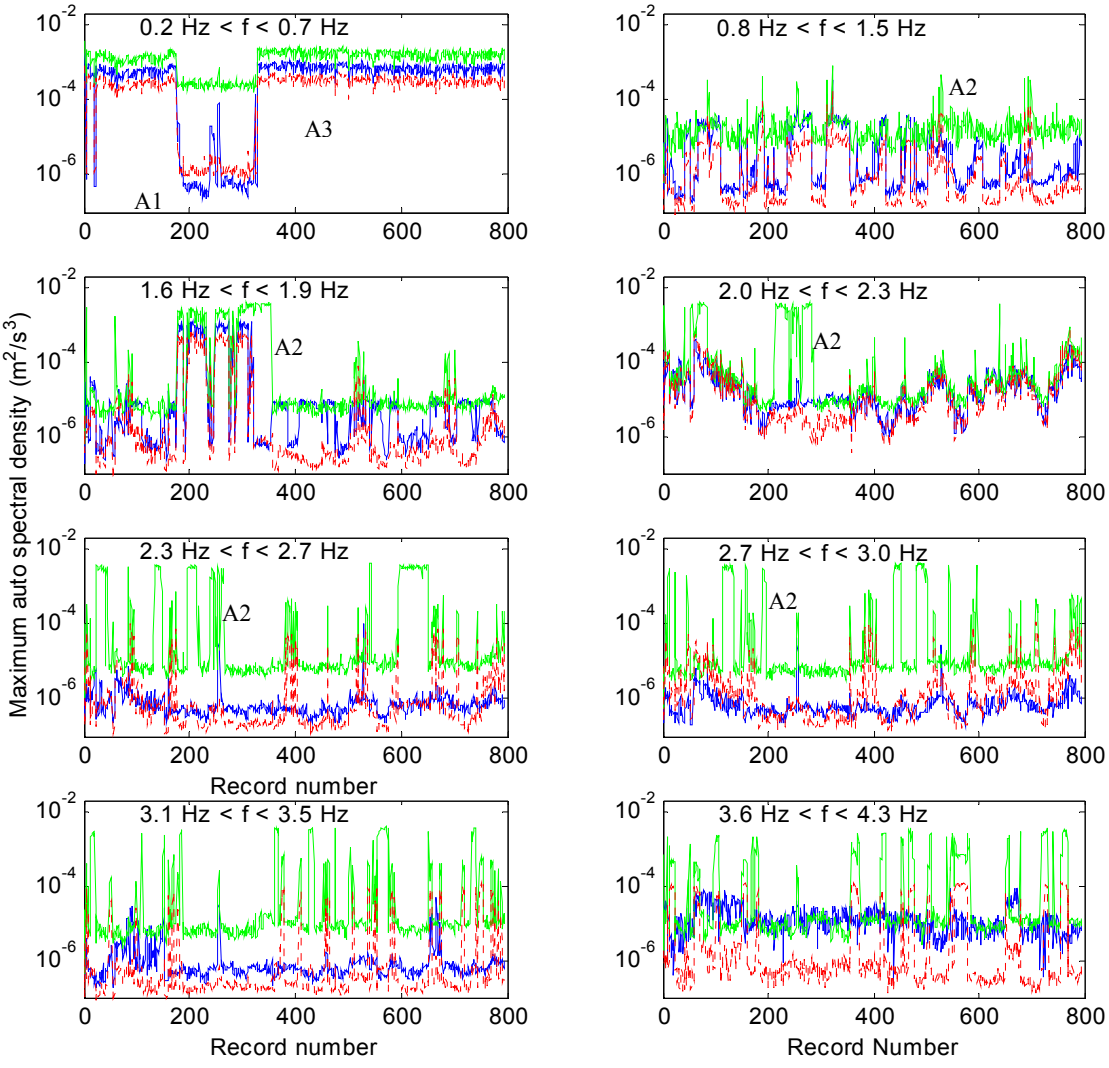

Figure 6.8 Maximum auto spectral density value for six specific frequency ranges plotted for each record as a function of record number. The top curve represents channel A2 (green), the bottom curves are from channels A1 and A3, usually with channel A3 (red) below A1 (blue).

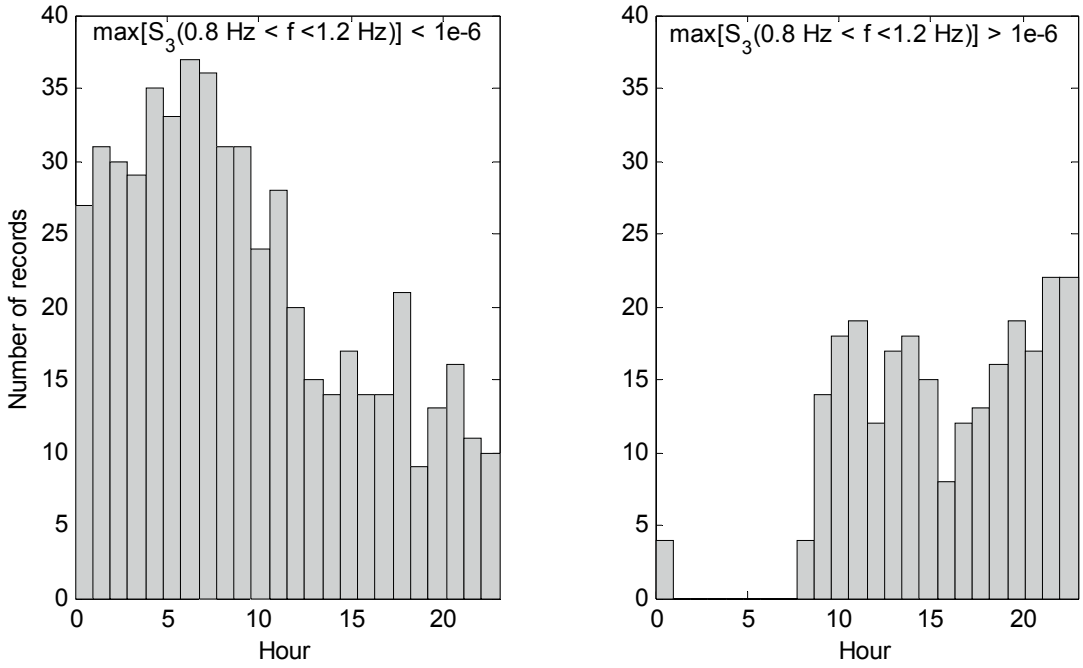

Figure 6.9 A histogram showing the number of unfiltered records with spectral density above and below 1e-6 m^2/s^3 at a frequency around 1 Hz as a function of hour.

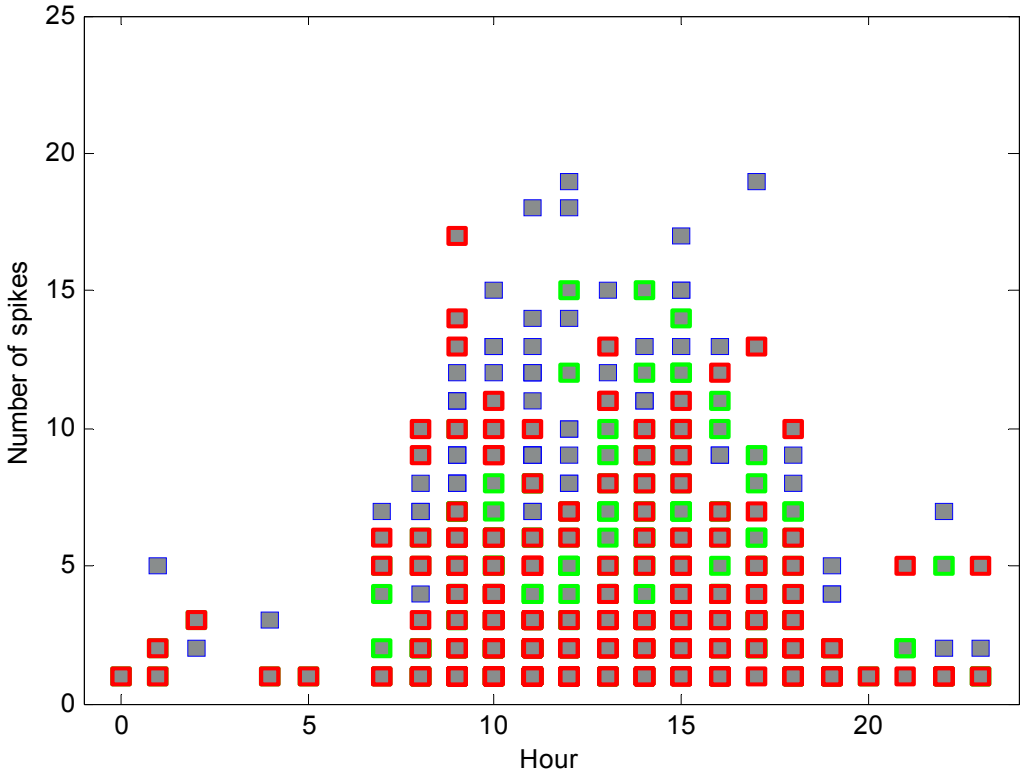

Figure 6.10 Number of acceleration spikes per unfiltered record as a function of the hour. A spike value is defined as an acceleration value larger than 6 standard deviations.

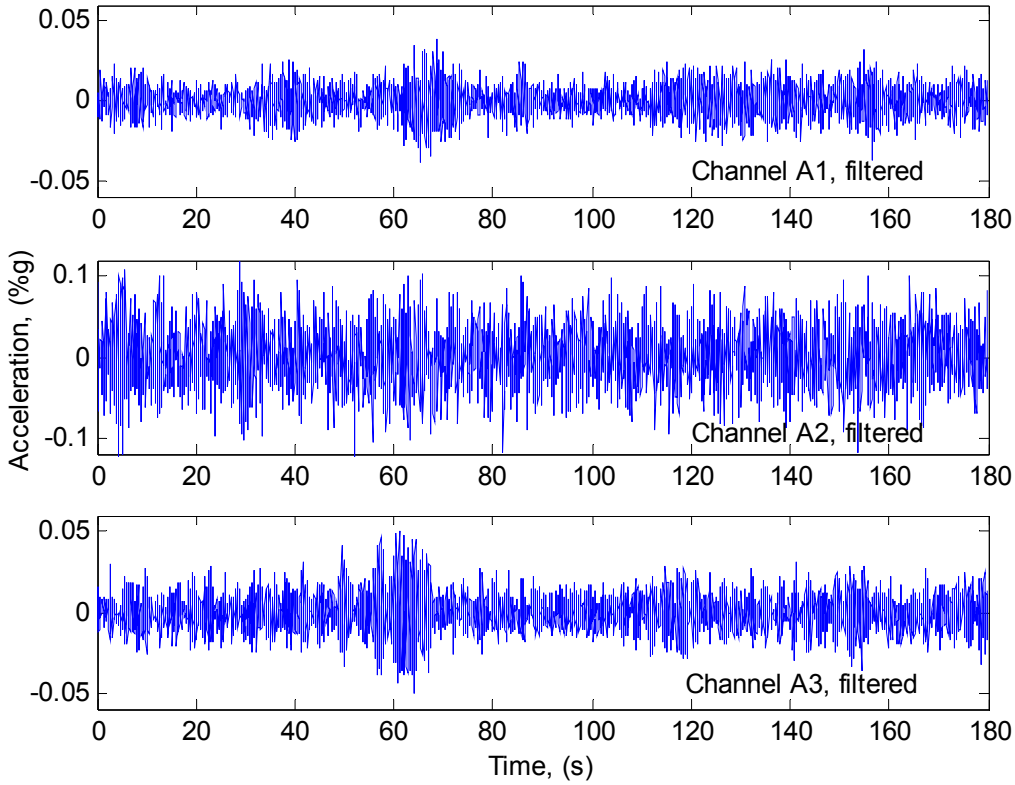

Figure 6.11 Example of band-pass filtered acceleration records.

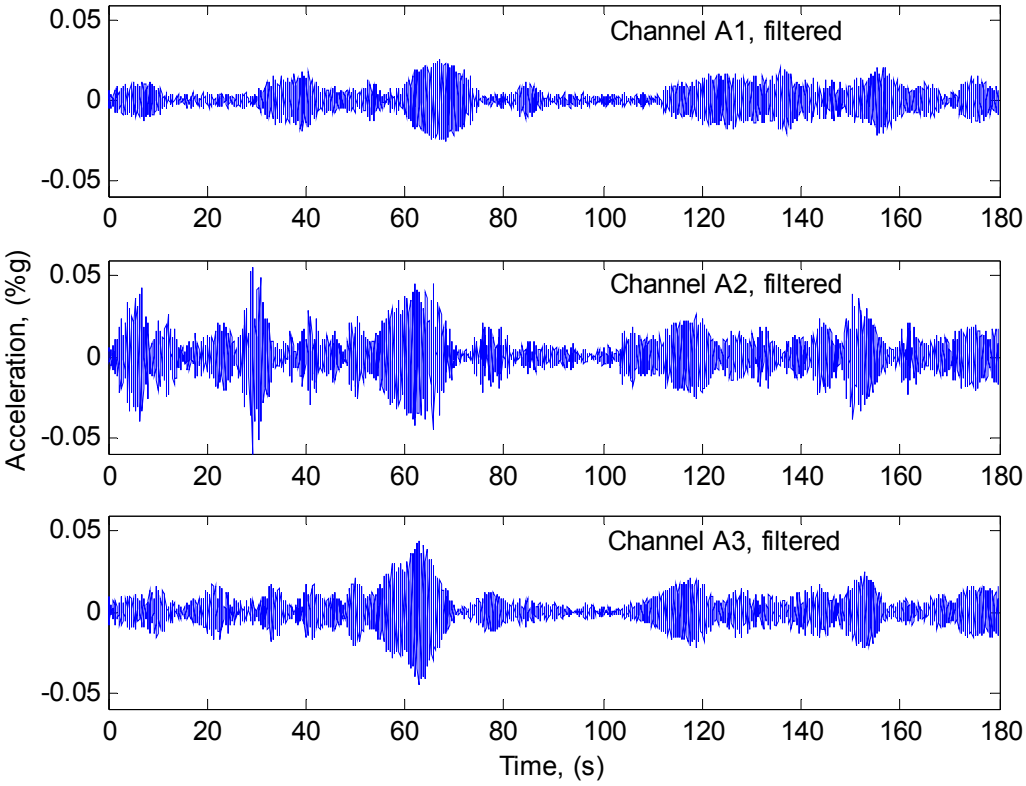

Figure 6.12 Example of multi-band-pass filtered acceleration records.

6.3 Filtered acceleration data

As the relevant response signal was buried in noise, it was necessary to apply a band-pass filter to the raw acceleration data to remove the environmental noise. A zero-phase forward and reverse digital filtering was used, applying a sharp FIR filter. The result has zero phase distortion and care was taken to minimize start-up and ending transients by matching initial conditions. Figure 6.11 and Figure 6.12 show examples of band-pass filtered time series. On one hand, Figure 6.11 shows time series containing the frequency band 1.9 Hz to 3.1 Hz, and on the other Figure 6.12 shows the same time series containing two separate frequency bands of 1.9 Hz to 2.3 Hz and 2.7 Hz to 3.0 Hz. As can be seen these time series are very different from the raw time series pictured in Figure 6.3. A base level Gaussian random noise is added to the filtered series in Figure 6.11. The random noise is generated based on the base level of the auto-spectral density of an unfiltered signal and added to each filtered signal. This was primarily done in order to facilitate system identification, which will be discussed later, but it also creates a more realistic signal where the added random noise can be taken as the measurement noise inherent in any signal. On the other hand, no noise is added to the time series in Figure 6.12. Comparing these two figures gives an idea of the effect of limiting the noise level. The signal pictured in Figure 6.12 is a typical narrow band process. Noticeable are the bursts of high acceleration of 5 to 10 s duration. These bursts correspond well to the motion perceived by the author in the building during the storm in February 1991.

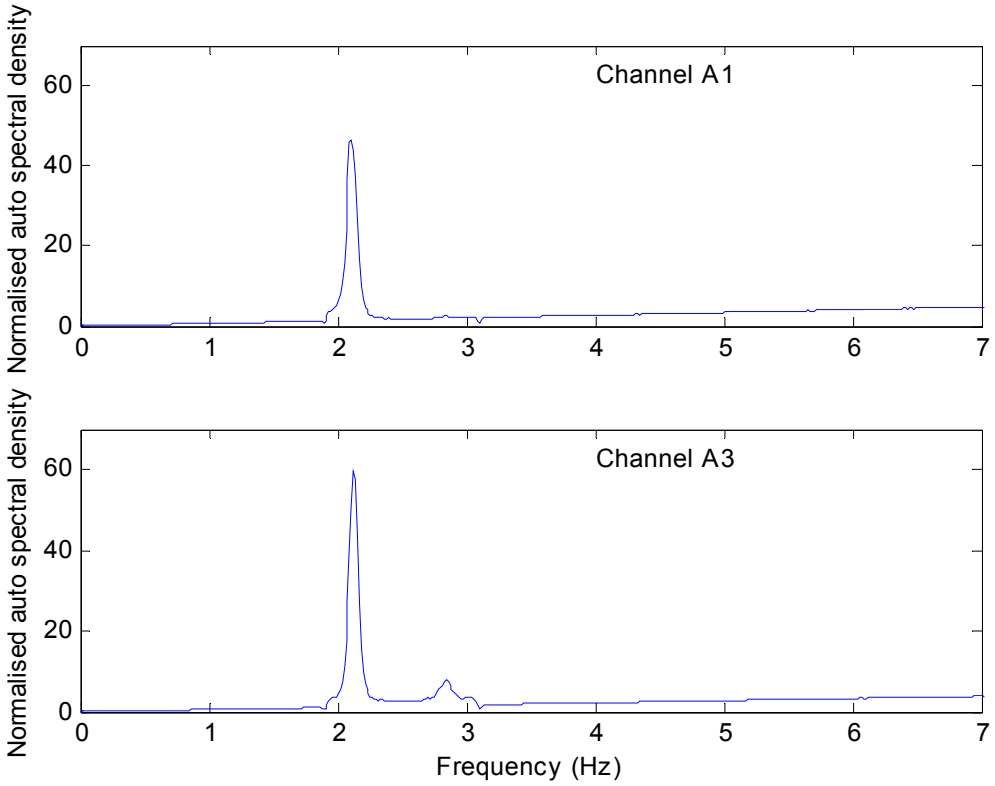

Figure 6.13 Average normalised auto-spectral density ($fS_a(f)/\sigma_a^2$) from 796 acceleration records after band-pass filtering the signals.

Velocity and displacement can be evaluated by integrating the acceleration. When integrating acceleration, care should be taken to filter out any artificial low frequency components in the time series. It is also important to have a relatively high sampling frequency for accurate time-series description, especially if simple cumulative summing is used. Integrating the acceleration gave results that followed the relation:

$$\sigma_a \cong \omega_n \sigma_v \cong \omega_n^2 \sigma_d \tag{6.2}$$

where, ω_n is the natural frequency (≈2.1 Hz), σ is the standard deviation and the indices a, v and d stand for acceleration, velocity and displacement respectively. Although Eq. (6.2) is strictly only valid for narrow banded single mode systems, the relation gives a good approximation for this case because the first two modes of vibration dominate the response and both have approximately the same natural frequency.

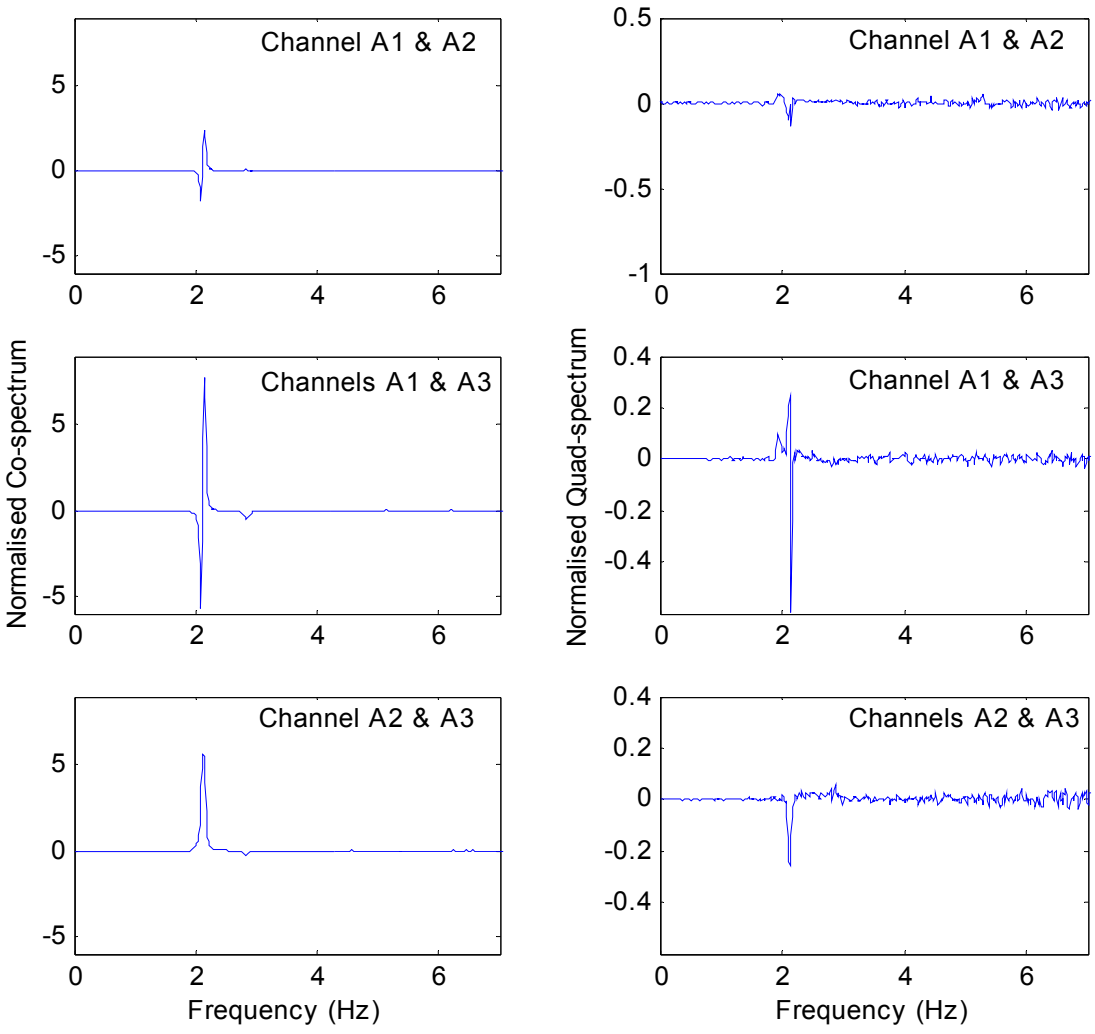

Figure 6.14 Average normalised cross-spectral density ($fS_{xy}(f)/\sigma_x\sigma_y$) from 796 acceleration records after band-pass filtering the signals.

The spectral density for the filtered acceleration was calculated in the same way as described above for the original signals. The normalised spectral densities for the three

channels are shown in Figure 6.13 and Figure 6.14. Similarly, the phase and coherence are shown in Figure 6.15 and Figure 6.16. The spectral densities clearly show the narrow-band nature of the response with energy clustered mainly at the fundamental modes of vibration. As expected, they are dominated by a spectral peak at a frequency around 2.1 Hz, and a second one can be noticed at 2.8 Hz. Looking at the phase angle in Figure 6.15 and the coherence function Figure 6.16 the same features are seen as before in Figure 6.6 and Figure 6.7 for the frequency range between 2 and 3 Hz. The perpendicular signals are out of phase at frequencies around 2.1 Hz but in phase at frequencies 2.8 Hz. Similarly they are coherent at 2.8 Hz but at 2.1 Hz the coherence peak is split. The parallel signals are in phase at 2.1 Hz, but out of phase around 2.8 Hz. They also show good coherence at 2.1 Hz but not as good at 2.8 Hz, which may be due to the weak presence of that mode of vibration in the data, especially from channel A2. As before, this suggests that there are two translational modes at frequencies around 2.1 Hz, and a torsional mode at frequency around 2.8 Hz. Clearly the translational components are coupled with torsion. The split Co-spectrum peak for perpendicular channels in Figure 6.5 further supports the fact, that there are two modes at around 2.1 Hz.

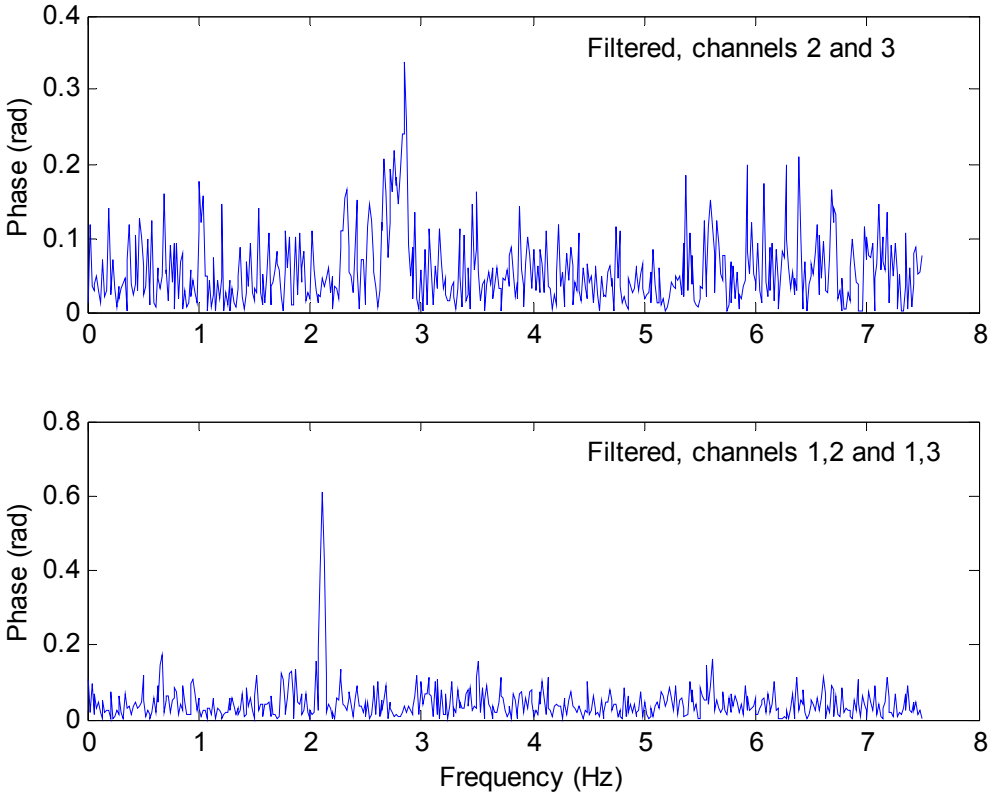

Figure 6.15 Average phase angle of 796 filtered acceleration records.

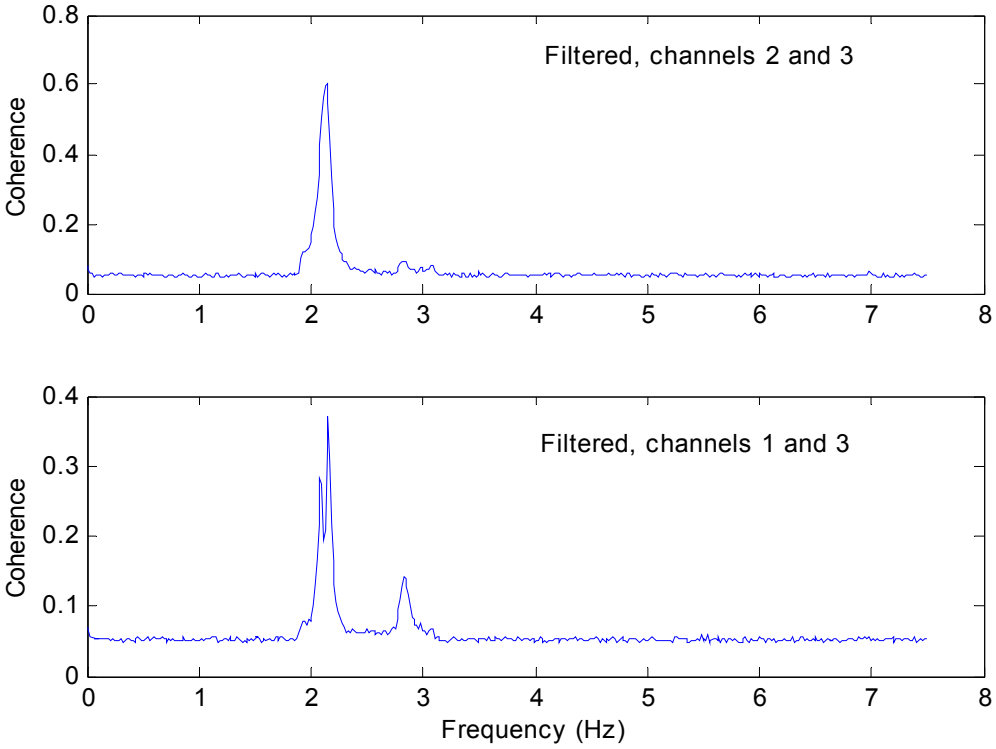

Figure 6.16 Average coherence of 796 filtered acceleration records.

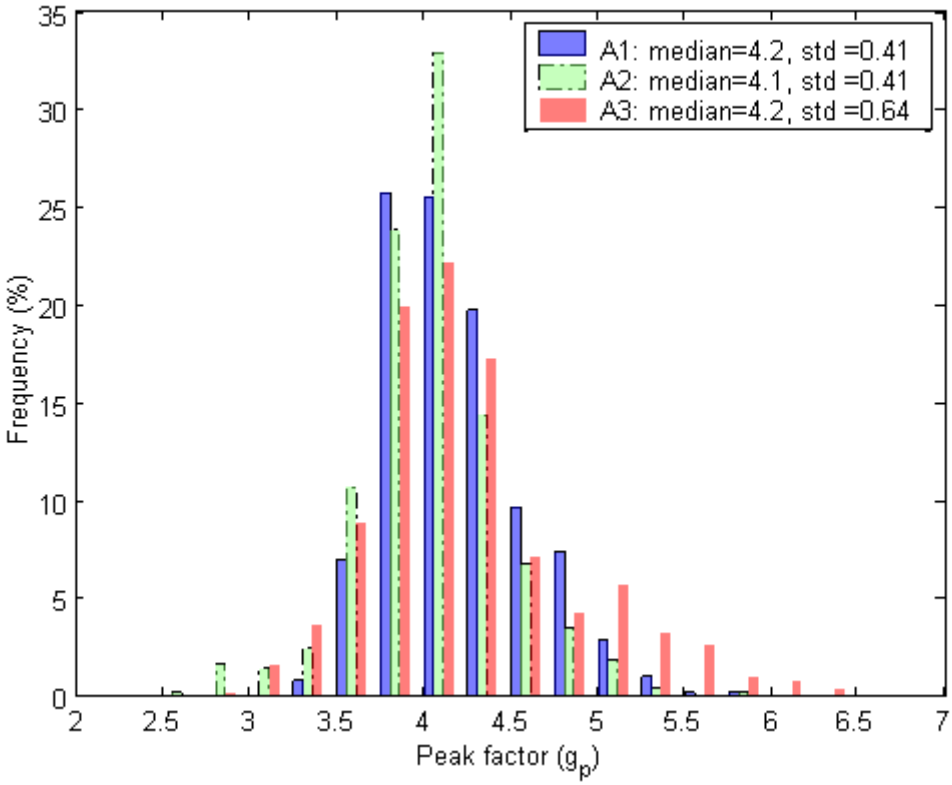

Figure 6.17 Histogram showing the frequency distribution for the peak factor evaluated for filtered data from the three acceleration channels.

It was stated earlier that the acceleration would be described by two parameters, a peak function (see Eq. (6.1)) and standard deviation. The reason for this choice is mainly, that the peak values are generally more affected by the choice of sampling frequency and random environmental noise than the standard deviation. The peak function, as defined herein, is half the difference between maximum and minimum amplitude, normalised with standard deviation and thereby, to some extent, also less affected by the choice of sampling frequency and random environmental noise than the peak values directly. The histogram in Figure 6.17 shows the distribution of the peak function as evaluated for the three acceleration channels. As can be seen, the most common peak factor value for all channels is around 4.

The standard deviation of the recorded acceleration for channels 1 and 2 is shown in Figure 6.18 as a function of the recorded wind velocity and as a function of the "corrected" wind velocity using the correction method put forward in Chapter 5. Comparing the two figures seems to support the relevance of the velocity correction, and thereby the methodology put forward in Chapter 5.

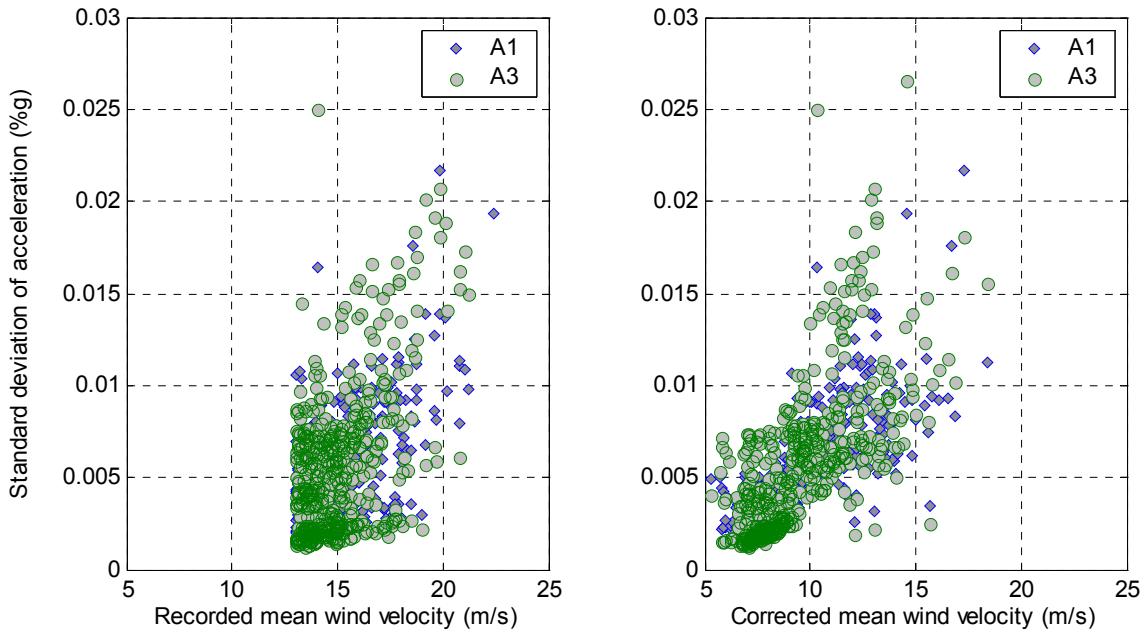

Figure 6.18 Standard deviation of acceleration from channel A1 and A3 as a function of a) recorded mean wind velocity and b) corrected reference mean wind velocity.

Plotting the ratio of standard deviation of acceleration from the perpendicular directed channels A1 and A3 versus mean wind direction reveals an interesting pattern that can be seen in Figure 6.19. It should be noted that 180° and 360° represent the direction along the X- axis. To simplify the picture, each circle on the graph represents an average ratio for each directional degree. The dotted line is a sine-function plotted on the graph to underline the main trend seen in the data. Figure 6.19 demonstrates that the response at A1 is at least 60% larger than the response at A3 when the wind direction is approximately

perpendicular to the east or west face of the building and vice versa when the wind direction is approximately perpendicular to the north or south face of the building. In other words, the along-wind acceleration dominates the across-wind acceleration by at least 60% when the wind direction is perpendicular to the building walls.

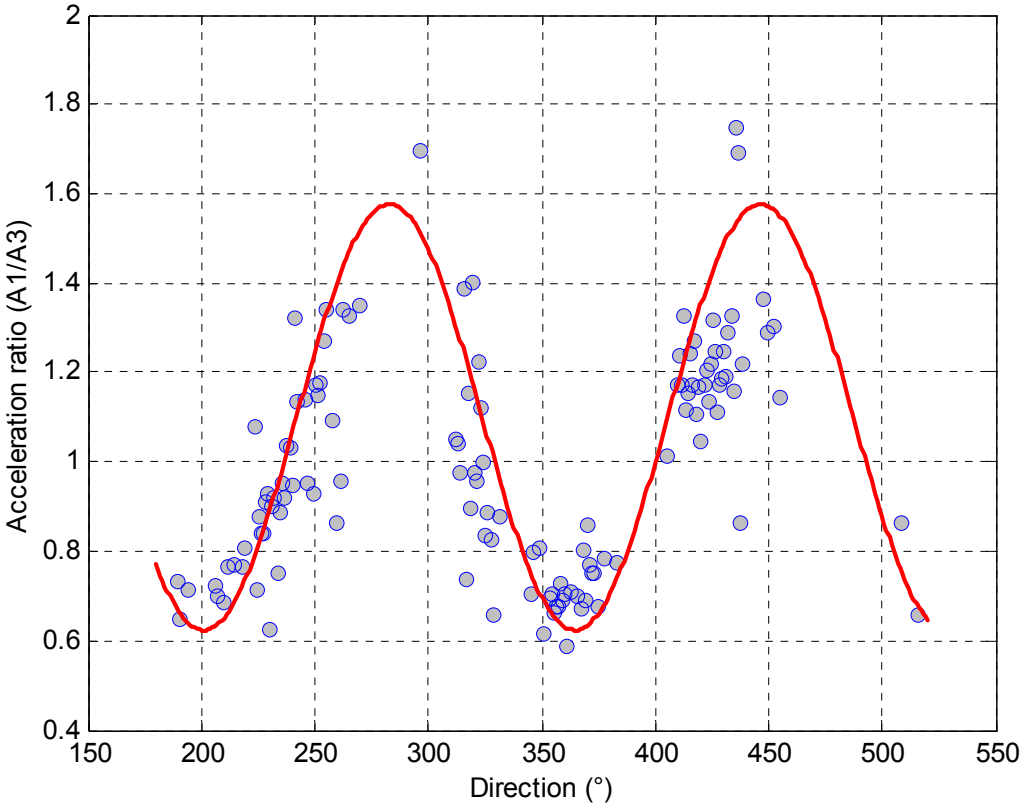

Figure 6.19 Ratio of standard deviation of acceleration from the perpendicular directed channels A1 and A3. 180° and 360° represent the direction along the X- axis. Each circle represents an average ratio for each directional degree. The dotted line is a sine-function underlining the main trend in data.

Various engineering models have been proposed to relate the characteristics of the incident flow and structural response. In fact, the list of prominent people involved in studies of wind-induced response is very long ([25] [237] [206] [243] [63] [38] [191] [52] [58] [91]). Most of the models developed are based on a random or spectral approach, often applying a "strip" assumption to relate the forces on a section of the structure with the flow conditions upstream of the section. It is conventional to distinguish between the along-, cross- and torsional motion and different equations are used to predict the response for each component. For the along-wind response a distinction is also often made between the so-called "background" response representing the quasi-static response caused by gusts below the natural frequency of the structure and "resonant" response controlled by the dynamic characteristics of the building.

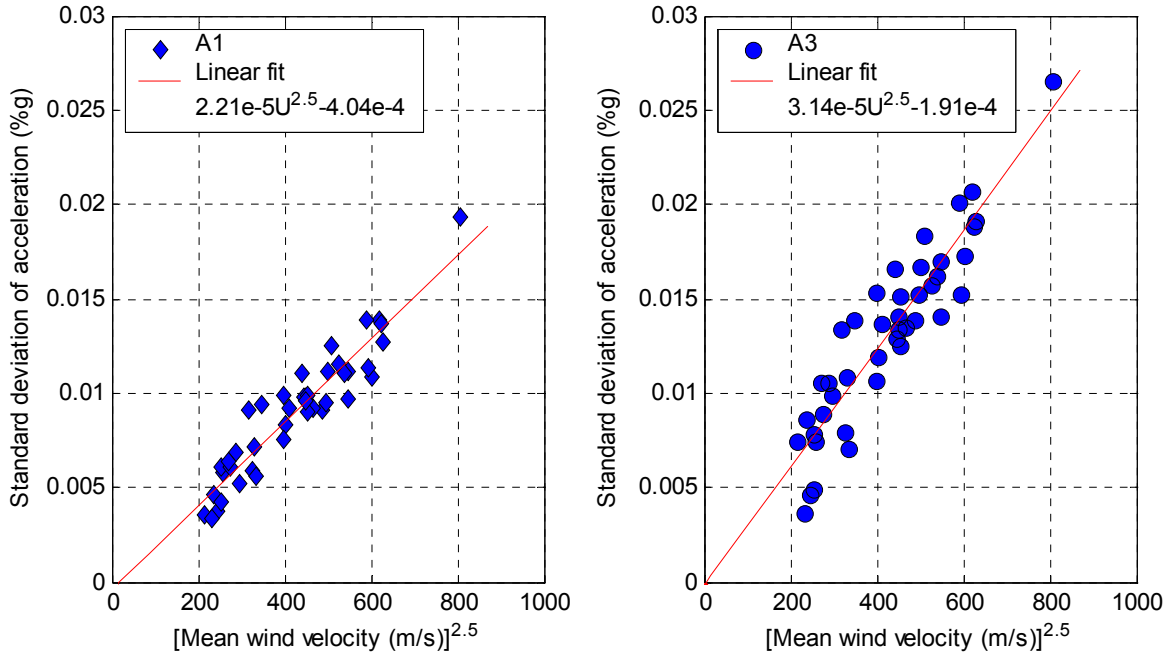

Figure 6.20 Standard deviation of acceleration at channel A1 and A3 for storms with mean wind direction between 350° and 370° as a function of corrected reference mean wind velocity to the power of 2.5. The data points represent recorded data while the solid lines are a linear fit to the data according to the formula given in the legend of each figure.

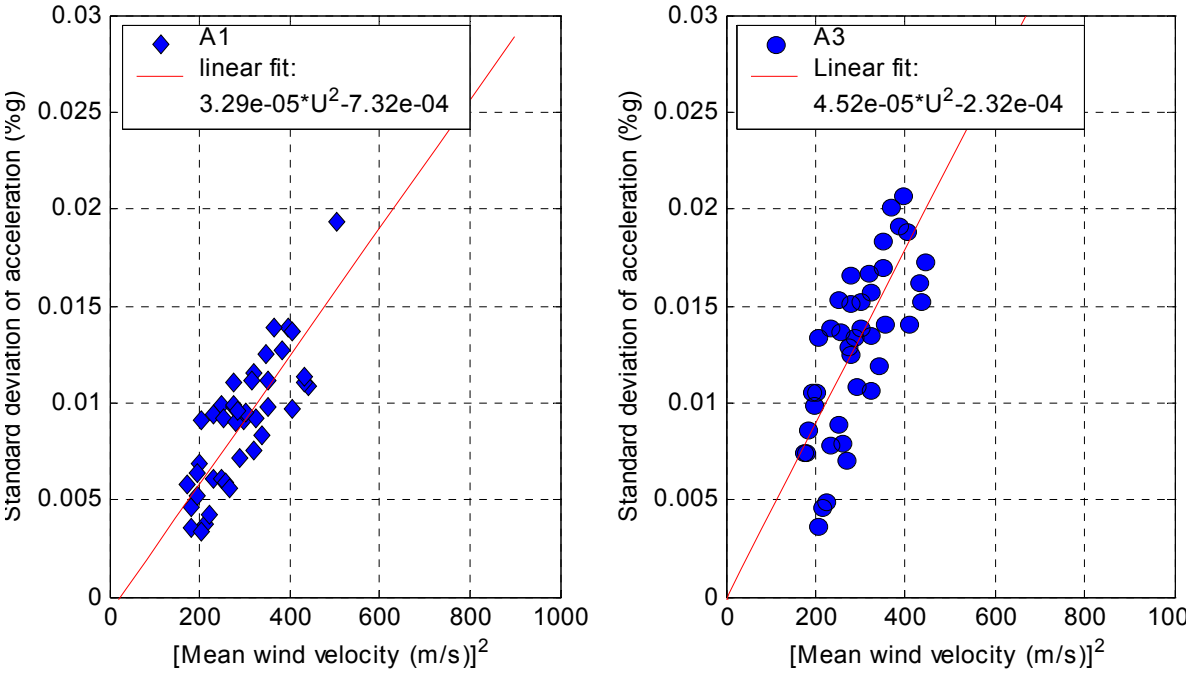

Figure 6.21 Standard deviation of acceleration at channel A1 and A3 for storms with mean wind direction between 350° and 370° as a function of uncorrected reference mean wind velocity to the power of 2. The data points represent recorded data while the solid lines are a linear fit to the data according to the formula given in the legend of each figure.

When the response is dominated by the resonant components it can be demonstrated, in accordance with the studies mentioned above, that the root-mean-square of acceleration at the top of a tall building of given geometry in a stationary (synoptic) wind, is approximated for the along response by:

$$\left(\frac{\sigma_{\ddot{x}}}{4\pi^2 h_b f_1^2}\right) = \frac{A_x}{\sqrt{\zeta_1}}\left(\frac{\rho_a}{\rho_b}\right)\left(\frac{\overline{U}_h}{Bf_1}\right)^{k_x} \tag{6.3}$$

and for the cross-wind response:

$$\left(\frac{\sigma_{\ddot{y}}}{4\pi^2 h_b f_1^2}\right) = \frac{A_y}{\sqrt{\zeta_1}}\left(\frac{\rho_a}{\rho_b}\right)\left(\frac{\overline{U}_h}{Bf_1}\right)^{k_y} \tag{6.4}$$

where, h_b is the building height, A_x, A_y are constants for a particular building shape, ρ_a is the density of air, ρ_b is the average building density, $\overline{U}_h$ is mean wind velocity at roof level of the building, B is the building width, k_x, k_y are exponents, f_1 is the first mode natural frequency and ζ_1 is the critical damping ratio in the first mode of vibration.

The exponent for along-wind response, k_x, is greater than 2, since the spectral density of the wind velocity and the aerodynamic admittance function ([238], [18]) both increase at a greater power than two near the natural frequency. The exponent for cross wind response, k_y, is often around 3 but can be as high as 4. However, in this case the data seems to suggest that a power of 2.5 is the best fit for both along– and across-wind response.

Figure 6.18 does not allow for a sophisticated relation between response and wind velocity, as all such relations depend on wind direction in relation to building geometry and sensor orientation. To explore such relations further it is possible to select a wind direction sector, pick out data recorded for that wind direction sector and plot up the response data versus wind velocity. This has been done for storms with mean wind direction between 350° and 370°. This wind sector was chosen as it represents wind direction approximately perpendicular to the building face and therefore the acceleration recorded during theses storms represents the along- and across wind induced response. The standard deviation of acceleration recorded for this wind sector is plotted in Figure 6.20 as a function of corrected reference mean wind velocity to the power of 2.5. The power of 2.5 was chosen as a good representation through linear fitting of the data using zero acceleration at zero velocity as a bounding condition. The resulting relation is given for each channel in the legend of the respective figures. It should be noted that in this context channel A1 represents the across-wind response and channel A3 the along-wind response.

Although the velocity correction seems justified, the methodology may be questioned. Therefore, it is of interest to explore the same relationship using uncorrected wind velocity. The results are shown Figure 6.21. As can be seen, similar linear relationships are achieved but in this case, the power of the mean wind velocity is 2. In addition, the gradient coefficients are slightly different as the ratio between the gradient coefficients for corrected and uncorrected velocity is approximately the average velocity correction-coefficient.

It is in some ways surprising to find such a clear dependence between acceleration and wind velocity for a building of this type. Although it has been reported, that across wind motion is primarily due to energy available in the high frequency band of the mechanism of vortex shedding [185]. These wind velocity - acceleration relations could be studied further and compared with some of the models presented in the literature ([206] [38]). This will not be done herein, but could be an interesting future task. However, the relation given in Figure 6.20 and Figure 6.21 can be tested against earlier recordings of wind and acceleration at the site. This will be done in the following section.

6.4 Uncoupling the recorded acceleration components

The present acceleration measurements are from the centre core of the building and as has been seen in the previous sections of this chapter the torsional component is not strongly noticeable. However, former acceleration recordings at the same site were taken at the building perimeter in opposite corners. In those records, the torsional component contributed considerably to the total acceleration recorded. It was therefore of interest to decouple the recorded motion in order to evaluate the three fundamental components of motion, i.e. two perpendicular translational components and one rotational. Decoupling the signals is advantageous when comparing records from different locations and it simplifies the system identification process.

The magnitude of the recorded motion, can be expressed in terms of the translation and the rotation providing that the centre of twist is known and assuming that the building floors act as rigid diaphragms in torsion. For a positive motion in the *x*- and *y*-directions and anticlockwise rotation around the *z*-axis, the measured motion can be written as:

$$\begin{aligned} a_{x1}(t) &= a_x(t) - r_{y1}a_\theta(t) \\ a_{x2}(t) &= a_x(t) - r_{y2}a_\theta(t) \\ a_{y1}(t) &= a_y(t) + r_{x1}a_\theta(t) \end{aligned} \tag{6.5}$$

where a_{x1}, a_{x2} and a_{y1} are respectively the instantaneous accelerations obtained by the accelerometers (see [181], [31]), but $a_x(t)$, $a_y(t)$ and $a_\theta(t)$ are respectively the instantaneous uncoupled N-S translational acceleration, instantaneous uncoupled E-W translational acceleration and instantaneous uncoupled rotational acceleration, with r_{x1}, r_{x2}, and r_{y1} being the distances between the four accelerometers and the centre of rotation in a rectangular co-ordinate system.

The rotational component can be evaluated from two accelerometers measuring motion in the same translational direction. Using the two sensors recording N-S motion gives the following relation:

$$a_\theta(t) = \frac{a_{x1}(t) - a_{x2}(t)}{r_{y2} - r_{y1}} = -\frac{a_{x1}(t) - a_{x2}(t)}{y_1 - y_2} \tag{6.6}$$

Similarly, the translational components (x,y) for pure E-W and N-S motion can be expressed by:

$$a_x(t) = a_{x1}(t) + r_{y1}a_\theta(t) = a_{x1}(t) + (y_1 - y_R)a_\theta(t)$$
$$a_y(t) = a_{y1}(t) - r_{x1}a_\theta(t) = a_{y1}(t) - (x_1 - x_R)a_\theta(t) \tag{6.7}$$

where (x_1,y_1) *and* (x_2,y_2) are the co-ordinates of the two sets of accelerometers and (x_R,y_R) is the co-ordinate of the centre of rotation.

If there are two accelerometers measuring motion in two perpendicular directions there will be two equations for each uncoupled motion component. It is possible to combine them linearly and thereby reduce any extraneous independent noise. Another possibility of utilising this extra information to increase the accuracy of correlation and spectral estimates is to evaluate their cross-correlation and cross-spectra.

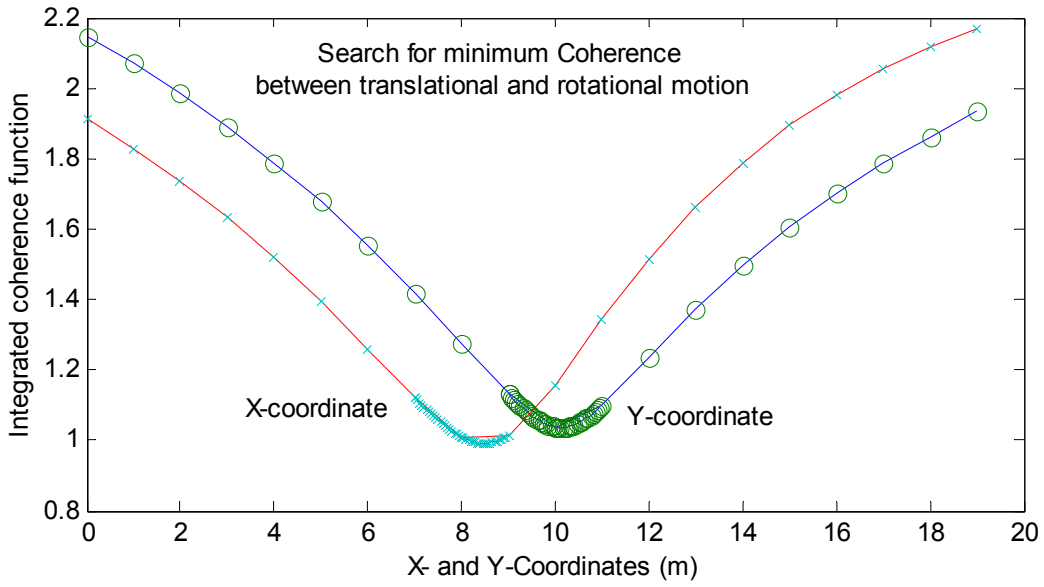

Figure 6.22 Coherence integration as a function of x and y co-ordinates. The minimum indicates the coordinates for centre of rotation.

The centre of rotation can be determined from the acceleration recordings by minimising the coherence between the recorded translational and rotational motion. This is based on the criterion, that the coherence between translational and rotational motion is minimum at the centre of rigidity. The coherence function of a_x and a_θ is for example given as:

$$C_{x\theta}(f) = \frac{|S_{x\theta}(f)|^2}{S_{xx}(f)S_{\theta\theta}(f)} \tag{6.8}$$

where $S_{xx}(f)$, $S_{\theta\theta}(f)$ and $S_{x\theta}(f)$ are respectively the auto spectra and the cross-spectrum of a_x and a_θ, and f is frequency. The auto- and cross-spectrum can be defined as the Fourier transform of the auto- and cross-correlation, $R_{x\theta}(\tau)$, respectively. The coherence function for the a_y and a_θ components can be defined in a similar fashion. As the coherence is a function of frequency, its measure, in the form of an integral of the coherence function over frequency, is minimised. This is done by selecting trial values for (x_R,y_R), thereby

obtaining a_x, a_y and a_θ, calculating the respective coherence functions and integrating over frequency. The co-ordinates that minimise the coherence integral are then taken as the centre of rotation. Figure 6.22 shows the results from the coherence integrals as a function of co-ordinates. It is seen that the centre of rotation is at (x_R,y_R) = (8.5 m, 10.2 m,), measured from the location (Ox_2, Oy_2). That means that an overall centre of operational motion is about 1 m east and 1 m south of the geometric centre.

6.4.1 Comparison of coupled and uncoupled acceleration data

To demonstrate the effect of the uncoupling procedure, it is of interest to compare the signals and the spectral information for coupled and uncoupled data. Figure 6.23 shows typical spectral information for the time series recorded in 1991. As mentioned earlier, various spectral peaks can be seen in the data, especially in log log scale, whereas the linear scale shows that at this location the structural response dominates the noise from the environment. Before decoupling a band pass filter was used to filter out the unidentified noise below 0.2 Hz and above 5 Hz. The phase and coherence relations are similar to the ones already described for the data from 1997 (see Figure 6.24).

An example of an uncoupled acceleration time series is seen in Figure 6.25. It is interesting to note the burst in the angular acceleration. It is uncertain to what extent the angular motion is responsible for similar bursts seen in the data, but it is conceivable that it may play a part in the creation of peak motion of this type. The normalised auto-spectral densities for the three fundamental modes are shown in Figure 6.26. Looking at the spectral densities it can be seen that the decoupling was successful, although slight coupling is still noticeable in the angular acceleration. Looking at the coherence functions shown in Figure 6.27 the two translational components are now clearly incoherent. However, there is coherence between the translational modes and rotation at 2.1 Hz and 2.8 Hz, which is understandable as some coupling is still present in the rotation.

The auto-correlation functions for translational and angular accelerations are shown in Figure 6.28. The auto-correlation functions were calculated directly by convolution in the time domain. The auto-correlation function can give an estimate of fundamental frequencies and structural damping (see Appendix C). Some irregularities can be seen in the auto-correlation functions at $\tau \approx 0$, especially for the rotational component. This is to be expected, as the data is still slightly coupled. In addition there is some baseline noise in the signals, as can be seen at $\tau = 0$, especially for the X component.

Modes of vibration with uncoupled degrees of motion, $a_x(t)$, $a_y(t)$ and $a_\theta(t)$ are due to motions in separate orthogonal modes of vibration and hence should be statistically independent. An example of the statistics describing coupled and uncoupled motion are displayed in Table 6.1.

Table 6.1. Statistics of coupled and uncoupled acceleration records for a mean wind velocity of 17.5 m/s and mean wind direction of 134°.

Coupled motion			Uncoupled motion		
Motion component	Standard deviation	Peak factor g_a	Motion component	Standard deviation	Peak factor g_a
Ox1	0.0377 % g	4.32	X-translation	0.0329 % g	3.99
Ox2	0.0352 % g	4.21	Y-translation	0.0281 % g	5.34
Oy1	0.0343 % g	5.30	Rotation	0.0016 %g/m	5.84
Oy2	0.0335 % g	4.96			

Taking the mean wind velocity of 17.5 m/s and using the relations from section 6.3, one can estimate the standard deviation of motion and compare with the values recorded 1991. This is done in Table 6.2 using both the best-fit equations for corrected and uncorrected reference mean wind velocity. It is clear that the standard deviation values from the equations developed using uncorrected reference mean wind velocity give values that are much to low. The standard deviation values from the equations developed using corrected reference mean wind velocity, are similar to the uncoupled values from 1991, especially for the Y-component. As there is some rotational contribution in the X-component of the 1997 data it is reasonable that the estimate for that component is higher than the uncoupled value although it should not exceed the values recorded at the corners. It should be recalled that the anemometer was located in a 5 m high mast at the edge of the southeast corner of the building and should give reasonable along wind values for the mean wind direction in question, i.e. 134°, which is directly from southeast. This further supports the validity of the correction used for the reference mean wind velocity from the 1997 full-scale experiment.

Table 6.2. Evaluation of standard deviation for along and across response based on the best line fit from Figure 6.20 and Figure 6.21 and a mean wind velocity of 17.5 m/s.

Mean wind velocity used:	Motion component	Equation	Standard deviation (% g)
Uncorrected	Along	4.52e-5 U^2 - 2.32e-4	0.0136
	Across	3.29e-5 U^2 - 7.32e-4	0.0093
Corrected	Along	3.14e-5 $U^{2.5}$ - 1.91e-4	0.0400
	Across	2.21e-5 $U^{2.5}$ - 4.04e-4	0.0279

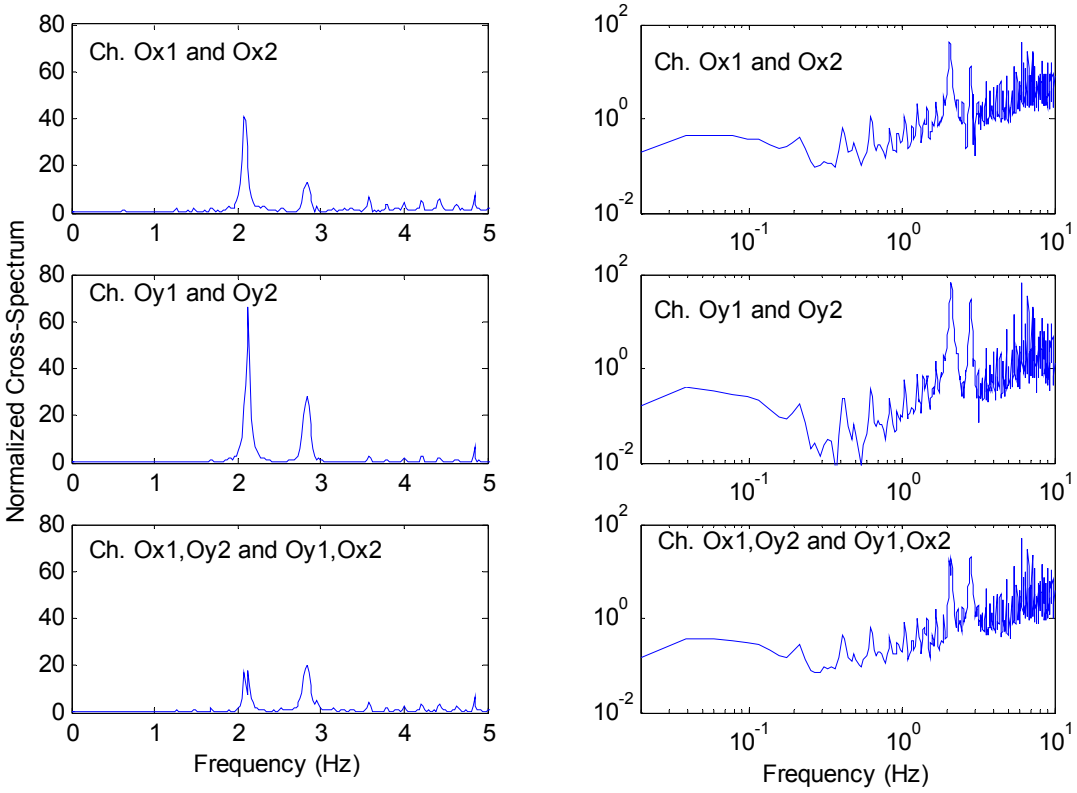

Figure 6.23 Normalised cross-spectral density as a function of frequency for parallel and perpendicular channels from the data recorded in 1991.

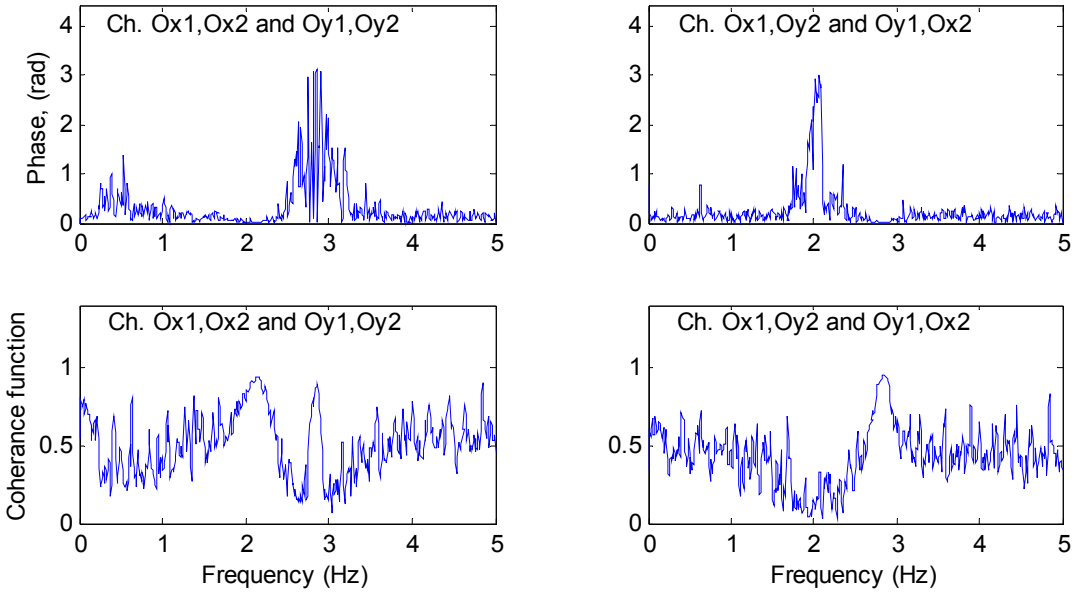

Figure 6.24 Phase and coherence as a function of frequency for parallel and perpendicular channels from the data recorded in 1991.

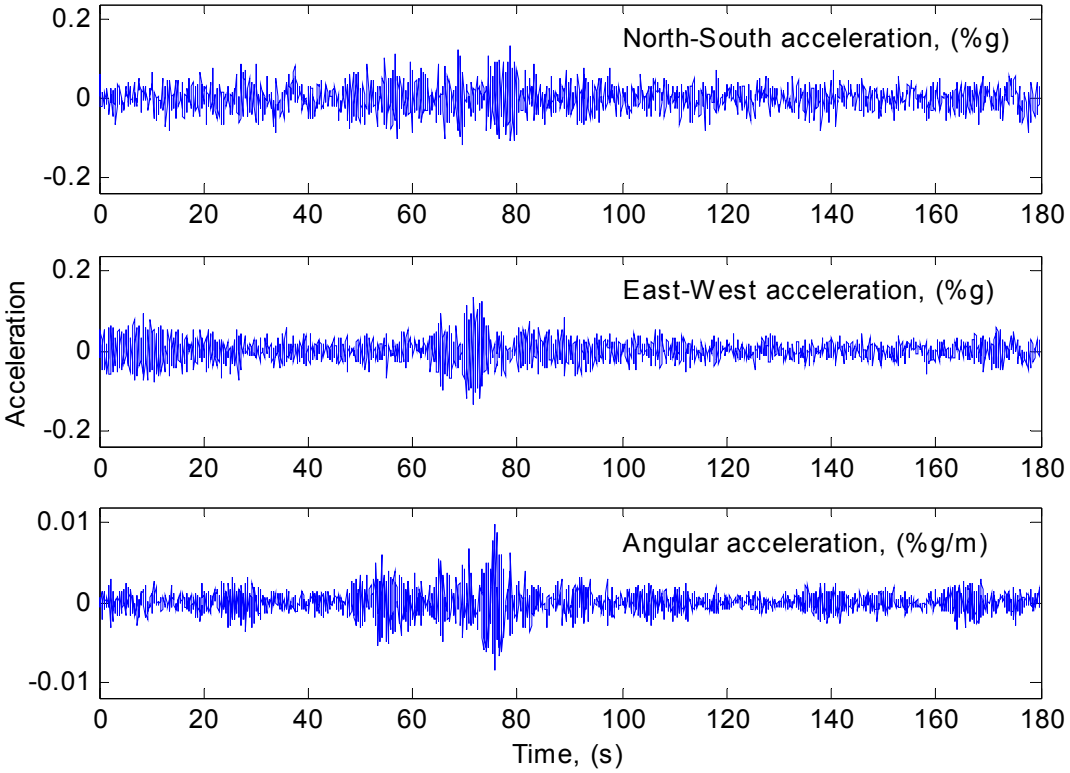

Figure 6.25 Example of uncoupled acceleration.

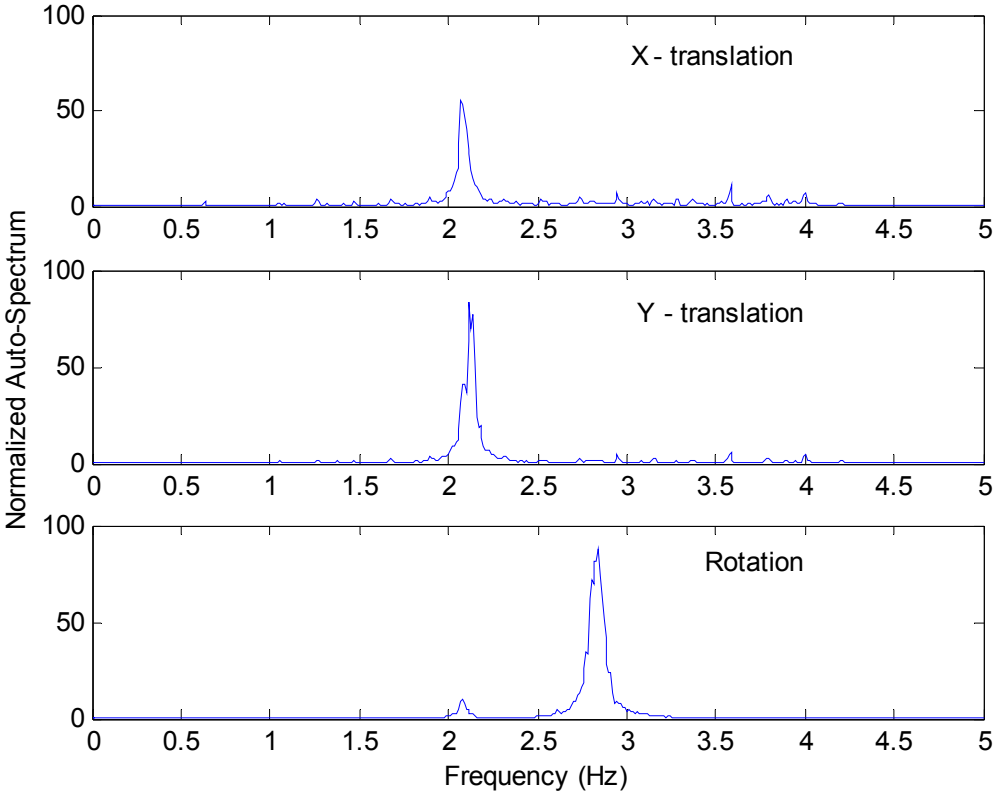

Figure 6.26 Normalised power spectral density of uncoupled acceleration.

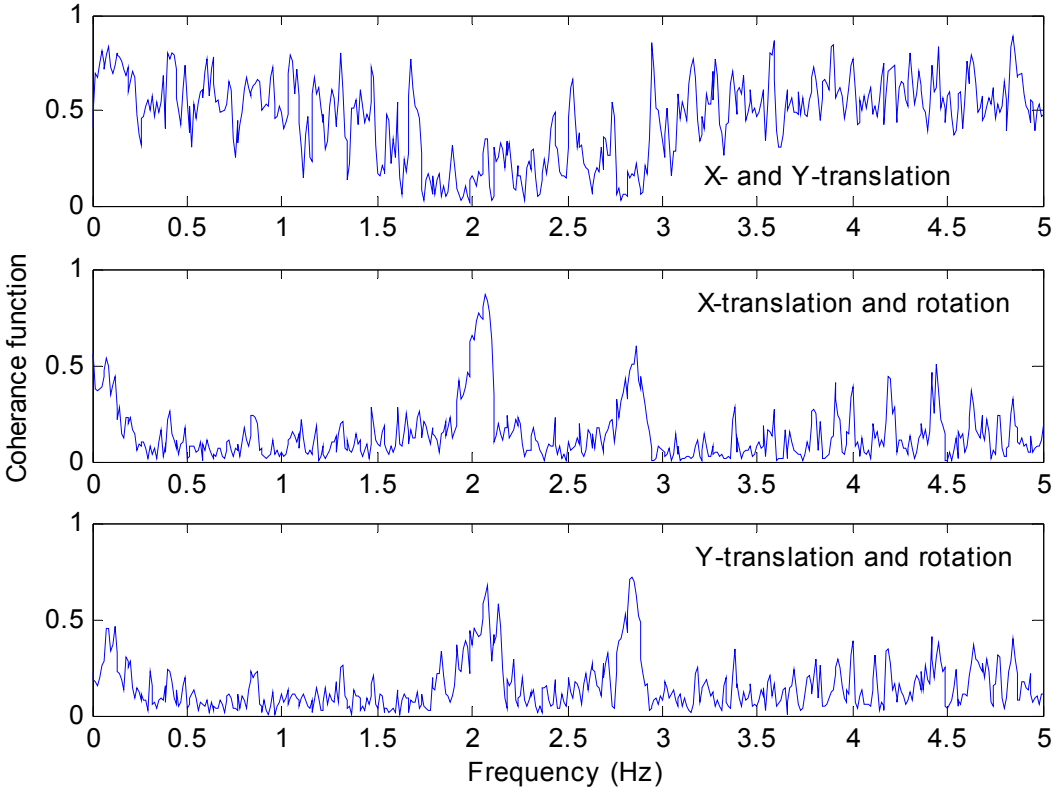

Figure 6.27 Coherence functions of uncoupled acceleration.

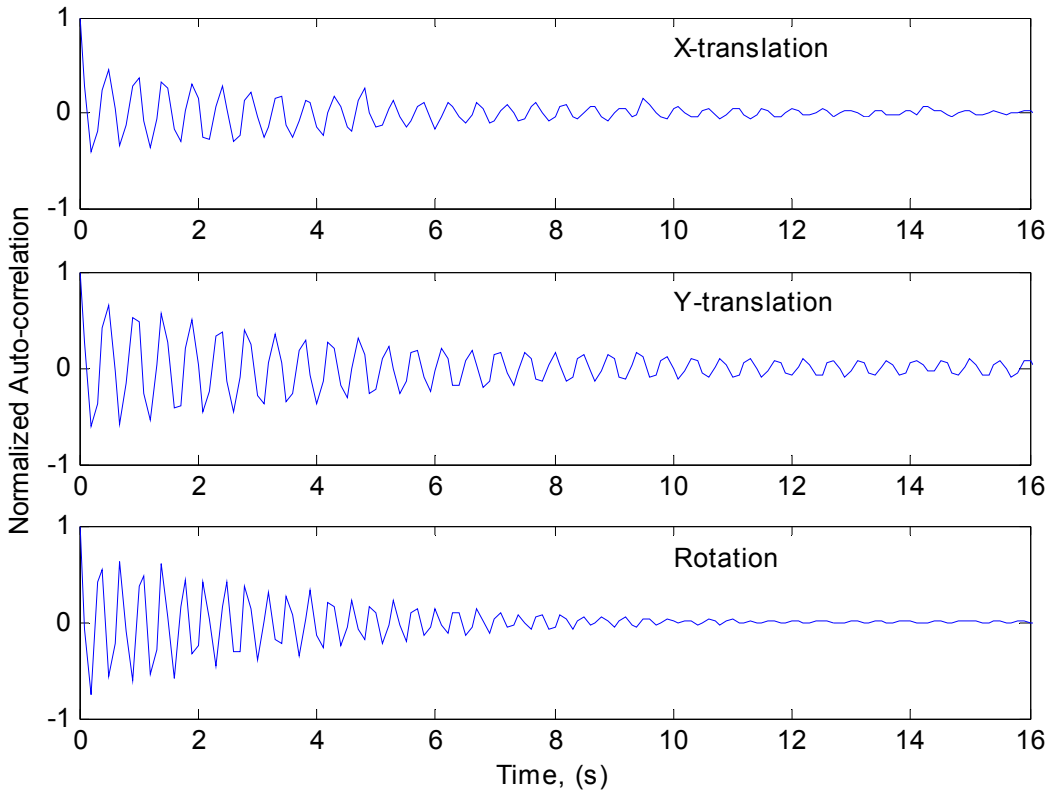

Figure 6.28 Normalised auto-correlation function for uncoupled data.

6.5 System identification using wind induced response

The recorded acceleration data was used for system identification of the building. The aim was to estimate the natural frequencies and critical damping ratios for the three main modes of vibration identified in the spectral analysis. The intention was also to explore the variability in the parameter estimation. For this purpose, parametric methods were applied, but an overview on possible non-parametric methods is given in Appendix A.

A simple damped oscillator with zero-mean white-noise excitation can be represented by the following continuous equation of motion:

$$\ddot{y}(t) + 2\varsigma_j \omega_j \dot{y}(t) + \omega_j^2 y(t) = \frac{1}{m} e(t) \tag{6.9}$$

where $e(t)$ is a white-noise input, $y(t)$ is the response and m, ζ_j, and ω_j denote the oscillators mass, damping ratio and natural circular frequency, respectively.

A corresponding discrete system can be determined by requiring that the output covariance function coincide at all the sampled points with that of the continuous system. This results in the following equation:

$$y_t + \alpha_1 y_{t-1} + \alpha_2 y_{t-2} = \beta_1 x_{t-1} + \beta_2 x_{t-2} \tag{6.10}$$

The coefficients α and β can be calculated in terms of m, ζ_j, ω_j and sampling period, Δt, from the equivalence of the continuous and discrete output covariance functions. They are given as [44]:

$$\begin{aligned}
\alpha_1 &= -2\exp(-\varsigma\omega_j \Delta t)\cos(\omega_j \Delta t\sqrt{1-\varsigma_j^2}) \\
\alpha_2 &= 2\exp(-\varsigma_j \omega_j \Delta t) \\
\beta_1 &= \frac{1}{2}(\sqrt{\delta_0 + 2\delta_1} + \sqrt{\delta_0 + 2\delta_1}) \\
\beta_2 &= \frac{1}{2}(\sqrt{\delta_0 + 2\delta_1} - \sqrt{\delta_0 + 2\delta_1}) \\
\delta_1 &= R_y(1) + \alpha_1 R_y(0) + \alpha_2 R_y(1) \\
\delta_2 &= R_y(0) + \alpha_1 R_y(1) + \alpha_2 R_y(2) + \alpha_1 \delta_1
\end{aligned} \tag{6.11}$$

where $R_y(k)$ denotes the autocorrelation of $y(t)$ for lag k.

Regardless of the approach used for discretisation, the equivalent discrete-time equation for a SISO (single input, single output) system can be written in following form:

$$y_t + a_1 y_{t-1} + ... + a_n y_{t-n_a} = b_1 x_{t-1} + ... + b_n x_{t-n_b} \tag{6.12}$$

Here x_t and y_t are the input and output sequences, respectively; a_j and b_j are the parameters of the system, which are constants for time invariant systems but functions of time for time-varying systems. When data for a physical input process is not available, a sequence of uncorrelated noise is often used as input.

The difference equation given in Eq. (6.12) can be presented in the frequency domain by a transfer function obtained through a *z*-transform. This yields the following transfer function:

$$Y(z) = H(z)X(z) = \frac{B(z)}{A(z)}X(z) = \frac{b_0 + b_1 z^{-1} + \cdots + b_{nb} z^{-nb}}{1 + a_1 z^{-1} + \cdots + a_{na} z^{-na}} X(z) \tag{6.13}$$

Here $X(z)$ and $Y(z)$ are the *z*-transform of the input and output sequence respectively, and $z = \exp(j\omega\Delta t)$, where ω is circular frequency and Δt is the sampling interval. As can be seen the coefficients a_j and b_j are the same in time and frequency domain. If x_n starts from zero, then a_0 equals one. The roots of the numerator polynomial are termed the zeros of the transfer function, whereas the roots of the denominator polynomial are termed the poles of the transfer function. The transfer function can also be expressed in a partial fraction expansion or residue form, as (for $n_a \geq n_b$):

$$H(z) = \frac{q_1}{1 - p_1 z^{-1}} + \frac{q_2}{1 - p_2 z^{-1}} + \cdots + \frac{q_{n_a}}{1 - p_{n_a} z^{-1}} = \sum_{j=1}^{n_a} \frac{q_j}{1 - p_j z^{-1}} \tag{6.14}$$

Here p represents the poles and q is the corresponding residue of *H(z)*. For stable structures, i.e. structures without negative damping, the poles are in complex pairs. If the pairs of terms corresponding to pairs of complex-conjugate roots are combined, then

$$H(z) = \sum_{j=1}^{n_a/2} H_j(z) = \sum_{j=1}^{n_a/2} 2\frac{\mathrm{Re}(q_j) - \mathrm{Re}(q_j \overline{p}_j) z^{-1}}{1 - 2\,\mathrm{Re}(p_j) z^{-1} + |p_j| z^{-2}} \tag{6.15}$$

Each $H_j(z)$ can be considered as a mode of the system. The denominator of H_j, i.e. the poles of the transfer function, then defines the dynamic characteristics of the system, natural frequency and damping. By comparing the denominator of H_j in Eq. (6.15) with Eq. (6.10) and (6.11) we get the following parallel realisation:

$$\begin{aligned} \alpha_1 &= -2\,\mathrm{Re}(p_j) = -2\exp(-\varsigma_j 2\pi f_j \Delta t)\cos(2\pi f_j \Delta t\sqrt{1-\varsigma_j{}^2}) \\ \alpha_2 &= |p_j|^2 = -2\exp(-\varsigma_j 2\pi f_j \Delta t) \end{aligned} \tag{6.16}$$

Solving for ζ_j and f_j gives the damping ratios and natural frequencies (in Hz) of the corresponding mode in terms of pole locations by the following equations [181]:

$$\zeta_j = \frac{\ln\left(\frac{1}{r_j}\right)}{\sqrt{\left[\phi_j^2 + \ln^2\left(\frac{1}{r_j}\right)\right]}} \qquad \text{and} \quad f_j = \frac{1}{2\pi\Delta t}\sqrt{\left[\phi_j^2 + \ln^2\left(\frac{1}{r_j}\right)\right]} \tag{6.17}$$

Here r_j and ϕ_j are the modulus and argument of the *j*-th pole (or its complex conjugate) and Δt is the sampling interval. As mentioned before, the frequencies and damping ratios corresponding to the complex-conjugate pairs are identical. Therefore, n_a-poles result in $n_a/2$ distinct frequencies and damping ratios.

Various parametric representations and modelling techniques are available. The difference equation given in Eq. (6.12) represents a basic ARX model. There are handful of variants of this model known as Output-Error models, ARMAX models, FIR models

and Box-Jenkins models ([125] [126]). These models can be fitted to response series of time invariant systems using standard methods [203]. In an AR-model representation, there is only one b constant, i.e. $b_1 = 1$. The use of the more complicated ARMA-models, allows the modelling of sharp dips as well as sharp peaks with fewer parameters.

State-Space-Models are another common representation of dynamical systems. They describe the same type of linear difference relation as the ARX model but they are rearranged by introducing some extra variables, the *state-variables*, so that only one delay is used in the expressions. The state-space representation can be written as:

$$\begin{aligned} v(t+1) &= Av(t) + Bx(t) + w(t) \\ y(t) &= Cv(t) + Dx(t) + e(t) \end{aligned} \tag{6.18}$$

with input x, output y, state vector v and zero-mean disturbance of stochastic processes e and w. The system identification problem is to find estimates of the system matrices A, B, C, D, from finite sequences of input-output data.

In earlier studies where autoregressive models have been used for system identification by the author, the simple AR-model has proved to be well suited for simulating wind induced acceleration data ([200] [202]). The first step in such parametric modelling is to select the appropriate model order for the system. Various methods for model order selection have been suggested. One of the better known is Akaike's final prediction error criterion, defined as:

$$FPE = \frac{1 + n/N}{1 - n/N} V \tag{6.19}$$

where n is the total number of estimated parameters and N is the number of samples in the data record. V is the loss function (quadratic fit) for the model structure in question. The approach is to investigate how the total estimation error varies with increased model order. Note that the criterion penalises for using too many parameters. Normally the total estimation error decreases with increased model order. However, the decrease is generally sharp at the beginning and then gradually flattens out as the order increases. This is seen in Figure 6.29, where Akaike's final prediction error is plotted versus model order for three single-input-output (SISO) AR-models using the uncoupled acceleration series as output and a white noise input. As can be seen from Figure 6.29, it is not entirely a straightforward matter to choose an appropriate model order on the bases of the FPE-criteria alone. A useful approach in choosing the most suitable model order is to compare the power spectral density functions estimated based on recorded data and an AR-model. This is done in Figure 6.30, which display the estimated spectra based on different model orders for the three components of acceleration. A higher model order generally results in a sharper and narrower spectral peak. As Figure 6.31 shows, a model order of 10 seems to give a fair comparison to the spectra estimated using the N-S component of the 1991 acceleration data, whereas order of 7 and 5 respectively give the best comparison for the E-W and angular components.

An integral part of an identification process is to confirm that the estimated model is a realistic approximation to the actual system, or model validation. The following simple tests can be applied:

- To compare the estimated transfer function (spectrum) with that obtained from a standard Fourier analysis.
- To compare the output time series of the estimated system with the actual output.
- To test if the residual of the model (difference between the model output and the actual output) is a white noise as it should be. This can be achieved by considering auto-covariance and/or Fourier amplitude spectrum.
- To test if there is any correlation between the residuals and the input. If there are, it means that more output/input information can be extracted from the residuals.

Figure 6.32 shows some results from residual analysis plus a comparison of simulated series and the uncoupled data from 1991. It is concluded that the residual of the model is a white noise like process and the AR-model gives a fair approximation of the output.

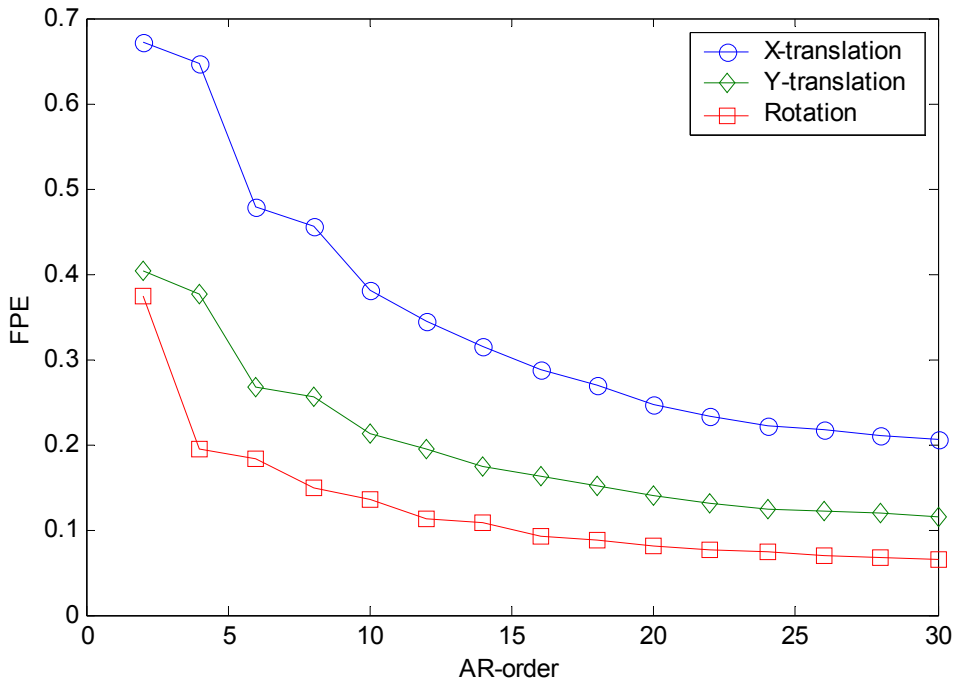

Figure 6.29 Akaike's final prediction error as a function of model order, for three SISO AR-models using uncoupled acceleration series as output and a white noise input.

When using basic auto-regressive models and traditional estimation procedures [126] the model order needed for a reliable estimate of the original sequence is usually higher than the number of contributing natural frequencies of the structure. This has been demonstrated in Figure 6.31. The result of this is that Eq. (6.16) gives number of values that do not represent the actual dynamic characteristics of the structure. Schemes are therefore needed to reduce the number of extra parameters. Writing the transfer function in Eq. (6.15) in both forward and backward fashion, evaluating and comparing two sets of frequency and damping values, can facilitate the exclusion of some of the values unrelated to the dynamic characteristics of the structure, since the natural frequency and damping

values of true modes should be the same in each case. Modes with "excessive" damping can usually also be excluded as the critical damping for common civil engineering structures is generally well below 10% for relevant or identifiable modes of vibration. However, verification of the dynamics of the structure and engineering judgement is always an integral part in ensuring a proper identification of the actual system parameters.

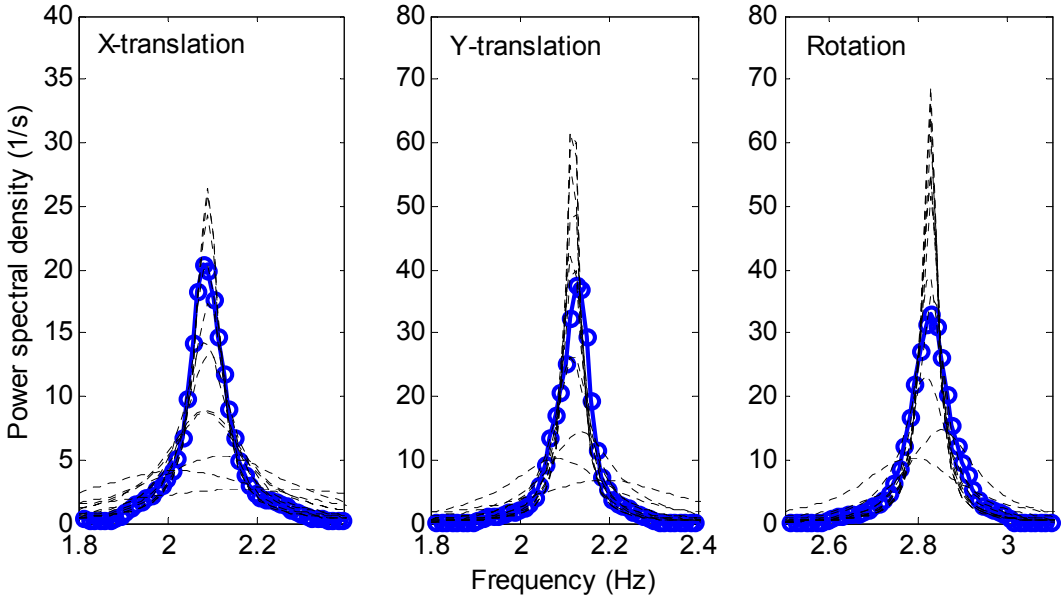

Figure 6.30 Power spectral density for normalised acceleration components estimated using AR-models of order from 2 to 20 (the dotted lines) and recorded data (solid line and o-marker).

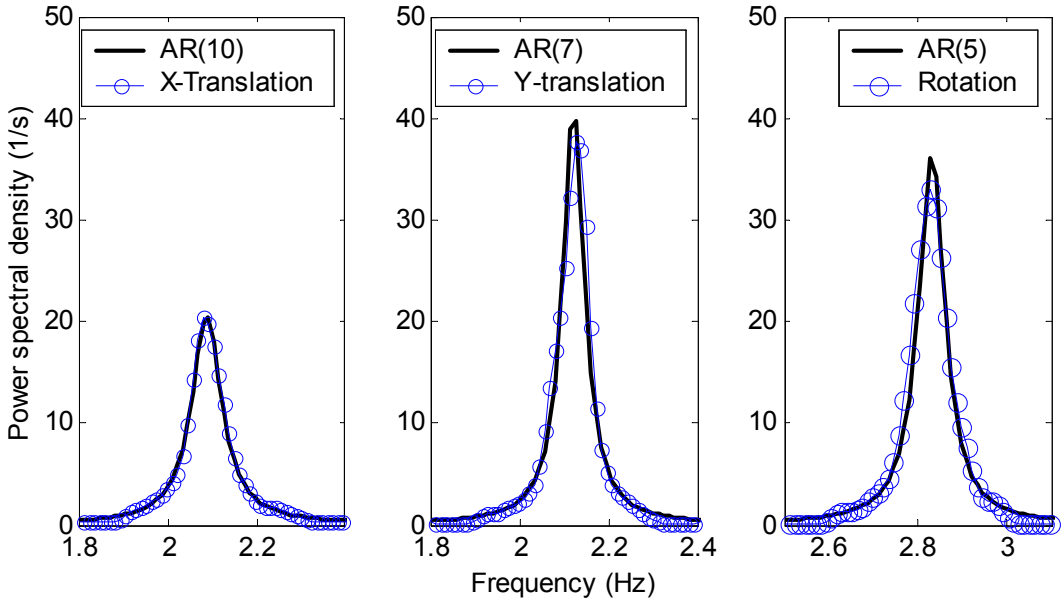

Figure 6.31 Power spectral density for normalised acceleration components estimated using recorded data (thin line and o-marker) and the AR-models giving the "best" spectral fit (solid line).

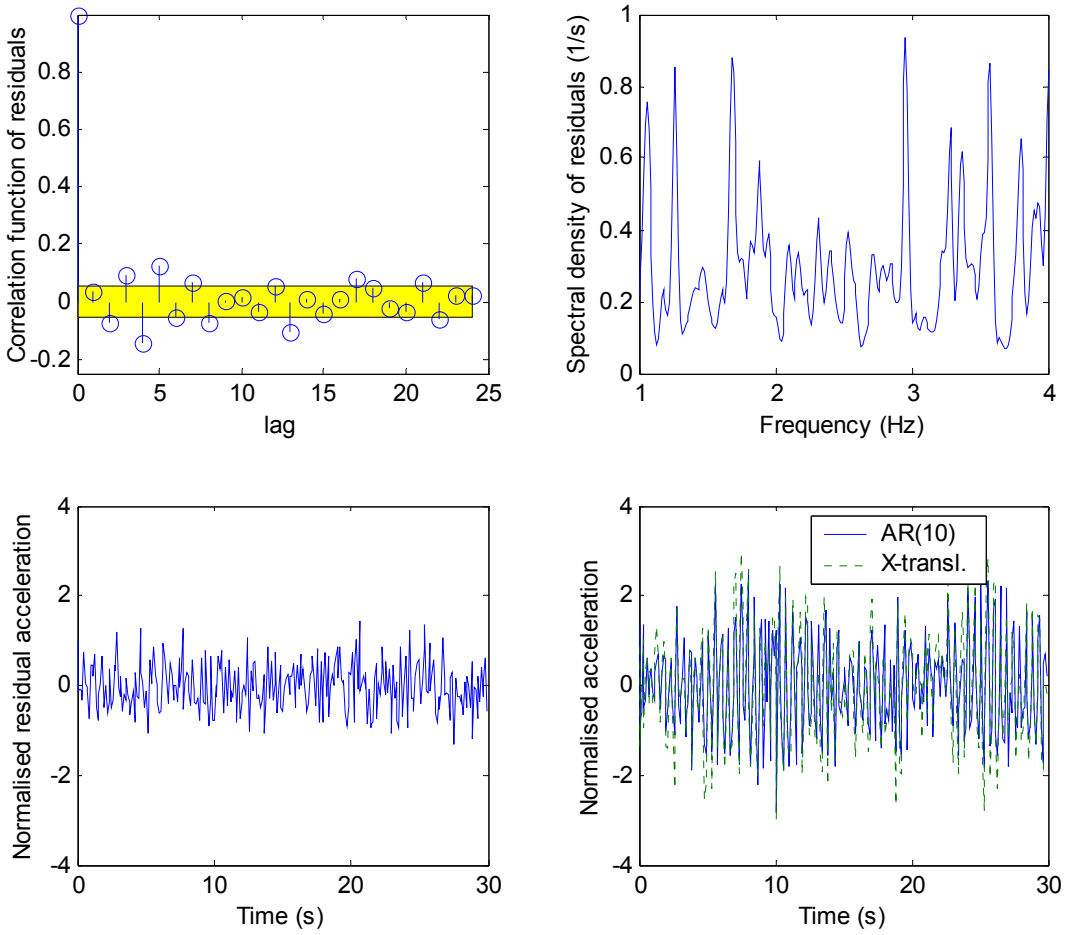

Figure 6.32 Model validation through residual analysis of simulated acceleration. Top: Correlation function and auto-spectral density. Bottom: Time series of residuals and comparison between simulated and recorded time series.

In order to avoid the complications described, a different approach was taken for system identification using the data from 1997. As the amount of data is considerable, the analysis procedure needed to be as automatic as possible. Therefore, it was decided to use a state-space model identification (SMI) toolbox developed at Delft University of Technology [56]. The approach of the SMI toolbox rationalises the large number of linear time invariant (LTI) identification problems of the prediction error method (PEM) into three basic identification problems: The output-error model, innovation model, and Wiener model. After proper pre-processing, the SMI toolbox only requires the two parameters for an output-error model identification problem. That is the upper bound on the expected order of the system and the true order of the system to be extracted from the data.

To simplify the modelling procedure it was decided to use a SISO model, as the single-input-multi-output (SIMO) model is considerably more difficult to achieve, although perhaps more appropriate as three response (output) series are recorded simultaneously. It was also decided to model only one mode at a time, i.e. equivalent

SDOF system of which the true order is 2. Therefore, a sharp band-pass FIR-filter was applied to each time series filtering out data representing the three pre-identified modes of vibration. To imitate a more realistic SDOF response some Gaussian noise was added to the time series. The variance of the Gaussian noise was determined based on the underlying power spectral noise of each time series using a constant spectral density assumption. A second sequence of Gaussian noise of the same variance was used as input. The model order identified in Figure 6.31 can be used as an upper bound on the expected system order. As the true order of each sub-system (mode of vibration) is 2, the identification approach delivers only one set of a natural frequency and damping ratio. This reduces the post-processing of the identification process.

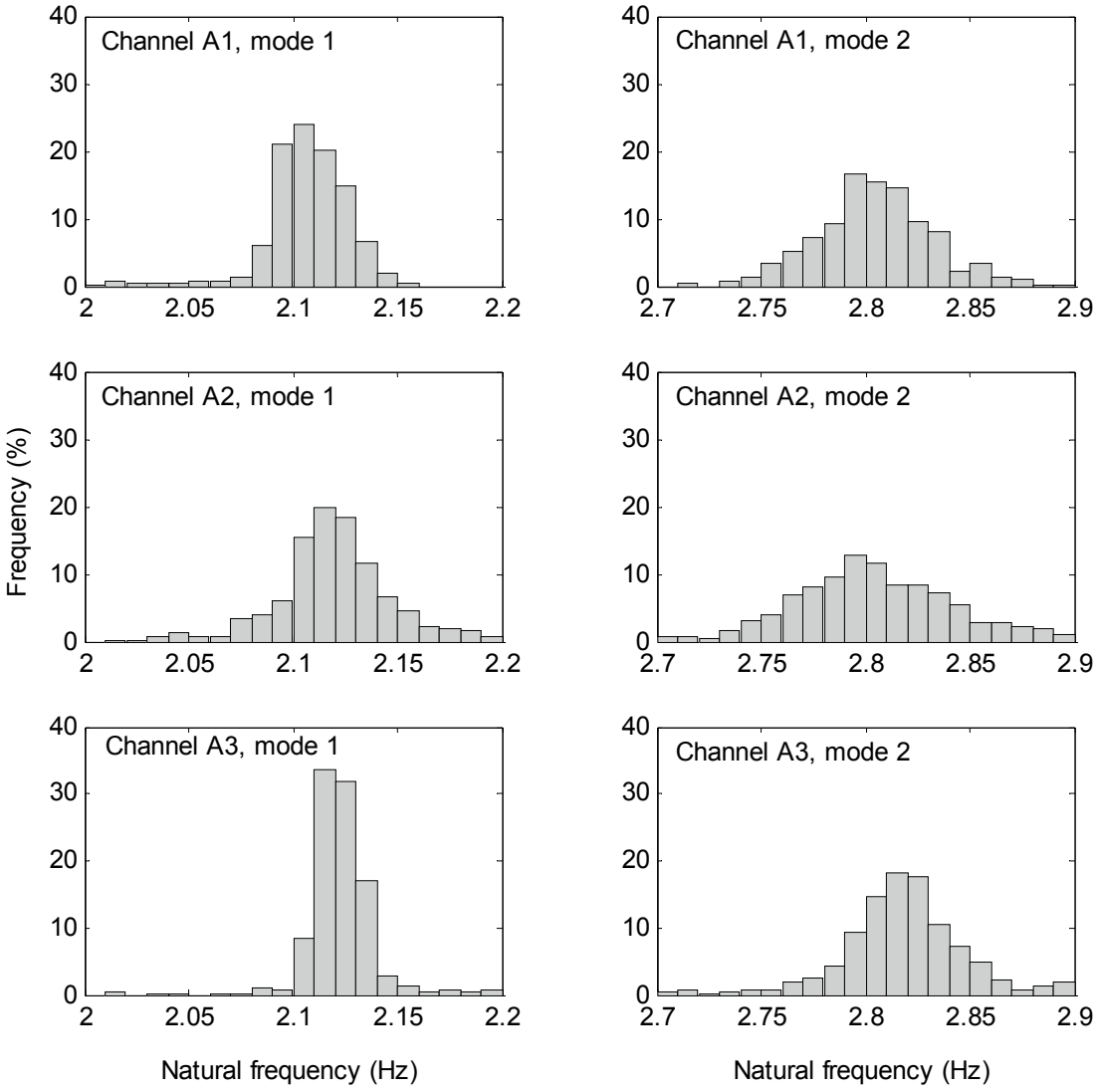

Figure 6.33 Histograms of evaluated natural frequencies from channels A1, A2 and A3. Mode 1 represents translational mode of vibration in the respective direction whereas mode 2 represents a common rotational mode of vibration.

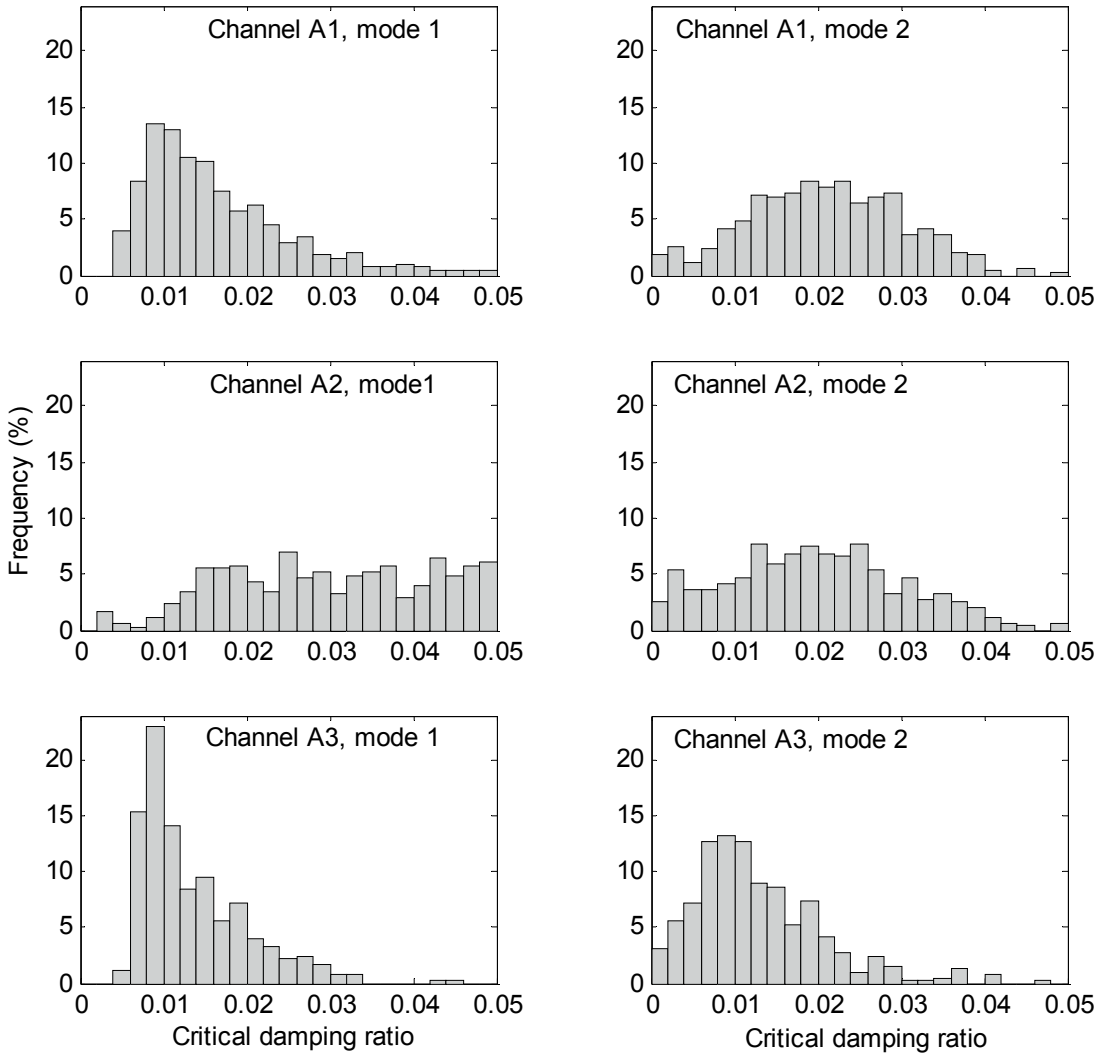

Figure 6.34 Histograms of evaluated critical damping ratios from channels A1, A2 and A3. Mode 1 represents translational mode of vibration in the respective direction whereas mode 2 represents a common rotational mode of vibration.

The outlined procedure was applied to the acceleration data at hand. The results can be seen in Figure 6.33 through Figure 6.35 and Table 6.3 through Table 6.5. Figure 6.33 shows histograms for estimates of natural frequencies from channels A1, A2 and A3. Figure 6.34 shows corresponding histograms for estimates of critical damping ratio. The histograms are not expected to follow a particular distribution. Their purpose is primarily to give an indication of the variability in the estimates from each channel. As can be seen the estimates from channel A2 seem rather unreliable, especially for damping, in spite of considerable sorting and selecting of the data. It is noticeable that the variation in the damping estimates is considerably greater than for the frequency estimates. This is a common finding in system identification of civil engineering structures. In a statistical sensitivity analysis of modal parameters to measurement noise [154], Peterson et. al. observed, that the absolute error in the modal damping ratio is approximately the relative

error in the modal frequency. This implies that an identified model can have significant error in the damping ratio, even when the natural frequency is well resolved.

Also of interest, is that the frequency estimates are centred at a specific number whereas the damping estimates, especially for the translational modes, have distributions that are skewed towards lower values. Comparing damping and natural frequency in this way is perhaps unreasonable as damping, which reflects the capacity of a structure to dissipate the kinetic energy of vibration, does not relate to unique physical phenomenon unlike the mass and the stiffness characteristics of a structural system.

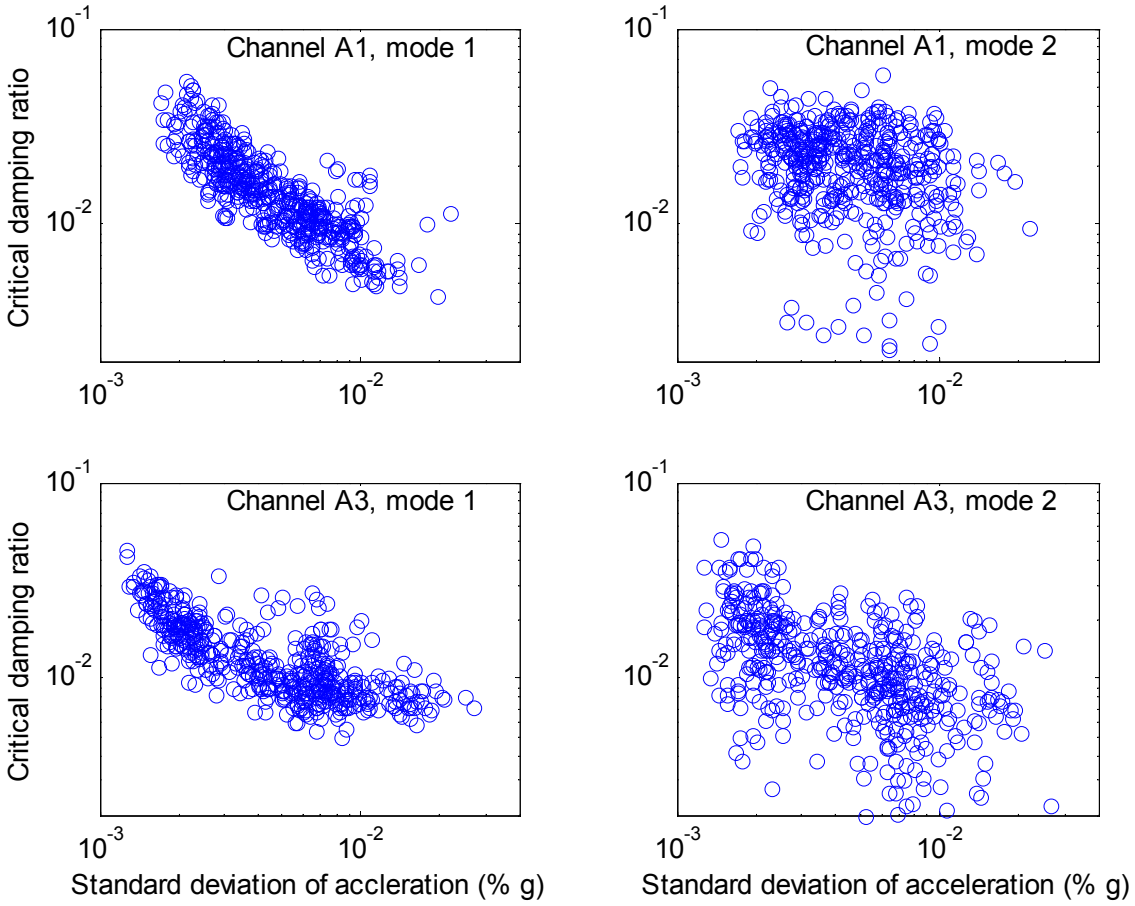

Figure 6.35 Estimated critical damping ratio as a function of standard deviation of recorded acceleration at channels A1 and A3. Mode 1 represents translational mode of vibration in the respective direction whereas mode 2 represents a common rotational mode of vibration.

In Figure 6.35 the damping estimates are studied from a different angle, as the damping estimates are plotted versus standard deviation of acceleration. The plots show a clear trend of reduced damping with increased standard deviation of vibration. It is tempting to interpret this trend as an indication of a simple friction-type damping mechanism. It would be a reasonable assumption for a reinforced concrete building of this type that would concur with Wyatt's [244] proposal that friction could be assumed as the cause of significant energy losses. However, the trend is not entirely true to the summation effect of many statistical stiction/friction mechanisms throughout a complex structure a la Wyatt. Also, the trend in Figure 6.35 contradicts in a way the findings of Jeary ([82] [82])

which has investigated the mechanism for the amplitude-dependent damping for tall buildings and has suggested that damping is constant at low amplitudes, increases with amplitude for intermediate amplitudes and then levels of to a constant value for high amplitudes. The building in this case is not tall, and that may affect the damping characteristics. However, it is this author's opinion, that in this case it is probably, primarily, lack of resolution in the low amplitude data that results in higher damping estimates, i.e. overestimation of damping. In other words, errors, noise etc. produces artificial damping. This fact may reflect to some extent on the older damping value estimates for civil engineering structures (see [57]), which are in many instances, in the opinion of this author, excessively high. Improved measurement and data analysis techniques have resulted, generally speaking, in reduced and hopefully more reliable estimates of critical damping ratios for buildings. Figure 6.35 may therefore demonstrate that as the amplitude increases, the errors are less significant and the damping estimate goes down. It should also be noted that for Channel A3 the damping estimates are seen to level off for standard deviation above 0.005% g. Further statistics of the system parameters will therefore be done only for records that have standard deviation above 0.005% g.

Table 6.3 and Table 6.4 summarise the basic statistics of the analysis using only acceleration records that have standard deviation above 0.005% g. It should be noted that the choice of showing 3 significant digits is not to be interpreted as indicative of the accuracy of the estimates, but rather to stress the uniqueness of each value. Different averages are evaluated, i.e. the median, the mean and the geometric mean, in order to see how that effects the result. As expected the choice of average value is not relevant for the natural frequency estimates, but it does matter for the damping.

The frequency estimates for all channels are in fair agreement. There is a slight difference in the second digit for the average values of the rotational mode (mode 2 of each channel), whereas there is an agreement up to the third digit for the *x*-translational mode of channel A2 and A3. For the damping on the other hand, the differences are much greater. The rotational mode is not very prominent in the data except in the data from channel A3. Therefore, the damping values for the rotational mode are severely overestimated using the data from channel A1 and A2. Similarly, the damping values for the translational mode are overestimated using the data from channel A2. The damping for *x*-translation seems to be around 1% for X-translation, 0.9% for Y-translation and about 0.8% for the rotation. The standard deviation is however high, or about 0.4% for translation and about 0.5% for rotation. The corresponding natural frequencies are 2.10 Hz, 2.12 Hz and 2.82 Hz with a standard deviation below 0.05 Hz.

It is of interest to compare these values with estimates based on the data recorded 1991, which are listed in Table 6.5. What is most noticeable is that the natural frequencies for the translational modes are lower and the damping values are higher than the estimates given in Table 6.3 and Table 6.4. The wind velocity and acceleration amplitudes during the storm in 1991 were greater than the average wind velocity and acceleration amplitudes for the 1997 data. It is therefore likely that the difference seen can be related to the fact that natural frequency estimates for reinforced concrete structures tend to decrease with increased amplitude of vibration, while the damping ratio increases. Figure 6.36

demonstrates this trend with respect to the natural frequency estimates based on records associated with mean wind direction between 350° and 370°. The data does not warrant a corresponding figure for damping.

Table 6.3 Statistics for estimated natural frequencies.

Statistic	Number for channel and mode of vibration					
	A1-mode1 (Hz)	A1-mode 2 (Hz)	A2-mode1 (Hz)	A2-mode 2 (Hz)	A3-mode1 (Hz)	A3-mode 2 (Hz)
median	2.102	2.803	2.117	2.806	2.118	2.819
mean	2.103	2.803	2.124	2.808	2.120	2.819
geometric mean	2.103	2.803	2.123	2.807	2.120	2.818
standard deviation	0.012	0.027	0.044	0.058	0.030	0.051
maximum	2.146	2.879	2.306	2.964	2.266	2.954
minimum	2.057	2.716	1.973	2.659	1.985	2.659

Table 6.4 Statistics for estimated critical damping ratios.

Statistic	Number for channel and mode of vibration					
	A1-mode 1 (%)	A1-mode 2 (%)	A2-mode 1 (%)	A2-mode 2 (%)	A3-mode 1 (%)	A3-mode 2 (%)
median	1.001	1.890	2.583	1.918	0.875	0.817
mean	1.069	1.947	2.769	1.910	0.981	0.905
geometric mean	1.007	1.602	2.522	1.470	0.934	0.740
standard deviation	0.381	0.985	1.198	1.145	0.353	0.515
maximum	2.683	5.817	7.181	6.058	2.731	2.609
minimum	0.428	0.023	0.777	0.068	0.503	0.016

Table 6.5 Average values for natural frequencies and critical damping ratios estimated from data recorded 1991.

Data set	Natural Frequency (Hz) Mode of vibration			Critical damping ratio (%) Mode of vibration		
	X-transl.	Y-transl.	Rotation	X-transl.	Y-transl.	Rotation
Coupled	2.0847	2.1167	2.8276	1.819	1.373	1.201
Uncoupled	2.0838	2.1168	2.8278	1.693	1.148	0.715
Average	2.084	2.117	2.828	1.756	1.261	0.958

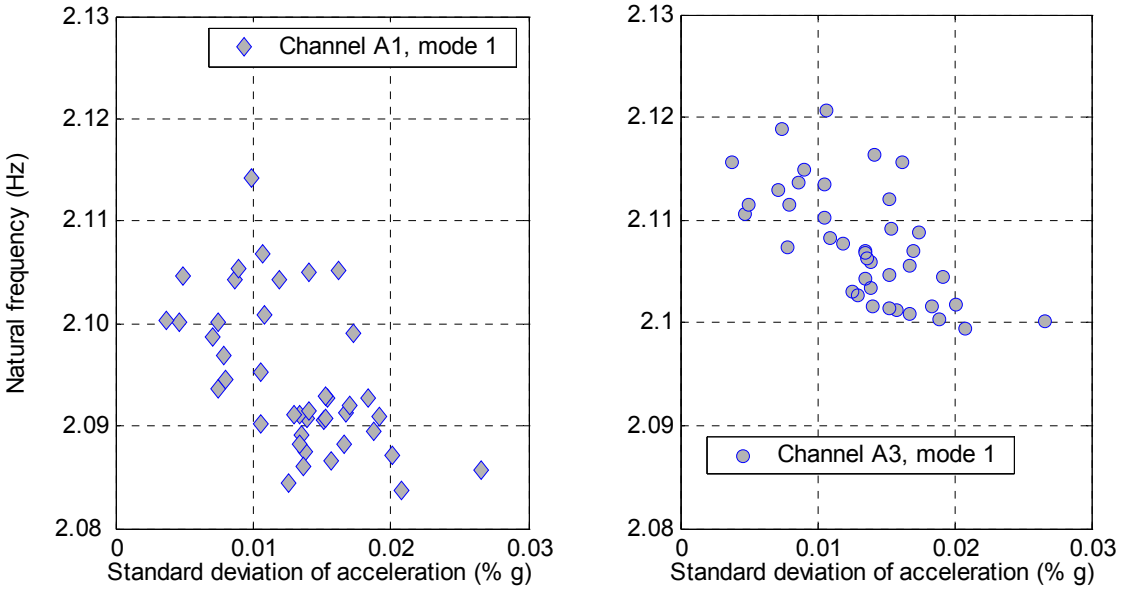

Figure 6.36 Estimated natural frequency as a function of standard deviation of recorded acceleration at channels A1 and A3. Mode 1 represents translational mode of vibration in the respective directions of each channel.

6.6 Summary and discussion

Recorded wind-induced acceleration response of a building has been studied. The data from the full-scale testing period in 1997 is noisy and of low intensity, whereas data from a single storm in 1991 is of higher intensity and better quality. Considerable effort went into establishing the sources of noise, quality checking the data and filtering out the frequency range representing the relevant building resonances. It was found after filtering, that the wind-induced acceleration of the building might be interpreted as a narrow-band process, identifiable by temporal sequences of acceleration bursts of 5 to 10 s duration.

Natural frequencies and damping ratios of the structure have been identified. Traditional Fourier analysis as well as parametric system identification methods has been applied for that purpose. It is the opinion of the author, that the identified values for natural frequency and damping are reliable, in spite of the varied quality of the data. It should be noted that the displacements of the building are small and therefore it is unlikely that aerodynamic damping contributes to the damping.

As the amount of sampled acceleration data is considerable and the data is recorded for various excitation levels, it is possible to investigate various relations that a single storm data could not resolve. The analysis has revealed a dependence between: Vibration amplitude and wind velocity and direction; vibration amplitude and damping estimates; and vibration amplitude and natural frequency. These relations should be studied further.

The along-wind acceleration dominates the across-wind acceleration by at least 60% when the wind direction is perpendicular to the building walls. In addition, the ratio of perpendicular components of acceleration is found to follow an almost sine-like curve

depending on the mean wind direction. The acceleration components are equal for an azimuth of about 45°.

It is observed that that natural frequency estimates tend to decrease with increased amplitude of vibration, which is a common observation for reinforced concrete structures [202].

It is hypothesised by the author that lack of resolution in the low amplitude data results in higher damping estimates for the lower amplitudes, i.e. errors, noise etc. produces artificial damping which results in overestimation of damping.

Based on the experience gained, a state-space model could be developed for the building to be used in further analysis of response and excitation. It would be of interest to link the model parameters with the basic dynamic parameters of the building such as modal stiffness, mass and damping. That would increase the value of the model for a more general application and give additional insight into the modelling process. By including a relation similar to the one seen between basic wind parameters and vibration amplitude should make it possible to predict with some accuracy the response level for a specific wind velocity.

Comparing data recorded within the shear core of the building and data recorded at the building perimeter has underlined the importance of rotational motion in the overall response of buildings, especially of the form presented here. Acceleration at the building perimeter is clearly magnified by the angular motion. This may combine with visual cues to push the vibration into the perception range and add to the occupants' awareness or discomfort. It is therefore important at design stage to pay attention to rotational effects in the structural behaviour.

Chapter 7 Conclusions and further research

7.1 Concluding remarks

A research project, combining a full-scale and a model-scale investigation into wind loading of a medium rise office building has been presented. The objective of the study was to provide a sound wind loading chain a la Davenport [29] in the form of data that would facilitate the study of the links connecting the main parameters i.e. Wind – Pressure – Response.

Information on the study-building and the experimental setup and procedures has been given, for both full-scale and model scale. The full-scale and model scale data have been systematically compared through the evaluation of descriptive parameters of both wind turbulence and surface pressures. In general, the evaluated full-scale parameters are in qualitatively good agreement with the model scale parameters, confirming a successful wind tunnel simulation and full-scale investigation.

However, the analyses have revealed some characteristic differences between full-scale and model scale behaviour. These differences are largely related to the fact that significant variability is found to be inherent in the full-scale data. Considerably less variability seems to be associated with the wind tunnel data. It appears that the randomness in nature has more dimensions than the wind tunnel can simulate effectively. For example in neutral wind conditions the standard deviation of wind direction can be 10°. This fact can have implications for the applicability and use of wind tunnel results. For instance frequency sensitive behaviour that depends on stable flow conditions may be overestimated in the wind tunnel, as the flow pattern is unlikely to be as stable in full-scale as in the wind tunnel.

7.1.1 The wind environment

The full- and model scale wind characteristics were introduced and investigated along with some information on the wind climate in Reykjavik.

In general, the evaluated full-scale wind parameters are in qualitatively good agreement with the model scale parameters, which is indicative of a successful wind tunnel simulation.

It is found that the recorded turbulence level at the building site is comparable to the turbulence level at the Icelandic Meteorological Office. However, the evaluated profile parameters differ in the sense that the average estimates as well as the variability in the values based on data from the IMO-site is considerably greater than for data from the study-building. This can be related to more seasonal variability in the IMO data as well as different evaluation methodology and difference in reference height.

The surface roughness characteristics at the IMO site were found to be approximately representative of terrain category II as defined in the ENV1991-1-4, both in terms of turbulence parameters and mean wind profile parameters. This was a smoother terrain category than expected based on illustrative definitions of terrain categories. This may be related to the relatively short distances from the sites either to a smooth rural terrain or to the sea. In addition, the fact that Reykjavik is rather sparsely built may result in a terrain that is not very homogeneous, which can increase the required length of fetch for a stable mean wind profile. Therefore, the wind profile may be in a transition state between the smooth terrain (sea or rural) and the rougher urban terrain.

Neutral atmospheric stability conditions were found to exist for about 58% of the full-scale testing period. However, mean wind velocities above 10 m/s were frequently recorded during the 38% of the time when the atmospheric conditions were defined as slightly, moderately or highly unstable.

The spectral characteristics were similar for full-scale and model scale. That can be explained by the relatively low full-scale time and length scales, which were comparable to the equivalent scales in the wind tunnel. The normalised spectral density was found to follow the ESDU spectral expression reasonably well.

7.1.2 The surface pressure

The full-scale and model scale pressure data have been systematically compared through the evaluation of descriptive parameters of surface pressure. The comparison is found, generally speaking, to be satisfactory.

Spectral- and coherence analysis of surface pressures were performed and the results from full- and model scale data were compared. The comparison is found, on the whole, to be satisfactory. However, the spectral analyses reveal some characteristic differences in the spectral behaviour.

The data reduction was complicated by the fact that the reference wind data from the full-scale measurements was found to be distorted by the flow conditions created by the building. Thermal effects were found to have strong influence on the reference data,

especially during periods of low atmospheric temperatures. It is probable that at least partly these thermal flow effects originate from the heat radiated from the building and/or convection from the outlet of the ventilation system. A correction methodology for mean pressure coefficient values from full-scale data has been developed. The methodology is based on a temperature dependent correction factor for mean wind velocity and an offset correction using the difference between the corrected mean velocity pressure and the Reynolds stresses.

Spectral analyses of surface pressures indicate that the pressure fluctuations are partly produced by a mixture of alternating and staggered vortex shedding. The influence of vortex shedding is much stronger in the wind tunnel date than in full scale. The vortex shedding response in full-scale and model scale does not correspond to exactly the same equivalent full-scale frequency bands.

The normalised spectral values are similar for all taps on sides with positive pressure. Whereas the spectral values of taps on suction sides show some variability, depending on tap location, as pressure at taps close to the leeward side of the building show a lower energy content in the low frequency range but a higher energy content in the high frequency range relative to the taps closer to the windward side.

The velocity-pressure admittance functions for windward sides show a conventional behaviour. A combination of the models by Kawai and Sharma is seen to give an approximate fit to the full-scale data. The admittance relation for the suction sides of the building show a different behaviour, especially data from taps on, or close to, the leeward side where admittance is low for normalised frequencies below 0.1 but increases for frequency above 0.1 and peaks at normalised frequencies around 1.

The full- and model scale coherence of surface pressure shows a fairly good overall comparison. Coherence is reduced with an increased tap distance along each wall of the building. However, it is clear that the coherence relation depends not only on distance, but also on tap position with regard to the characteristics of the flow surrounding the building. Coherence on the suction sides is seen to depend on the frequency content of the flow regimes around the building and strong coherence is seen at frequency bands related to vortex shedding. In general, similar average coherence behaviour is observed for two different wind directions, indicating that the main features of the coherence characteristics are not strongly dependent on wind direction.

The variability in wind direction results in a greater variance in full-scale pressures. Especially on the windward sides, which are more susceptible to changes in azimuth than the leeward sides.

7.1.3 Wind induced acceleration response

Wind-induced acceleration data, recorded in the building have been studied. The data is from the full-scale testing period in 1997 as well as from a single storm in 1991.

The wind-induced acceleration response of the building can be defined as a narrow-band process. The raw-data, generally include some additional random, or not so random,

noise components. In fact, when monitoring low amplitude vibrations in buildings, it is recommended that all possible sources of environmental noise should be identified and analysed.

Natural frequencies and damping ratios of the structure have been identified, applying traditional Fourier analysis as well as parametric system identification methods.

As the amount of sampled acceleration data is considerable and the data is recorded for various excitation levels, it is possible to investigate various relations that a single storm data could not resolve.

The analyses have revealed dependence between vibration amplitude and mean wind velocity and direction. The along-wind acceleration dominates the across-wind acceleration by at least 60% when the wind direction is perpendicular to the building walls. In addition, the ratio of perpendicular components of acceleration is found to follow an almost sine-like curve depending on the mean wind direction. The acceleration components are equal for an azimuth of about 45°.

Natural frequency estimates are observed to decrease with increased vibration amplitude, which is a common observation for reinforced concrete structures.

Damping estimates are seen to decrease as the vibration amplitude increases. Although there may well be a physical cause for this behaviour, it is hypothesised by the author that lack of resolution in the low amplitude data results in higher damping estimates for the lower amplitudes. In other words, errors, noise etc. produces artificial damping effects, which results in overestimation of structural damping.

Comparing data recorded within the shear core of the building and data recorded at the building perimeter has underlined the importance of rotational motion in the overall response of buildings, especially of the form presented here. Acceleration at the building perimeter is clearly magnified by the angular motion. This may combine with visual cues to push the vibration into the perception range and add to the occupants' awareness or discomfort. It is therefore important at design stage to pay attention to rotational effects in the structural behaviour.

7.2 Comments on the present work

On one hand, the presented work has to a great extend evolved around experimental data acquisition in both full- and model scale, whereas on the other it has evolved around basic data reduction, understanding and interpretation of the acquired data. In the beginning, a considerable work went into preparing, planning and performing the experiments, especially the full-scale testing. Then an enormous effort has gone into getting a grip on the data, particularly the full-scale data.

This has been, in many ways, an intricate process, the main reasons being unforeseen complications regarding reference dynamic pressures in addition to imperfect data caused by various influence from the environment. Snow, sleet and radio waves (electric interference) disturbed the sonic anemometer, which on several occasions resulted in false recordings not fulfilling the true mean velocity criteria. Sleet and frost-rain clogged the

pressure-taps on occasion. Building noise from ventilation and elevators influenced the acceleration recordings. This called for a considerable amount of effort dedicated to get an overview of the available data and its qualities. Because of the amount of sampled data, it was necessary to establish an automatic procedure that would extract the faulty recordings, either as a whole or partly by correcting faulty spikes and other minor disturbances within the recordings in such a way that they could be used. This work has not been fully documented herein.

The wind tunnel data is not perfect either, which is mainly because the wind tunnel study was done before the full-scale study.

- It would be desirable to have larger number of runs for each setup of transducer placement and wind direction to increase the statistical accuracy of the results.
- The wind tunnel study was planned according to an average wind-rose for Reykjavik which differed substantially from the distribution of wind directions during the full-scale test, therefore the directional sectors for which the largest part of the full-scale data is gathered are not adequately covered.
- The locations of the pressure taps on the model are not exactly the same as in full-scale. It would have desirable to do an additional wind-tunnel test after the full-scale testing, to get a more representative comparison of full-scale and wind tunnel data.
- It could have been useful to have turbulence data (hotwire data) recorded at a location representing the full-scale anemometer location for the appropriate wind directions.

The idea of further wind tunnel tests was suggested, but the circumstance did not arise and the author felt it more important to get a handle on the data already available rather than gathering more data.

It has been said that as a thesis project this was an over ambitious one. However, even though not all of the original goals have been achieved, a decision has been made to make an intermission at this stage and publish the work as it stands. The author chooses to use the term intermission rather than the end, because it is his belief that there are still many interesting avenues to explore where the available data could prove valuable. Some of the author's present ideas are discussed in the following section.

7.3 Further research

7.3.1 Further processing of experimental data

As mentioned above one of the objectives of this investigation was to acquire data that would facilitate the study of the relation between wind, pressure and response. This has been at least semi successfully achieved. However the utilisation of the data is, in many respects, in its infancy. Further processing of experimental data is required to develop the early results presented herein.

7.3.1.1 The correlation between recorded parameters

Information on the interrelation between different parameters is an integral part of overall understanding of the various phenomena involved in the wind-pressure-response processes. The following list gives few examples of possible interrelations that deserve a further study.

- The correlation between the recorded full-scale surface pressures and the recorded wind velocity has not been fully explored, at least not in the time domain.
- The correlation of pressures (front-to-back, side-to-side, side-to-front/back) has not been systematically determined.
- Correlation of pressures as a function of both time and frequency using wavelets might give additional information and understanding of the flow around the building.
- Simultaneous occurrences between recorded parameters should be explored further. This would entail studies of: wind and pressure, pressure at different taps, pressure and acceleration response, wind and acceleration response etc.
- Correlation of energy peaks at specific frequencies for different variables should be studied. This could possibly be achieved by filtering and cross-correlation analysis or by using wavelets.

7.3.1.2 The relation between mean wind velocity and dynamic response

As mentioned before, a clear dependence was found between the buildings rms acceleration and mean wind velocity. For a building with natural frequencies above 2 Hz, this was a bit surprising, even though Wyatt and Best [242] found conventional stochastic model of gust excitation to be adequate for prediction of rms acceleration response for a similar building.

Balandra et al. [4] did an interesting study on longitudinal, lateral and torsional oscillations of a square model with a height/depth ratio of 7:1 in an atmospheric boundary layer for various damping ratios and wind directions. Their findings correspond quite well to the tentative results presented in Chapter 6.

However, further processing of experimental data is required to develop the early results presented in Chapter 6. For instance, a regression analysis is required to determine the most appropriate power for a log-log fit between the mean wind velocity and acceleration. It would also be worthwhile to write a literature review to explore other experimental results on this topic and compare them in a systematic way with the available prediction models.

7.3.1.3 Study the temperature effect on the speed up above the building

The flow conditions above the building, which interfered with the evaluation of reference wind velocity and dynamic pressure, is an interesting phenomenon that deserves a closer look. The decision to use a corrected velocity in calculating a dynamic pressure reference and the methodology of evaluating the correction was taken at a relatively early stage of this work. That was a necessary step in the validation of the data. However, since then this

flow phenomenon has been a constant source of speculation and search for parallels or enlightenment. Although no fully proven explanation exists at present, the author has found many interesting sources that may be a path for deeper understanding of the problem.

Flow studies around buildings may explain parts of the problem. Nagib and Corke [136] for example show velocity increase above an isolated building due to the formation of delta-wing vortices when the building has one corner facing upstream. Judging from their photographs, such a delta-wing vortex might possibly extend it influence to the height of the anemometer. However, they also mention that such vortices are sensitive to upstream conditions and, in particular, to the surface-layer velocity profile. They further conclude that these vortices are also sensitive to the Reynolds number.

An important topic in wind engineering today, are studies of air motion in urban environment [17], whereas most wind engineering studies of buildings assume, in effect, a rural conditions. The urban conditions introduce at least two complicating features to the rural boundary layer built up in the approach flow to the urban area. The roughness elements are typically much larger than the rural roughness elements and the urban area is associated with surface heating. An urban settlement can therefore be considered a rough, warm 'spot' or 'heat island' within the surrounding rural area [178]. These effects introduce a developing boundary layer over the urban area, which modifies the incident profile. An *internal boundary layer* [224] develops at the rural-urban interface that is both mechanical and thermal in origin. Far enough from this transitional region the *urban boundary layer* (UBL) has replaced the former rural boundary layer. The lowest atmospheric layer of this UBL can be considered as a *roughness sublayer* (RS). This layer constitutes the viscous sublayer over 'smooth walls' but unlike the latter the RS has a vertical extension of several tens of meters over typical urban settings and is therefore of importance when modelling flow in urban environment. In refs. [97], [177] and [231] speed up above street canyons was found to exist. Rotach's full-scale study [177] and Uehara's wind tunnel study [231] found scaled profiles of the mean wind velocity and variances to be strongly stability dependent. Rotach found the air in the street canyon to be consistently warmer than the air in the upper part of the sublayer, but on average, the roughness sublayer was near-neutrally stratified at night and unstable during the day.

Smith et al [195] assessed radiatively induced thermal effects on flow around a cubical building. Their simulation showed a significant transport of heat from the rooftop, which was advected leeward of the building.

Yamada et al [249] studied pedestrian level wind environment around buildings using infrared thermography. The building was placed on a heated floor and immersed in a flow in the wind tunnel. They developed a relation between the surface temperature and the mean wind speed by introducing an '*effective wind speed*' (*Ue*), which reflected the effects of the mean and fluctuating wind speeds on the surface temperature. The introduction of *Ue* was necessary to get an acceptable correlation between undisturbed reference velocity and surface temperature changes. This result is likely reversible, in the sense that an '*effective wind speed*' might also reflect the effects of surface temperature on the flow.

Many of the sources referred to above, relate to the field of pollution dispersion, where low wind velocity are critical and temperature effects often control. It is the view of the author that the urban conditions described above, do have an effect on the wind flow around buildings during strong winds that need to be studied more carefully, with regard to wind loading of structures, especially roofs. The data available from this study may be inconclusive for such investigation. However, it might provide a valuable reference for a numerical study. There are also several avenues that have not been fully explored within this experiment. Such as systematic parametric studies of selected data sets, chosen on the basis of wind direction, stability, wind velocity and temperature. Also, the pressures recorded on the roof of the model in the wind tunnel have not been studied fully. Even though they do not incorporate temperature effects, they may shed some further light on the flow conditions above the building.

7.3.1.4 Study of interference effects on the building using available wind tunnel data

In the wind tunnel, it is possible to investigate interference effects of neighbouring buildings, by simply removing the appropriate building blocks. East and south of the study-building, several four-story apartment buildings were located. In the wind tunnel they were modelled as removable solid blocks. Several datasets are available where the apartment buildings were removed and the study-building tested as an almost isolated structure. These data have only been explored superficially at the present. No conclusive interference has been noticed, but it would be interesting to study these data more thoroughly in line with refs. [100] and [219].

7.3.1.5 Evaluation of building response based on the fluctuating pressures recorded on the model in the wind tunnel

The fluctuating pressure measurements from the wind tunnel study have already been validated in Chapter 5, by comparison with the full-scale recordings of fluctuating pressure.

Pressure time-series from 84 taps on the building for different azimuth angles are available from the wind tunnel study. Sets of 16 time series are sampled simultaneously. For each set there is a common tap to another set. It should be possible, for example by maximising the correlation for the common taps between different sets of time series, to develop ‘time delay constants’ that would allow simultaneous application of the 84 pressure time-series. These times series could then be used in connection with a structural modal description of the building to evaluate the building response, which then would be compared to the recorded full-scale response, at least the resonant part.

This would be a considerable task, and how it would be best achieved is not clear in any details. A traditional frequency response analysis in modal form, combining Fourier transformations of the pressure-series, and finite element modelling of the building might be applied in various ways. One of the main problems would be considering the effective

area of loading associated with each pressure tap. A statistical approach in accordance with the methodologies applied by Reinhold and Kareem is also a possibility.

Reinhold [161] measured simultaneous pressures on three levels of a square building with four taps on each side at each level, and used analogue integration scheme to evaluate forces and moments at six levels by using three combinations of simultaneous tests using the fourth level as a common reference. The records were subsequently analysed to determine the power spectra and cross-spectra at different levels, which were then used to estimate modal forces. Kareem [90] used a relatively small number of pressure transducers in a large number of tests where the transducers were moved to various positions in order to describe the surface pressure field and the relationships between pressures at various levels throughout two opposite sides of a square building model. A statistical integration procedure was then used to obtain estimates on an integral wind loading function of the building for along- and across-wind excitation. They were therefore both working with a statistical description based on power spectral densities of forces, rather then the deterministic time-series of pressures directly.

Cheong et al [19] have also proposed a technique for distribution of dynamic wind loads on buildings. Simultaneous measurements of pressures is only required from two tappings at a time. Fluctuating pressure data is converted into the frequency domain using auto- and cross power spectral densities for computation of modal forces, from which the acceleration and the variation of shear and moments along the height of the building.

Holmes [67] has suggested an *effective static load distribution* methodology to estimate the peak wind load effect. Proper analysis of the recorded pressures could supply such a distribution.

An interesting possibility is also to utilise new techniques, such as proper orthogonal decomposition (POD) or wavelets. Such methods have been useful in understanding the flow mechanisms, as well as evaluating extreme values. An interesting aspect of the POD method is to use double modal transformation to combine structural and loading eigensolutions, thereby expressing structural response as a double series in which few structural and loading modes are needed [204].

7.3.2 “New” tools in wind engineering

Bienkiewicz [11] and Gurley et. al. [49] have recently published articles titled ‘*New tools in wind engineering*’ and ‘*Analysis and Simulation Tools For Wind Engineering’*, respectively. These articles introduce several interesting approaches that could be useful in further analysis of the present data. A brief overview of two of these tools is given in following sections as well as a short comment on the use of Computational fluid dynamics.

7.3.2.1 Proper orthogonal decomposition

Proper orthogonal decomposition, or POD, is the name given to a method of decomposing time histories of a variable. As used in wind engineering it is a simplified version of much

wider class of techniques (principle component analysis or Karhunen-Loeve analysis [211]). It was used by Lumley and Armitt in the 1960's, but within the field of wind engineering it was publicised in the Holmes in the 1980's [64]. It has since been explored by several researchers ([3], [84], [85], [101], [205]).

Time histories of variables, such as normalised pressure field, can be described through POD analysis as series of orthogonal spatial functions and uncorrelated temporal functions. The spatial functions are eigenvectors of the variables covariance matrix, whereas the mean squares of the temporal functions are the eigenvalues of the matrix. The first few modes contain the significant energy and therefore an unsteady flow field can be specified by a relatively small number of spatial and temporal functions. The orthogonality and non-correlation imply spatial and temporal independence of physical flow mechanisms. This may be true to the first order, but flow mechanisms must interact to some degree. It can be hypothesised that most energetic modes reflect major flow mechanisms, whereas less energetic modes reflect a number of different mechanisms.

It has been found that some POD modes appear to be associated with physical causes, in particular quasi-steady effects. However, this does not explain all POD modes and the identified correspondence is not exact. This has raised the question whether less energetic modes have a physical meaning and/or whether the mathematical constraints of orthogonality perhaps make the identification of modes with physical causes fictitious in some cases.

The method offers the possibility of specifying unsteady datasets by a few modes shapes and mode spectra, which can be useful in understanding the flow mechanisms, as well as evaluating extreme values. An interesting aspect of the method is to use double modal transformation to combine structural and loading eigensolutions, thereby expressing structural response as a double series in which few structural and loading modes are needed [204].

7.3.2.2 Wavelets

Wavelet analysis has become an increasingly popular approach in studies of turbulent flow in recent years. This is probably due to the ability of wavelet analysis to provide a compromise between traditional time- and frequency-domain representations of turbulence.

Fourier analysis decomposes signals into sinusoidal waves. These sinusoids are very well localized in the frequency, but not in time, since their support has an infinite length, which is a consequence of periodicity. The windowed Fourier transform (or a short-time Fourier transform) replaces the Fourier transforms sinusoidal wave by the product of a sinusoid and a window function, which is localized in time. The windowed Fourier transform has a constant time frequency resolution.

Wavelets are window functions that are localised in space and time. They can be translated (stepped through time) and dilated (scaled) to capture different frequency content. There are number of valid wavelet functions available, and choosing or

developing an appropriate wavelet function for each task is one of the complications in applying wavelet analysis.

The wavelet transform is the convolution of the data time series with the scaled and translated wavelet function. Its time range is proportional to the scale. Its frequency range is proportional to the inverse of scale. The wavelet transform thus has a time frequency resolution that depends on the scale. The wavelet power spectrum is a plot of the power in the wavelet transform (or the square of the magnitude of the wavelet transform) against time and scale. The average wavelet power at each scale throughout the time series is an approximation of the Fourier spectrum.

An advantage of wavelet transforms is the frequency-dependent window size. In order to isolate signal discontinuities, one would like to have short basis functions. At the same time, in order to obtain detailed frequency analysis, one would like to have long basis functions. A way to achieve this is to have short high-frequency basis functions and long low-frequency ones, which is what wavelet transforms provide.

Wavelet applications in wind engineering include: event identification, frequency – time distribution (scalograms) and velocity – pressure correlation (coscalograms). Other possible uses are in simulation of time series and as an aid in understanding flow and loading mechanisms, particularly intermittency. The following references give a relevant overview on the application of the method (Pettit & Jones [155], Jordan, Hajj & Tieleman [86], Gurley & Kareem [48], Bienkiewicz [10]).

7.3.2.3 Computational fluid dynamics

The possibilities offered by computational fluid dynamics are very appealing. However, Stathopoulos [208] recently published a paper where he asks and seeks an answer to the question: Is the numerical wind tunnel for industrial aerodynamics real or virtual in the new millennium? His result is, that in spite of some interesting and visually impressive results produced with Computational Wind Engineering (CWE), the numerical wind tunnel is still virtual rather than real and many more parallel studies - numerical and experimental - will be required to increase the level of confidence in the computational results.

Bienkiewicz arrives at a similar conclusion in his review of new tools in wind engineering [11] and suggests that for the time being the most optimal use of CFD is in a hybrid analysis combining experimental data with numerical simulations.

The data available from the present study could serve as a valuable part of such hybrid of experimental and numerical analysis, although it would be more of a serial than parallel study. Such investigation should be done in collaboration with experts in the CWE field already working on further development of the methodology.

References and Bibliography

[1] Abbott, M.B. & D.R. Basco (1989), *Computational Fluid Dynamics: An Introduction for Engineers*, Longman Publishers.

[2] Azad, R.S. (1993). *The Atmospheric Boundary Layer for Engineers*, Kluwer Academic Publishers.

[3] Baker, C.J. (1999), Aspects of the use of proper orthogonal decomposition of surface pressure fields, *Wind and Structures*, **3**, 97-115.

[4] Balendra, T. & G.K. Nathan (1987), Longitudinal, lateral and torsional oscillations of a square model in an atmospheric boundary layer, *Eng. Struct.* **9** (4).

[5] Batchelor, G.K. (1967), *An Introduction to Fluid Dynamics*, Cambridge Press.

[6] Bech, A. & Hjorth-Hansen, E. (1986), *Wind loads on the Valhall quarters platform on the Norwegian Continental Shelf - Model tests and comparison with full-scale measurements*, SINTEF Report, STF71-A86005.

[7] Bendat, J.S. & A.G. Piersol (1971), *Random Data; Analysis and measurement procedures*, John Wiley & Sons, New York.

[8] Bendat, J.S. & A.G. Piersol (1980), *Engineering applications of correlation and spectral analysis*, John Wiley & Sons, New York.

[9] Bergh, H. & H. Tijdeman (1965), *Theoretical and experimental results for the dynamic response of pressure measurement systems*, National Aero- and Astronautical Research Institute (Netherlands), Report NRL-TR F.238 (1965).

[10] Bienkiewicz, B. & H. J. Ham (1997), Wavelet study of approach-wind velocity and building pressure, *J. Wind Eng. Ind. Aerodyn*, **69-71** (10): 671-683.-

[11] Bienkiewicz, B. (1996), New tools in wind engineering, *J. Wind Eng. Ind. Aerodyn*, **65** (1-3): 279-300.

[12] Breeze, G. (1992), Wind-tunnel investigation upon the coherence of pressure measurements taken around a tall building in open site terrain, *J. Wind Eng. Ind. Aerodyn.* **42** (1-3): 1151-1161.

[13] Cartwright, D.W. & M.S. Longuet-Higgins (1956), The statistical distribution of maxima of the random functions, *Proc. of the Royal Society of London*, Vol. 237.

[14] Castro, I.P. & A.G.Robins (1977), The flow around a surface-mounted cube in uniform,turbulent streams, *J.Fluid Mech*. **79** (pt 2) 307.

[15] Cermak, J.E. (1975), Applications of Fluid Mechanics to Wind Engineering, *J. Fluids Eng.* ASME, **97**: 9-38.

[16] Cermak, J.E. (1976), Aerodynamics of Buildings, *Annual Review of Fluid Mechanics*, **8**: 75-106.

[17] Cermak, J.E., A.G. Davenport, E.J. Plate & D.X. Viegas (editors) (1993), *Wind Climate in Cities*, NATO ASI Series E: Applied Sciences – Vol. 277, ISBN 0-7923-3203-4, Kluwer Academic Publishers 1995.

[18] Cheng C.M., P.C. LU & R.H. Chen (1992), Wind Loads on Square Cylinder in Homogeneous Turbulent Flows, *J Wind Eng Ind Aerodyn.* **41** (1-3): 739-749.

[19] Cheong, H.F., T. Balendra, Y.T. Chew, T.S. Lee & S.L. Lee (1992), An experimental technique for distribution of dynamic wind loads on tall building, *J Wind Eng Ind Aerodyn.* **40** (3): 249-261.

[20] Conover, W. J. 1980, *Practical Nonparametric Statistics*. New York, Wiley.

[21] Cook, N.J. (1985), *The designers guide to wind loading of building structures - Part 1: Background, damage survey, wind data and structural classification*, Butterworths, London UK.

[22] Cook, N.J. (1990), *The designers guide to wind loading of building structures - Part 2: Static structures*, Butterworths, London UK.

[23] Dalgliesh, W.A. (1975), Comparison of model/full-scale wind pressures on a high-rise building, *J. of Ind. Aerodyn.* **1**, 55-66.

[24] Dalgliesh, W.A. Cooper K.R. & Templin J.T. (1983), Comparison of model and full-scale accelerations of a high rise building, *J. Wind Eng. Ind. Aerodyn.* **13**, p.217-228.

[25] Davenport, A.G. (1961), The application of statistical concepts to the wind loading on structures, *Proc. the Inst. of Civil Eng.* London, **19**: 449-472.

[26] Davenport, A.G. (1961), The spectrum of horizontal gustiness near the ground in high winds, *J. of Royal Soc.* **87**, 194-211.

[27] Davenport, A.G. (1978), The prediction of the response of structures, in: *Safety of structures under dynamic loading*, Holand et.al (ed.), Tapir, Norway, pp. 257-284.

[28] Davenport, A.G. (1978), The wind structure and wind climate, in: *Safety of structures under dynamic loading*, Holand et.al (ed.), Tapir, Norway, pp. 209-256.

[29] Davenport, A.G. (1982), The interaction of wind and structures, in: *Engineering Meteorology*, E.J.Plate (Ed.), Elsevier, Amsterdam, pp. 527 –572.

[30] Doeblin, E.O. (1990), *Measurement systems*, 4th edition, McGraw-Hill International.

[31] Dobryn, C., Isyumov N. & Masciantonio A. (1987), Prediction and Measurement of Wind Response: Case Story of a Wind Sensitive Building, *Proc. of the Structures Congress 1987: Dynamics of Structures*, ASCE: 616-631.

[32] Durgin F.H. N. Isyumov, J.E. Cermak, A.G. Davenport, P.A. Irwin, J.A. Peterka, S.R. Ramsay, T.A. Reinhold, R.H. Scanlan, T. Stathopoulos, A.C. Steckley, H. Tieleman, P.J. Vickery (1996), Wind-tunnel studies of buildings and structures. *J. of Aerospace Eng.* ASCE, **9** (1): 19-36.

[33] Durgin, F.H.; T.J. Gilbert, & J.R. Macachor (1990), Available full-scale on-site wind-induced data from a major tall building, *J. Wind Eng. Ind. Aerodyn.* **36** (1/3) part 2: 1201-1215.

[34] Dyrbye, C. & S.O. Hansen (1989), *Vindlast på bærende konstruktioner*, SBI-Anvisning 158, 1989.

[35] Dyrbye, C. & S.O. Hansen (1997), *Wind Loads on Structures*, John Wiley & Sons (Sd); ISBN: 0471956511.

[36] Eaton, K.J. & J.R. Mayne (1968), Instrumentation and analysis of full-scale wind pressure measurements, *Proc. of the National Phys. Lab. Symp. on Instrumentation and data processing for ind. Aerodyn*, Teddington, Middlesex.

[37] Eaton, K.J. & J.R. Mayne (1975), The measurement of wind pressures on two-storey houses at Aylesbury, *J. of Ind. Aerodyn*, 1, pp. 67-109.

[38] ESDU, Dynamic response*, Wind Engineering Series Vol. 3a & 3b*, ESDU International, London.

[39] ESDU, Mean loads on structures, *Wind Engineering Series Vol. 2b*, ESDU International, London.

[40] ESDU, Wind speeds and turbulence, *Wind Engineering Series Vol. 1a*, ESDU International, London.

[41] European Standard prEN 1991-1-4, Eurocode 1: Actions on Structures, Part 1-4 General Actions: Wind Actions, prepared on behalf of Technical Committee CEN/TC250 - Structural Eurocodes. Version from November 2001.

[42] Farell, C. & A.K.S. Iyengar (1999), Experiments on the wind tunnel simulation of atmospheric boundary layers, *J. Wind Eng. Ind. Aerodyn.* **79** (1-2): 11-35.

[43] Flay, R.G.J. & D.C. Stevenson (1988), Integral length scales in strong winds below 20 m, *J. Wind Eng. Ind. Aerodyn.* **28**: 21-30.

[44] Gersch, & S. Luo (1972), Discrete time series synthesis of randomly excited structural system response, *J. Acoust. Soc. Amer.* **51**.

[45] Geurts, C. P.W. (1996), *Wind induced pressures on the main building of Eindhoven Univ. of Technology*, Report TUE/BKO/96.13, Eindhoven Univ. of Technology.

[46] Geurts, C.P.W. H.S. Rutten & J.A. Wisse (1997), Spectral characteristics of wind induced pressures on a full scale building in suburban terrain, *J. Wind Eng. Ind. Aerodyn.* **69-71**: 609-618.

[47] Gumley, S.J. (1983), Tubing systems for pneumatic averaging of fluctuating pressures, *J. Wind Eng. Ind. Aerodyn*, **12** (2): 189-228.

[48] Gurley, K.R. & A. Kareem (1998), A conditional simulation of non-normal velocity/pressure fields, *J. Wind Eng. Ind. Aerodyn.* **77-78** (1): 39-51.

[49] Gurley, K.R., M.A. Tognarelli & A. Kareem (1997), Analysis and Simulation Tools For Wind Engineering, *Prob. Eng. Mech.* **12** (1): 9-31.

[50] Hajj, M.R., H. W. Tieleman & L. Tian (2000), Wind tunnel simulation of time variations of turbulence and effects on pressure on surface-mounted prisms, *J. Wind Eng. Ind. Aerodyn*, **88** (2-3): 197-212.

[51] Hajj, M.R., I.M. Janajreh, H. W. Tieleman & T.A. Reinhold (1997), On frequency-domain analysis of the relation between incident turbulence and fluctuating pressures, *J. Wind Eng. Ind. Aerodyn*, **69-71**: 539-545.

[52] Hansen, S.O. & S. Krenk (1999), Dynamic along-wind response of simple structures, *J. Wind Eng. Ind. Aerodyn.* **82** 147-171.

[53] Harris, I.R. (1971), The nature of wind, *The modern design of wind sensitive structures*, CIRIA publication, London.

[54] Harris, I.R. (1986), Longer turbulence length scales, *J. Wind Eng. Ind. Aerodyn*. **24** (1): 61-68.

[55] Harris, I.R. (1990), Some further thoughts on the spectrum of gustiness in strong winds, *J. Wind Eng. Ind. Aerodyn*. **33** (3): 461-477.

[56] Haverkamp B. & M. Verhaegen (1997) *State Space Model Identification Software for Multivariable Dynamical Systems*, TU Delft /ET/SCE96.015.

[57] Haviland R. (1976), *A study of the uncertainties in the fundamental translational periods and damping values for real buildings*, Publication No. R76-12, Order No. 531, Dept. of Civil Eng. MIT, Cambridge, MA, USA.

[58] Hjorth-Hansen, E. (1977), Regular drag fluctuations due to air flow normal to a plate-type structure, *J. of Ind. Aerodynamics*, **2**: 129-132.

[59] Hjorth-Hansen, E. (1993), *Fluctuating drag loading by wind*, Wind Engineering - Lecture Note No. 1, Div. of Struct. Eng., Norwegian Univ. of Science and Techn., Rep. no. R-5-89.

[60] Ho, T.C.E., D. Surry & A.G. Davenport (1991), Variability of low building wind loads due to surroundings, *J. Wind Eng. Ind. Aerodyn*. **38**: 297-310.

[61] Ho, T.C.E., D. Surry & A.G. Davenport (1992), Spatial distribution of peak cladding loads on tall buildings, *Can. J. Civ. Eng.* **19**: 199-211.

[62] Holdo, A.E., E.L. Houghton, F.S. Bhinder (1982), Some effects due to variations in turbulence integral length scales on the pressure distribution on wind-tunnel models of low-rise buildings, *J. Wind Eng. and Ind. Aerodyn*. **10**: 103-115.

[63] Holmes J.D. (1976), Pressure-fluctuations on a large building and along-wind structural loading, *J. Ind. Aerodyn.* **1** (3): 249-278.

[64] Holmes, J.D. (1990), Analysis and synthesis of pressure fluctuations on bluff bodies using eigenvectors, *J. of Wind Eng. and Ind. Aerodyn.* **33** (1-2): 219-230.

[65] Holmes, J.D. (1994), Methods of fluctuating pressures measurement in wind engineering, *A State of the Art in Wind Engineering*, published in connection with the 9th Int. Conf. on Wind Eng. Wiley Eastern Limited.

[66] Holmes, J.D. (2001), *Wind loading of structures*, Spon Press, London.

[67] Holmes, J.D. (2002), Effective static load distributions in wind engineering, *J. of Wind Eng. and Ind. Aerodyn.* **90**: 91-109.

[68] Hoxey, R.P. & P. Moran (1983), A full-scale study of the geometric parameters that influence wind loads on low rise buildings, *J. of Wind Eng. and Ind. Aerodyn.* **13** (1/3): 277-288.

[69] Hoxey, R.P. (1996), private communication.

[70] Hoxey, R.P., P.J. Richards & J.L. Short (2002), A 6m cube in an atmospheric boundary layer flow - Part 1. Full-scale and wind-tunnel results, *Wind and Structures,* **5** (2-4): 177-192.

[71] Hoxey, R.P., A.P. Robertson & A.D. Quinn (2001), The Atmospheric Flow Laboratory - a new facility for wind engineering, *Proc. the 3rd European & African Conference on Wind Engineering*, Eindhoven, The Netherlands, pp. 235-240.

[72] Hunt A. (1982), Wind-tunnel measurements of surface pressures on cubic building models at several scales, *J. of Ind. Aerodyn*, **10**: 137-163.

[73] Hunt, J.N. (1964), *Incompressible Fluid Dynamics*, Math. physics series, Longmans.

[74] Huot, J.P., C. Rey & H. Arbey (1986), Experimental analysis of the pressure field induced on a square cylinder by a turbulent flow, *J. Fluid Mech.* **162**: 283-298.

[75] Irwin, H.P.A.H, K.R. Cooper & R. Girard (1979), Correction of distortion effects caused by tubing systems in measurements of fluctuating pressures, *J. Ind. Aerodyn.* **5** (1-2): 93-107.

[76] Isyumov, M. & R.A. Halvorson, (1984) Dynamic Response of Allied Bank Plaza during Hurricane Alicia, *Proc. of the ASCE Specialty Conference: Alicia - One Year Later*, Galveston, TX, USA.

[77] Isyumov, N (1982), The Aeroelastic Modelling of Tall Buildings, in: *Wind tunnel modelling for civil engineering applications*, T. Reinhold (ed.), Cambridge University Press.

[78] Isyumov, N. & M. Poole (1983), Wind induced torque on square and rectangular building shapes, *J. Wind Eng. Ind. Aerodyn.* **13**: 183-196.

[79] Iyengar, A.K.S. & C. Farell, (2001), Experimental issues in atmospheric boundary layer simulations: roughness length and integral length scale determination, *J. Wind Eng. Ind. Aerodyn.* **89** (11-12): 1059-1080.

[80] Jeary A.P. & B.R. Ellis (1983), On predicting the response of tall buildings to wind excitation, *J. Wind Eng. Ind. Aerodyn.* **13**: 173-182.

[81] Jeary, A.P. (1986), Damping in tall building - A mechanism and a predictor, *Earthquake Eng. Struct. Dyn.* **14**: 733-750.

[82] Jeary, A.P. (1997), Damping in structures, *J. Wind Eng. Ind. Aerodyn.* 72 (1-3): 345-355.

[83] Jensen, M. & N. Franck (1965), *Model-scale tests in turbulent wind - Part II*, The Danish Technical Press, Copenhagen.

[84] Jeong, S. H. & B. Bienkiewicz (1997), Application of autoregressive modeling in proper orthogonal decomposition of building wind pressure, *J. Wind Eng. Ind. Aerodyn*, **69-71**: 685-695.

[85] Jeong, S.H., B. Bienkiewicz & H.-J. Ham (2000), Proper orthogonal decomposition of building wind pressure specified at non-uniformly distributed pressure taps, *J. Wind Eng. Ind. Aerodyn.* **87** (1): 1-14.

[86] Jordan, D. A., M.R. Hajj & H.W. Tieleman (1997), Wavelet analysis of the relation between atmospheric wind and pressure fluctuations on a low-rise building, *J. Wind Eng. Ind. Aerodyn.* **69-71**: 647-655.

[87] Kaimal et al. (1972), Spectral characteristics of surface-layer turbulence, *J. Royal Meteorological Society*, **98**: 563-589.

[88] Kanda, J. & T. Ohkuma (1990), Recent developments in full-scale wind pressure measurements in Japan, *J. of Wind Eng. Ind. Aerodyn.* **33** (1-2): 243-252.

[89] Kareem, A. & J.E. Cermak (1984), Pressure-fluctuations on a square building model in boundary-layer flows, *J. of Wind Eng. Ind. Aerodyn.* **16** (1): 17-41.

[90] Kareem, A. (1982), Measurement of total wind loads using surface pressures, in: *Wind tunnel modelling for civil engineering applications*, T. Reinhold (ed.), Cambridge University Press.

[91] Kareem, A. (1985), Lateral-Torsional Motion of Tall Buildings to Wind Loads, *J. of Struct. Eng.* ASCE, **111** (11): 2749-2496.

[92] Kareem, A. (1987), Wind effects on structures: a probabilistic viewpoint, *Probabilistic Engineering Mechanics*, **2** (4).

[93] Kareem, A. and K. Gurley (1996), Damping in Structures: Its Evaluation and Treatment of Uncertainty, *J. Wind Eng. Ind. Aero*. **59** (2-3), 131-157.

[94] Kaspersen, H. & P-A. Krogstad (1993), The effect of transition to turbulent flow in tubing networks for fluctuating pressure measurement. *J. Wind Eng. Ind. Aerodyn.* **48**: 1-11.

[95] Kasperski, M. & H.J. Niemann (1992), The LRC (Load-Response-Correlation) method: A general method of estimating unfavourable wind load distributions for linear and non-linear structural behaviour, *J. Wind Eng. Ind. Aerodyn*. **43**: 1753-1763.

[96] Kasperski, M. (1996), Design wind loads for low-rise buildings: a critical review of wind load specifications for industrial buildings, *J. Wind Eng. Ind. Aerodyn*. **61**: 169-179.

[97] Kastner-Klein, P. E. Fedorovich & M.W. Rotach (2001), A wind tunnel study of organised and turbulent air motions in urban street canyons, *J. Wind Eng. Ind. Aerodyn*. **89**: 849 –861.

[98] Kawai, H. (1983), Pressure fluctuations on square prisms – applicability of strip and quasi-steady theories. *J. Wind Eng. Ind. Aerodyn.* **13**: 197–208.

[99] Kawai, H. J. Katsura and H. Ishizaki (1979), Characteristics of pressure fluctuations on the windward wall of a tall building, *Proc. of the 5th Int. Conf. of Wind Eng.*, pp. 519-528.

[100] Khanduri, A.C., T. Stathopoulos & C. Bédard (1998), Wind-induced interference effects on buildings – a review of the state-of-the-art. *Eng. Struct.* **20** (7): 617-630.

[101] Kikuchi, H., Y. Tamura, H. Ueda & K. Hibi (1997), Dynamic wind pressures acting on a tall building model - proper orthogonal decomposition, *J. Wind Eng. Ind. Aerodyn.* **69-71**: 631-646.

[102] Krauss, T.P., L. Shure, & J.N. Little (1994), *Signal processing Toolbox*, for use with Matlab, The MathWorks Inc.

[103] Krishna, P. (1995) Wind loads on low rise buildings - a review, *J. Wind Eng. Ind. Aerodyn.* **54/55**: 383-396.

[104] Krogstad, P-Å, J-H Kaspersen & L.E. Thorbergsen (1994), *Raftasundet Bridge - Wind tunnel tests of static forces and pressure loading*, SINTEF STF70-F94065 (in Norwegian).

[105] Kwok, K.C.S. (1995), Aerodynamics of tall buildings, *A State of the Art in Wind Engineering*, publ. in connection with the 9th Int. Conf. on Wind Eng., Wiley Eastern Ltd.

[106] Landahl, M.T. & E. Mollo-Christensen (1986), *Turbulence and random processes in fluid mechanics*, Cambridge University Press.

[107] Landau, L.D. & E.M. Lifshitz, (1959), *Fluid Mechanics*, Pergamon Press.

[108] Lawson T.V. (1980), *Wind effects on buildings*, vol.1 & 2, Applied Science Publishers Ltd. London.

[109] Lee, B.E. (1975), The effect of turbulence on the surface pressure field of a square prism, *J. Fluid Mech.*, **69**: 263-282.

[110] Lee, Y., H. Tanaka & C.Y. Shaw (1982), Distribution of wind-induced and temperature-induced pressure differences across the walls of a 20-story compartmentalized building. *J. Wind Eng. Ind. Aerodyn.* **10** (3): 287-301.

[111] Letchford, C.W., P. Sandri, M.L. Levitan & C. Mehta (1992), Frequency response requirements for fluctuating wind pressure measurements, *J. Wind Eng. Ind. Aerodyn.* **40**: 263-276.

[112] Letchford, C.W., R.E. Iverson & J.R. McDonald (1993), Application of the quasi-steady theory to full scale measurements on the Texas tech building *J. Wind Eng. Ind. Aerodyn.* **48** (1): 111-132.

[113] Levitan, M.L. & K.C. Metha (1992), Texas Tech field experiments for wind loads, part I: Building and pressure measuring system, *J. Wind Eng. Ind. Aerodyn.* **43** (1): 1565-1576.

[114] Levitan, M.L. & K.C. Metha (1992), Texas Tech field experiments for wind loads, part II: Meteorological instrumentation and terrain parameters, *J. Wind Eng. Ind. Aerodyn.* **43**(1) 1577-1588.

[115] Levitan, M.L. (1993), *Analysis of Reference Pressure Systems used in Field Measurements Wind Loads*, Ph.D. Dissertation, Texas Tech, Lubbock USA, 9312526.

[116] Levitan, M.L., K.C. Mehta, W.P. Vann & J.D. Holmes (1991), Field measurements of pressures on the Texas Tech Building, *J. Wind Eng. Ind. Aerodyn*. **38** (2-3): 227-234.

[117] Li, Q.S. & W.H. Melbourne (1999), The effect of large-scale turbulence on pressure fluctuations in separated and reattaching flows, *J. Wind Eng. Ind. Aerodyn.* **83**: 159-169.

[118] Li, Q.S. & W.H. Melbourne (1999), Turbulence effects on surface pressures of rectangular cylinders, *Wind and Structures* **2**(4): 253-266.

[119] Li, Q.S., J.Q. Fang, A.P. Jeary & C.K. Wong (1998), Full scale measurements of wind effects on tall buildings, *J. Wind Eng. Ind. Aerodyn.* **74-76:** 741-750.

[120] Li, Y. & A. Kareem (1990), ARMA systems in wind engineering, *Prob. Eng. Mech.* **5** (2): 50-59.

[121] Li, Y. & A. Kareem 1990. Recursive modeling of dynamic systems. *J. of Eng. Mech.* **116** (3): 660-679.

[122] Littler, J.D. & B.R. Ellis (1990) Interim findings from full-scale measurements at Hume Point, *J. Wind Eng. Ind. Aerodyn.* **36** (1-3): 1181-1190.

[123] Littler, J.D. & B.R. Ellis (1992), Full-scale measurements to determine the response of Hume Point to wind loading, *J. Wind Eng. Ind. Aerodyn.* **42**: 1085-1096.

[124] Littler, J.D. & P.D. Murphy (1994), A comparison between the full-scale measured response of Hume Point and that calculated by some predictive methods, *J. Wind Eng. Ind. Aerodyn.* **52**: 219-228.

[125] Ljung, L, 1987, *System identification: Theory for the User*, Prentice-Hall.

[126] Ljung, L. 1995, *System identification toolbox, for use with Matlab*, The MathWorks Inc.

[127] Maalej M., A. Karasaridis, D. Hatzinakos & S.J. Pantazopoulou (1999), Spectral analysis of sensor data in civil engineering structures, *Computers and Structures*, **70**: 675-689

[128] Macdonald, A.J. (1975), *Wind loadings on buildings*, Applied Science Publishers Ltd.

[129] Matsui, G., K. Suda & K. Higuchi (1982), Full-scale measurement of wind pressures acting on high-rise building of rectangular plan, *J. of Ind. Aerodyn*, **10**: 267-286.

[130] Melbourne, W.H. (1980), Comparison of measurements on the CAARC standard tall building model in simulated model wind flows*, J. of Ind. Aerodyn*. **6** 73-88.

[131] Melbourne, W.H. (1989), Bluff body aerodynamics – Review lecture, *Recent Advances in Wind Engineering - Proc. of the 2nd Asia-Pasific Symp. on Wind Eng.*, Vol 1, T.F. Sun (ed.), International Academic Publisher - Pergamon Press.

[132] Milford, R.V., A.M. Goliger & J. L. Waldeck (1992), Jan Smuts experiment: Comparison of Full-scale and Wind-tunnel results, *J. Wind Eng. Ind. Aerodyn.* **41-44**: 1705-1716.

[133] Milford, R.V., J. L. Waldeck & A.M. Goliger (1992), Jan Smuts Experiment: Details of Full-scale Experiment, *J. Wind Eng. Ind. Aerodyn.* **41-44**: 1693-1704.

[134] Mohan M. & T.A. Siddiqui (1998), Analysis of various schemes for the estimation of atmospheric stability classification, *Atmospheric Environment*, **32** (21): 3775-3781.

[135] Moran, P. & R.P. Hoxey (1979), A probe for sensing static pressure in two-dimensional flow, *J. Physics-E*, **12**.

[136] Nagib, H.M. & T.C. Corke (1984), Wind microclimate around buildings: Characteristics and Control, *J. Wind Eng. Ind. Aerodyn.* **16**: 1-15. .

[137] Nakagawa, T. & R. Nakagawa. (1993), Vortex shedding mechanism from prisms having H and I sections, *J. of Wind Eng. Ind. Aerodyn.* **49**: 197-206.

[138] National Land Survey of Iceland (1994), An aerial photograph of Reykjavík.

[139] Newberry, C.W., K.J. Eaton & J.R. Mayne (1973), Wind loading on tall buildings - further results from Royex House, *Ind. Aerodyn Abstracts*, **4** (4).

[140] Newberry, C.W., K.J. Eaton, & J.R. Mayne (1967), The nature of gust loading on tall buildings, *Int. Seminar on Wind Effects on Build. and Struct.,* Ottawa.

[141] Newberry, C.W., K.J. Eaton, & J.R. Mayne (1970), Wind loading on Vickers Tower, Millbank, *Building,* **219** (6639):53-56.

[142] Newland, D.E. (1993), *An introduction to random vibrations, spectral and wavelet analysis*, 3rd ed., Longmann Group Ltd. England.

[143] Ohkuma, T., H. Marukawa, Y. Niihori & N. Kato (1991), Full-scale measurement of wind pressures and response accelerations of a high-rise building, *J. Wind Eng. Ind. Aerodyn.* **38** (2-3): 185-196.

[144] Ohtake K., Y. Mataki, T. Ohkuma, J. Kanda & H. Kitamura (1992), Full-scale measurements of wind actions on Chiba Port Tower. *J. Wind Eng. Ind. Aerodyn*. **41-44** (1-3): 2225-2236.

[145] Okuda, Y., J. Katsura & S. Kawamura (1997), Local severe suctions on the side of a prism model on a field, *J. Wind Eng. Ind. Aerodyn*. **72**: 23-32.

[146] Oppenheim, A.V. & R.W. Shafer, 1989, *Discrete-Time Signal Processing*, Prentice-Hall 1989.

[147] Panovsky, H.A. & Dutton, J.A. (1984), *Atmospheric Turbulence, models and methods for engineering applications*, John Wiley & Sons, Inc. USA.

[148] Panovsky, H.A. (1977), Wind Structure in Strong Winds Below 150 m, *Wind Engineering* 1(2): 91-103.

[149] Pasquill, F. & F.B Smith (1983), *Atmospheric Diffusion*, John Wiley and Sons.

[150] Parmentier, B., S. Schaerlaekens & J. Vyncke (2001), Net pressures on the roof of a low-rise building - full-scale experiments, *Proc. the 3rd European & African Conference on Wind Engineering*, Eindhoven, The Netherlands.

[151] Paterson, D.A. & J.D. Holmes (1992), Computation of wind pressures on low-rise structures *J. Wind Eng. Ind. Aerodyn.* **43**: 1629-1640.

[152] Peixoto, J.P. & A.H. Oort (1992), *Physics of climate*, American Institute of Physics, New York.

[153] Peterka J.A., R.N. Meroney and K.M. Kothari (1985), Wind flow patterns about buildings, *J. Wind Eng. Ind. Aerodyn.* **21**: 21-38.

[154] Peterson, L.D., S.J. Bullock & S.W. Doebling (1996), The statistical sensitivity of experimental modal frequencies and damping ratios to measurement noise, *Modal Anal.* **11** (1-2): 63-75.

[155] Pettit, C.L., N.P. Jones & R. Ghanem (2002), Detection and simulation of roof-corner pressure transients, *J. Wind Eng. Ind. Aerodyn.* **90**: 171-200.

[156] Pewarden, A.D. & A.F.E Wise (1975), *Wind environment around buildings*, BRE Report, London HMSO, ISBN 0 11 6705337.

[157] Piccardo, G. & G. Solari (1998), Closed form prediction of 3-D wind-excited response of slender structures, *J. Wind Eng. Ind. Aerodyn.* **74-76**: 697-708.

[158] Plate, E.J. & J-H. Kiefer (2001), Wind loads in urban areas, *J. Wind Eng. Ind. Aerodyn.* **89**: 1233-1256.

[159] Plate, E.J. (ed.) (1982), *Engineering Meterology*, Elsevier Scientific Publishing Company.

[160] Porterfield, M.L. & N.P. Jones (2001), The development of a field measurement instrumentation system for low-rise construction. *Wind and Structures* **4** (3).

[161] Reinhold, T. A. (1983), Distribution and Correlation of Dynamic Wind Loads, *J. of Eng. Mech.* ASCE, **109** (6): 1419-1436.

[162] Reinhold, T. A. (ed.) (1982) Wind tunnel modelling for civil engineering applications, *Proc. of the international workshop on wind tunnel modelling criteria and techniques in civil engineering applications*, Gaithersburg, Maryland, USA, Cambridge University Press.

[163] Reykjavík City's Geographical Information System: http://www.borgarvefsja.is/website/bvs.

[164] Richards, P.J., A.D. Quinn & S. Parker (2002), A 6m cube in an atmospheric boundary layer flow - Part 2. Computation solutions, *Wind and Structures,* **5** (2-4): 177-192.

[165] Richards, P.J., R.P. Hoxey & B.S. Wanigaratne (1995), Effect of directional variations on the observed mean and rms pressure coefficients, *J. Wind Eng. Ind. Aerodyn.* **54-55**: 359-367.

[166] Richards, P.J., R.P. Hoxey & J.L. Short (2001), Wind pressures on a 6m cube, *J. Wind Eng. Ind. Aerodyn.* **89** (14-15) 1553-1564.

[167] Richardson, G. M. & D. Surry (1991), Comparisons of wind-tunnel and full-scale surface pressure measurements on low-rise pitched roof buildings, *J. Wind Eng. Ind. Aerodyn.* **38**: 249-256.

[168] Richardson, G. M. & D. Surry (1992), The Silsoe Building: a comparison of pressure coefficients and spectra at model and full-scale, *J. Wind Eng. Ind. Aerodyn.* **41-44**: 1653-1664.

[169] Richardson, G. M. & D. Surry (1994), The Silsoe Structures Building: Comparison between full-scale and wind-tunnel data, *J. Wind Eng. Ind. Aerodyn.* **51**: 157-176.

[170] Richardson, G.M. & P.A. Blackmore (1995) Silsoe structures building: comparison of 1:100 model-scale data with full-scale data, *J. Wind Eng. Ind. Aerodyn.* **57** (2-3): 191-201.

[171] Richardson, G.M., A.P. Robertson, R.P. Hoxey & D. Surry (1990), Full-scale and Model investigations of pressures on an Industrial/Agricultural Building, *J. Wind Eng. Ind. Aerodyn.* **36**: 1053-1062.

[172] Roberts, J.B. & M. Vasta (2000), Parametric identification of systems with non-Gaussian excitation using measured response spectra, *Prob. Eng. Mechanics*, **15**: 59–71.

[173] Robertson, A. P. & Glass, A. G. (1988). *The Silsoe Structures Building-its design, instrumentation & research facilities*. Divisional Note DN 1482, AFRC Institute of Engineering Research, Silsoe, UK.

[174] Robertson, A. P. (1991), Effect of eaves detail on wind pressures over an industrial building. *J. Wind Eng. Ind. Aerodyn.* **38**: 325-333.

[175] Robertson, A. P. (1992), The wind-induced response of full-scale portal framed building, *J. Wind Eng. Ind. Aerodyn.* **41-44**: 1677-1688.

[176] Robertson, A.P., R.P. Hoxey & P. Moran (1985), A Full-Scale Study of Wind loads on Agricultural Ridged Canopy Roof Structures and Proposals for Design, *J. Wind Eng. Ind. Aerodyn.* **21**: 167-205.

[177] Rotach, M.W. (1995), Profiles of turbulence statistics in and above an urban street canyon, *Atmos. Environ.* **29**: 1473 - 1486.

[178] Rotach, M.W. (1999), On the influence of the urban roughness sublayer on turbulence and dispersion. *Atmos. Environ.* **33**: 4001 - 4008.

[179] Saathoff, P.J. & W.H. Melbourne (1999), Effects of freestream turbulence on streamwise pressure measured on a square-section cylinder *J. Wind Eng. Ind. Aerodyn.* **79** (1-2): 61-78.

[180] Safak, E. & D.A. Foutch (1987), Coupled vibrations of rectangular building subjected to normally-incident random wind loads, *J. Wind Eng. Ind. Aerodyn.* **26**: 129-148.

[181] Safak, E. (1989), Adaptive modelling, identification, and control of dynamic structural systems, I: Theory & II: Applications, *J. Engr. Mech.* ASCE, **115** (11).

[182] Safak, E. 1990, Method to estimate centre of rigidity using vibration recordings, *J.Struct Engr.* ASCE, **116** (1).

[183] Sanada, S. & M.Yoshida (1995), Full-scale measurement of wind pressure acting on a tall building, *Wind Engineering Retrospect and Prospect - Papers for the Ninth Int. Conf. in Wind Eng.*, Vol. 5. New Age Int. Ltd. Publishers, New Delhi, India

[184] Sanni, R.A., D. Surry, A.G. Davenport (1992), Wind Loading on Intermediate Height Buildings, *Can. J. Civil Eng*. **19** (1): 148-163.

[185] Saunders, J.W. & D.A. Melbourne (1975), Tall Rectangular Building Response to Cross-Wind Excitation, *Proc. 4th Int. Conf. Wind Effects on Buildings and Structures*, Cambridge Univ. pp. 369-379.

[186] Schmidt, S. & F. Thiele (2002), Comparison of numerical methods applied to the flow over wall-mounted cubes, *Int. J. of Heat and Fluid Flow.* **23**: 330 - 339.

[187] Scorer, R.S. (1978), *Environmental Aerodynamics*, Ellis Harwood Ltd. Publishers.

[188] Sedefian L. & E. Bennett (1980), A comparison of turbulence classification schemes, *Atmos. Environ*. **14** (7): 741-750.

[189] Sharma, R. N. & Richards, P. J. (1996), Windward Wall Pressure Admittance Functions for Low-rise Buildings, *Book of Abstracts for The 3rd International Colloquium on Bluff Body Aerodynamics and Applications*, Virginia Polytechnic Institute and State University, USA.

[190] Sharma, R. N. (1996) *The Influence of Internal Pressure on Wind Loading Under Tropical Cyclone Conditions*, PhD Thesis in Mechanical Engineering, Department of Mechanical Engineering, The University of Auckland, New Zealand, 428pp.

[191] Sigbjörnsson, R. (1974), *On the theory of structural vibrations due to natural wind*, Danmarks Tekniske Hojskole, Rapport nr. R 59 (160 pages, PhD thesis).

[192] Sill, B.L., N.J. Cook & C. Fang (1992), The Aylesbury comparative experiment: a final report, *J. Wind Eng. Ind. Aerodyn*. **41-44**: 1553-1564.

[193] Simiu, E. & R.H. Scanlan, (1986), *Wind effects on structures*, 2nd ed., John Wiley & Sons.

[194] Sitheeq M.M., A.K.S. Iyengar & C. Farell (1997), Effect of turbulence and its scales on the pressure field on the pressure field on the surface of a three-dimensional square prism, *J. Wind Eng. Ind. Aerodyn.* **69-71**: 461-471.

[195] Smith, W.S., J.M. Reisner & C.-Y.J. Kao (2001), Simulations of flow around a cubical building: comparison with towing-tank data and assessment of radiatively induced thermal effects, *Atmospheric Environment*, **35**: 3811-3821.

[196] Snæbjörnsson, J.Th. 1989, *Wind Induced Accelerations in a Multi-storey Building*, MSCE thesis, University of Washington.

[197] Snæbjörnsson, J.T. & D.A. Reed (1991), Wind-induced Accelerations of a Building: A case study, *Engineering Structures*, **13**: 268-280.

[198] Snæbjörnsson, J.Th. & D.A. Reed (1992), Wind-induced Motion in Multi-Storey Buildings, *J. of Wind Engineering and Industrial Aerodynamics*, **42** (1-3): 1113-1123.

[199] Snæbjörnsson, J.Th. & R. Sigbjörnsson (1992), Wind structure over postglacial lava surface, *J. of Wind Eng. and Ind. Aerodyn.* **41** (1-3):305-315.

[200] Snæbjörnsson, J.Th. & R. Sigbjörnsson (1995), Estimation of Structural Parameters from Full-Scale Wind-Induced Response, *Wind Engineering Retrospect and Prospect - Papers for the Ninth Int. Conf. in Wind Eng.*, Vol. 3, Wiley Eastern Ltd. New Delhi, India.

[201] Snæbjörnsson, J.Th. (1997), Wind Loading and Response of a Medium Rise Building in a Built up Area, *Proceedings of the 2nd European & African Conference on Wind Engineering*, Giovanni Solari (ed.), © 1997, SGE, Padova, Italy, pp. 1255-1262.

[202] Snæbjörnsson, J.Th., E. Hjorth-Hansen & R. Sigbjörnsson (1996), Variability of Natural Frequency and Damping ratio of a Concrete Building- Case study in System Identification, *Proceedings of the 3rd European Conference on Structural Dynamics-EURODYN '96*, Augusti et al. (eds.), Vol. 2, Balkema, Rotterdam, ISBN 90 5410 813 4, pp. 949-956.

[203] Söderström, T. & P. Stoica (1989), *System Identification*, Prentice Hall.

[204] Solari, G. & G. Piccardo (2001), Probabilistic 3-D turbulence modelling for gust buffeting of structures, *Prob. Eng. Mech.* **16**: 73-86.

[205] Solari, G. & L. Carassale (2000), Modal transformation tools in structural dynamics and wind engineering, *Wind & Structures*, **3** (4): 221-241.

[206] Soliari, G. (1985), Mathematical model to predict 3-D wind loading on buildings, *J. of Eng. Mech.* ASCE, **111** (2).

[207] Sólnes, J. & R. Sigbjörnsson (1973), Along-Wind Response of Large Bluff Buildings, *J. Struct. Div.* ASCE, **99**: 381-398.

[208] Stathopoulos T. (2002), The numerical wind tunnel for industrial aerodynamics: Real or virtual in the new millennium?, *Wind and Structures.* **5** (2-4): 193-208.

[209] Stathopoulos, T. (1984), Wind loads on low-rise buildings: a review of the state of the art, *Eng. Struct*. 6: 119-135.

[210] Stathopoulos, T., B. Dumitrescu, M. Rulotte (1989) Design recommendations for wind loading on buildings of intermediate height, *Can. J. of Civil Eng*. **16** (6): 910-916.

[211] Stewart, G.W. (1993), On the Early History of the Singular Value Decomposition, *SIAM Review* **35**: 551-566.

[212] Strømmen, E. & E. Hjorth-Hansen (1995), The buffeting wind loading of structural members at an arbitrary attitude in the flow, *J. Wind Eng. Ind. Aerodyn*. **56**: 267-290.

[213] Strømmen, E., H.P. Brathaug & E. Hjorth-Hansen (1988), *Helgeland bridge - model test in wind tunnel for a balanced cantilevered box girder bridge during construction stage*, SINTEF Structural Engineering, STF71 F88013 (in Norwegian).

[214] Surry D., T. Stathopoulos & A.G. Davenport (1978), Wind Loading of Low Rise Buildings, *Proc. Canadian Structural Engineering Conference*.

[215] Surry, D. & D. Djakovich (1995), Fluctuating pressures on models of tall buildings, *J. Wind Eng. Ind. Aerodyn.* **58**: 81-112.

[216] Surry, D. (1992), Wind tunnel simulation of the Texas Tech Building, *J. Wind Eng. Ind. Aerodyn.* **43**, pp. 1613-1614.

[217] Tamura, Y. & S. Suganuma (1996), Evaluation of Amplitude-Dependent Damping and Natural Frequency of Buildings During Strong Winds, *J. Wind Eng. Ind. Aerodyn*. **59** (2,3): 115-130.

[218] Tamura, Y., H. Kikuchi & K. Hibi (2001), Extreme wind pressure distributions on low-rise building models, *J. Wind Eng. Ind. Aerodyn*. **89**: 1635 - 1646.

[219] Tamura, Y., S. Suganuma, H. Kikuchi & K. Hibi (1999), Proper orthogonal decomposition of random wind pressure field, *J. Fluids & Structures,* **13**: 1069 - 1095.

[220] Taniike, Y. (1992), Interference mechanism for enhanced wind forces on neighbouring tall buildings, *J. Wind Eng. Ind. Aerodyn*. **41-44**: 1073 - 1083.

[221] Taoka G.T. (1981), Damping measurements of tall structures, Dynamic Response of Structures: *Proc. of the 2nd Eng. Mech. Div. Specialty Conf.* ASCE, Atlanta, USA.

[222] Tennekes, H. (1973), The Logarithmic Wind Profile, *J. Atmospheric Sciences,* **30**: 234-238.

[223] Tennekes, H. and Lumley,J.L. (1972), *A first course in turbulence*, The MIT Press, Cambridge, MA, USA.

[224] Teunissen, H.W. (1979), Measurements of planetary boundary layer wind and turbulence characteristics over a small suburban airport, *J. Ind. Aerodyn*. **4**: 1 - 34.

[225] The Experimental Fluid Dynamics research group at Dept. of Applied Mechanics, Thermo- and Fluid Dynamics, NTNU: http://www.mtf.ntnu.no/people/pak/lab/.

[226] The Icelandic Meteorological Office. Data recorded at station no. 040300. Data available at: http://www.ncdc.noaa.gov.

[227] Tieleman, H.W. (1993), Pressures on surface-mounted prisms: the effects of incident turbulence, *J. Wind Eng. Ind. Aerodyn.* **49**: 289-300.

[228] Tieleman, H.W. (1995), Universality of velocity spectra, *J. Wind Eng. Ind. Aerodyn.* **56**: 55-69.

[229] Tschanz, T (1982), Measurement of Total Dynamic Loads Using Elastic Models With a High Natural Frequency, *Int. Workshop on Wind Tunnel Modelling for Civil Engineering Applications*, Cambridge Univ. Press.

[230] Turner, J.S. (1973), *Buoyancy effects in fluids*, Cambridge University Press.

[231] Uehara K., S. Murakami, S. Oikawa & S. Wakamatsu (2000), Wind tunnel experiments on how thermal stratification affects flow in and above urban street canyons, *Atmospheric Environment*, **34**, (10): 1553-1562.

[232] Uematsu, Y. & N. Isyumov (1998), Peak gust pressures acting on the roof and wall edges of a low-rise building, *J. Wind Eng. Ind. Aerodyn.* **77-78**: 217-231.

[233] Uematsu, Y. & N. Isyumov (1999), Wind pressures acting on low-rise buildings, *J. Wind Eng. Ind. Aerodyn.* **82**: 1-25.

[234] Ueng, J.-M., C.-C. Lin & P.-L. Lin (2000), System identification of torsionally coupled buildings, *Computers and Structures*, **74**: 667-686.

[235] Vanmarcke, E. H. (1972), Properties of spectral moments with applications to random vibration, *J. Engr. Mech. Div.* ASCE, **98** (EM2).

[236] Vickery B.J. & R. Basu (1983), Simplified Approaches to the Evaluation of the Across-Wind Response of Chimneys, *J. of Wind Eng. and Ind. Aerodyn.* **14** (1-3): 153-166.

[237] Vickery, B.J. & A.W. Clark (1972), Lift and across-wind response of tapered stacks, *J. of Struc. Div.* ASCE, **98** (ST1), Proc. Paper 8634: 1-20.

[238] Vickery, B.J. (1965), *On the flow behind a coarse grid and its use as a model of atmospheric turbulence for studies related to wind loads on buildings*, National Physical Laboratory (UK) Aero Report 1143.

[239] von Karman, T. (1948), Progress in statistical theory of turbulence, *Proc. Nat. Acad. Sci*. Washington D.C.: 530-539.

[240] Wagaman, S.A., K.A. Rainwater, K.C. Mehta & R.H. Ramsey (2002), Full-scale flow visualization over a low-rise building, *J. Wind Eng. Ind. Aerodyn,* **90** (1): 1-8.

[241] Waldeck, J.L. (1983), A digital system for the measurement of wind effects on large structures, *J. of Wind Eng. and Ind. Aerodyn.* **13** (1/3): 453-464.

[242] Wyatt, T.A. & G. Best (1984), Case-Study of the Dynamic Response of a Medium-Height Building to Wind-Gust Loading, *Eng. Struct.* 6 (4): 256-261.

[243] Wyatt, T.A. (1971), The calculation of structural response, *The modern design of wind sensitive structures*, CIRIA publication, London, p. 83-94.

[244] Wyatt, T.A. (1977), Mechanism of damping, *Symp. Dyn. Behavior Bridge Transport and Road Research Laboratory*, Growthrone, Berkshire.

[245] Wyatt, T.A. (1981), Evaluation of gust response in practice, *Wind Eng. in the Eighties*, CIRIA publication, London, p. 7.1-7.27.

[246] Wyatt, T.A. (1992), Dynamic Gust Response of Inclined Towers, *J. Wind Eng. Ind. Aerodyn.* **43** (1-3): 2153-2163.

[247] Wyatt, T.A. (1995), Engineering applications and requirements of prediction of extreme wind gust effects, *Proc. Instn. Civ. Engs. Structs. & Bldgs.,* **110**: 322-325.

[248] Wyatt, T.A. (2002), Wind loading. In *Dynamic loading and design of structures*, Kappos, A.J. (editor) Spon Press, London.

[249] Yamada, M., Y. Uematsu & R. Sasaki (1996), A visual technique for the evaluation of the pedestrian-level wind environment around buildings by using infrared thermography, *J. Wind Eng. Ind. Aerodyn.* **65**: 261-271.

[250] Yong, L. & N.C. Mickleborough (1989), Modal identification of vibrating structures using ARMA model, *J. Engr. Mech.* ASCE, **115** (10).

[251] Yoshida, M., K. Kondo & M. Suzuki (1992), Fluctuating wind pressure measured with tubing system, *J. Wind Eng. Ind. Aerodyn.* **42**(1-3): 987-998.

Appendix A - Photographs of local surroundings

The appendix contains photographs meant to provide further information and understanding of the local surroundings of the study-building. Figures A-1 through A-8 are taken from the building roof. Whereas Figure A-9 and A-10 give an idea of the terrain differences between summer and winter and related surface roughness.

Figure A-1 View from the study-building towards southwest. The location of the anemometer mast at the Meteorological Office is marked.

Figure A-2 View from the study-building towards west.

Figure A-3 View from the study-building towards northwest. The location of the anemometer mast at the Meteorological Office is marked.

Figure A-4 View from the study-building towards north.

Figure A-5 View from the study-building towards northeast.

Figure A-6 View from the study-building towards southeast.

Figure A-7 View from the study-building towards east.

Figure A-8 View from the study-building towards south.

(a) Summer - view towards southwest.

(a) Winter - view towards southeast.

Figure A-9 A view across the neighbourhood of the study-building showing the contrast between summer and winter. The study-building is not visible.

Appendix B - Coherence of pressure

In this section, the coherence characteristics of full-scale and model scale data will be compared in a similar fashion as the spectral characteristics. Figure B-1 and Figure B-2 show examples of coherence as a function of frequency for both full-scale and model scale. The wind direction is 90°from north. The full-scale coherence shown in Figure B-1 is referred to the Tap F9 on the east side (windward side), whereas the coherence shown in Figure B-2 is referred to Tap F1 on the south side (leeward side). The model scale coherence is referred to equivalent locations on the model (see Figure 5.9). However, it should be noted that the full- and model scale tap locations compared are not in all cases equivalent (see Figure 5.9), which does distort the comparison in some instances.

On average, the full- and model scale coherence show a good comparison. Most of the major discrepancies can be explained by differences in tap location between model and building.

As expected the coherence between pressure at Tap F9 and other taps along the east side is reduced with an increased distance between Taps. However, it is interesting that pressure at Tap F9 shows a stronger coherence with pressure at Taps 3, 4 and 7 than for Taps F1, F2, F5, F6 and F8. It is therefore clear that the coherence relation depends not only on distance, but also very strongly on Tap position with regard to the characteristics of the flow surrounding the building.

Pressure at Tap F1 shows a rather different coherence behaviour, which seems to be more dependent on the frequency content of the different flow regimes around the building.

It can be noted that the coherence is often higher at frequency bands above the “zero” frequency. For instance looking at the coherence between taps on the south side of the building and taps on the east and west side of the building, one can see a peak coherence in the frequency band of 0.04 to 0.1 Hz, depending on which taps are involved. Transforming

this frequency into length through the mean wind velocity would result in a length scale of 105 to 250 m, which may indicate the area affected by the wake created by the flow around the building. On the other hand if we look at the taps at the corners on the other side of the building, i.e. taps 6, 7, 8 and 9, it is clear that the coherence has a peak at a higher frequency band or at 0.4 to 0.6 Hz. That frequency band would transform to a length scale of about 20 m/s, i.e. approximately the side and height dimensions of the tower.

To gain a different view on the average coherence involved, the coherence evaluated for each tap combination was averaged over frequency. It can then be plotted as a function of distance between taps along the perimeter of the building. This is shown in Figure B-3 along with some exponential functions representing the simplified coherence description often used. It is clear that the frequency-averaged coherence could be modelled by a combination of exponential functions. A relatively good comparison is found between the full-scale and model scale frequency averages of coherence, although a slightly more variation is seen in the model scale data. Figure B-4 and Figure B-5 show the frequency maximum and standard deviation of coherence as a function of perimeter distance between taps. They give a further indication of the variability involved.

Another possibility of evaluating average statistics of coherence is to look at the statistics across all the tap combinations and view the coherence statistics as a function of frequency. This is done in Figure B-6 and Figure B-7. The figures show a generally fair agreement between full-scale and model scale. In addition, the frequency dependence already seen in the spectrum is magnified in this representation. For the model scale data, coherence peaks are seen at 0.035 Hz, 0.07 Hz and then at frequencies above 0.2 Hz, especially at 0.6 Hz. In the model scale, the frequency of 0.035 may correspond to a length scale of about 2 m and is perhaps in some way related to the dimensions of the wind tunnel. The frequency 0.07 Hz, which is also noticeable in the full-scale coherence, is more likely to be related to the wake created by the building. The frequency of 0.6 Hz on the other hand could correspond to the dimensions of the building. It is noteworthy that the standard deviation as show in Figure B-7 is at a minimum when the spatial average of coherence is at maximum.

Figure B-8 to Figure B-13 show the same information as Figure B-1 to Figure B-7, but for another mean wind direction, that is 19° from north. The coherence is evaluated based on the same full-scale data as the spectral information shown in Figure 5.31 to Figure 5.35. Generally, similar tendencies are seen as for the 90° wind direction, which indicates that the main features of the coherence characteristics are not very strongly dependent on wind direction.

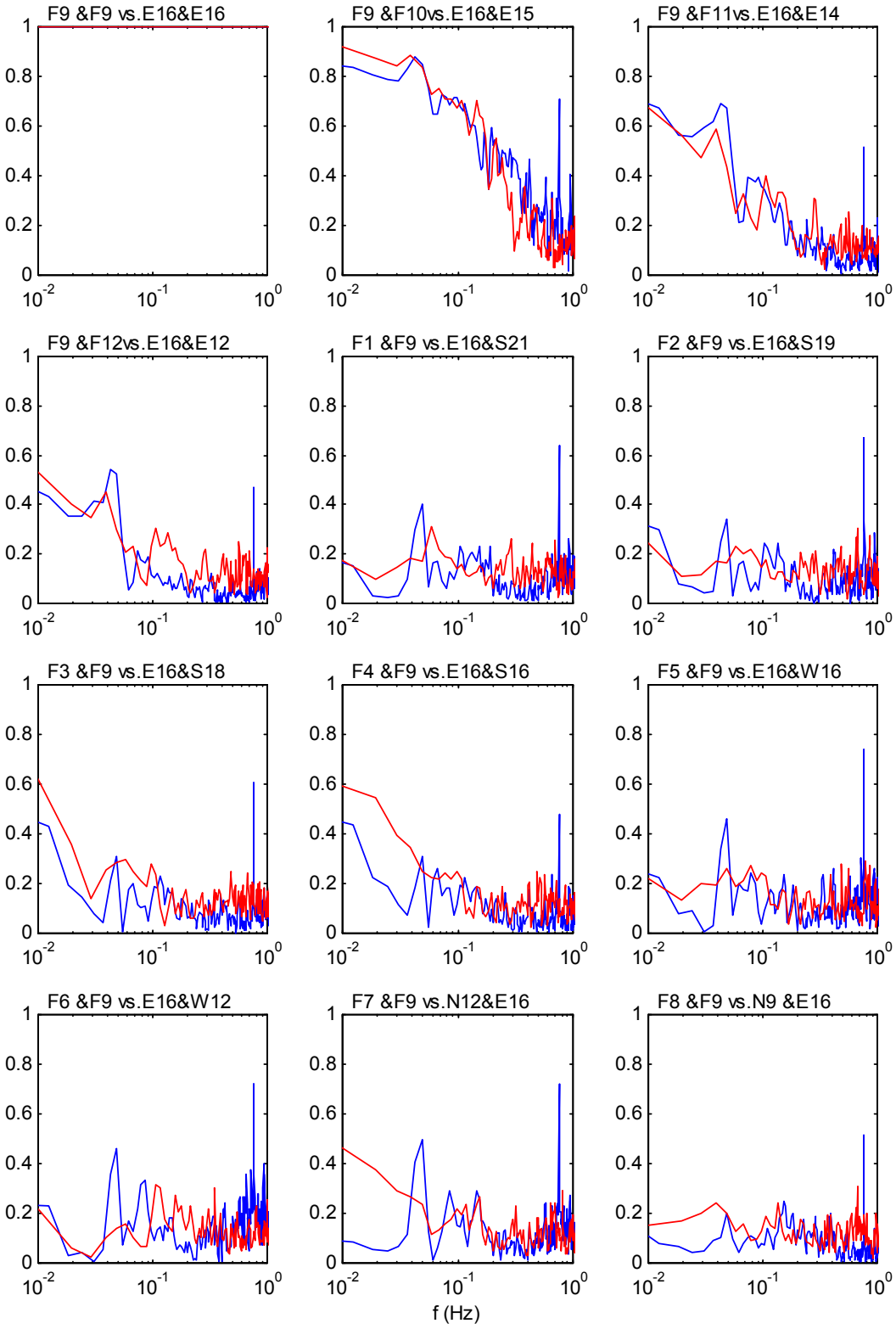

Figure B-1 Example of coherence between pressure coefficients as measured at different taps as a function of frequency for a mean wind direction of 90° from north. The whole lines show coherence evaluated based on full-scale recordings and the dotted line shows coherence evaluated based the model in the wind tunnel. The tap numbers involved are given above each curve and can be referred to **Figure 5.1** and **Figure 5.9** for reference.

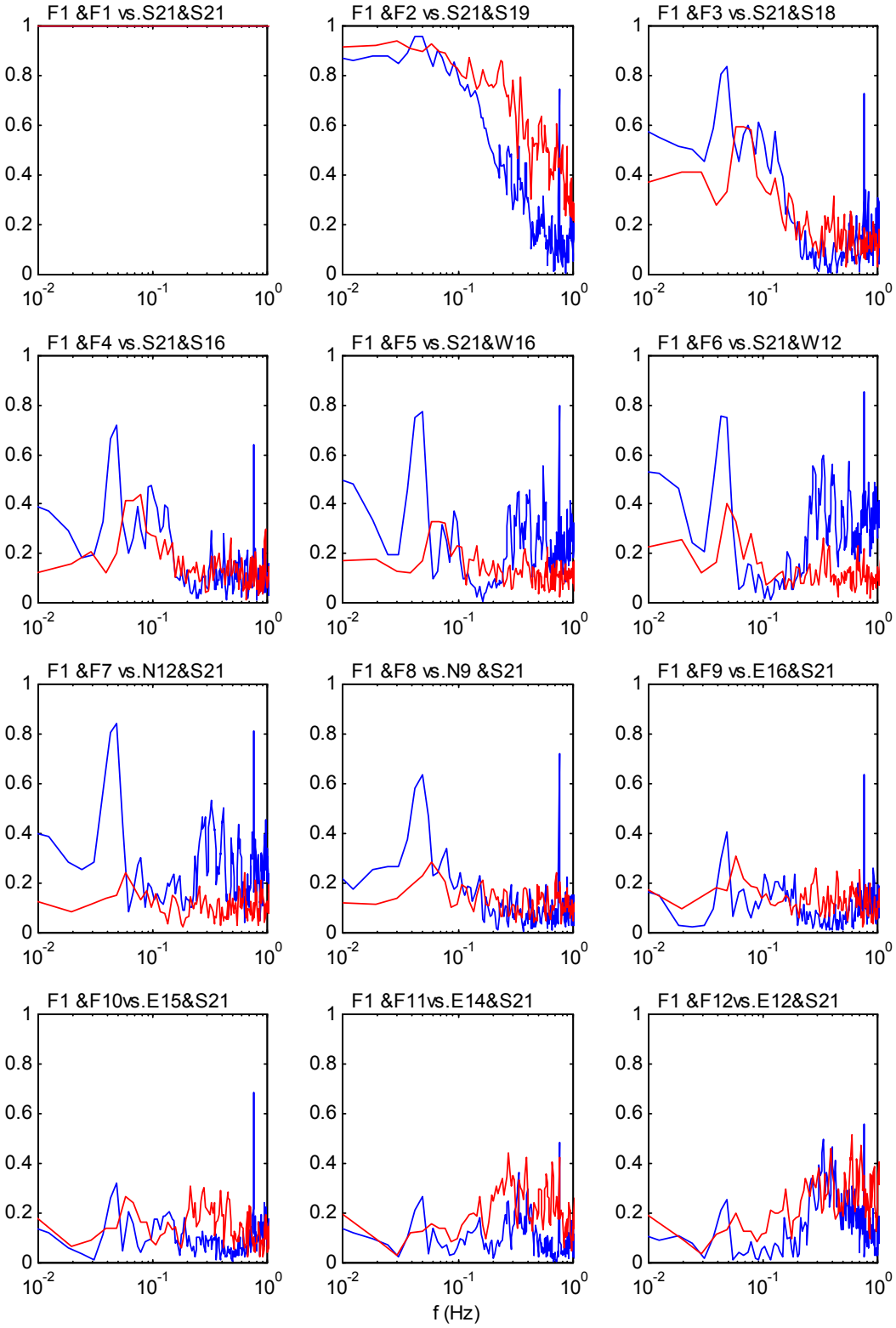

Figure B-2. Example of coherence between pressure coefficients as measured at different taps as a function of frequency for a mean wind direction of 90° from north. The whole lines show coherence evaluated based on full-scale recordings and the dotted line shows coherence evaluated based the model in the wind tunnel. The tap numbers involved are given above each curve and can be referred to **Figure 5.1** and **Figure 5.9** for reference.

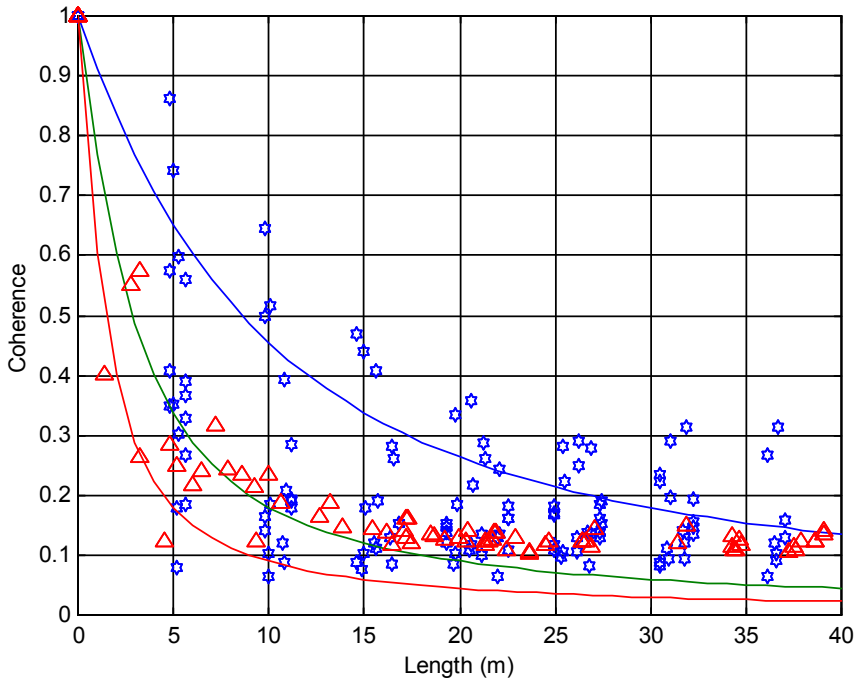

Figure B-3. Frequency average of coherence between taps distributed around the top perimeter of the building, as a function of perimeter distance between taps. The hexagons represent wind tunnel data while the triangles represent full-scale data for a mean wind direction of 90° from north. The solid lines represent the frequency average from a traditional exponential coherence model, with decay exponent values of 2, 4 and 12.

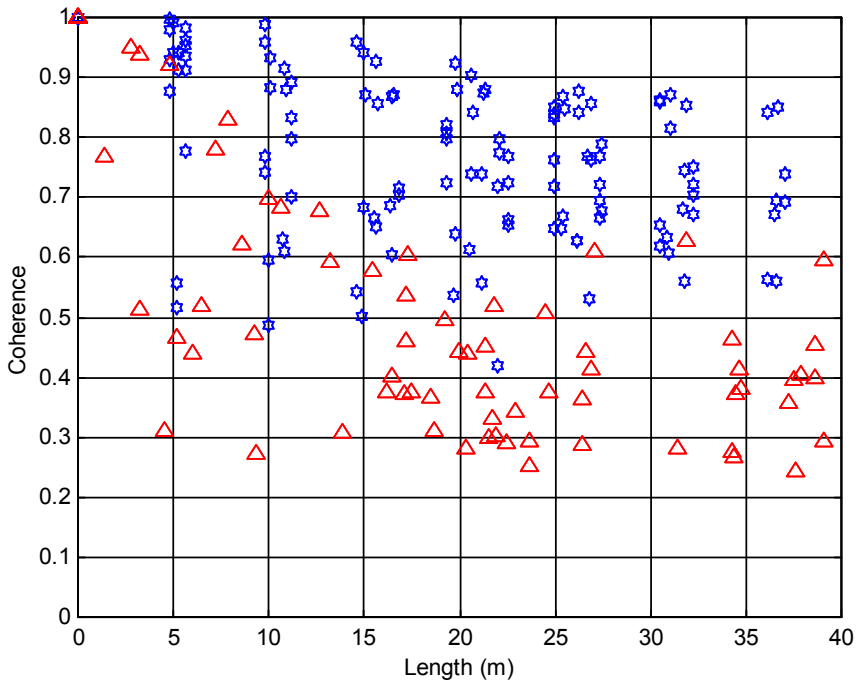

Figure B-4. Frequency maximum of coherence between taps distributed around the top perimeter of the building, as a function of perimeter distance between taps. The hexagons represent wind tunnel data while the triangles represent full-scale data for a mean wind direction of 90° from north.

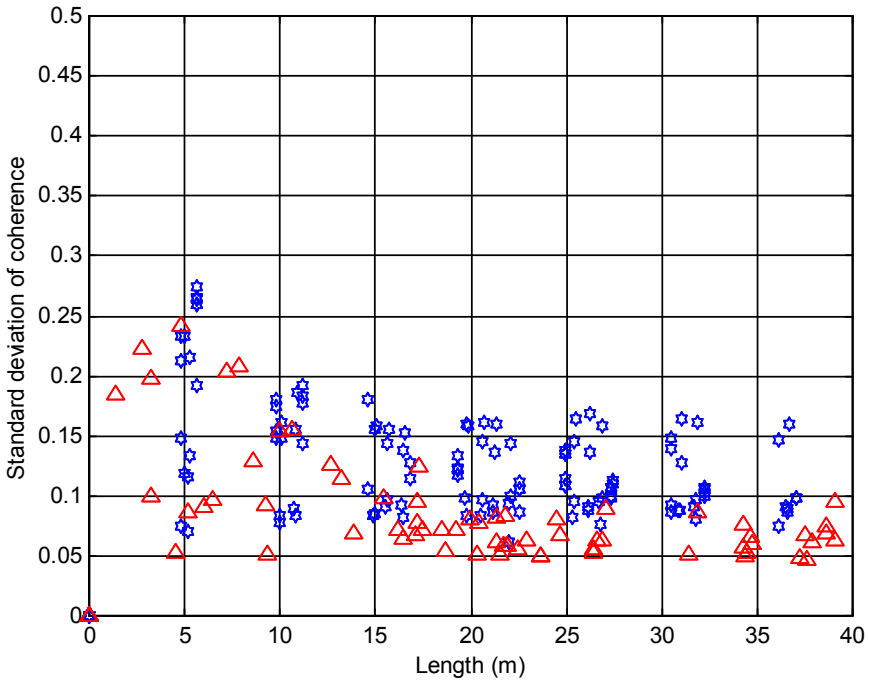

Figure B-5 Frequency standard deviation of coherence between taps distributed around the top perimeter of the building, as a function of perimeter distance between taps. The hexagons represent wind tunnel data while the triangles represent full-scale data for a mean wind direction of 90° from north.

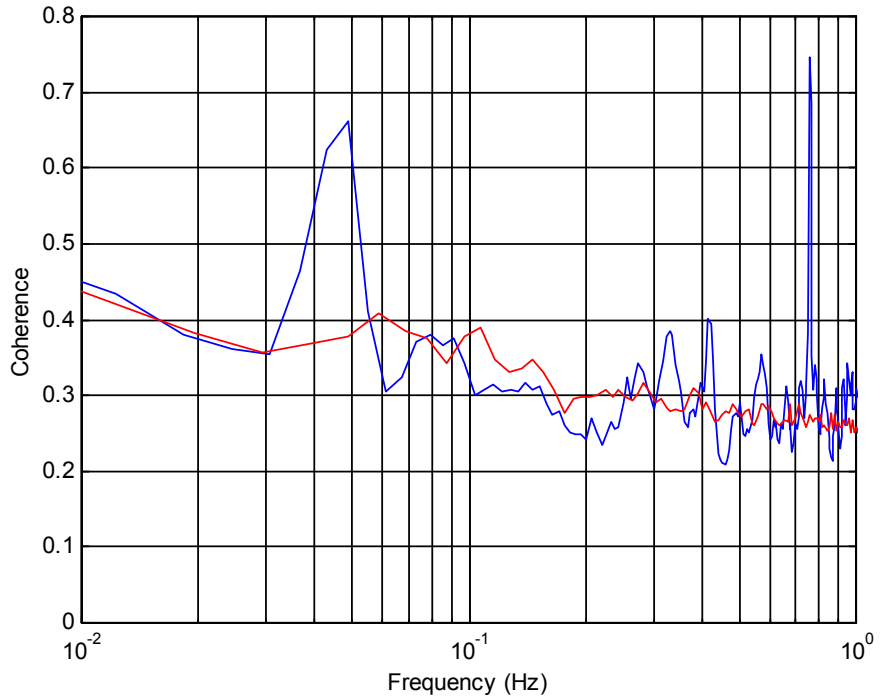

Figure B-6 Spatial average of coherence between taps distributed around the top perimeter of the building as a function of frequency. The whole line represents full-scale data whereas the dotted line represents wind tunnel data for a mean wind direction of 90° from north.

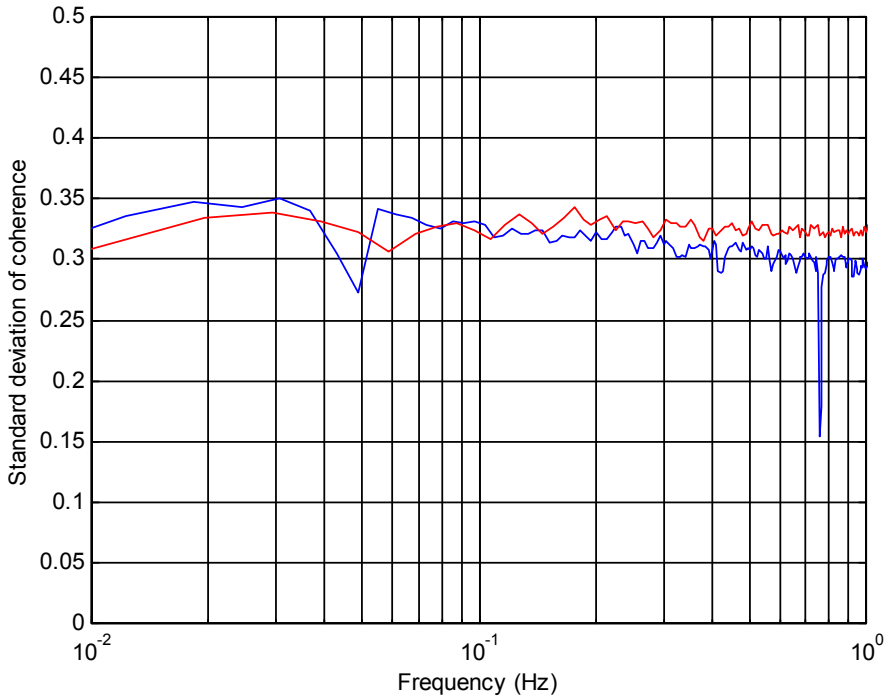

Figure B-7 Spatial standard deviation of coherence between taps distributed around the top perimeter of the building as a function of frequency. The whole line represents full-scale data whereas the dotted line represents wind tunnel data for a mean wind direction of 90° from north.

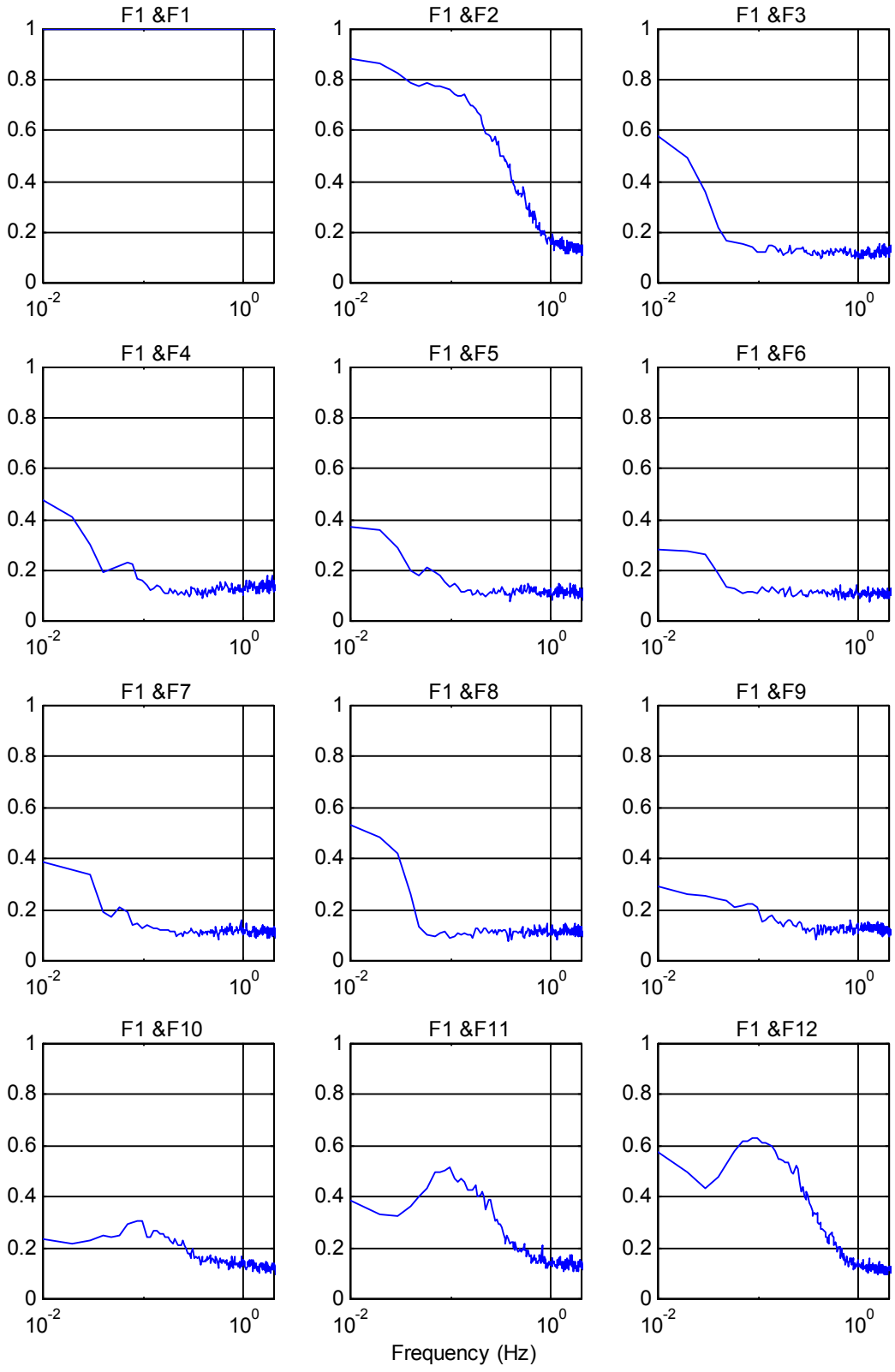

Figure B-8 Example of coherence between pressure coefficients as measured at different taps as a function of frequency. The coherence is evaluated for a mean wind direction of 360° from north, based on 73 full-scale runs. The tap numbers involved are given above each curve and can be referred to **Figure 5.1** and **Figure 5.9** for reference.

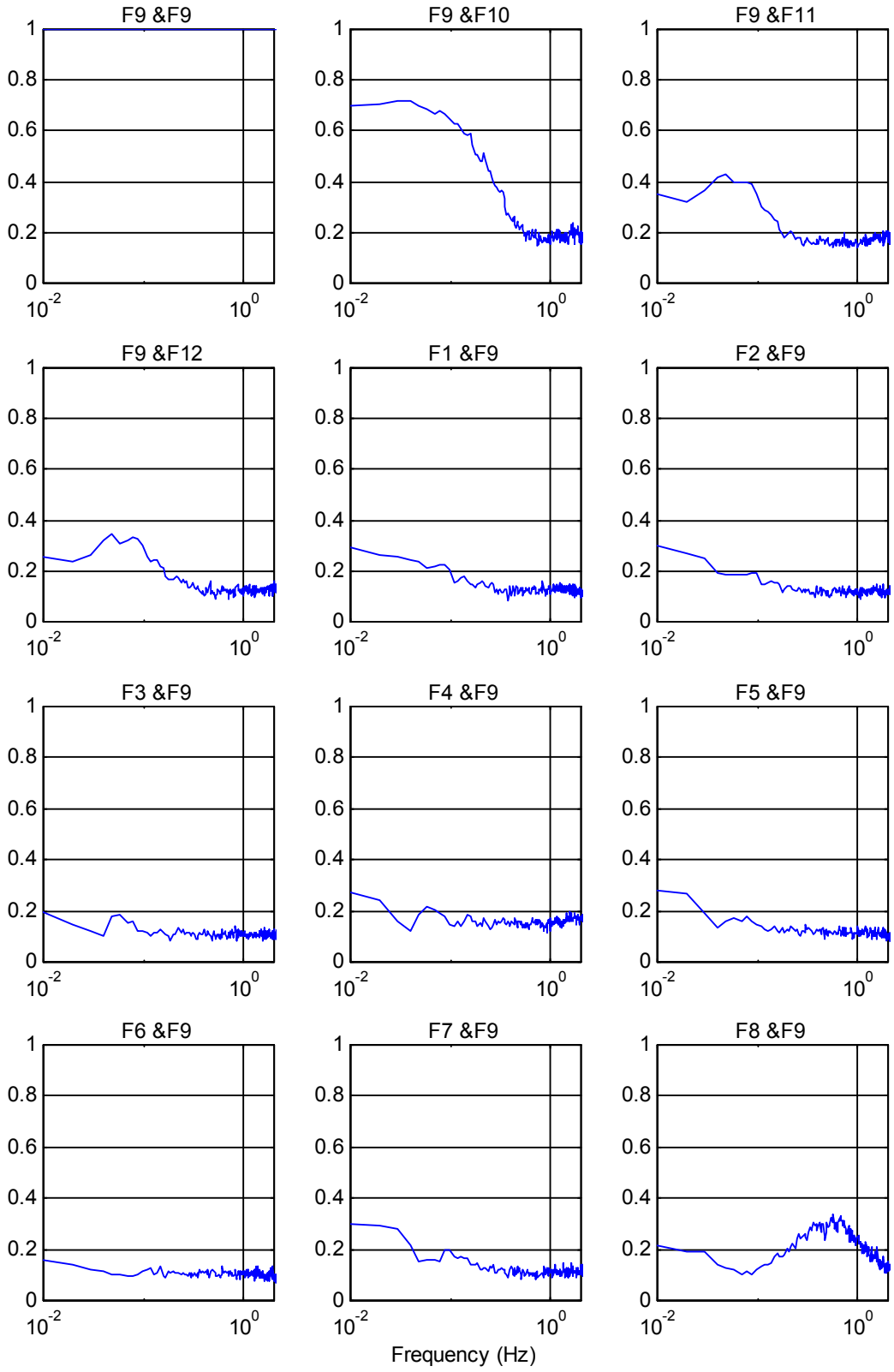

Figure B-9 Example of coherence between pressure coefficients as measured at different taps as a function of frequency. The coherence is evaluated for a mean wind direction of 360° from north, based on 73 full-scale runs. The tap numbers involved are given above each curve and can be referred to **Figure 5.1** and **Figure 5.9** for reference.

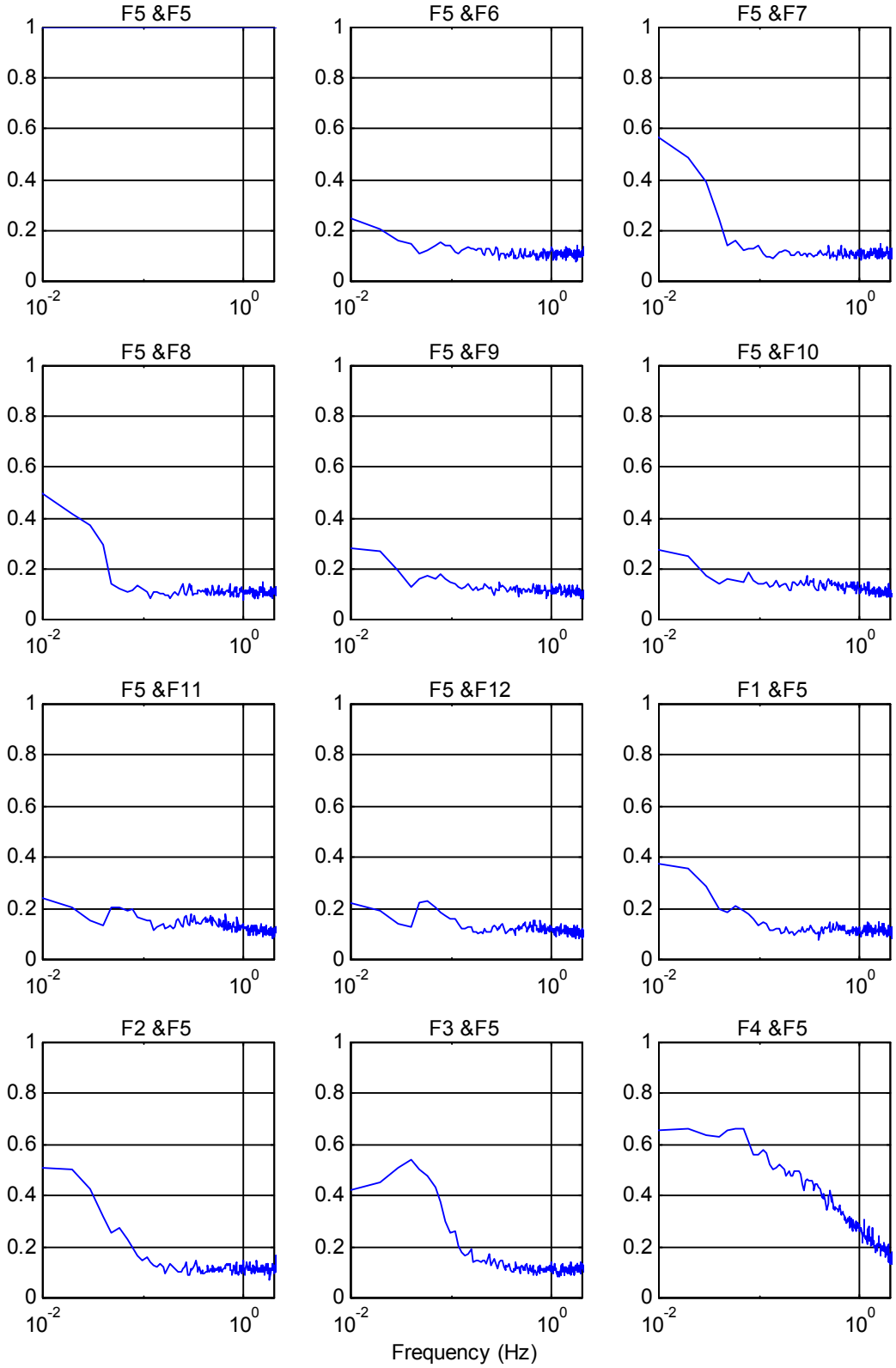

Figure B-10 Example of coherence between pressure coefficients as measured at different taps as a function of frequency. The coherence is evaluated for a mean wind direction of 360° from north, based on 73 full-scale runs. The tap numbers involved are given above each curve and can be referred to **Figure 5.1** and **Figure 5.9** for reference.

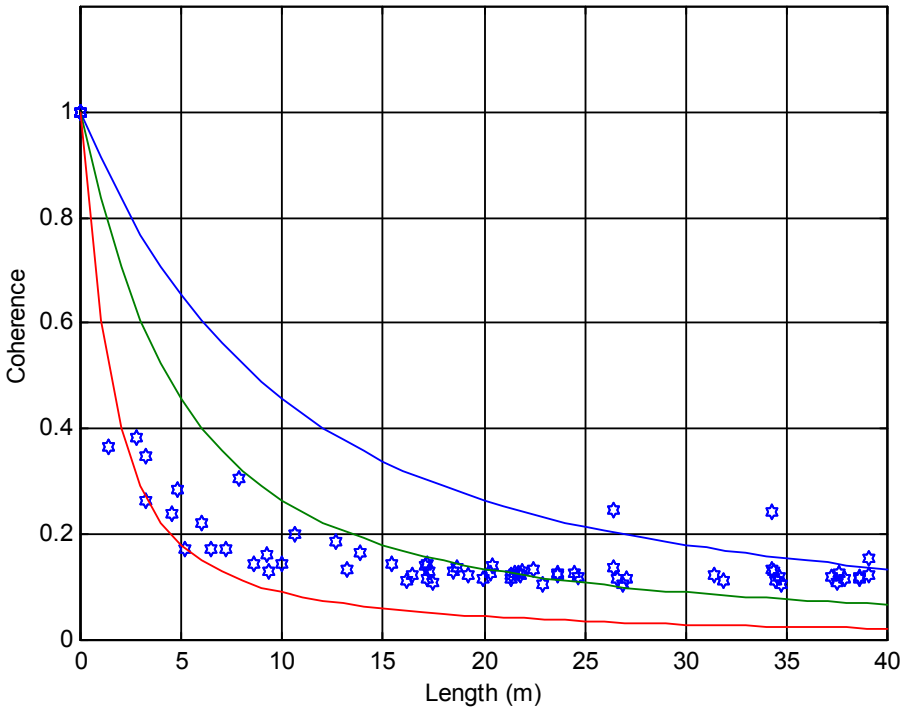

Figure B-11 Frequency average of coherence between taps distributed around the top perimeter of the building, as a function of perimeter distance between taps. The hexagons represent coherence evaluated for a mean wind direction of 360° from north, based on 73 full-scale runs. The solid lines represent the frequency average from a traditional exponential coherence model, with decay exponent values of 2, 4 and 12.

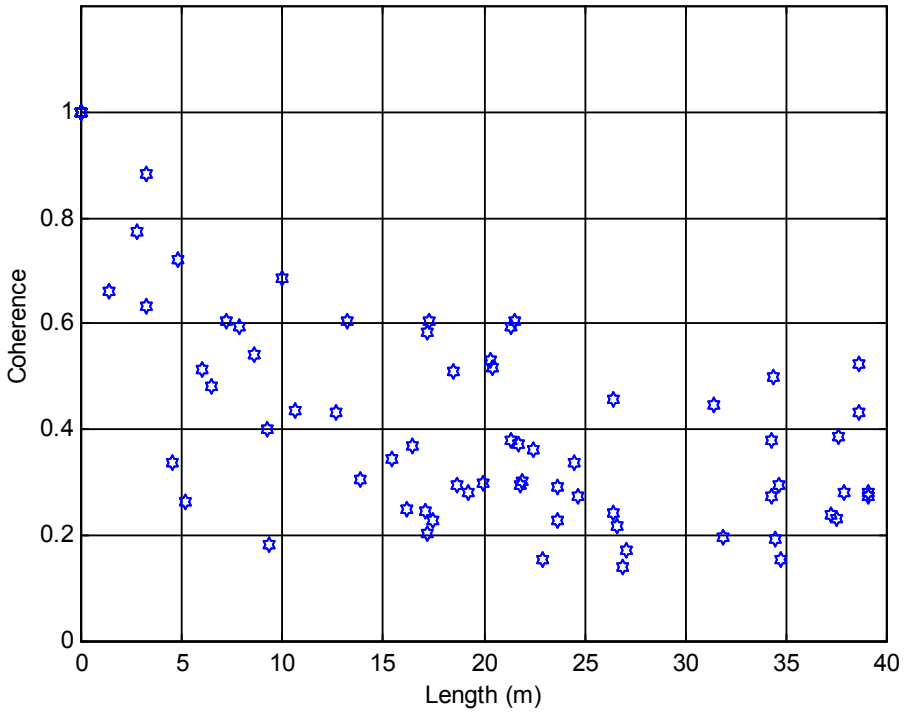

Figure B-12 Frequency maximum of coherence between taps distributed around the top perimeter of the building, as a function of perimeter distance between taps. The hexagons represent coherence evaluated for a mean wind direction of 360° from north, based on 73 full-scale runs.

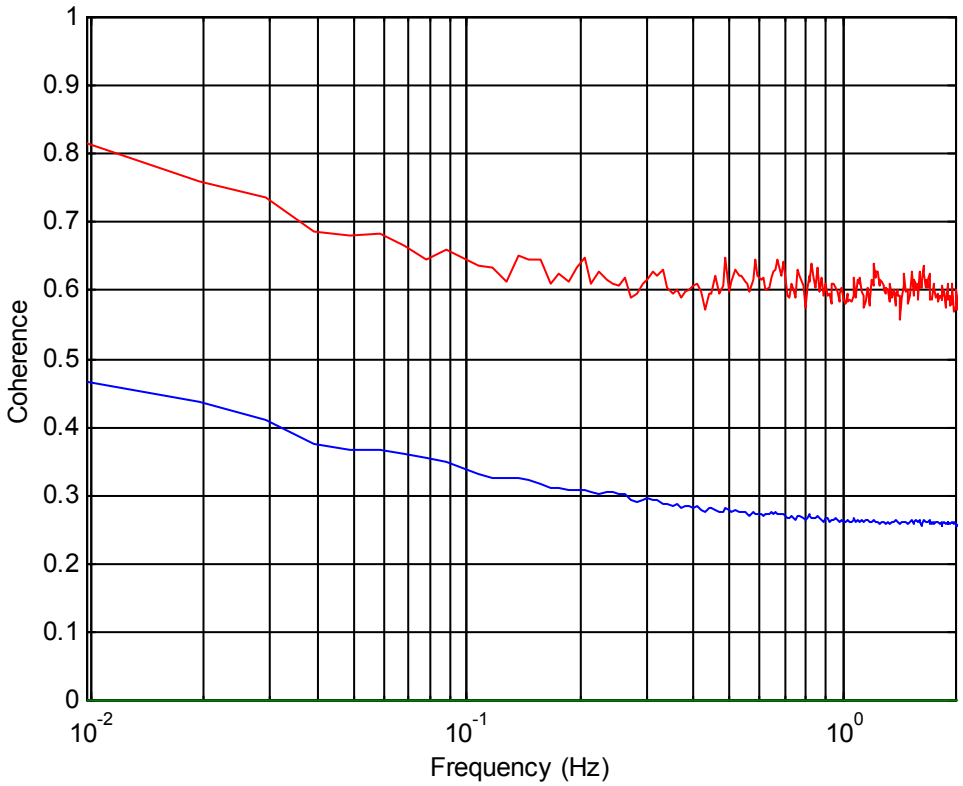

Figure B-13 Spatial average of coherence between taps distributed around the top perimeter of the building as a function of frequency. The coherence is evaluated for a mean wind direction of 360° from north, based on 73 full-scale runs. The whole line represents the spatial average of the mean coherence from the 73 runs, whereas the dotted line represents the spatial average of maximum coherence values at each frequency.

Appendix C - Traditional system identification methods

The following method description applies for lightly damped linear structures subjected to broadband excitation. For common civil engineering structures, damping is less than 10 % and consequently there is little difference between the damped and undamped natural frequencies. By assuming a broadband excitation with substantially flat spectral density for the frequency-range of interest, it is possible to estimate natural frequencies and damping ratios by only measuring the structural response.

C.1 The time domain - The autocorrelation function method

In accordance with the assumptions mentioned above, the damping ratio for a single degree-of-freedom system can be determined from the autocorrelation function as:

$$\zeta = \frac{1}{2\pi n_c} \ln\left(\frac{\max(R_y)_k}{\max(R_y)_{k+n_c}} \right) \tag{C.1}$$

Here ζ is the critical damping ratio, $\max(R_y)_k$ is the peak amplitude of the autocorrelation function of the response y, at cycle k, and n_c refers to the number of cycles considered. The natural frequency can be estimated by counting the number of waves per time interval. This approach can be applied to multi-degree-of-freedom systems by considering each mode separately using band-pass filtering.

C.2 The frequency domain - spectral density methods

C.2.1 The power spectral density method

The power spectral density of the response is characterised by narrow peak located at the natural frequency. The critical damping ratio, ζ, can be estimated from the bandwidth of the spectral peak as:

$$\zeta \cong \frac{A_b}{2}\left[1-\frac{3A_b^2}{8}\right] \text{ where } \qquad A_b = \frac{\left(f_b^2 - f_a^2\right)}{\left(f_b^2 - f_a^2\right)\sqrt{q_s - 1}} \tag{C.2}$$

Here f_a and f_b are the frequencies where the response spectral densities become $1/q_s$ of its maximum. In practice, $q_s = 2$ is usually used for simplicity, and the method therefore often named the half power point method.

C.2.2 The spectral moment method

Vanmarcke proposed in 1972 [235], to use the first three spectral moments in estimating the natural frequency and damping parameters for lightly damped systems through the following relations:

$$\zeta = \frac{\pi}{4}\left(1-\frac{\mu_1^2}{\mu_0\mu_2}\right) \qquad \text{and} \qquad f = \frac{1}{2\pi}\sqrt{\frac{\mu_2}{\mu_0}} \tag{C.3}$$

The spectral moments and system parameters deduced from them are sensitive to baseline noise, which can be induced by the recording instruments and by influences from other modes of vibration. To minimise these disturbances, a band-pass filter can be applied to exclude any spectral contribution from frequencies outside the band-limits ($\omega_a < \omega_j < \omega_b$). It can be shown, that this does not change the estimated natural frequency. However, the critical damping ratio for the j-th mode, ζ_j, has to be corrected according to the relation:

$$\zeta_j = \frac{\pi}{4}\left(1-\frac{\mu_1^2}{\mu_0\mu_2}\right)\left(\frac{1+\left(\omega_a/\omega_j\right)}{1-\left(\omega_j/\omega_b\right)}\right) \tag{C.4}$$

This correction is valid for the case when $\omega_a/\omega_j = \omega_j/\omega_b$.

ISBN 82-471-5495-1
ISSN 0809-103X